Dissertation
submitted to the
Combined Faculties for the Natural Sciences and for Mathematics
of the Ruperto-Carola University of Heidelberg, Germany
for the degree of
Doctor of Natural Sciences

Put forward by

Diplom-Physiker Ronny Zhao-Geisler

Born in: Dohna, Germany

Oral examination: 15th November, 2010

The Surprising mid-IR Appearance of the Asymptotic Giant Branch Stars R Aql, R Aqr, R Hya, V Hya and W Hya

Molecular and dust shell diameters and their pulsation dependence probed with the MIDI Interferometer

Referees: Prof. Dr. Andreas Quirrenbach
Dr. Cornelis Dullemond

Abstract

Asymptotic Giant Branch (AGB) stars are the main distributors of dust into the interstellar medium due to their high mass loss rates in combination with an effective dust condensation. It is therefore important to understand the dust formation process and sequence in their extended atmosphere. The wind of these stars is driven by strong stellar pulsation in combination with radiation pressure on dust. High-resolution mid-IR interferometry is sensitive to the structure of the stellar atmosphere, consisting of the continuum photosphere and overlying molecular layers, as well as to the properties of the dust shell.

This work studies the location of molecular layers and newly formed dust as a function of pulsation cycle and chemistry, as well as tries to identify molecules and dust species which cause the diameter of the star to vary across the N-band spectral domain ($8 - 13$ μm).

Mid-IR interferometric data of the oxygen-rich AGB stars R Aql, R Aqr, R Hya and W Hya, and the carbon rich AGB star V Hya were obtained with MIDI/VLTI between April 2007 and September 2009, covering several pulsation cycles. The spectrally dispersed visibility data are modeled by fitting a fully limb-darkened disk in order to analyze the molecular layers, and by fitting a Gaussian in order to constrain the extension of the dust shell. Because uv-coverage was sufficient for R Hya and W Hya, asymmetries could be studied with an elliptical fully limb-darkened disk.

The angular diameters of all oxygen-rich stars in the sample appear to be about two times larger in the mid-IR than their photospheric diameters estimated from the near-IR. The overall larger diameter in the mid-IR originates from a warm optically thick molecular layer of H_2O, and a detected gradual increase longword of 10 μm can be attributed to the contribution of a spatially resolved, optically thin, close corundum (Al_2O_3) dust shell. A significant contribution of SiO shortward of 10 μm cannot be ruled out for R Aqr. The circumstellar silicate dust shells of all oxygen-rich stars are found to be very extended except for R Aqr. For the carbon-rich star V Hya, it can only be concluded that amorphous carbon and SiC dust is already present close to the star.

The observed angular diameters are smaller at visual minimum than at visual maximum with peak-to-peak variations on the oder of 20% to 30% except for W Hya for which the variation is 6%. The diameter periodicity can be explained with the phase-dependent water vapor and corundum dust presence and its temperature sensitivity. Since this variation traces only the location of constituents which are not relevant for the wind formation, no firm conclusions can be drawn concerning the mass loss mechanism. One can only speculate that more dust forms at visual minimum. Cycle-to-cycle variations of the layer traced with MIDI are lower than intracycle variations, and are on the order of 6%. R Hya does not show any deviations from circular symmetry, while an asymmetry of the extended atmosphere of W Hya can be confirmed.

These observations of a larger sample of stars than available before confirm previous results, and emphasize the need for dynamic stellar model atmospheres with consistently included dust formation close to the star. It can also be concluded that interferometric observations in the N-band are an irreplaceable tool to resolve close stellar structures and to search for atmospheric constituents.

Zusammenfassung

Asymptotische Riesenast-Sterne (AGB-Sterne) sind aufgrund ihrer hohen Massenverlustrate in Kombination mit einer effektiven Staubkondensation die Hauptverteiler von Staub an das interstellare Medium. Es ist deswegen wichtig, die Staubentstehung in den ausgedehnten Atmosphären zu verstehen. Der Wind dieser Sterne wird durch starke Pulsationen in Kombination mit Strahlungsdruck an Staub angetrieben. Hochauflösende Interferometry im mittleren Infrarot (IR) ist empfindlich auf die Struktur der Sternenatmosphäre, bestehend aus der Photosphäre, der darüberliegenden Molekülschichten sowie der Eigenschaften der Staubsphäre.

Diese Arbeit studiert den Ort der Molekülschichten und des entstehenden Staubes als Funktion des Pulsationszyklus und der zugrundeliegenden Chemie, sowie versucht herauszufinden welche Moleküle und Staubarten existieren und dafür verantwortlich sind dass der gemessene Durchmesser innerhalb das N-Bandes variiert ($8 - 13$ μm).

Interferometrische Daten der sauerstoffreichen AGB Sterne R Aql, R Aqr, R Hya und W Hya, und des kohlenstoffreichen AGB Sterns V Hya wurden im mittleren IR mit MIDI/VLTI zwischen April 2007 und September 2009 aufgenommen und decken mehrere Pulsationszyklen ab. Die spektral aufgelösten Visibility Daten wurden modelliert durch eine Scheibe mit Randverdunkelung, um die Molekülschalen zu analysieren, und durch eine Gaußverteilung um die Ausdehnung der Staubsphäre zu untersuchen. Aufgrund einer guten uv-Abdeckung für R Hya and W Hya konnten Asymmetrien mit einer elliptischen Scheibe mit Randverdunkelung untersucht werden.

Der Winkeldurchmesser aller beobachteten sauerstoffreichen Sterne scheint im mittleren IR etwa zweimal so groß zu sein wie die im nahen IR abgeschätzten photosphärischen Durchmesser. Der insgesamt größere Durchmesser im mittleren IR wird verursacht durch optisch dicke Molekülschalen bestehend aus H_2O, und der gefundene gleichmäßige Anstieg bei Wellenlängen größer als 10 μm kann der Existenz einer räumlich aufgelösten, nahen, optisch dünnen Al_2O_3 Staubsphäre zugeordnet werden. Ein zusätzlicher Beitrag von SiO bei Wellenlängen kürzer als 10 μm kann bei R Aqr nicht ausgeschlossen werden. Die größere umgebende, aus Silikaten bestehende Staubschale ist außer für R Aqr für alle untersuchten sauerstoffreichen Sterne sehr ausgedehnt. Für den kohlenstoffreichen Stern V Hya konnte nur festgestellt werden, dass amorpher Kohlenstoff und SiC Staub nahe am Stern existiert.

Die beobachteten Winkeldurchmesser sind während des optischen Minimums geringer als während des optischen Maximums, mit einer Variationen von Maximum zu Maximum zwischen 20% und 30%, außer für W Hya, wo die Variation nur 6% ausmacht. Die Periodizität des Durchmessers kann mit der phasenabhängigen Präsenz von Wassermolekülen und Aluminiumstaub und deren Temperaturabhäng-igkeit erklärt werden. Da sich diese Durchmesserveränderung nur auf Regionen bezieht, die aus Bestandteilen zusammengesetzt sind, die nicht für die Windentstehung verantwortlich sind, kann keine Beziehung zur Massenverlustrate hergestellt werden. Es kann nur vermutet werden, dass mehr Staub während des optischen Minimums entsteht. Zyklus-zu-Zyklus Veränderungen des Durchmessers der mit MIDI beobachteten Schicht sind geringer als intrazyklische Variationen und in der Größenordnung von 6%. R Hya zeigt keine Abweichung von kreisrunder Symmetrie, während ein asymmetrischer Charakter für W Hya belegt werden kann.

Diese Beobachtungen bestätigen an einer größeren Anzahl von Sternen frühere Ergebnisse und unterstreichen die Tatsache, dass dynamische Atmosphärenmodelle für Sterne mit einer konsistenten Einbeziehung der Staubentstehung benötigt werden. Es kann auch gefolgert werden, dass interferometrische Beobachtungen im N-Band unverzichtbar sind, um atmosphärische Strukturen bei AGB-Sternen aufzulösen und deren Zusammensetzung zu untersuchen.

Contents

List of Figures

List of Tables

Symbols, Constants and Acronyms

In this thesis, preferably cgs or natural units are given for comparability and convenience. Table 1 and 2 lists the used symbols and constants, respectively. Acronyms are listed in Table 3.

Table 1: Symbols.

Description	Symbol	Unit
Chi square	χ^2	dimensionless
Emissivity	η	dimensionless
Opacity	κ	dimensionless
Visibility (complex)	V ($\mathcal{V}$)	dimensionless
Spatial frequency	u, v	cycles/arcsec
Wavelength	λ	cm, μm
Wavenumber	k	1/m, 1/cm, 1/μm
Frequency	ν	Hz
Luminosity	L	W, $L_\odot$
Intensity	I	W/m^2
Flux density	S	Jy
Magnitude	m_i, M_i	mag (e.g. i = B, V, J, H, K, L, M, N, Q)
Temperature	T, T_eff	K
Mass	m, M	g, kg, $M_\odot$
Mass loss	$\dot{M}$	$M_\odot$/yr
Density	ρ	g/cm^3, kg/m^3
Coordinates	α, δ	degree ($^\circ$ $'$ $''$), hours ($^\mathrm{h}$ $^\mathrm{m}$ $^\mathrm{s}$)
Proper motion	$\mu_\alpha \cos\delta$, μ_δ	mas/yr
Phase	ϕ	radiant (rad), degree ($^\circ$ $'$ $''$)
Angle	ϑ, PA	radiant (rad), degree ($^\circ$ $'$ $''$)
Angular diameter	θ	milli-arcseconds (mas)
Distance	D	cm, m, pc
Radius	R	cm, m, $R_\odot$, AU
Time, Period	t, T, P	s, d, yr
Velocity	v	cm/s, m/s, km/s
Electrical field	E	V/m
Pressure	p	N/m^2

Table 2: Constants and conversions.

Description	Constant	Value	Unit
Speed of light	c	$2.997\,924\,58 \cdot 10^{8}$	m/s
Gravitational constant	G	$6.672\,59 \cdot 10^{-11}$	$\mathrm{Nm^2/kg^2}$
Planck's constant	h	$6.626\,076 \cdot 10^{-34}$	Js
Boltzmann's constant	k	$1.380\,651 \cdot 10^{-23}$	J/K
Solar mass	$\mathrm{M}_\odot$	$1.9891 \cdot 10^{30}$	kg
Solar radius	$\mathrm{R}_\odot$	$6.96 \cdot 10^{8}$	m
Solar luminosity	$\mathrm{L}_\odot$	$3.845 \cdot 10^{26}$	W
Astronomical unit	AU	$1.495\,979 \cdot 10^{11}$	m
Parsec ($1\,\mathrm{kpc} = 10^3\,\mathrm{pc}$)	pc	$3.085\,678 \cdot 10^{16}$	m
Julian Year ($1\,\mathrm{day} = 86\,400\,\mathrm{s}$)	yr	$3.155\,760 \cdot 10^{7}$	s
Flux density	Jy	$1 \cdot 10^{-26}$	$\mathrm{W/m^2/Hz}$
Angle	rad	$2.062\,648 \cdot 10^{8}$	mas
Gas constant	R	8.314 472	J/K/mol
Pi	π	3.141 592	

Table 3: Acronyms.

Acronym	Meaning
AGB	Asymptotic Giant Branch
AMC	AMorphous Carbon
AT	Auxiliary Telescope
CLV	Center to Limb Variation
CSE	CircumStellar Environment
C-rich	Carbon-rich
ESO	European Southern Observatory
EWS	Expert Work Station
FDD	Fully limb-Darkened Disk
FOV	Field Of View
FWHM	Full Width at Half Maximum
G	Gaussian
HB	Horizontal Branch
HBB	Hot Bottom Burning
HRD	Hertzsprung-Russel Diagram
IR	InfraRed
IRIS	InfraRed Image Sensor
ISO	Infrared Space Observatory
L	irregular
LMC	Large Magellanic Cloud
LTE	Local Thermal Equilibrium
MASER	Microwave Amplification by Stimulated Emission of Radiation
MIA	Midi Interactive Analyses
MIDI	MID-infrared Interferometric instrument
MS	Main Sequence
O-rich	Oxygen-rich
PAH	Polycyclic Aromatic Hydrocarbons
PDCZ	Pulse-Driven Convective Zone
PL	Period-Luminosity
PMR	Period-Mass-Radius
PN	Planetary Nebula
PSF	Point Spread Function
RGB	Red Giant Branch
RSG	Red Super Giant
SED	Spectral Energy Distribution
SN	SuperNova
SR	SemiRegular
STRAP	System for Tip-tilt Removal with Avalanche Photodiodes
TP	Thermal Pulse
UD	Uniform Disk
UT	Unit Telescope

...continues on next page

Acronym	Meaning
VCM	Variable Curvature Mirror
VLT	Very Large Telescope
VLTI	Very Large Telescope Interferometer
WD	White Dwarf
WDS	Washington visual Double Star catalog
WR	Wolf-Rayet

Chapter 1

Motivation

The formation of the Earth and the solar system was only possible since Asymptotic Giant Branch stars previously existed. The question where the building material for the planets and at the end also the life came from, and why it has exactly this abundance, is still an important research area. After the Big Bang, only hydrogen and helium (mixed with a few light elements) existed. Therefore, almost all other known elements must be synthesized later. As we know today, the nucleosynthesis of new elements takes place mainly in stars. Only a few stellar candidates come into consideration, since this material has to be distributed throughout the galaxy from the interior of the star. These are Asymptotic Giant Branch (AGB) stars, Red Super Giant (RSG) stars, Wolf-Rayet (WR) stars and Supernovae (SN). They contribute through strong stellar winds, heavily enriched in Li, C, N, F and s-process elements, or in the case of a SN, through the disruption of the star, producing e.g. p-process elements, to the metal[1] enrichment in galaxies.

AGB stars are the main contributors due to their high mass loss rates in combination with an effective dust condensation. Its fraction is about 90% (Gehrz, 1989; Sedlmayr, 1994). They do not only contribute by ejecting gas, but also by ejecting dust grains into the interstellar medium (ISM). Especially, the dust plays a crucial role for the formation and acceleration of the dense wind. By providing the seed particles for interstellar grains, they contribute to the chemical evolution of the ISM and facilitate further star and planet formation. Due to their high luminosity, variability, large radius and widely distribution throughout the Milky Way, AGB stars are in principle easily detectable and good targets for explorations (an overview of typical properties are given in the next chapter). However, a disadvantage is that their relative low surface temperature shifts the peak emission into the infrared (IR) domain. The earth atmosphere only allows observations in distinct bands in the near-IR and mid-IR, namely J, H, K, L, M, N and Q. In addition, Earth's atmosphere adds a lot of thermal background radiation to the faint radiation from the star and its circumstellar environment.

The closest AGB stars are at a distance of about 100 pc. Together with their enormous radii, they are excellent targets for interferometric observations. In comparison to radio interferometry, optical and IR interferometry is still at the beginning and many achievements can be made, since the use of shorter wavelengths involves more instrumental complications. However, the possibility to spatially resolve the star and its environment makes optical and IR interferometry to a very powerful tool to study AGB stars. With a resolution proportional to $\lambda/B_{\rm proj}$, where $B_{\rm proj}$ is the projected separation on the sky of the two telescopes, measurements of stellar diameters are now achievable for a long time. Simple model assumptions are still necessary to made, but high resolution image techniques are starting to become very successful.

In this thesis, results from observations of the dusty circumstellar environment of AGB stars are analyzed. They are obtained with the mid-IR interferometer MIDI. MIDI operates in the

[1] All elements with Z > 2 are called metals in astronomy.

N-band ($8-13\ \mu$m) with a spectral resolution between 30 and 230. These observations allow to fit stellar diameters and to study warm layers of molecules and dust, as well as the structure of the dense stellar wind. One objective is to identify molecules and dust species that are present in the layers above the photosphere and that cause the diameter of the star to vary across the N-band spectral domain. Candidates are H_2O, SiO and alumina dust (corundum). Responsible for the presence of warm molecular and dust layers is most probably the pulsation, which causes a strong increase in atmospheric scale height. This has been observed in many AGB stars.

The wind of these stars is driven by stellar pulsations in combination with radiation pressure on dust. In order to support this current understanding, the location and composition of newly formed dust as function of the pulsation cycle, mass loss rate and chemistry is investigated in this work. The size of the inner region free of dust is one of the parameters best constrained from mid-IR interferometric observations. This quantity is fundamental for understanding the condition of dust formation. Planetary nebula, the remnants of the AGB evolution, show a rich diversity of shapes. The formation of these asymmetries is unknown, but observations of the spatial distribution of dust near AGB stars may give insight into their origin and probe the most recent mass loss events.

In summary, several important results can be expected:

- the size of the stellar diameter, the molecular layer and the dust forming region and its link to the location of SiO, H_2O and OH masers
- the molecular composition of the layers and the identification of first dust condensates
- constraints on the mass loss geometry from a good spatial frequency coverage
- an understanding of the temporal evolution of dust formation and mass loss
- providing new necessary inputs for dust driven wind theories and stellar atmospheric models

Chapter 2 and 3 gives an introduction to AGB stars and IR interferometry, respectively. In particularly, some background details of the observed AGB stars (R Aql, R Aqr, R Hya, V Hya and W Hya) are summarized at the end of Chapter 2. Chapter 4 is mainly dedicated to the observation strategy and data reduction. It includes as an important part the description how raw MIDI interferometric data are converted into visibilities. Chapter 5 shows the light curves, spectra and visibilities as well as the results of the applied different visibility models. The interpretation and discussion on the obtained molecular and dust shell diameters, its pulsation dependence and the detected asymmetries is given in Chapter 6. Chapter 7 summarizes and concludes this work.

Chapter 2

Asymptotic Giant Branch Stars

Asymptotic Giant Branch (AGB) stars are the final evolutionary stage of low and intermediate mass stars. This phase of evolution is characterized by nuclear burning of hydrogen and helium in thin shells on top of an electron-degenerate core of carbon and oxygen, or for the most massive AGB stars a core of oxygen, neon and magnesium. New elements produced in the nucleosynthesis are dragged up and mixed with the outer layers via huge convection zones. Due to the highly extended atmosphere and a therefore very low surface gravity, in combination with a large amplitude pulsation, a large fraction of the initial mass drifts away through a strong stellar wind initiated by cicumstellar dust formation. This leads to the enrichment of the stellar environment with nuclear burning products. In addition to the quasi periodical pulsation, which is responsible for the observed variability at different wavelengths, AGB stars undergo several He-shell flashes. This thermal pulsing is a main characteristic of AGB stars[1].

The stars investigated in this work are all AGB stars at different evolutionary stages and have hence slightly different characteristics. Section 2.1 describes how a main-sequence star of moderate mass evolves via a Red Giant Branch (RGB) star to an AGB star and beyond. The consecutive Section 2.2 deals with the activities in the highly extended atmosphere of these stars, namely the pulsation and the production of molecules and dust. Section 2.3 introduces the mass loss mechanism leading to the high mass loss rates and the influence of a companion on AGB stars. The last section characterizes the five AGB stars, R Aql, R Aqr, R Hya, V Hya and W Hya, observed for this work. Many of the following content can be found in more detail in the book of Habing & Olofsson (2004) and the review article of Herwig (2005).

Table 2.1: Typical global properties of AGB stars.

Parameter	Value Range
Mass, M	$0.8 - 8$ $M_\odot$
Radius, R	$200 - 600$ $R_\odot$, $(1 - 3$ AU$)$
Temperature, $T_{\rm eff}$	$2500 - 3500$ K
Luminosity, $M_{\rm bol}$, (L)	-3.6 to -7.1 mag, $(10^3 - 10^4$ $L_\odot)$
Mass loss rate, $\dot{M}$	$10^{-8} - 10^{-4}$ $M_\odot yr^{-1}$
Variability period, P	$30 - 2800$ days
AGB timescale, $\tau_{\rm AGB}$	$10^5 - 5 \cdot 10^6$ yrs

[1]The AGB stars evolution is divided into two phases, the Early AGB (E-AGB) and Thermally Pulsing AGB (TP-AGB) phase. An E-AGB star has similar characteristics as a RGB star.

2.1 Evolution and Characteristics

2.1.1 Observational Properties and Structure

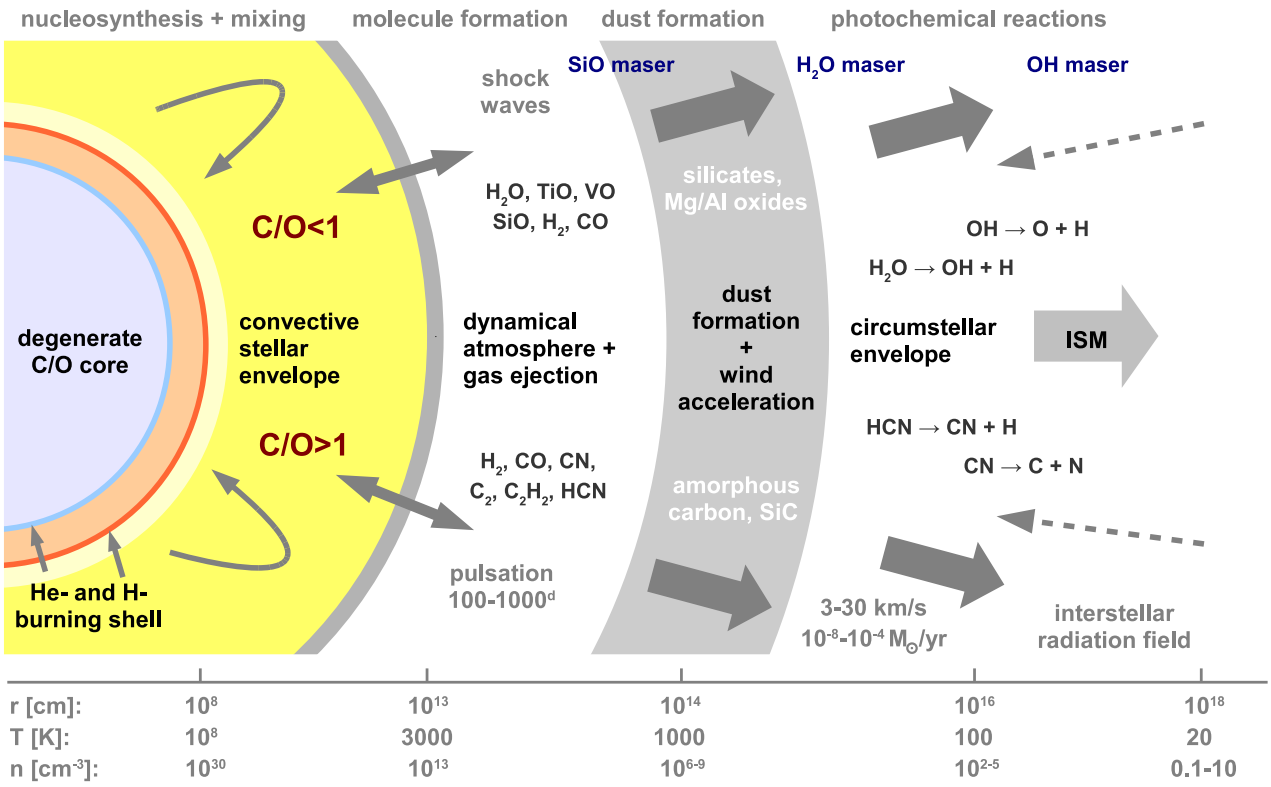

Figure 2.1: The structure and environment of an AGB star. Important physical and chemical processes are indicated.

AGB stars are very luminous stars with bolometric magnitudes between those of RGB stars and supergiants. They can easily be identified throughout the Milky Way, as well as galaxies within about 10 Mpc. Due to their low effective temperatures, AGB stars are especially very prominent in the infrared. They are old and define relaxed systems. These properties make them good probes of galactic structures and dynamics, as well as of star formation histories. Table 2.1 (page 3) lists typical global properties of AGB stars. They are analyzed in more detail in this and the following sections.

AGB stars are spectrally classified as M, S or C. M stars are characterized by strong TiO absorption lines and large numbers of metallic oxide lines. In the mid-infrared, silicate dust emission is observed as well. The S stars show very distinct ZrO bands. In contrast to the M and S type, C type stars do not show metallic oxides. They are dominated by carbon molecule bands and their dust consists mainly of amorphous carbon grains.

The existence of these three types can be explained with the abundance of C and O. M stars have a C/O number ratio of less than unity, while S stars have a C/O ratio of approximately one[2]. C stars are characterized by a C/O ratio greater than one. Since CO is the most strongly

[2]Since this depends also on the s-element abundance, the actual C/O ratio is between 0.5 and 1.0.

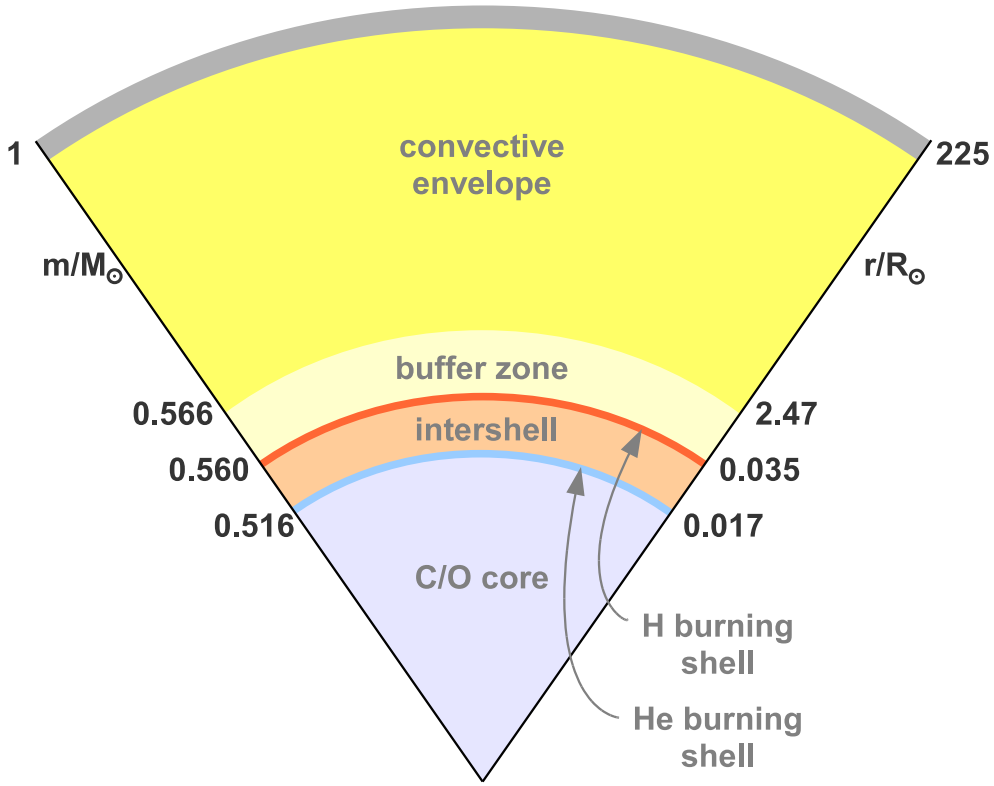

Figure 2.2: The mass and radius scaling for the layers within an AGB star of solar mass (Habing & Olofsson, 2004).

bound molecule in the atmosphere of cool stars, in M stars all C is locked and in C stars all O is locked. Only the remaining C or O is available to form molecules like TiO or CN in M and C stars, respectively (see Section 2.2.2 and 2.2.3 for more details). For this reason M stars are called *oxygen-rich* (O-rich) and C stars *carbon-rich*[3] (C-rich). The extra added C to the envelope comes from the third dredge-up and only AGB stars with certain properties can become a S or even a C star. This is described in Section 2.1.2 in more detail.

Other observational characteristics are the variability (see Section 2.2.1) and the existence of a rich circumstellar envelope (CSE) structure. A sketch of an AGB star, showing the interior structure, the convective envelope, the dynamic atmosphere and the CSE is given in Figure 2.1. The core is very hot and dense. Above the degenerate C/O core, which represents already the later white dwarf, with a temperature of 10^8 K and a size of 10^8 cm, exists He and H burning shells. Both shells are separated by an intershell. Depending on the mass a radiative buffer zone disconnect the tiny interior part from the large, hot and less dense stellar envelope with huge convection cells, going from the bottom to the top. The mass and radius scaling for the layers within an AGB star is shown in Figure 2.2 for a one solar mass star.

In the tenuous, warm and pulsating atmosphere, with temperatures of around 3000 K, molecules are formed depending on the C/O ratio. At photospheric radii of 5 to 10 the temperatures get low enough that molecules can condensate in order to form dust. The interplay of dust with

[3]By default all newborn stars are oxygen-rich, since there is more oxygen than carbon in interstellar space. Being carbon-rich is special.

the radiation of the star initiates a slow wind that leads to the characteristic high mass loss rates of AGB stars. In the outer, very large, very diluted and cool circumstellar envelope most of the molecules are destroyed by the interstellar radiation field. Dust particles survive longer in the interstellar medium at temperatures of around 10 K, and can be incorporated in new star and planet formation.

2.1.2 Evolution and Hertzsprung-Russel Diagram

A star with an initial mass between 0.8 and 8 $M_{\odot}$ will become an AGB star. After staying most of its time on the Main Sequence (MS) the star evolves to a Red Giant Branch (RGB) star. At this stage, the star spends another relatively long time at the Horizontal Branch (HB), before the short but intensive AGB phase and post-AGB phase with heavy mass loss begins. The remaining star will be for a short time the central star of a Planetary Nebulae (PN), before it reaches its final stage as White Dwarf (WD). This is shown in the Hertzsprung-Russel (HR) diagram in Figure 2.3 for a two solar mass star of solar metallicity. More massive stars, with masses higher than about 8 $M_{\odot}$, do not become AGB stars. They will end as Neutron Stars or Black Holes after a Supernova explosion. Lower mass stars will not become hot enough in the core to burn helium and reach the AGB phase.

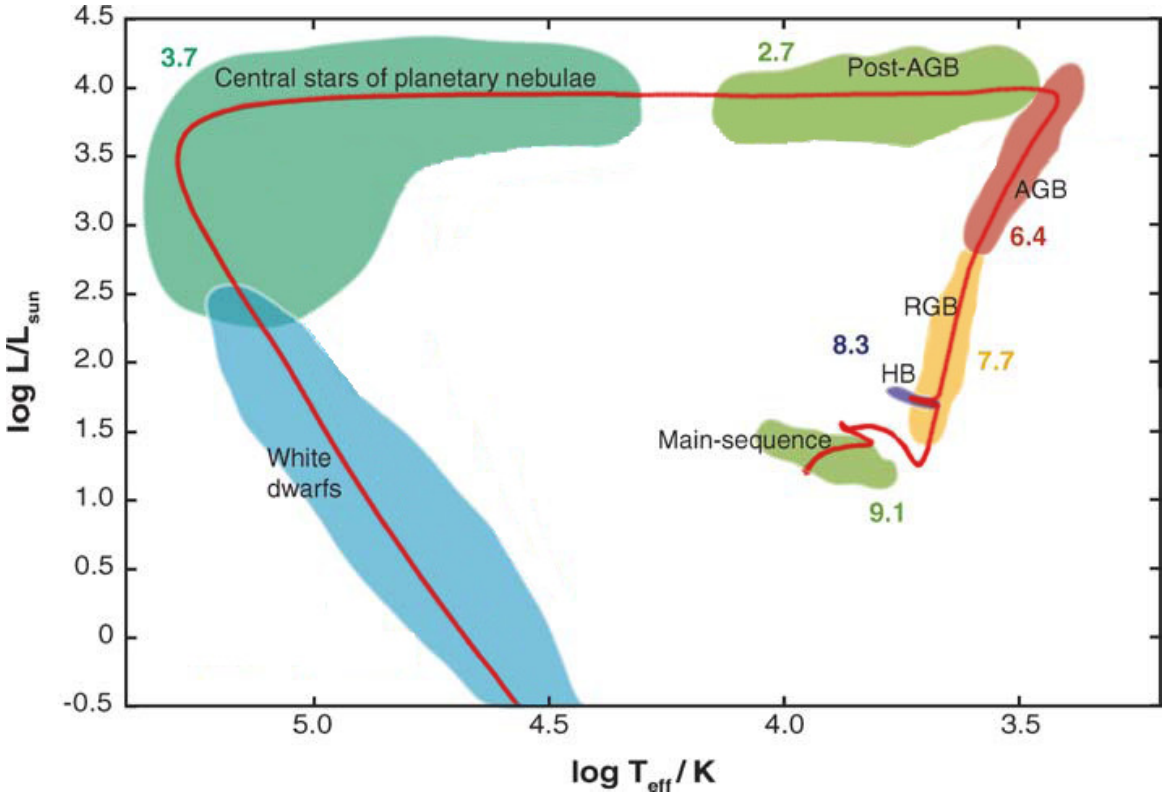

Figure 2.3: Sketch of the complete evolution of a star with two solar masses from the Main Sequence to its final stage as White Dwarf. The numbers indicate for each evolutionary phase the logarithm of the approximate duration in years (Herwig, 2005).

Important features of the evolution of an one solar mass MS star to an AGB star are shown in

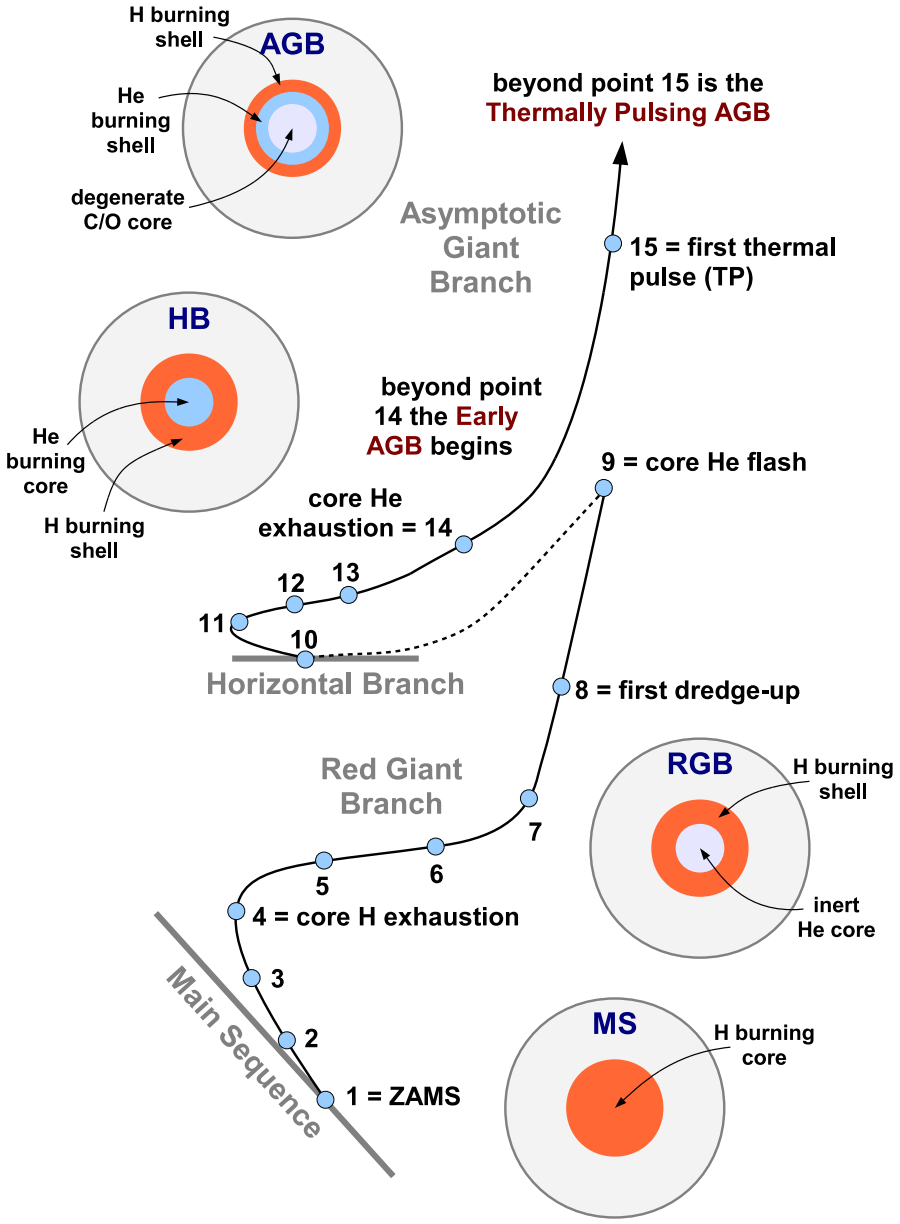

Figure 2.4: Schematic evolutionary track of a solar mass Main Sequence (MS) star via a RGB star to an AGB star in the HR diagram, see text (adopted from Habing & Olofsson, 2004).

Figure 2.4 in more detail. The composition of the star is always given next to the corresponding evolutionary stage. The H-burning on the MS occurs radiatively in the core. Due to the conversion of H to He and a therefore increased molecular weight, the central temperature and density grows until central H exhaustion (point $1-4$ in Figure 2.4). Then the star leaves the MS and crosses the Hertzsprung Gap (point $5-7$), while the central He core becomes electron degenerate and nuclear burning of H establishes in a shell surrounding this core. Caused by the higher energy production the star starts to expand, and the outer layers become convective.

Once the star reaches the Hayashi limit (around point 7), convection extends deeply inward from the surface, and the convective envelope penetrates into the region where partial H-burning has

occurred in the earlier evolution. As a result of this *first dredge-up*, material enriched in ^{4}He and the products of the CN cycle, primarily ^{14}N and ^{13}C, are mixed to the surface (point 8). The He core continues to contract and heats up as the star ascends the giant branch. Energy losses from neutrinos in the center cause the temperature maximum to move outward. For stars with masses higher than 0.8 solar masses the temperature becomes high enough that triple-alpha reactions are ignited. This ignition is very intensive and is referred to as the *core helium flash* (point 9).

After helium ignition the star moves quickly to the horizontal branch (HB) or the red giant clump. In this phase, the star burns ^{4}He gently in a convective core and H in a shell (points 10−13) for a relatively long time (about 1/10 of the time the star lived on the MS). Helium burning increases the mass fraction of ^{12}C and ^{16}O, the latter through $^{12}\mathrm{C}(\alpha,\gamma)^{16}\mathrm{O}$. After the exhaustion of He (point 14) the star begins to ascend the giant branch a second time. The core becomes electron degenerate, and the energy output of the star is provided by the He-burning shell, which is located between the C-O core and H-burning shell. Above both shells is the deep convective envelope. This is the beginning of the AGB phase.

At the early-AGB stage, where both H- and He-burning shells have been established, the structure of all AGB stars is qualitatively similar regardless of the stellar mass. The degeneracy of the C-O core, supported by the pressure of degenerate electrons, ensure that no carbon burning will occur in the center of the star. This sets the upper mass limit for AGB stars at about 8 $M_\odot$. As shown in Figure 2.2, the region interior to the H-burning shell contains roughly half the mass of a one solar mass AGB star. The volume of its core is tiny and similar to that of a white dwarf. Almost the entire volume of the star is taken up by the convective envelope, where stellar pulsation takes place.

The He-shell burning on the AGB does not proceed smoothly, but is subject to thermal instabilities. The instabilities arise because of the high temperature sensitivity of the triple-alpha reaction coupled with the thinness of the shell. A modest temperature perturbation causes a large increase in nuclear energy production via the triple-alpha reaction. On the other hand, a shell which is not too thin ensures that the corresponding increase in energy loss is not too large due to the lower temperature gradient. The increased energy input accelerates the nuclear reactions and leads to a thermal runaway. A constant pressure in this layer due to a temporary strong electron degeneracy can enhance the instability mechanism further. This first thermal pulse (point 15) marks the beginning of the thermally pulsing AGB (TP-AGB).

AGB stars experience several thermal pulses until the convective envelope is dissipated by mass loss. Low mass AGB stars undergo on the order of 10 thermal pulses with a total AGB lifetime of approximately 10^6 years, while high mass AGB stars undergo several tens of thermal pulses with a lifetime of roughly 3×10^5 years. As illustrated in Figure 2.5, the H-burning shell is the main energy source between thermal pulses. During a thermal pulse, the He-burning shell provides most of the star's luminosity with up to 10^8 $L_\odot$, and the H-burning shell even extinguishes. Directly after a thermal pulse, material from the nuclear burning is mixed up to the stellar envelope. This is called the *third dredge-up* (Section 2.1.3). Between thermal pulses a radiative buffer zone prevents that nuclear burning products are transported outwards. Throughout the whole AGB evolution the total luminosity goes up, while the effective temperature decreases slightly, moving an AGB star asymptotically to the upper right part of the HR-diagram.

The star becomes the central star of a planetary nebula after the ejection of the stellar envelope

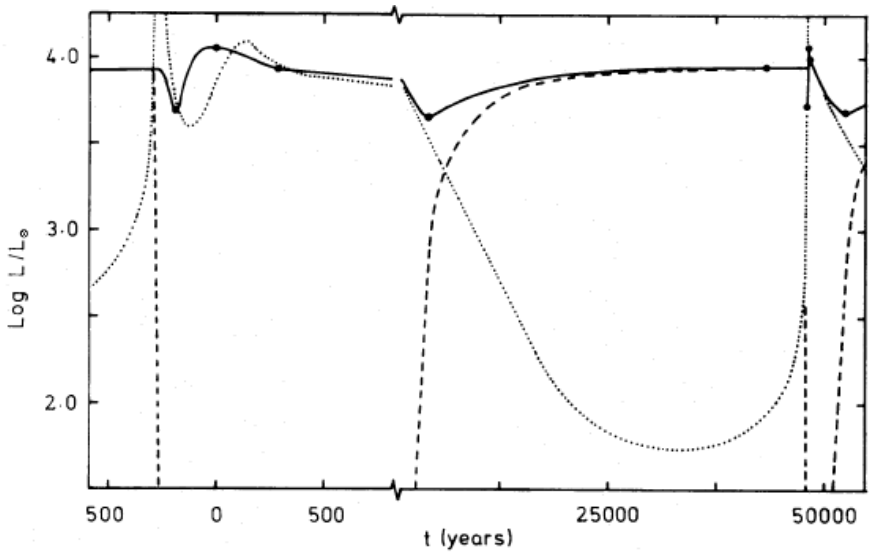

Figure 2.5: The surface luminosity (solid line), the H-burning luminosity (dashed line) and the He-burning luminosity (dotted line) plotted against time for two consecutive thermal pulses in a two solar mass star (Wood & Zarro, 1981).

through a *superwind* mass loss phase at the end of the AGB stage (post-AGB phase). The unaffected core, under the still existing radiative layer and a more and more shrinking small envelope (less than 0.01 $M_\odot$), evolves at essentially constant luminosity to hotter temperatures in the HR-diagram. After spending about 10,000 years at the PN phase, with consuming and losing the remaining H-rich envelope, the burning stops at some point and the dead star, with a temperature of $T_{\rm eff} \geq 30{,}000$ K, cools off as a white dwarf. Depending on the initial mass, the final mass of the WD is between 0.5 and the Chandrasekhar mass limit of 1.44 $M_\odot$.

2.1.3 Third Dredge-Up and Nucleosynthesis

The release of products of nuclear burning makes the AGB star phase very important in the stellar evolution. As already shown in Figure 2.3, a first dredge-up occurs in the RGB star phase, enriching the stellar envelope in helium-rich material, ^{14}N, ^{13}C and ^{17}O, and depleting it of ^{12}C, ^{16}O and ^{18}O. For AGB stars with masses greater than four solar masses a second dredge-up event happens with the first thermal pulse at the beginning of the thermally pulsing AGB phase. The convective envelope penetrates a region that completely burned all hydrogen, and the resulting material is added again to the envelope.

All consecutive thermal pulses are accompanied by repeated dredge-up. These successive third dredge-ups are common for almost all AGB stars[4], mixing the products of He-burning to the stellar surface where they are emitted with the stellar wind. Figure 2.6 shows a thermal pulse with a subsequent third dredge-up for a two solar mass AGB star. During a thermal pulse, indicated with time stamp zero, a pulse-driven convective zone (PDCZ) develops, since the energy deposited by the He-burning reaction cannot be transported by radiation alone. The PDCZ is mostly composed of ^{4}He (about 75%) and ^{12}C (about 22%). After the decline of

[4]AGB stars with masses less than 1.2 solar mass exhibit probably no third dredge-up.

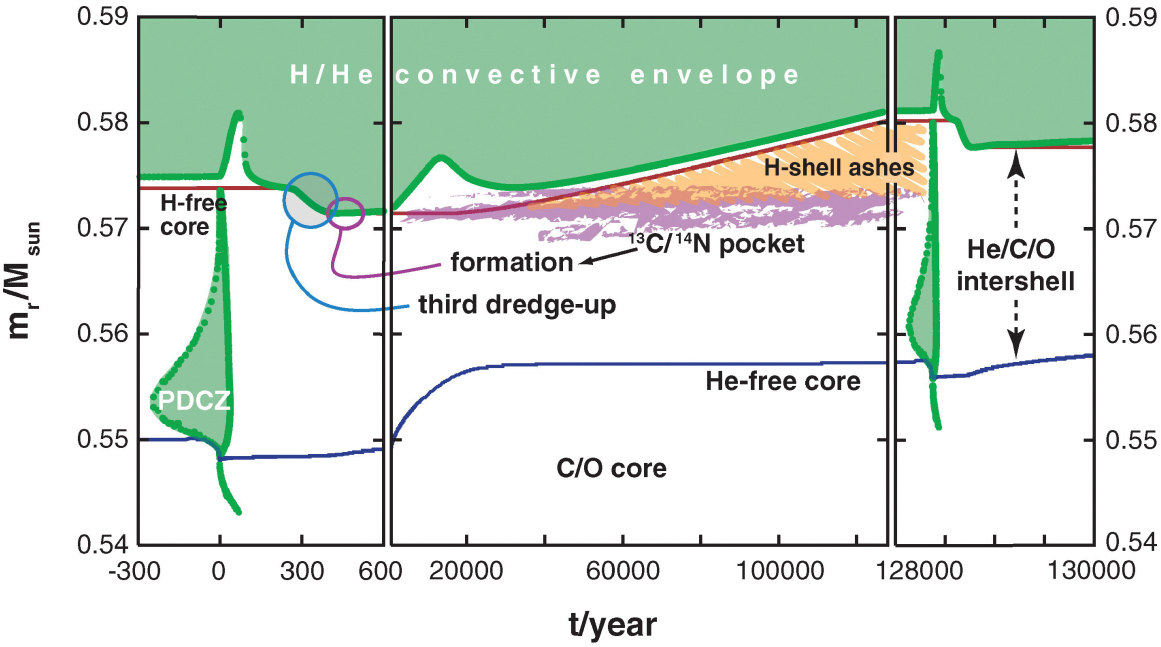

Figure 2.6: Third dredge-up in a two solar mass AGB star after a thermal pulse. The red and blue line indicate the boundary of the H and He free core, respectively. Green are the zones of convection (Herwig, 2005).

the He-shell burning and the disappearance of the PDCZ, this intershell region expands and H-burning extinguishes. The released energy from the shell flash causes that the convective envelope penetrates for a few hundred years into the mass zone previously occupied by the PDCZ. This mixes up ^{12}C into the stellar envelope with an efficiency depending on the the core mass, envelope mass, number of previously thermal pulses and overshoot phenomena.

Due to the repeated enrichment of carbon in the convective envelope an O-rich M-star can become first an S-star with mixed chemistry and then a C-rich C-star. Low-mass and high-mass AGB stars do not become S or C stars. At the lower mass end, the fewer thermal pulses do not mix up enough carbon, while at the higher mass end, hot bottom burning (HBB) prevents the star from accumulating carbon in the atmosphere. In high-mass AGB stars ($M > 4$ M$_\odot$) exists no radiative buffer zone and the temperature at the bottom of the convective envelope becomes high enough to burn excessive carbon into nitrogen via ^{12}C(p,γ)^{13}N(β^+)^{13}C(p,γ)^{14}N (CN cycle). This explains why very luminous C-stars are not discovered. However, after losing a part of the envelope they could still become a C-star at the end of the AGB phase.

The nucleosynthesis in AGB stars is mostly associated with H- and He-burning complemented by neutron capture. Of particular importance is the action of repeated third dredge-up events. The He-burning products in the deeper parts of the stellar envelope are subject to proton captures in the H-burning shell during the interpulse phase, giving rise to a combination of H and He processed material. These processes are basically responsible for the production of ^{4}He, ^{7}Li, ^{12}C, ^{14}N, ^{16}O, ^{19}F, ^{22}Ne, ^{23}Na, ^{25}Mg, ^{26}Mg, ^{26}Al and ^{27}Al, in addition to products from the HBB. Figure 2.7 shows the mass fraction of the most abundant elements in an interpulse phase.

During the thermal instability of the He-shell, the production of ^{12}C from ^{4}He via the triple-

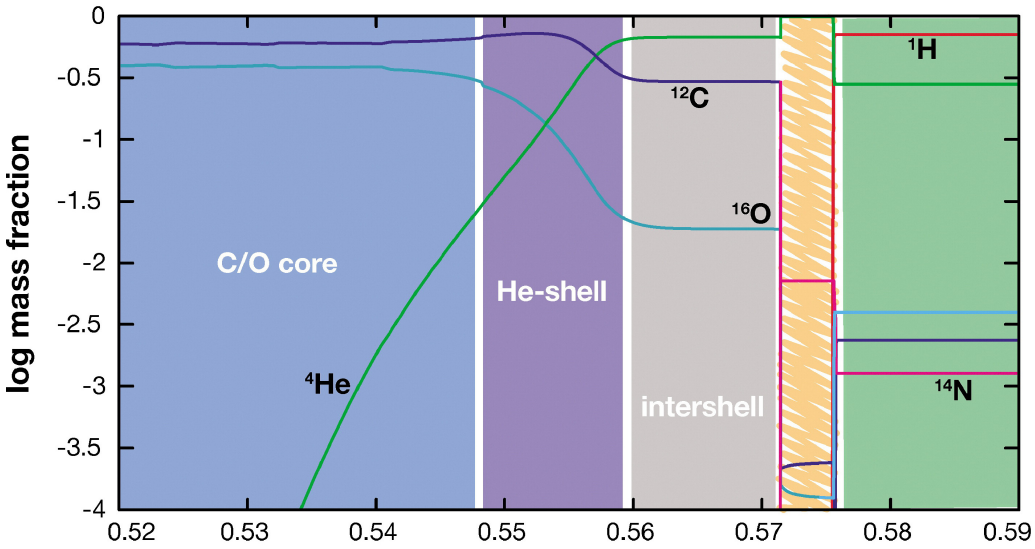

Figure 2.7: Element abundance of H, He, C, N and O in the interior of a two solar mass AGB star between thermal pulses. Clearly, the abundance of C and O is very high in the core while H and He disappeared. The abscissa is in units of solar mass (Herwig, 2005).

alpha reaction ($3\,^4\mathrm{He} \longrightarrow {}^{12}\mathrm{C} + \gamma$) is the main occurring nuclear reaction. The PDCZ brings fresh ^{4}He down while ^{12}C is mixed up. Additional α-capturing can produce ^{22}Ne from ^{14}N, left over from the CNO cycle, and some ^{16}O as well. Overshooting, i.e. penetrating the CO core, can increase the amount of mixed up ^{16}O further.

Perhaps the most important nucleosynthesis in AGB stars after the ^{12}C formation is the slow neutron capture[5] producing the so-called (main) s-process elements (light s-process elements including Y, Sr and Zr with a peak abundance at around A $\approx$ 90, and heavy s-process elements including Ba, La, Ce, Nd and Sm with a peak abundance at around A $\approx$ 140). There exist two neutron sources in AGB stars, one is the reaction of ^{13}C, leading to ^{13}C(α,n)^{16}O, and the other the reaction of ^{22}Ne, leading to ^{22}Ne(α,n)^{25}Mg. The latter one occurs only in high mass AGB stars or at high temperatures during a He-shell flash in low mass AGB stars.

^{13}C is built via proton capture after the third dredge-up. For not too high proton fluxes a ^{13}C shell, or pocket, establishes[6], and its release of neutrons forms the s-process elements. With the formation of the PDCZ, more s-process elements are produced and mixed up by the subsequent third dredge-up (cf. Figure 2.6). The s-process builds approximately half of the isotopes of the elements heavier than ^{56}Fe, and multiple n-exposures can easily produce the main component of the solar system distribution of s-elements. Even for stars with Z = 0, s-process elements can be produced. This is possible, since Ne and Mg, produced during the thermal pulses, can form the basis for neutron captures, producing elements all the way through Pb and Bi.

[5]It is slow compared to the competing β-decay.
[6]It competes with a further reaction to ^{14}N.

2.2 Dynamic Atmosphere and Circumstellar Envelope

The dynamic behavior of the atmosphere is a main characteristic of AGB stars. The pulsation leads to a periodic visual variability and a time dependent molecule and dust formation. The extended atmospheric and circumstellar structure is responsible that all phenomena are distributed over a large distance scale with mutual complex influences. This section summarizes important aspects on the pulsation, the molecule formation and the dust production process.

2.2.1 Variability and Pulsation

Variability is a very common feature of AGB stars. Its cause is mainly pulsation, but there is also some evidence for variations originating from episodic ejections of dust shells or orbiting dust clouds. Giant branch variable stars can be divided into three groups, namely the Mira variables, the semi-regular variables (SRa to SRd) and the irregular variables (L). Mira variables have large visual amplitudes (larger than 2.5 mag) with an almost regular variation. SR variables exhibit smaller visual amplitudes (less than 2.5 mag) with some definite periodicity, while irregular variables show only little periodicity. AGB stars exhibit an important fourth class, known as OH/IR stars. These dust-enshrouded infrared variables are too faint to be discovered in the visual. They have been found by their 1612 MHz OH maser emission (O-rich type) or by infrared surveys (all types).

Although the amplitudes of the visual light curves are high, the bolometric amplitudes are much smaller, typically less than 1 mag. This is because most of the light is emitted in the infrared (the peak emission is at around 1 μm) where the light curve amplitudes are low. The reason for this difference is the result of two effects. First, at shorter wavelengths the absorption by TiO varies strongly throughout the pulsation cycle, and second, these shorter visual wavelengths are in the Wien part of the spectrum and a moderate change of the effective temperature induces therefore a large change of the flux.

Mira and SR variables occur over the whole mass range occupied by AGB stars. It is found that more than 90% of thermally pulsing AGB stars are variable at the level of a few percent or more[7]. Stars with $M \leq 1.1$ $M_\odot$ have typical periods below 300 days, while stars with $M \geq 1.1$ $M_\odot$ have periods above 300 days. Figure 2.8 shows the period-luminosity (PL) relations for optically visible Mira and SR variables in the Large Magellanic Cloud (LMC). Four[8] parallel PL sequences (A-D) exist. Sequence A and B are populated with SR variables, while sequence C consists mainly of Mira variables.

The sequences A, B and C represent pulsation in different modes. SR variables can pulsate in a number of modes, often simultaneously, while Mira variables are confined to a single pulsation mode corresponding to sequence C. Stars in sequence D have multiple periods and cannot be associated with a physical pulsation mode so far. Mira variables pulsate in its fundamental mode, and their PL relation (Hughes & Wood, 1990) is given by

$$K_0 \;=\; 11.13 \;-\; 3.78\,(\log P \;-\; 2.4)\;. \tag{2.1}$$

[7]Irregular variables were not included in this study.

[8]Recent work shows that sequence B splits into two sequences B_1 and B_2, and sequence E consists mainly of stars in the RGB.

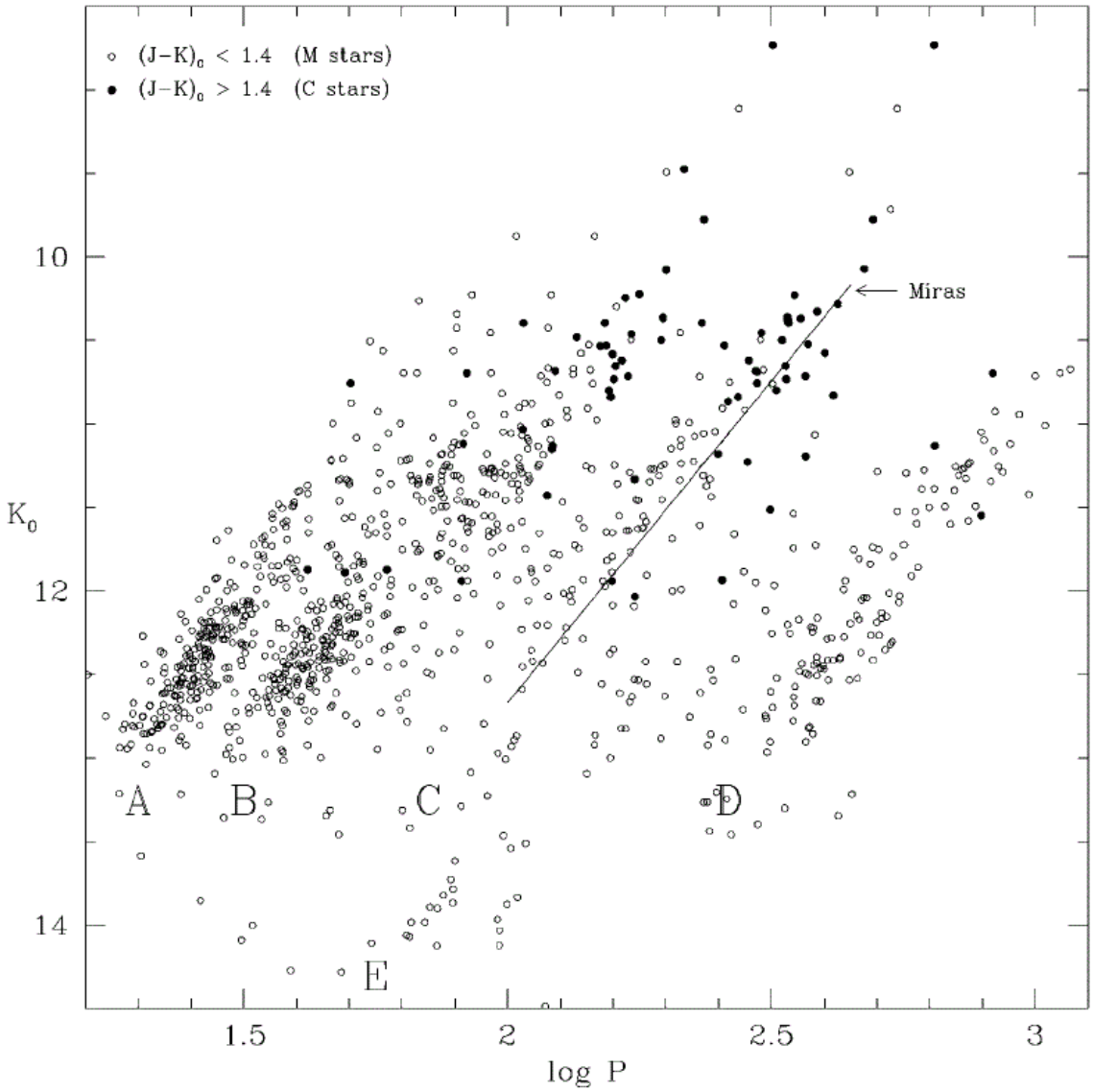

Figure 2.8: The period-luminosity relation for optically visible red variables in a 0.5×0.5 degree area of the LMC. The letters label the different sequences. The solid line is the $K-\log P$ relation from Hughes & Wood (1990). Solid circles correspond to stars with $J - K > 1.4$ and they are assumed to be carbon stars. Other stars are assumed to be oxygen-rich M or K stars (Wood, 2000).

SR variables on the other hand can pulsate in the first, second, third overtone and fundamental mode, corresponding to sequence A, B (which splits into B_1 and B_2) and C.

The different modes are connected with distinct evolutionary stages. The atmospheres of AGB stars become pulsational unstable in the early-AGB phase with a pulsation period dependent on radius and mass. This period-mass-radius (PMR) relation is given by Fox & Wood (1982) as

$$P \propto R^{\alpha} M^{-\beta} , \tag{2.2}$$

where $\alpha \approx 1.5 - 2.5$ and $\beta \approx 0.5 - 1.0$. With rising luminosity, i.e. with an increasing radius during the progressive evolution according to $L = 4\pi\sigma_{\mathrm{R}} R^2 T_{\mathrm{eff}}^4$, the initial SR variables[9] at sequence A switch to sequence B and then to sequence C, reaching the fundamental mode pulsation as Mira variables. With increasing pulsation period the visual light amplitude increases as well. In addition to the sidewards movement due to mode switching, AGB stars move also upwards in Figure 2.8 due to the increased luminosity. It is notable from the figure that the carbon-rich stars, representing later evolutionary stages, populate the upper right region.

The mass dependency of equation 2.2 enhances this effect further. Even though the mass loss is relevant in this stages, most of it is ejected at the very end of the AGB phase. In this late stage the AGB stars are enshrouded by dust and are only visible as OH/IR stars. They are found to lie mainly on sequence D and have therefore pulsation periods greater than 600 days.

It should be mentioned that the assignment of the fundamental mode to the Mira variables is not definitive. The PMR would suggest a first overtone pulsation if compared with observations. This is because the measured diameters are too large to fit into the relation. However, over the intervening years it was found that the out sized diameters are due to molecular spheres and that the fundamental mode hypothesis explains the pulsation ratios of the ABC sequence best.

Radial oscillations are the result of sound waves resonating in the interior of the star. The physical process leading to the pulsation is the κ mechanism (opacity mechanism). In the convective stellar envelope exists a hydrogen ionization zone which drives the pulsation. The star expands by releasing recombination energy from the partially ionized zone. In the contraction phase the energy is stored by ionizing the hydrogen in this zone again. The ionization increases the opacity and the layer is able to absorb the heat.

The described increase of the pulsation period over the whole AGB evolution is modified by the thermal pulses. The additional short time luminosity growth leads to a temporary increase of the pulsation period followed by a decrease. This is shown for three observed AGB stars in Figure 2.9. It illustrates the variation of the surface luminosity as deduced from the changes in period as a function of time for different values of the core mass (Wood & Zarro, 1981). The period of R Aql has decreased from about 320 d in 1915 to about 264 d in 2010, while R Hya has changed its period from about 500 d in 1700 to about 374 d in 2010. This provides direct evidence for the existence of a recent helium shell flash and of the existence of helium flashes in general.

2.2.2 Molecule Formation

In the cool and extended atmosphere of AGB stars, with effective temperatures between 2500 and 3500 K, a rich variation of different molecule species can develop. The distinct absorption and emission features of molecules above the continuum forming photosphere lead to a complicated spectrum. Dependent on the underlying chemistry completely different chemical reactions are favored. Due to the high binding energy of CO, only excess atoms of C or O can form new compounds in carbon-rich or oxygen-rich stars, respectively. Table 2.2 (page 16) lists the most abundant atoms and molecules in both kinds of stars, obtained for a local thermal equilibrium (LTE) calculation by Markwick (2000).

[9] The initial luminosity of the SR variables is of course a function of mass as well.

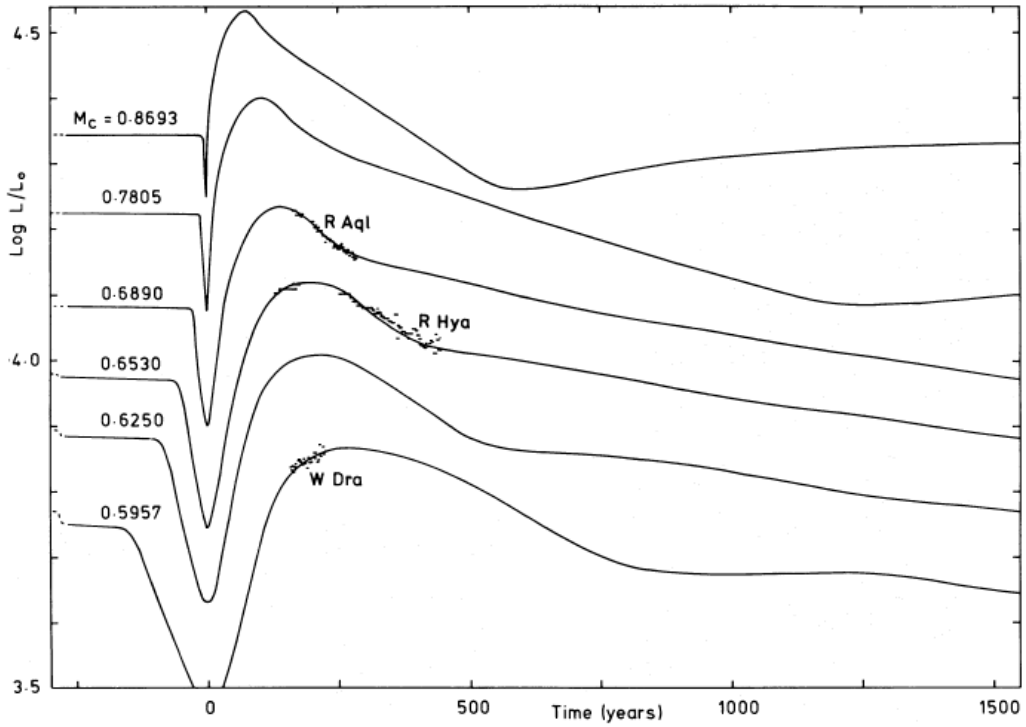

Figure 2.9: Variation of the surface luminosity as deduced from the changes in period as a function of time for different values of the core mass (time stamp zero indicates the thermal pulse) (Wood & Zarro, 1981).

The LTE[10] approximation is only valid very close to the star where the reaction time-scale is much shorter than the expansion time of the gas. In general, the abundance is strongly dependent on the radius. In the region above the continuum forming layer, shock waves from the pulsation can heat, compress and trap the gas, modifying the individual abundances and destroying CO. In particular, OH, H_2O and SiO is enhanced in O-rich stars, and polycyclic aromatic hydrocarbons (PAH) are formed in C-rich stars. The shock chemistry can even produce carbon-bearing molecules (e.g. CO_2, CS and HCN) in an oxygen-rich environment and vice versa (e.g. SiO in C-stars).

The relevance of each species for the shape of the spectral energy distribution depends on its optical properties, i.e. its emissivity η and opacity[11] χ. Both are coupled indirectly to the radiation field through the populations of different atomic and molecule levels. The continuous absorption in AGB stars is dominated by H^- bound-free and free-free absorption as well as H_2^- free-free absorption. In addition, Rayleigh scattering by H atoms and H_2 molecules is significant. Spectral line absorption from electron transitions of atoms is less important (except for the shortest wavelengths), while molecular lines with their many additional vibration-rotation states are very prominent in the infrared and radio in these cool stars.

[10]In LTE the Gibbs free energy of the system is at minimum and is given by $G = \sum f_i x_i$, where x_i is the number of moles of species i and f_i its chemical potential, given by $f_i = (G/RT)_i + \ln P + \ln(x_i/\bar{x})$, where $(G/RT)_i$ is the Gibbs free energy of species i, P the total pressure of the system, $\bar{x} = \sum x_i$, and R the gas constant. The free energy of i is a temperature dependent quantity.

[11]The opacity, or extinction, is the sum of absorption and scattering.

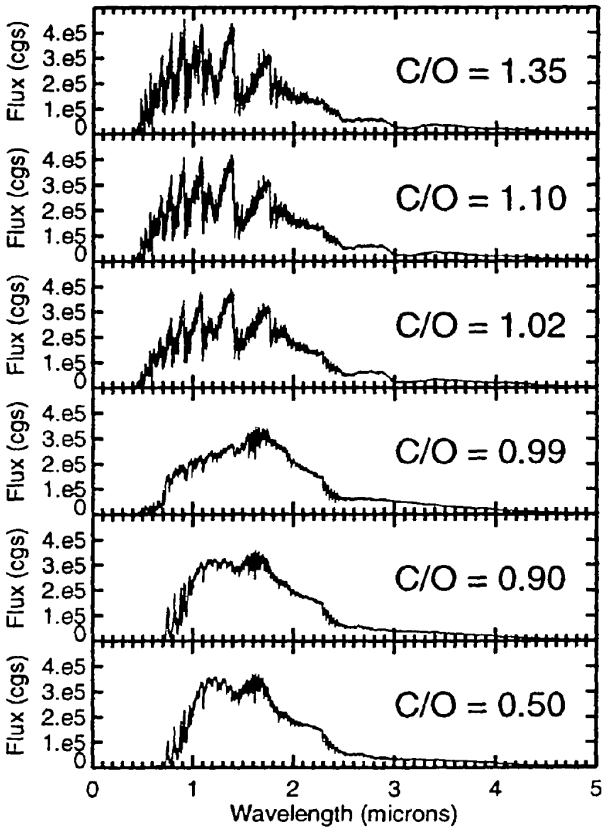

Figure 2.10: Model spectra for stars of one solar mass, $T_{\rm eff} = 3000$ K, $\log g = 0$ and different C/O ratios (Gustafsson et al., 2003).

O-rich		C-rich	
Species	Abundance	Species	Abundance
H_2	1	H_2	1
H	2.1(-1)	H	3.5(-1)
CO	1.1(-3)	CO	1.6(-3)
H_2O	2.9(-4)	C_2H_2	2.2(-4)
N_2	1.2(-4)	C_2H	1.1(-4)
SiO	6.9(-5)	N_2	9.5(-5)
S	2.6(-5)	HCN	8.5(-5)
OH	9.0(-6)	Si	6.3(-5)
SH	7.7(-6)	CS	2.3(-5)
O	1.3(-6)	SiS	9.8(-6)
H_2S	7.2(-7)	C_3H	9.5(-6)

Table 2.2: Most abundant atoms and molecules present in a LTE atmosphere of an O-rich (C/O = 0.75 and $T_{\rm eff} = 2215$ K) and a C-rich (C/O = 1.5 and $T_{\rm eff} = 2300$ K) star. The fractional abundance is given with respect to H_2 with $a(b) = a \times 10^b$ (Markwick, 2000).

The most relevant molecule opacity sources in oxygen-rich AGB stars are H_2O, CO, TiO, VO, ZrO, SiO, OH and CN. Despite of its low abundance, TiO is important in the visual and near-infrared due to its very high absorption coefficient in these regimes. Flux from the visual and near-infrared is shifted to longer wavelength by heavy blocking (blanketing). The other important molecule is H_2O. It has a lot of broad absorption and emission bands across the whole infrared. In contrast, carbon-rich spectra are dominated by CN, C_2, C_2H_2, CO, C_3, HCN and CH besides the continuum opacities (Gautschy-Loidl et al., 2004). Figure 2.10 shows synthetic spectra of AGB stars with different C/O ratios. It is remarkable how the spectra change while going from the oxygen-rich case to the carbon-rich case.

The extended atmospheric structure with decreasing temperature and densities leads to the formation of distinct shells, where the abundance of certain molecules are enhanced. These opaque shells or *molspheres* are located at different distances above the continuum forming photosphere and are responsible for measuring different stellar diameters at different wavelengths due to probing spectral features of different molecules like TiO, H_2O and SiO (O-rich) or C_2H_2 and HCN (C-rich) (Baschek et al., 1991; Scholz, 2001).

It is therefore difficult to define a diameter for these stars, since these molecular layers can easily have radii twice the continuum radius in the molecular bands in the optical and infrared (e.g. Mennesson et al., 2002; Tej et al., 2003; Ohnaka, 2004). The most common definition

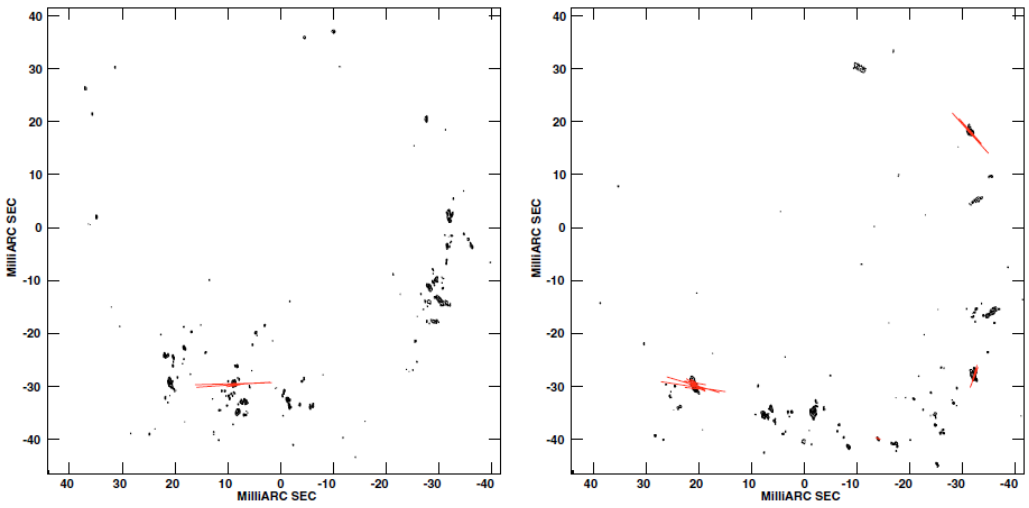

Figure 2.11: Maser emission of W Hya. Shown are the total intensity contours with polarization "E" vectors over-plotted in red. *Left:* The $\nu = 2$, $J = 1 - 0$ transition of SiO at 42.8 GHz. *Right:* The $\nu = 1$, $J = 1 - 0$ transition of SiO at 43.1 GHz (Cotton et al., 2008).

refers to the position of the atmospheric layer where the radial Rosseland optical depth equals unity, $R = r(\tau_{\text{Ross}} = 1)$. This radius is called the Rosseland radius and is a standard definition in stellar models, but no observable quantity, since photons collected by the observer often originate from a wide range of depths around the $\tau = 1$ layer. Therefore, there is no trivial relation between the radius dependent brightness distribution of the star and the value of R.

A result of the formation of plenty of molecules is the excitation of maser[12] emission. Population inversion of excited states is fairly common in numerous regions in the circumstellar environment (CSE), where deviations from LTE are the rule rather than the exception. By stimulated emission the masing species amplifies the background radiation or the internally generated radiation. The typical brightness temperature of this strong maser emission is much higher than the local temperature. Since the creation of masers is very sensitive to any changes in optical depths and other local characteristics, maser emission traces regions where specific physical conditions are fulfilled. Thus, they are important to get insights into the innermost atmospheric regions of the CSE. These regions are dominated by the mass loss process and pervaded by propagating shock waves associated with stellar pulsation.

In oxygen-CSEs maser emission of SiO, H_2O and OH is frequently observed. The SiO maser emission at 42.8 ($\nu = 2$, J $= 1 - 0$), 43.1 ($\nu = 1$, J $= 1 - 0$) and 86 GHz traces regions very close to the star at typically 1.5 to 2 photospheric radii. Figure 2.11 shows as example the SiO maser emission spots of W Hya. H_2O is detectable further out at about 5 to 10 photospheric radii by its 22 GHz rotational transition ($6_{16} - 5_{23}$), and OH masers are observable in the outer region where the molecules are hit by the interstellar radiation generating enough OH to exhibit maser emission at 1612, 1665 and 1667 MHz (cf. Figure 2.1, page 4). In carbon-CSEs, prominent maser emission comes from vibrationally-excited rotational lines of HCN, CS and SiS.

[12]Microwave Amplification by Stimulated Emission of Radiation

2.2.3 Dust Formation

AGB stars produce most of the dust in the galaxy. Their high mass loss rates in combination with an effective dust condensation makes them produce about 90% of the total dust originating from stars (Gehrz, 1989; Sedlmayr, 1994). SN, RSG stars and WR stars contribute only with about 10%. Since dust grains are difficult to destroy by interstellar radiation, they can survive long time periods in the interstellar medium. After some reprocessing they are the seed grains for further dust growth in dark clouds[13] and the ingredients for new star and planet formation.

In order to form dust from the gas phase in the expanding circumstellar environment (CSE) two requirements have to be fulfilled. First, the temperature must be low enough that condensation is possible, and second, the density must be high enough to allow sufficient interactions. These contradictory requirements allow an effective grain growth only in a certain distance from the star. In an hydrostatic atmosphere, the gas density basically decreases exponentially with distance, while the radial distribution of the grain temperature in the CSE can be written as

$$T_{\rm d}(r) \;=\; T_* \left(\frac{R_*}{2r}\right)^{\frac{2}{4+s}}, \tag{2.3}$$

with R_* the photospheric radius and T_* the blackbody temperature of the star (Habing & Olofsson, 2004; Höfner, 2008). The parameter s can be derived from observations which suggest a value around 1. By using Wien's displacement law, $\lambda_{\rm max}T \approx 2900$ μm·K, the radius at which the peak of the blackbody emission occurs at wavelength λ can be crudely estimated. The result is

$$r_{{\rm d},\lambda}(\lambda) \;\approx\; 4 \times 10^{15} \left[\frac{\lambda}{10}\right]^{2.5} {\rm cm}, \tag{2.4}$$

where λ is measured in μm. Although this is not the same as the radius from which most of the flux at wavelength λ originates, it is clear that dust emission at different wavelength probe different parts of the CSE. Dependent on the specific condensation temperatures of the grains, the condensation radius is between 5 and 10 stellar radii. The temperature in this range drops from 1000 to 600 K and the total number density from 10^{10} to 10^8. Materials with a high condensation temperature condensate already at lower distances of about 2 photospheric radii and can act as seed particles for further dust growth (Lorenz-Martins & Pompeia, 2000).

After the nucleation of seed particles, the dust grains grow by coagulation (collision), accretion and surface reactions. The growth time scale of the grains in a non-equilibrium kinetic process, i.e. the efficiency of dust formation, is enhanced by the pulsation of the star. Propagating shock waves create temporary reservoirs of relatively dense gas at a certain distance from the photosphere, thus increasing the depletion of condensible species. However, the periodical reheating might also destroy some previously generated dust material. The final gas-to-dust mass ratio, φ, in the outgoing wind is typically between 100 and 300. Figure 2.12 shows a simulation of the dust formation in the CSE of a carbon-rich AGB star from Woitke & Niccolini (2005). Both, the temperature structure and degree of condensation are illustrated.

[13] In these extremely cold dark clouds, with temperatures of typically 10 to 20 K, grains grow by building mantles of ice at least doubling their mass.

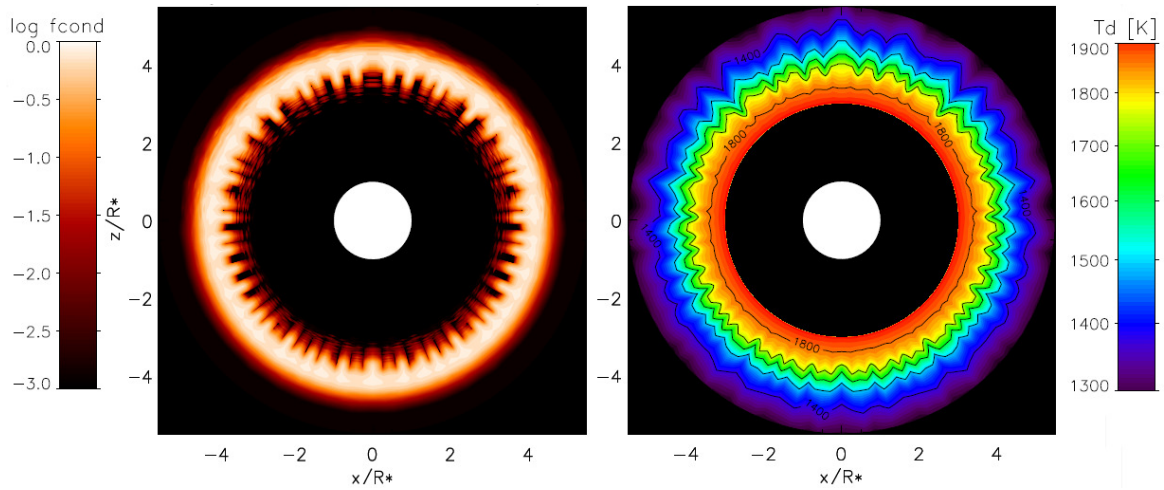

Figure 2.12: Formation of a dust shell around a carbon-rich AGB star by radiative/thermal instabilities. The white circles mark the star and black indicates regions not included in the model. Parameters: $T_{\rm eff} = 3600$ K, $L_* = 3000$ L$_\odot$, C/O = 2 (Woitke & Niccolini, 2005). *Left:* Degree of condensation. *Right:* Dust temperature.

Typical dust grains consist of tens of atoms or aggregates of dust grains and are in general irregularly shaped with a porosity between fluffy and compact (Dominik & Tielens, 1997). They have a typical density between 2.2 and 3.5 g/cm^3 and their sizes range from a few nm to several μm. The different chemical composition of O-rich and C-rich AGB stars leads to the formation of completely different dust species. In an oxygen-rich environment, silicates and oxides are formed, while in a carbon-rich CSE mainly carbonaceous dust is produced.

The first species condensing in M-stars are TiO and $CaTiO_3$. At a temperature of less than 1400 K mainly solid (s) TiO is formed via

$$TiO_2 + H_2 \longrightarrow TiO\,(s) + H_2O\ . \tag{2.5}$$

At lower temperatures of about 1000 K, AlO, MgO, Al_2O_3 (corundum), $Ca_2Al_2SiO_7$ (augite), $CaMgSi_2O_6$ (diopside), $MgAl_2O_4$ (spinel) and Fe-free silicates (e.g. forsterite, $2\,Mg + SiO + 3\,H_2O \longrightarrow Mg_2SiO_4 + 3\,H_2$) condensate to seed particles. One of the most stable and abundant of these is probably corundum. However, the nucleation rate of Al_2O_3 is low and its formation might therefore be difficult. Thus, its function as seed nuclei could be questionable. Its relevance in the dust formation process is still an open issue.

The largest amount of oxygen-rich dust is produced further out in the CSE at an even lower temperature of around 700 K and below. The main component of the silicates, SiO, is formed from the gas phase by

$$SiO + H_2O \longrightarrow SiO_2\,(s) + H_2\ , \tag{2.6}$$

and deposited on seed nuclei. Other important components are Fe, Fe_3O_4, $MgSiO_3$ (enstatite), $(Mg,Fe)_2SiO_4$ (olivine) and $CaAl_2Si_2O_8$ (anorthite). In the very cold outer CSE the condensation of water might be possible as well. More details on the dust-condensation sequence on

M-type stars can be found in Tielens (1990), Blommaert et al. (2006), Lebzelter et al. (2006) and Verhoelst et al. (2009).

In C-stars, amorphous carbon settles down at temperatures around 1800 K. Most of the further condensing material is amorphous carbon as well, but also more regular structured lattices, like graphite and diamonds, are formed in addition to SiC (10%). The formation of PAHs[14] from monomers like C_2H_2 with a successive coagulation leads to energetically favorable clusters as well. Most of the dust in O-rich and C-rich CSEs is amorphous and only a small amount of up to 10% exists in a crystalline state. Of the 90% of dust produced by AGB stars, about 65% are silicates and 25% are carbonaceous (Gehrz, 1989; Draine, 2003).

The influence of dust on the shape of the SED depends on their optical properties. Dust absorbs and scatters the short wavelength radiation from the star and re-emits it at longer wavelengths according to the dust temperature. Using the limit of Mie theory, the opacity of an ensemble of spherical dust grains with grain radius $a_{\rm gr}$ can be formulated as

$$\chi(\lambda) \;=\; \frac{\pi Q_{\rm ext}(\lambda)}{a_{\rm gr}} \int_0^\infty a_{\rm gr}^3 n(a_{\rm gr})\,{\rm d}a_{\rm gr}\;, \tag{2.7}$$

where $n(a_{\rm gr}){\rm d}a_{\rm gr}$ is the number density of grains in the grain radius interval between $a_{\rm gr}$ and $a_{\rm gr} + {\rm d}a_{\rm gr}$ and $Q_{\rm ext}$ is the extinction efficiency ($Q_{\rm ext} = Q_{\rm scat} + Q_{\rm abs}$). $Q_{\rm ext}/a_{\rm gr}$ is different for each dust species (see e.g. Woitke, 2006a, and references therein), and can be calculated from the complex refractive index, which must be determined by laboratory experiments.

The grain size distribution can be approximated by a power law with ${\rm d}n/{\rm d}a \propto a_{\rm gr}^{\alpha}$ between a minimum and maximum grain radius ($a_{\rm gr,min}$, $a_{\rm gr,max}$). The best current values are obtained with $\alpha = 3.0$, $a_{\rm gr,max} \leq 0.14$ μm and $\alpha = 3.5$, $a_{\rm gr,max} \leq 0.1$ μm for an O- and C-CSE, respectively (Jura, 1996, 1997). Putting a lower limit on the grain size is not easy, since the distinction between a large molecule and a solid particle is not clear. Equation 2.7 is valid as long as the particles are small compared to the wavelength of the radiation. With a radiation peak of the photosphere at around 1 μm and dust grains below μm size, this criterion is mostly satisfied for the major fraction of the spectrum. In general, dust particles provide broad-band emission and absorption features due to internally correlated motions of the atoms. More distinct spectral lines are particularly possible if atoms are grouped in a lattice performing various vibrational motions.

Table 2.3 lists important dust species in O- and C-CSEs with their spectral signatures in the infrared. The characteristics of a SED of oxygen-rich stars in the infrared can be explained with amorphous silicates. The SED shows two prominent spectral features, the 9.7 and 18 μm bands from the Si-O stretching mode and O-Si-O bending mode, respectively. In comparison, the infrared excess of carbon-rich stars, originating from the amorphous carbon dust, is mainly featureless (Ivezic & Elitzur, 1995). In order to distinguish between O-rich ans C-rich AGB stars color-color diagrams can be used, e.g. the IRAS[15] color [12-25] and near-IR color [H-K]. O-CSEs show a larger excess in the 10-20 μm range, relative to the 1-5 μm range, compared to C-CSEs.

With the occurrence of dust, diameter determinations are influenced at certain wavelengths as

[14]Polycyclic Aromatic Hydrocarbons

[15]http://irsa.ipac.caltech.edu/Missions/iras.html and Neugebauer et al. (1984)

O-rich CSE				C-rich CSE			
Species		λ (μm)	Transition	Species		λ (μm)	Transition
Spinel	a	13, 17		AMC	a	featureless	
Al_2O_3	a	11.5		Diamond	c	3.52	
Silicates	a	9.7	Si-O[a]	SiC	a+c	11.3	Si-C[a]
	a	18	O-Si-O[b]	PAHs	a+c	$3-17$	C-H[a, b], C-C[a]
	c	$15-50$					
H_2O	a	3.1	O-H[a]				
	c	43, 62					

Table 2.3: Important dust species in O- and C-CSEs with their prominent spectral signatures in the infrared, see text ([a] stretching mode, [b] bending mode; a = amorphous, c = crystalline; AMC = amorphous carbon, PAHs = polycyclic aromatic hydrocarbons).

well. According to equation 2.4, the infrared emission from dust probes in general the cooler regions in the CSE, while the visual and infrared emission from molecules trace the closer, warm molecular shells (Section 2.2.2). In the overlapping region, where still molspheres exist, but first dust seed particles are formed, both phases are responsible for the two times larger apparent diameters if compared with the photospheric diameter. The mid-infrared interferometer used in this work is able to observe this transition region. In O-rich stars, molecular shells of H_2O and SiO in combination with Al_2O_3 dust is expected (Ohnaka et al., 2005; Wittkowski et al., 2007; Perrin et al., 2007; Verhoelst et al., 2009). In particular in the N-band (8 to 13 μm), strong pure-rotation lines of H_2O in addition to SiO fundamental bands are important. Al_2O_3 provides significant opacity for wavelengths longward of 10 μm (Begemann et al., 1997). In C-rich stars molecular shells of C_2H_2 and HCN, in addition to amorphous carbon and SiC dust, are proposed (Aoki et al., 1998, 1999; Ohnaka et al., 2007).

It is therefore important to note again that different wavelengths probe different regions in an AGB star, according to the temperature, composition and optical properties of the region. In this context it should be mentioned that the temperature gradient in the non-equilibrium CSE is different for molecules and dust, since dust can cool and absorb more effectively. Another point which has to be taken into account is that the composition and environment dynamically changes with the pulsation.

2.3 Stellar Wind, Mass Loss and Binarity

The ignition and driving force for the stellar wind, leading to a high mass loss rate, is still an active research area. This can be coupled with the question how asymmetries are formed in AGB stars. With the end of the AGB phase and the transition to a planetary nebula high-velocity winds, jets and other non-circular symmetric structures develop. This section discusses the basic ideas of the formation of the wind, the mass loss, its connection to asymmetries, and how a close companion influence this.

2.3.1 Pulsation-Enhanced Dust-Driven Wind

The driving mechanism, i.e. the source of outward-directed momentum that overcomes gravity, could be provided by the gradient of gas pressure (thermal wind), by absorbing the outward-directed stellar radiation and re-emitting photons in all directions (radiation-driven winds) or by accelerating the gas through waves (sound waves, shocks), where the latter one is a rather ineffective mechanism. The current understanding is that the wind is dominantly driven by radiation. Dust grains accelerate by catching the momentum from the radiation of the star and the gas is dragged by the dust via momentum transfer by gas-grain collisions.

The winds of AGB stars are slow compared to other types of stars. Typical velocities are on the order of $10 - 20$ km/s[16] while mass loss rates are fairly high (typically 10^{-6} $M_\odot$/yr, cf. Section 2.3.2). These two facts imply high gas densities in the outflow, indicating that the wind originates in a dense environment. In order to create high densities at the region where dust can condensate, gas needs to be lifted up. This increase of the scale height of the atmosphere is naturally done by the large-amplitude pulsation and is the first necessary step in the wind formation scenario.

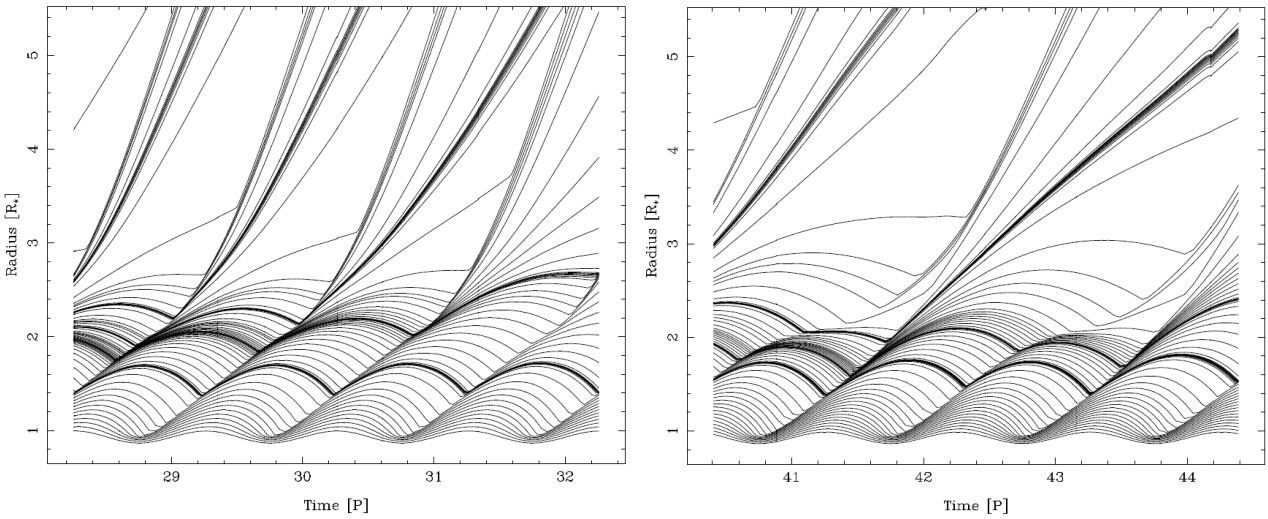

Figure 2.13: Positions of selected mass shells in AGB atmospheres as a function of time for two models (Höfner & Dorfi, 1997). The time is given in piston periods P and the radius in units of the stellar radius R_* of the corresponding hydrostatic initial model. Model parameters (L_*, M_*, T_*, C/O, P) are ($10^3\,L_\odot$, $1.0\,M_\odot$, 2700 K, 1.77, 650 d) *(left)*, and ($10^3\,L_\odot$, $1.0\,M_\odot$, 2700 K, 1.49, 650 d) *(right)*, respectively.

Figure 2.13 shows the position of selected atmospheric mass shells. The pulsation leads to a large scale motion of the outer layers. Shock fronts develop and compress, heat and push the upper layers outwards. Most of the mass falls back along their ballistic trajectory. For mass shells further out conditions may get favorable, i.e. they have high enough densities combined with sufficiently cool temperatures, that dust grains can develop. How much dust forms depends on the time scale for grain growth.

The higher mass absorption coefficient (opacity) of dust compared to gas, from which it was

[16]The solar wind has a final speed of typically 500 km/s.

formed, leads to an effective acceleration (see below). The further dust grain growth and acceleration is regulated by the competition between falling temperatures, which favors condensation, and decreasing gas density, which slows down grain growth. The final degree of condensation, together with the stellar parameters, determines the terminal velocity[17] of the pulsation-enhanced dust-driven wind and the mass loss rate. As illustrated in Figure 2.13, a dense wind may form at each or every second pulsation cycle, i.e. the outer mass shells may not escape at every pulsation cycle.

A simplified equation of motion for a dust-driven wind has the solution (Habing et al., 1994)

$$v_{\rm g}(r) \;=\; v_\infty \sqrt{1-\left(1-\frac{v_0^2}{v_\infty^2}\right)\frac{r}{r_0}}\,. \tag{2.8}$$

It assumes that the dust consists of one-size, non-evolving grains, and the drag force has only a r^{-2} dependence. If pressure terms are ignored as well, the terminal velocity v_∞ becomes

$$v_\infty \;=\; \sqrt{2GM(\Gamma-1)/r_0}\,, \tag{2.9}$$

where Γ is the ratio of the drag force and the gravitational force on the gas, given by

$$\Gamma \;=\; \frac{3(Q_{\rm p,F}/a_{gr})L\varphi}{16\pi GcM\rho_{\rm gr}}\frac{v_{\rm g}}{v_{\rm d}}\,. \tag{2.10}$$

M is the stellar mass, L the stellar luminosity, G the gravitational constant, r_0 the radius at which the acceleration starts (approximately the radius where first dust condensation takes place), v_0 the gas velocity at r_0 (approximately the sound speed), v_d the dust velocity, c the speed of light, $Q_{\rm p,F}$ the radiation pressure efficiency of a grain averaged over the stellar spectrum, a_{gr} the grain radius, ρ_{gr} the density of the grain and φ the dust-to-gas mass loss ratio. The velocity difference between the faster outwards moving dust and dragged gas particles is characterized by the drift velocity $v_{\rm drift} = v_{\rm d} - v_{\rm g}$. For very high mass loss rates, $v_{\rm drift}$ is relatively small, i.e. at around 3 km/s instead of up to 20 km/s.

The wind at the dust condensation radius starts subsonic and reaches supersonic velocity at termination. It passes through the sonic point which coincides in a isothermal CSE with the critical point in the Euler equation of the wind (Parker, 1958). In a real CSE of an AGB star this critical point can move inwards. The consequence of having a critical point is that only an outward force acting below the critical point increases the mass loss rate, and any force acting above the critical point only increases the velocity of the wind. Therefore, the region between the photosphere and the sonic point is where the important wind formation physical processes occur.

The above formulas give an indication of how the kinematics depend on luminosity (since r_0 is roughly proportional to $L^{0.5}$), on metallicity (through φ), on condensation radius and on grain radiative properties. With increasing main-sequence mass, i.e. with increasing luminosity, and higher metallicity, the terminal velocity increases. For reasonable values[18] the terminal velocity

[17] The terminal velocity is the asymptotic velocity at large r.

[18] $M = 1$ M$_\odot$, $L = 10^4$ L$_\odot$, $r_0 = 2{\cdot}10^{14}$ cm, $\rho_{\rm gr} = 2$ g/cm^3, $a_{\rm gr} = 10^{-5}$ cm, $Q_{\rm p,F} = 0.02$, $\varphi = 0.005$ and $v_{\rm g}/v_{\rm d} = 1$.

becomes about 16 km/s which is reached fairly rapidly, i.e. that at $r \approx 5\,r_0$ the wind has already a velocity of $0.9 \cdot v_\infty$. These are typical final characteristic values of winds of AGB stars with intermediate to high mass loss rates and luminosities. Nevertheless, it is quite possible that the wind mechanism may be different for an early and a late AGB star, a low- and a high-mass AGB star, during and between thermal pulses.

The terminal velocity depends also on the underlying chemistry. The distribution is slightly different between C-rich and O-rich stars. For similar mass loss rates and pulsation behaviors C-CSEs have higher expansion velocities than O-CSEs. The AMC dust in C-stars condensates at higher temperatures and has a higher opacity compared to the dust grains in M-stars. C-stars exhibit therefore in general a higher mass loss rate. In O-rich AGB stars, the scattering on micrometer-sized Fe-free silicates drives the wind, while in C-rich AGB stars, AMC grains of all sizes absorb the radiation and are responsible for the acceleration. The dust-driven wind formation scenario in C-rich stars is to a certain amount satisfactory solved (e.g. Gail & Sedlmayr, 1987; Gautschy-Loidl et al., 2004; Woitke, 2006b; Wachter et al., 2008), while the mechanism in O-rich stars is still under investigation.

In particular, the composition of the grains and their optical properties leads to different results. Woitke (2006a) concluded that a wind driven by radiation pressure on Mg-Fe-silicates is not sufficient, while Höfner (2008) came to the result that micrometer-sized Fe-free silicate grains have a considerable radiative scattering cross-section, compensating for their low absorption cross-section, leading to an efficient radiative acceleration in O-rich stars. Another complication is that typical silicates form in more distant wind regions, which requires that a previous mass loss in the inner region was initiated. However, Fe-free silicates may form close to the star and may solve this problem. The formation of other dust species, like Al_2O_3, happens close to the atmosphere as well and requires no mass loss.

2.3.2 Mass Loss

Mass loss by stellar winds plays a crucial role in the evolution of AGB stars, since it does not only determine the final mass at the end of the AGB phase, and hence the final luminosity, but also affects its internal structure. It sets up the evolutionary time scale of the stellar remnant and the formation of the planetary nebula. In addition, the matter lost during the AGB represents a significant fraction of the total metal-enriched gas-return to the interstellar medium. These particles are the seeds of the interstellar grains, probably facilitating star formation directly through their cooling capabilities and indirectly by protecting molecular coolants like CO and H_2O.

The mass loss is classically described by Reimers' law (Reimers, 1975), given as

$$\dot{M} \;=\; -\frac{\mathrm{d}M_*}{\mathrm{d}t} \;=\; \eta\,\frac{L_* R_*}{M_*}\,, \tag{2.11}$$

where L_*, R_* and M_* are the stellar luminosity, radius and mass, respectively, given in solar units, and η is a fitting parameter. Unfortunately, the above law is not very well suited to describe the high AGB mass loss rates, which are typically lie between 10^{-7} and 10^{-4} $M_\odot$/yr

with a minimum value of 10^{-8} $M_\odot$/yr[19]. The reason is that this formula was originally designed for RGB stars. Better mass loss prescriptions are based on theoretical arguments and empirical calibrations (e.g. Arndt et al., 1997; Fleischer et al., 1992; Girardi & Bertelli, 1998; Groenewegen & de Jong, 1994; Vassiliadis & Wood, 1993; Groenewegen et al., 2009), predicting also the so-called superwind regime and the ejection of planetary nebula in the final stage of the AGB phase. They consider the combined role of radiation pressure, stellar pulsation and dust formation.

Mass lose rates in AGB stars are estimated with different methods and probing different parts of the extended CSE. This is possible since the physical conditions vary extensively between the inner dense and warm regions close to the stellar photosphere and the tenuous and cool outer parts where the CSE gradually merges with the interstellar medium. Two methods are discussed in the following: a mass loss estimation based on the circumstellar CO radio line and a mass loss estimation based on the dust continuum emission.

The mass loss estimation from the *CO rotational line emission* at radio wavelength is the most used method (Olofsson et al., 2002). This method is applicable to O- and C-CSEs, as well as to a wide range of mass loss rates and objects in different evolutionary stages. The CO lines are strong and provide a large observational space. The energy level diagram of CO is simple and the radiative transition rates and collisional cross sections are known. This molecule has observable transitions of varying excitation energies and the molecular abundance can be relatively easy estimated. A formula based on modeling (Schöier & Olofsson, 2001) is

$$\dot{M} \;=\; s_J \, I_{\mathrm{CO},J}^{a_J} \, v_\infty^{b_J} \, f_{\mathrm{CO}}^{-c_J} \, \theta_\mathrm{b}^2 \, D^2 \; \mathrm{M}_\odot/\mathrm{yr} \; , \tag{2.12}$$

where $I_{\mathrm{CO},J}$ is the integrated intensity of the $J \;\rightarrow\; J-1$ line given in K·km/s, v_∞ the terminal velocity in km/s, D the distance in kpc and θ_b the angular diameter in arcsec. For the $J \;=\; 1 \rightarrow 0$ line the constants are $s_1 = 5.6{\cdot}10^{-13}$, $a_1 = 0.70$, $b_1 = 0.71$ and $c_1 = 0.83$. This formula gives values within a factor of two of the modeling in the ranges $10^{-7} \leq \dot{M} \leq 10^{-5}$ $M_\odot$/yr, $5 \leq \; v_\infty \leq 20$ km/s and $10^{-4} \leq f_{\mathrm{CO}} \leq 10^{-3}$ (fractional abundance of CO). There are uncertainties due to the treatment of CO photodissociation, the strong dependence on luminosity at low mass loss rates, the strong dependence on the gas-grain collision heating at high mass loss rates, and the determination of the true abundance of circumstellar CO. In the case of the $J \;=\; 1 \rightarrow 0$ CO line, the molecules are approximately excited out to the photodissociation limit. Thus, outer regions contribute most to the observed intensity probing that region, while higher transitions come from increasingly closer star regions. A further discussion on CO mass loss estimators can be found in Ramstedt et al. (2008).

An alternative method is provided by the *circumstellar dust emission*. An advantage is that there is no dependence on complicated line-transfer effects. On the other hand, the emitting properties of the dust grains need to be known, as well as the dust-to-gas ratio φ. Another disadvantage is that dust emission provides no kinematic information. From sufficiently long wavelengths, where the Rayleigh-Jeans approximation is valid, dust mass loss rates can be estimated from the monochromatic flux in the optically thin limit via

$$\dot{M}_\mathrm{dust} \;=\; \frac{\lambda^2}{\chi_{\mathrm{gr},\nu}} \frac{S_{\mathrm{d},\nu} v_\mathrm{d} D^{1.4}}{\theta_\mathrm{b}^{0.6} T_{15}} \; 10^{-3} \; \mathrm{M}_\odot/\mathrm{yr} \; , \tag{2.13}$$

[19]In comparison, the mass loss rate of the sun is 10^{-14} $M_\odot$/yr.

where $S_{\mathrm{d},\nu}$ is the flux density in Jy, v_{d} the dust velocity in km/s, D the distance in kpc, λ the wavelength in mm, $\chi_{\mathrm{gr},\nu}$ the opacity in cm^2/g, θ_{b} the angular diameter in arcsec and T_{15} the dust temperature at 10^{15} cm in K. Since most of the above parameters, including the dust-to-gas ratio, are barely known, mass loss rates obtained in this way are accurate only to within an order of magnitude. Other methods relying on dust observations are color relations, the modeling of SEDs or the use of dust features.

The outflowing gas and dust is in general not smooth as can be inferred from Figure 2.12. The spherical outflow is more clumpy rather than homogeneous with up to 30 times higher density regions. In the shadow of these dust clouds, the conditions for subsequent dust formation is improved, resulting in radially oriented, linear, cool dust structures surrounded by warmer, almost dust-free gases, through which the radiative flux preferably escapes. This might be related to tangential structures and asymmetries seen in PNe (Section 2.3.3).

The dependence of mass loss rates on various stellar properties can only be given on a qualitative basis, since the uncertainties are high and correlations are difficult to disentangle. From the fact that the final white dwarf masses are on the order of one solar mass, it is clear that stars with main-sequence progenitor masses of up to 8 solar masses have to lose much more material than lower mass stars, since only a few tenths of a solar mass are lost prior to the AGB phase. Higher masses are also accompanied with higher luminosities. From studies of the period, which is directly related with the main-sequence progenitor mass[20] (cf. equation 2.2), it can be concluded that with increasing mass (and therefore luminosity) mass loss rates are increasing. During the AGB evolution the stars lose mass, decreasing the mass loss rate, but this is more than compensated by the simultaneously increasing luminosity.

A dependence on the C/O ratio, period and pulsation amplitude could not be established, while there is only a weak dependence on effective temperature and metallicity ($\propto Z^{0.5}$). The left panel of Figure 2.14 shows the mass and mass loss evolution of a 1.5 solar mass star during the AGB phase, in addition to some other quantities discussed in previous sections. The luminosity L, period P and expansion velocity v_{exp} gradually increases while the effective temperature T_{eff} decreases. The extremely enhanced mass loss, accompanied by a steep decline of the mass at the end of the AGB phase, is clearly visible. After this superwind epoch a hot white dwarf with a stellar envelope mass of less than 0.001 $\mathrm{M}_\odot$ remains.

This figure shows also nicely the correlation of episodic mass loss with thermal pulses (TP). Probably, the observed detached shells, e.g. seen in R Hya (right panel of Figure 2.14), are the result of a short heavy mass loss during such a TP. The time period for episodic mass loss is on the order of 10^2 to 10^3 years. The total mass return of all AGB stars in the Galaxy is estimated to ≥ 0.3 $\mathrm{M}_\odot$/yr (Habing & Olofsson, 2004).

2.3.3 Asymmetry, Jets and Binarity

Stars are almost spherical during the longest time of their evolution. As they reach the end of the AGB phase, non-spherical shapes are getting more and more common. In particular, bipolar shapes, suggesting a concentration of remnant AGB matter in a toroidal region, are regularly detected. Nonsphericity is already to some degree present in the AGB phase, but with

[20] A little bit caution is needed here since the periods are getting longer with time.

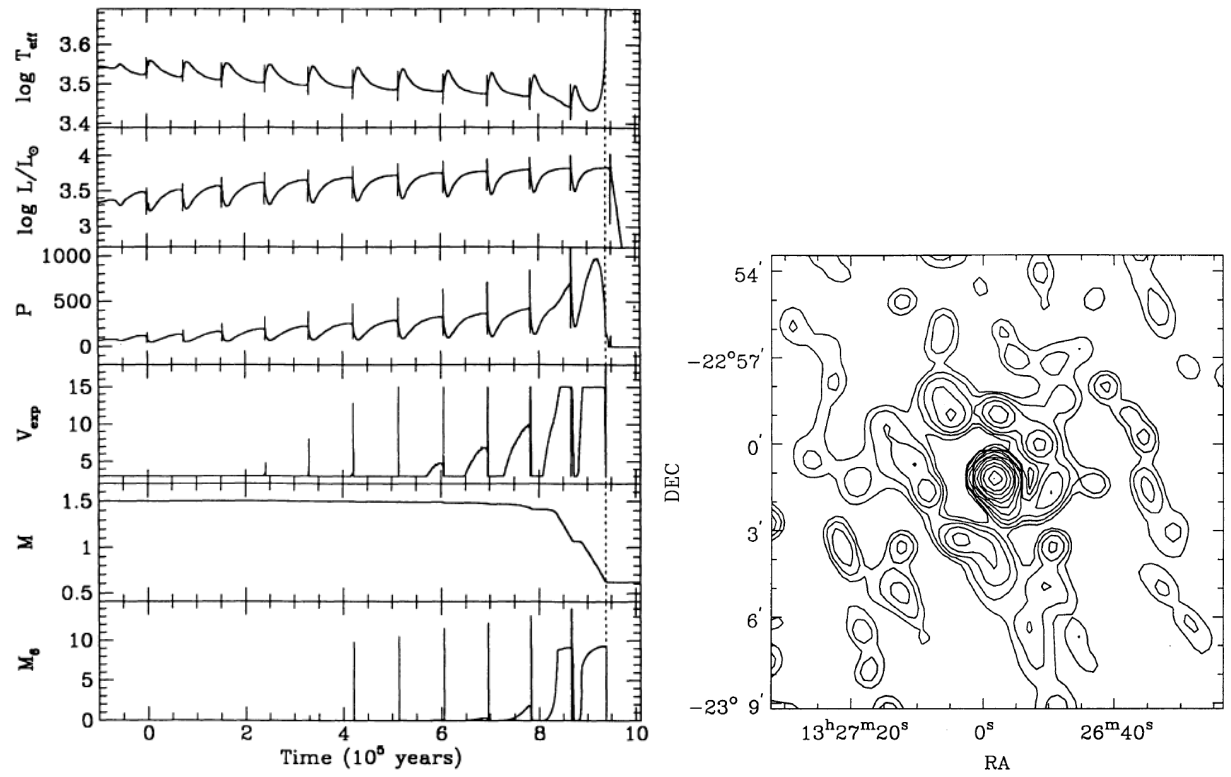

Figure 2.14: *Left:* Time dependence of various quantities during the TP-AGB phase of a star with $(M/\mathrm{M}_\odot,\ Y,\ Z) = (1.5,\ 0.25,\ 0.008)$. The abscissa represents the time after the first thermal pulse. The dotted vertical line on the right represents the end of the AGB phase. M_6 is the mass loss rate in units of 10^{-6} $\mathrm{M}_\odot\mathrm{yr}^{-1}$ (Vassiliadis & Wood, 1993). *Right:* Image of the detached dust shell of R Hya reconstructed from IRAS at 60 μm. Contour lines are 1, 2, 4, 8, 16, 32, 64, 128, 256, 512, and 1024 MJy/str (Hashimoto et al., 1998).

the transition from a post-AGB star to a planetary nebula (PN), departures from symmetry become very prominent, resulting in the varied shapes seen in PN.

Anisotropy can be due to a non-radial pulsation, density distribution, temperature distribution, UV photon flux, and mass loss rate. The reason why these properties vary with direction and why this happens in particular at the end of the AGB phase is not conclusively determined so far. Another unsolved problem is how the large scale asymmetries of PN ejecta are connected with the small scale nonsphericities of the previous AGB star. In some cases, it might be related to an interaction with magnetic fields, large convection zones, the clumpiness of the wind, its slow rotation or the presence of a binary companion.

Maser observations show that magnetic fields exist in AGB stars (Vlemmings et al., 2001). Magnetic fields may lead to the formation of magnetic cool spots. Their lower temperatures facilitate closer dust formation above the spots and are therefore a possible cause for deviations from spherical outflow. Large convection zones and the clumpiness of the wind could result in a similar behavior. The slow rotation, originating from their expansion after leaving the main sequence, reduces somewhat the gravity around the equatorial plane. Even if the centrifugal forces are by far not large enough to overcome gravity, they increase the density scale height and favor a more effective dust production above the equatorial region (Dorfi & Höfner, 1996).

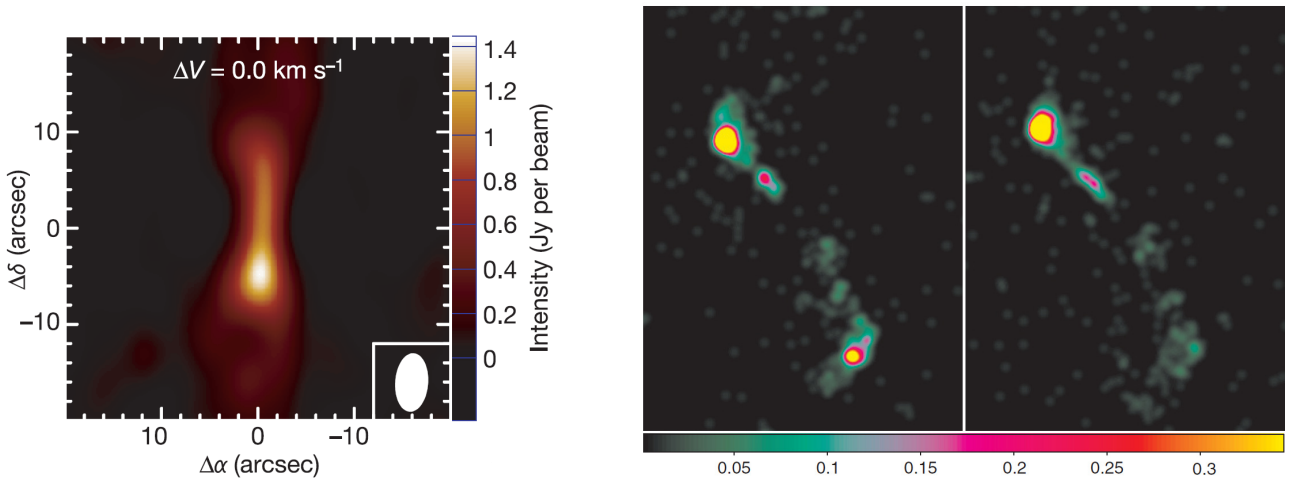

Figure 2.15: *Left:* Map of the CO $J = 1 - 0$ radio emission showing the jets of V Hya. The image is a cross-sectional cut of the sky-plane through the circumstellar envelope. The data are integrated over a small radial velocity interval around the systemic velocity (Sahai et al., 2003). *Right:* Chandra X-ray images showing the stellar jets of R Aqr. The size of each image is 45 × 50 arcsec. N is up and E is left (Nichols & Slavin, 2009).

However, of larger influence are interactions with a companion (a star or a massive planet). The transfer of angular momentum leads to huge structural changes of the dust distribution and the rotation parameters. These effects are possibly related to the axisymmetric appearance of many PNe, since there are a number of known binaries in wide systems among post-AGB stars with a highly axisymmetric distribution of gas and dust, presumably in a circumbinary disk (e.g. in the Red Rectangle). Another effect seen during the transition phase, between an AGB star and a PN, is the development of jets. Figure 2.15 shows jets in V Hya and R Aqr, observed in the radio and X-ray. The launch of large scale, high energy jets in both systems is caused by the presence of a compact companion/WD with an accretion disk (see also Section 2.4.2 and 2.4.4).

The connection of the AGB star evolution with binarity can be manifold. Two broad classes of binary systems can be distinguished. Either the primary[21] star is currently an AGB star, while the secondary is still an unevolved dwarf, or the secondary is a WD, while the primary is an AGB star and has been polluted by the secondary when the latter was an AGB star.

Both stars in a binary system start as main sequence stars. The star with higher zero-age mass will evolve first to an AGB star. Depending on the separation, a detached, semi-detached or common envelope system develops concerning the Roche equipotentials (left panel of Figure 2.16). In a detached system the secondary star accretes processed material from the AGB star via the wind, while in a semi-detached or common envelope system the mass transfer proceeds via the inner Lagrangian point L_1 (Roche lobe overflow). In all cases the spectrum of the dwarf shows peculiar abundances due to the polluted atmosphere. Another effect is that the mass loss of the mass-losing star could be enhanced, since the presence of a companion reduces the effective gravity.

[21]Defined as the star dominating the visual spectrum.

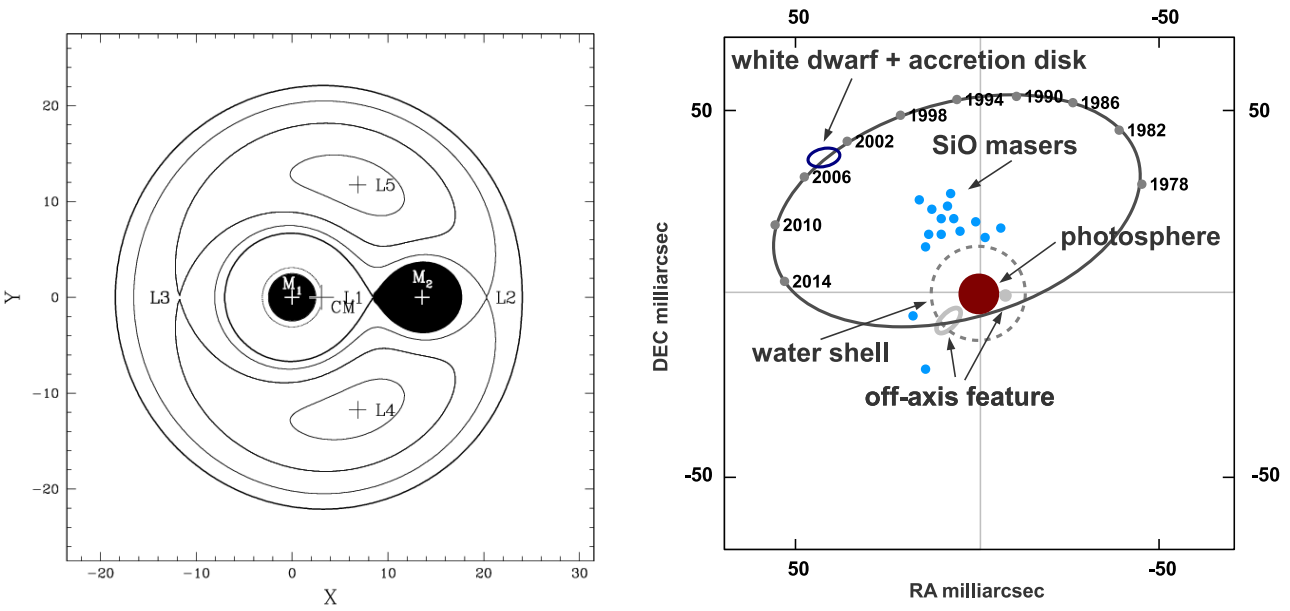

Figure 2.16: *Left:* Section in the orbital plane of Roche equipotentials for a binary system with a mass ratio of $M_2/M_1 = 0.3$. The positions of the Lagrangian points L1 to L5 are indicated, as well as that of the center of mass (CM). *Right:* Orbit of the white dwarf companion of R Aqr. The plot is based on the orbital elements published by Hollis et al. (1997). The Mira star, the H_2O shell, two off-axis features and the detected SiO maser emission is shown as well (adopted from Ragland et al., 2008).

After the AGB star becomes a PN, leaving a WD behind, the former secondary star eventually evolves to an AGB star. The WD can accrete material and a symbiotic system may form, where the hot WD or an accretion disk ionizes the gas and powers eruptions and jets. The right panel of Figure 2.16 shows the symbiotic system R Aqr, where the close WD has a period of about 44 years. In such systems dust obscuration episodes are typical phenomena, favor more dust condensation and the formation of a circumbinary disk.

2.4 The AGB Stars R Aql, R Aqr, R Hya, V Hya and W Hya

The five AGB stars observed in this work are described in this section[22]. For each star important theoretical and observational work from previous publications are summarized giving an overview of their characteristic properties. Table 2.4 lists some of the relevant phenomenological features for each star. The references can be found in the according subsection of the individual star. More data on the multiplicity are available in the Washington Visual Double Star Catalog (WDS, Mason et al., 2001) on e.g. VizieR[23]. Important quantitative data are summarized in Table 2.5 (page 42, Section 2.4.6). According SEDs and visual light curves for each star are shown in Section 5.1.

[22]The selection criteria for choosing these stars can be found in Section 4.1.1.
[23]http://vizier.u-strasbg.fr/viz-bin/VizieR

Table 2.4: Target phenomenologies

Target:	R Aql	R Aqr	R Hya	V Hya	W Hya
Type:	Mira	Mira	Mira	SRa/L	Mira/SRa
Chemistry:	O-rich	O-rich	O-rich	C-rich	O-rich
Mass:	1.0 $M_\odot$	1.5 $M_\odot$	2.0 $M_\odot$	1.0 $M_\odot$	1.0 $M_\odot$
Mass loss rate:	normal	low	variable	high	low
Multiplicity:	triple system	SB	wide binary	wide binary	wide binary
Evol. stage:	TP-AGB	TP-AGB	TP-AGB	post-AGB	early-AGB
Jets/fast wind:	no	yes	no	yes	no
Asymmetry:	maybe	yes	no	yes	yes
Maser:	SiO, H_2O, OH	SiO, H_2O, OH (indicative)	SiO, H_2O, OH	CO ?	SiO, H_2O, OH
Period:	decreasing	stable	decreasing	two periods	stable
Others:	recent He flash	symbiotic system (Mira+WD)	detached shell, recent He flash	common envelope, rapid rotator	-

2.4.1 R Aquilae

The variability of R Aql was discovered in 1856 in Bonn. Since 1900, the visual period of the star declined quite dramatically with an average rate of approximately 0.4 days per cycle (Greaves, 1998; Greaves & Howarth, 2000). This was accompanied by a decrease in amplitude of about 1 mag (Bedding et al., 2000). While in 1915 the period was about 320 days, it smoothly decreased to a value of about 264 days in 2010. As will be described for R Hya (Section 2.4.3), the shrinking of the period can be attributed to a recent thermal pulse as shown in Figure 2.9 (page 15, Section 2.2.1) (Wood & Zarro, 1981). Therefore, the Mira R Aql, with a spectral type of M7 III, is in the TP-AGB phase.

The distance to R Aql is relatively well known compared to other AGB stars. The Hipparcos catalog (van Leeuwen et al., 1997) gives a value of 211^{+71}_{-42} pc, while van Belle et al. (2002) estimated a distance of (224 ± 56) pc. Even the 220 pc, inferred from the PL relation and listed in Table 2.5 (page 42), does not strongly deviate. The mass and luminosity, obtained from modeling and observations, is 1 $M_\odot$ and 3470 $L_\odot$, respectively (Hofmann et al., 2000). Effective temperature determinations range from (2550 ± 150) K (Haniff et al., 1995), over 3072 ± 161 K (Hofmann et al., 2000) to 3198 ± 147 K (van Belle et al., 1996), where the two last values refer to observations near maximum visual phase.

R Aql is listed in the WDS as triple system. As can be inferred from the left panel of Figure 2.17, the first component has a separation of 78 arcsec at a position angle of 300°, and the second component is 180.2 arcsec away with a position angle of 260° (epoch 2002). However, the

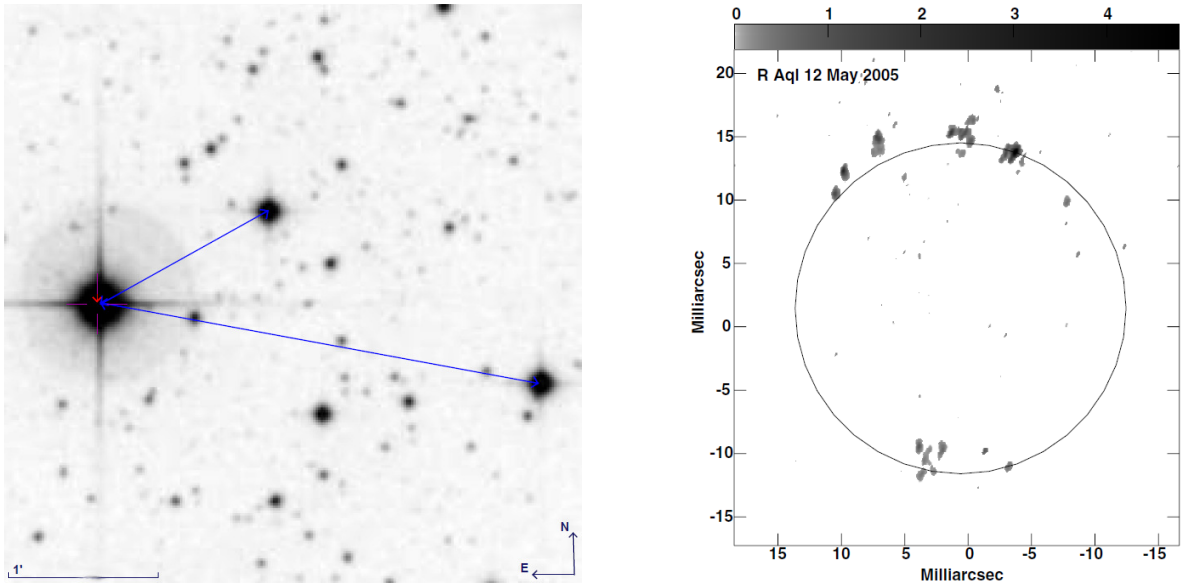

Figure 2.17: *Left:* Target star R Aql with its companions (Aladin DSS2-F-POSSII image). *Right:* Square root of the total SiO maser emission at 43.1 GHz as a gray scale in Jy/beam. The circle shows the location and size of the fitted ring, see text (Cotton et al., 2010).

two companion stars have dissimilar proper motions to R Aql and are probably only optical companions (Greaves & Howarth, 2000).

Interferometric angular diameter measurements for R Aql in the K-band (2.2 μm) by van Belle et al. (1996), Hofmann et al. (2000) and Millan-Gabet et al. (2005) gave uniform disk diameters of around 10.7 mas. Diameter determinations in the H-band (1.6 μm) were similar, with 9.3 to 12.7 mas (Millan-Gabet et al., 2005; Ragland et al., 2006), while a determination in the visual (700 to 710 nm) resulted in higher values of 24 to 30 mas (Haniff et al., 1995). More details on this can be found in Section 5.3. From the pulsation period, mass and linear radius (given by the angular diameter and the distance) the pulsation mode can be derived. Hofmann et al. (2000) came to the result that R Aql is a fundamental mode pulsator in agreement with recent considerations (Section 2.2.1).

SiO, H_2O and OH maser emission were monitored for the O-rich star R Aql. SiO maser emissions were reported by Benson et al. (1990), Pardo et al. (2004) and Cotton et al. (2010). The latter author derived for the 43.1 and 42.8 GHz emission an average ring diameter of (26.1 $\pm$ 1.5) mas and (22.3 $\pm$ 1.9) mas, respectively (right panel of Figure 2.17), in agreement with the supposed extended atmosphere. At a larger diameter of 330 mas, Lane et al. (1987) as well as Brand et al. (1994) detected H_2O maser emission. The maximum of this 22 GHz maser emission occurred every third time the visual period. This indicates that a superperiod as in W Hya (two visual periods) exists (Gomez Balboa & Lepine, 1986), and suggests that shock waves, leading to the clumping of H_2O and the formation of dust, may not appear every cycle as shown in Figure 2.13 (page 22). Studies of OH masers were performed by Bowers et al. (1989), Etoka & Le Squeren (2000) and He et al. (2005), showing that this maser emission originates at a ring with a diameter between 2000 and 3000 mas.

Responsible for different diameters at different wavelengths are the extended molecular spheres.

This was modeled for R Aql by Matsuura et al. (2002) with two layers of water of different temperatures. The radius of the hot layer varied from 1 to 2 photospheric radii between visual minimum and maximum. The model could explain the emission and absorption features seen in the near infrared ($2.5 - 4.0$ μm) as well. While Cotton et al. (2010) could not identify strong asymmetries in the SiO maser distribution, Lane et al. (1987) and Bowers et al. (1989) saw highly elongated and complex structures in the H_2O (NW-SE oriented) and OH masers (NE-SW oriented), respectively. In addition, the interferometric measurements by Ragland et al. (2006) gave a significantly non-zero closure phase, indicating an asymmetry as well.

Total mass loss rates were estimated to 8×10^{-7} $M_\odot yr^{-1}$ and 5.6×10^{-7} $M_\odot yr^{-1}$ by Gehrz & Woolf (1971) and Hagen (1982), respectively, whereas Knapp & Morris (1985) found a much higher value of 3.5×10^{-6} $M_\odot yr^{-1}$. The dust mass loss rate was derived by Hagen (1982) with a value of 6×10^{-8} $M_\odot yr^{-1}$, which is more consistent with the total mass loss rate of Knapp & Morris (1985). Derived wind velocities ranging from 7 to 10 km/s (Bowers et al., 1989, and references therein).

2.4.2 R Aquarii

R Aqr is the closest known symbiotic binary at a distance of about 220 pc (van Belle et al., 1996). Different distances were obtained by Perryman et al. (1997a) (Hipparcos), Hollis et al. (2001), Wyatt & Cahn (1983) and van Belle et al. (2002) with 197 ± 100 pc, 200 pc, 230 pc and 272 ± 68 pc, respectively. Table 2.5 (page 42) lists an intermediate value of 250 pc, derived from the PL relation by Whitelock et al. (2008). This D-type (dusty) symbiotic system consists of a $1.0 - 2.0$ $M_\odot$ Mira variable and a $0.6 - 1.0$ $M_\odot$ white dwarf (WD) (Hollis et al., 1997; Boboltz et al., 1997; Tatebe et al., 2006; Gromadzki & Mikołajewska, 2009) that accretes matter through a disk (e.g. Hollis et al., 2000). The presence of a hot companion with an accretion disc is inferred from UV spectra. The long-period variable is of spectral type M7 III pev with a 387 day pulsation period (GCVS, Neugebauer et al., 1984).

The binary system hosts a compact HII region within a filamentary oval nebula of 30 arcsec size along a N-S axis (e.g. Kafatos et al., 1986). It is surrounded by a large and expanding hour-glass shaped nebulosity with an extension of at least 120 arcsec along a E-W direction (Wallerstein & Greenstein, 1980; Hollis et al., 1985; Henney & Dyson, 1992; Corradi et al., 1999). This can be clearly seen in the left panel of Figure 2.18. The compact HII region is probably a dusty nebula produced by the Mira winds and ionized by the UV radiation from the hot companion star. The shaping is proposed to be a result of the interaction of a slow and a fast wind (Balick & Frank, 1997).

The R Aqr binary system was for the first time resolved in the continuum radio emission at 7 mm by Hollis et al. (1997). Willson et al. (1981), Hollis et al. (1997) and Gromadzki & Mikołajewska (2009) derived orbital solutions with a period of about 44 years, while McIntosh & Rustan (2007) estimated the orbit period to 34.6 years. The solution by Hollis et al. (1997) is plotted in the right panel of Figure 2.16 (page 29). They derived a high eccentricity of 0.8, which is contradictory to the latest calculation by Gromadzki & Mikołajewska (2009), since their solution has an eccentricity of 0.25. The fitted semi-major axis is in both cases on the order of 15 AU.

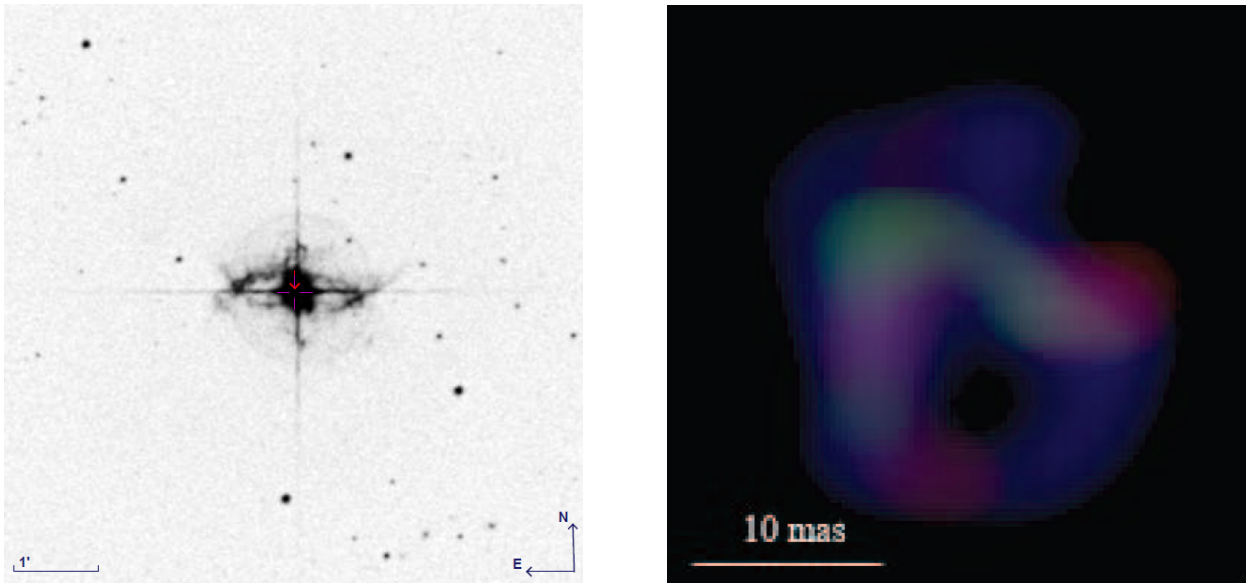

Figure 2.18: *Left:* Target star R Aqr with its nebula (Aladin DSS2-ER-SERC image). *Right:* Three wavelength image (from reconstructed near-infrared images) showing the clumpy water shell around R Aqr. For more details see Ragland et al. (2006).

A period of 44 years can be inferred from the observed decrease of the brightness in the visual and near-infrared light curves during 1975 − 1978 and on two previous occasions. This is interpreted as obscuring circumstellar dust clumps or neutral material in the accreting stream eclipsing R Aqr (Willson et al., 1981). Smaller observed periods may come from a differential rotation of the dust shell (see below).

The accretion disk, formed around the compact component, gives rise to prominent jets, detected at x-ray (Kellogg et al., 2001, 2007; Nichols & Slavin, 2009), ultraviolet (e.g. Hollis et al., 1991), optical (e.g. Herbig, 1980; Burgarella et al., 1992; Paresce et al., 1991; Paresce & Hack, 1994, with HST), and radio wavelengths (e.g. Hollis et al., 1985). The symmetric jets, oriented along a NE-SW axis, extend up to 2500 AU and have expansion velocities of 90 to 200 km/s (Hollis et al., 1991; Contini & Formiggini, 2003; Nichols & Slavin, 2009). The jet is probably refueled episodically with increased activity at periastron, when the hot companion passes through the CSE of the Mira. Stute & Sahai (2007) modeled the jet structure in x-ray emission.

The current mass loss rate of this star is rather low, but uncertainties are very high due to difficulties to obtain reliable gas-to-dust ratios, e.g. Contini & Formiggini (2003) estimated a relatively high value of 2500. Rates range from 1.3×10^{-8} $M_{\odot}yr^{-1}$ (Henney & Dyson, 1992) and 6×10^{-8} $M_{\odot}yr^{-1}$ (Matthews & Reid, 2007) to 3×10^{-7} $M_{\odot}yr^{-1}$ (Mennesson et al., 2002) and 8.9×10^{-7} $M_{\odot}yr^{-1}$ (Danchi et al., 1994). The effective temperature, determined for the WD, is between 4×10^4 and 8×10^4 K (Burgarella et al., 1992; Meier & Kafatos, 1995; Contini & Formiggini, 2003) with a proposed luminosity between 0.7 and 20 $L_{\odot}$ (Hinkle et al., 1989; Burgarella et al., 1992). In most calculations an effective temperature of 2800 K (Burgarella et al., 1992; Matthews & Reid, 2007) and a luminosity of 5000 $L_{\odot}$ (Ragland et al., 2008) is assumed for the Mira variable R Aqr.

R Aqr is one of only three among 48 symbiotic Miras that exhibits H_2O masers (Ivison et al., 1994, 1998; Whitelock et al., 2003). A complementary study of SiO masers showed strong emission at 42.8 and 43.1 GHz. SiO maser ring diameters were obtained by Boboltz et al. (1997), Hollis et al. (2001) and Cotton et al. (2004, 2006), with relatively consistent values between 30 and 33 mas and errors on the order of 1.5 mas. This corresponds to a radius of 1.9 R_*, where R_* is the stellar photospheric radius. A differential Keplerian rotation of the SiO maser shell is observed by Hollis et al. (2000, 2001) and Cotton et al. (2004), with rotational periods in the range of 8 to 34 years. OH maser and CO thermal lines are very weak and only tentative detections have been published by Ivison et al. (1998) and Groenewegen et al. (1999), respectively. In the most convincing model, UV radiation and a fast wind from the companion removes the outer envelope of dusty molecular gas, where an OH maser or a thermal CO line could originate, and leaves a relatively small cavity of dense neutral material within a large ionized nebula (Ivison et al., 1998).

R Aqr is the brightest symbiotic system at IR wavelengths. Strong amorphous silicate emission bands at 10 and 18 μm were found. This silicate dust shows features between a characteristic circumstellar environment and the interstellar medium, which indicates an increased reprocessing of grains in relation to the specific symbiotic behavior of the object with an overabundant presence of SiO molecules (Angeloni et al., 2007).

Near-IR interferometry of R Aqr gave uniform disk diameters in the J-band of $11-18$ mas, in the H-band of $14-19$ mas, in the K-band of $14-20$ mas and in the L-band of 34 mas (van Belle et al., 1996; Tuthill et al., 2000; Mennesson et al., 2002; Millan-Gabet et al., 2005; Ragland et al., 2006, 2008). In the visual at 830 nm a diameter of 14 mas was determined (Tuthill et al., 1999), while in the mid-infrared at 11.1 μm a photospheric diameter of 16 mas was claimed (Tuthill et al., 2000). More details, including error details, can be found in Section 5.3. The average of these values correspond to a radius of the Mira component of about 2 AU, i.e. even during periastron passage, the Mira variable remains relatively far from filling the Roche lobe (Gromadzki & Mikołajewska, 2009).

Ragland et al. (2008) modeled the star with a three-component model, consisting of a symmetric central star surrounded by a water shell with a radius of about 2.25 R_*, and an off-axis compact feature at about 2 R_* at a position angle of 131°. They conclude that the observations are best explained with a clumpy, extended H_2O circumstellar envelope as shown in the right panel of Figure 2.18. In this model the SiO masers appear at the outer edge of the molecular envelope, as reported for other Mira stars in the literature (cf. the right panel of Figure 2.16).

Possibly caused by interactions with the close companion, asymmetries could be identified in the close environment around R Aqr. Ragland et al. (2006, 2008) found non-zero closure phases, and Hollis et al. (2001) and Cotton et al. (2004, 2006) detected an asymmetric distribution of the SiO maser emission with position angles between 150° and 180°. Terminal velocity measurements are rare. Kotnik-Karuza et al. (2007) obtained a value of $6-7$ km/s, while Dougherty et al. (1995) assumed $10-30$ km/s.

2.4.3 R Hydrae

The variable star R Hya is one of the brightest Mira variables on the sky and has the distinction of being the third Mira-type variable to be discovered (1704, AAVSO[24]). This O-rich star of spectral type M7 III is well known for its declining period (Wood & Zarro, 1981; Zijlstra et al., 2002) and the presence of a detached shell. In the past few decades, the period of R Hya has declined by over a hundred days. More specifically, Zijlstra et al. (2002) found that the period was about 495 days around the year 1700, declined to 480 days by 1800, then to 450 days by 1850, 420 days in 1900, and finally to 380 days in 1950. It has remained near constant since then. The decline, they found, is nearly linear with a rate of 0.58 days/yr. The heights of maxima and depths of minima seen in R Hya have also changed considerably.

The steady decrease in the period can be possibly attributed to a recent thermal pulse (Wood & Zarro, 1981; Zijlstra et al., 2002) as shown in Figure 2.9 (page 15, Section 2.2.1). In the post thermal-pulse evolution the decline in luminosity causes a reduction in stellar radius, which in turn, causes the period to become shorter. The relaxation of the envelope due to switching the pulsation mode is another proposed explanation (Zijlstra et al., 2002). However, the gradual change in the period of R Hya implies that the pulsation mode has remained constant over the last few hundred years.

As shown in the right panel of Figure 2.14 (page 27), a detached shell could be observed around R Hya (Young et al., 1993; Hashimoto et al., 1998) indicating a change in mass loss rate some 220 years ago. The shell is located about 1.9 arcsec from the star ($\approx$ 250 AU with the given distance below). While the mass loss rate before 1770 is estimated to be between 1.5×10^{-7} $M_{\odot}yr^{-1}$ and 3×10^{-7} $M_{\odot}yr^{-1}$ (Hashimoto et al., 1998; Zijlstra et al., 2002), the present day mass loss rate is a factor of $\approx$ 20 lower and between 1×10^{-8} $M_{\odot}yr^{-1}$ and 4×10^{-8} $M_{\odot}yr^{-1}$ (Decin et al., 2008; Teyssier et al., 2006). A gas-to-dust ratio of 200 was assumed for most of the previous estimations.

This derived mass loss history nicely agrees with the period decline analyzed by Zijlstra et al. (2002). Even the stellar evolution tracks calculated by Vassiliadis & Wood (1993) confirmed that mass loss fluctuations during the thermal pulse cycle can lead to detached circumstellar shells. Hydrodynamic simulations by Steffen & Schönberner (2000) showed that a brief period of high mass loss can translate into a geometrically thin shell expanding around the star.

A separate explanation for large detached shells is the interaction of the AGB wind with the interstellar medium (ISM). Ueta et al. (2006) and Wareing et al. (2006) detected a far-IR nebula at a distance of about 100 arcsec to the west (right panel of Figure 2.19). Based on the parabolic structure of the nebula, the direction of the space motion of the star with respect to the nebula shape, and the presence of extended Hα emission cospatial to the nebula, suggests that the detected far-IR nebula is due to a bow shock at the interface of the interstellar medium and the AGB wind of this moving star. However, this shows that the detached shell detected in the 60 μm IRAS images can be explained by a slowing-down of the stellar wind by surrounding matter and that no extra mass loss modulation around 100 arcsec, i.e. around 10,000 years ago, needs to be invoked (Decin et al., 2008).

The detached shell, the declining period and the detection of the s-process element technetium[25],

[24] American Association of Variable Star Observers, http://www.aavso.org/

[25] The radioactive element ^{99}Tc has a lifetime on the order of the AGB lifetime, i.e. it must be mixed up by

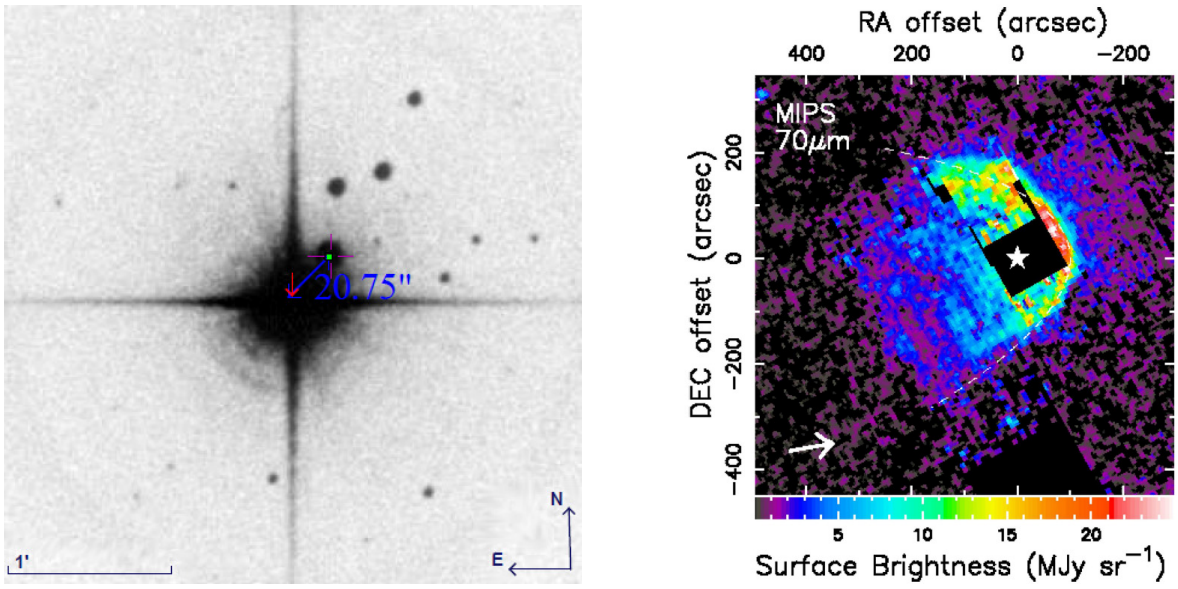

Figure 2.19: *Left:* Target star R Hya with its companion (Aladin MAMA-R-ESO image). *Right:* Background subtracted, mosaicked MIPS color maps at 70 μm. North is up, east is left and the position of R Hya is indicated by the star. The proper motion is indicated by the arrow in the bottom left (Wareing et al., 2006).

^{99}Tc, by Little et al. (1987) indicates that R Hya is in the thermal-pulsing AGB phase. R Hya shows a remarkable infrared excess in the IRAS photometric data due to the cool detached shell, while the silicate feature at around 10 μm is (almost) absent. However, this can be expected, since a declining mass loss leads to less silicate emission close to the star.

The consequence of a low mass loss rate in AGB stars is that the 13 μm dust feature becomes more prominent. This is correlated with the appearance of strong emission lines of CO_2. Both features are observed in R Hya and originating in a warm layer close to the star (Justtanont et al., 1998). Another remarkable feature is the newly identified fluorescent FeI line near 280.7 nm. This line is pumped by the thin CII emission line at 232.55 nm and has been seen only in cool carbon stars before (Luttermoser & Mahar, 1998; Luttermoser, 2000). This indicates that shock chemistry is relevant. The abundance of CO, bounding in LTE almost all C, is estimated by Bujarrabal et al. (1989) to 3.0×10^{-4}.

Distance estimations for R Hya range from (110 ± 21) pc (Jura & Kleinmann, 1992) to 165 pc (Zijlstra et al., 2002), while Table 2.5 (page 42) lists an intermediate value of 130 pc, calculated from the PL relation (Whitelock et al., 2008). The mass and luminosity, inferred from modeling and observations, is 2 $M_\odot$ and 11,600 $L_\odot$, respectively (Zijlstra et al., 2002). Effective temperature determinations range from 2600 K (Teyssier et al., 2006), over 2680 ± 70 K (Haniff et al., 1995) to 2830 K (Zijlstra et al., 2002). R Hya is believed to be a wide binary system with a very long orbital period. The angular separation is 21 arcsec at a position angle of 320° (epoch 2003, WDS) as shown in the left panel of Figure 2.19.

The wind in the inner CSE starts with a velocity of 1.5 km/s and accelerates to 6.5 km/s further out, as modeled by Teyssier et al. (2006), before reaching a terminal velocity of 7.5 km/s

third dredge-up.

(Justtanont et al., 1998) to 10.0 km/s (Hashimoto et al., 1998; Knapp et al., 1998). Interferometric diameter measurements for R Hya were performed by Millan-Gabet et al. (2005), Monnier et al. (2004), Ireland et al. (2004a) and Haniff et al. (1995), resulting in uniform disk angular diameters between about 20 mas in the near-infrared and about 35 mas in the visual (see Section 5.3). R Hya exhibits maser emission of SiO (Humphreys et al., 1997), H_2O (Takaba et al., 2001) and OH (Lewis et al., 1995). The resolution of these observations were too low in order to derive any spatial information of the maser distribution or ring diameters. Thus, asymmetries were not studied with masers. A complementary study in the visual ($0.7-1.0$ μm, Ireland et al., 2004a) and K-band (Monnier et al., 2004) gave no indications of a departure from symmetry. A complete overview about detected asymmetries can be found in Section 6.3.

2.4.4 V Hydrae

V Hya was the first classical (N type) carbon star ever detected by radio astronomers (Zuckerman et al., 1977). V Hya is believed to be in a short-lived but critical stage in the evolution of a mass-losing AGB star into a bipolar PN (Tsuji et al., 1988; Kahane et al., 1996). This dust-enshrouded carbon star has a C/O ratio of 1.05, an effective temperature of 2650 K and is of spectral type N; C7,5e (Lambert et al., 1986). The luminosity is estimated to 7850 $L_\odot$ (Knapp et al., 1997). Distance calculations ranging from 340 pc (Barnbaum et al., 1995) and 380 pc (Knapp et al., 1997) to 440 pc (Olivier et al., 2001) and 550 pc (Bergeat et al., 1998), while Table 2.5 (page 42) lists a value at the lower end with 360 pc, inferred from the PL relation by Whitelock et al. (2008).

V Hya has two variability periods, (529.4 ± 30) d with a peak-to-peak variation of 1.5 mag and (6160 ± 400) d (≈ 17 years) with a peak-to-peak variation of 3.5 mag[26], and is classified as semi-regular (SRa) or Mira variable by Mayall (1965) and Knapp et al. (1999), respectively. While the 529.4 d period is typical of a luminous AGB star, Knapp et al. (1999) suggests that the regular long period dimming of VHya is due to a thick dust cloud orbiting the star, since essentially the entire stellar photosphere is occulted for a long duration of time. This dust cloud could be attached to a binary companion. In this scenario, the AGB variable fills its Roche lobe, and loses mass to its companion. The overflowing material forms a dusty cloud of matter around the companion, which then obscures the star each time it crosses the line of sight. Different mechanism are proposed as well. The dimming could be e.g. due to large stellar spots (Schwarzschild, 1975) or the coupling of the pulsation with the rotation (Barnbaum et al., 1995).

However, another hint for the presence of a close binary is the rapid rotation of the Mira, suggested from a high resolution optical spectral broadening analysis by Barnbaum et al. (1995). The rotation velocity of an AGB star, evolving in isolation, is not likely to be greater than 2 km/s, even if its main-sequence progenitor rotated at breakup velocity. In contrast, the rotation velocity, $v \sin i$, derived for V Hya is on the order of 11 to 14 km/s and undergoes a periodic variation (Barnbaum et al., 1995; Kahane et al., 1996). Barnbaum et al. (1995) and Kahane et al. (1996) concluded that this rapid rotation, due to the spin-up by a companion in a common envelope configuration, is the most compelling explanation, but alternative explanations have

[26]The long secondary pulsation amplitudes in JHKL are 2.4, 2.1, 1.7, and 0.7 mag, respectively (Olivier et al., 2001).

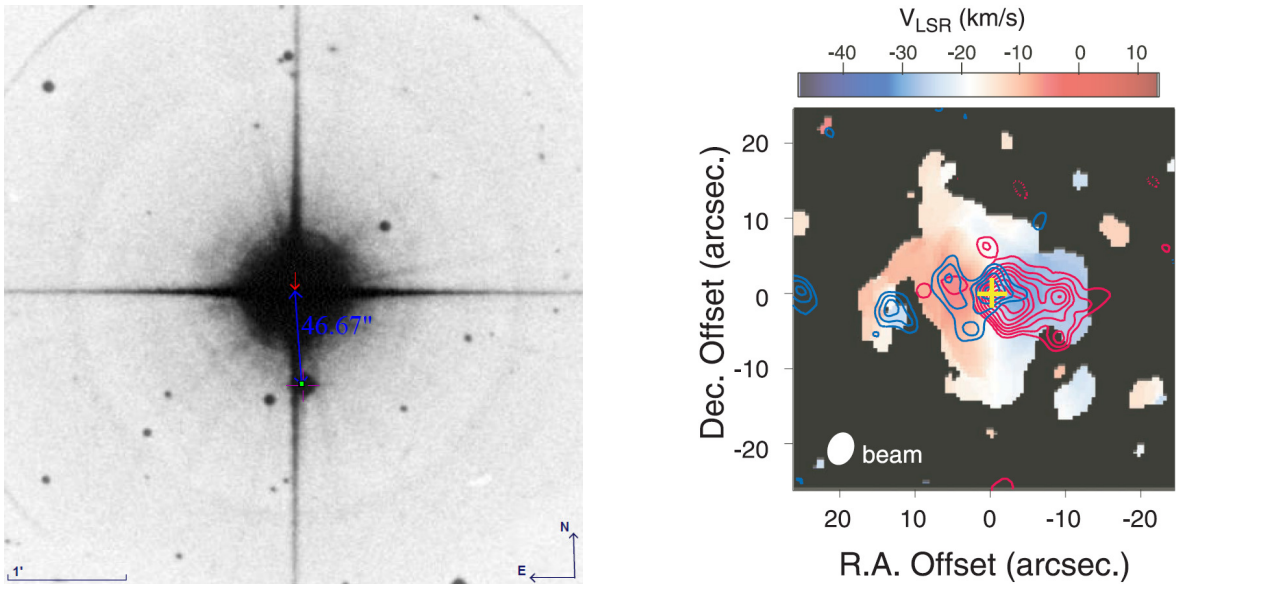

Figure 2.20: *Left:* Target star V Hya with its companion (Aladin MAMA-R-ESO image). *Right:* CO map integrated over the velocity range of ± (60.0 to 162.2) km/s from the systemic velocity of −17.5 km/s (blue and red contours) superposed on the intensity-weighted medium-velocity map of CO in the velocity range of ± 30 km/s from the systemic velocity (Hirano et al., 2004).

been also presented (Luttermoser & Brown, 1992; Olivier & Wood, 2003). Its change with phase are consistent with radial pulsation in the fundamental mode. The secondary star could by an early G or F star, implying a mass of $1.0 - 1.5$ $M_\odot$, or possibly a WD (Barnbaum et al., 1995). V Hya is instead inferred to have a mass of about 1 $M_\odot$ (Kahane et al., 1996). As can be seen from the left panel of Figure 2.20 an additional wide companion, with a separation of 46 arcsec at a position angle of 186°, exists (epoch 1991, WDS).

A consequence of the fast rotation is an enhanced equatorial mass loss producing a disk and a jet-like structure (e.g. Soker, 1992; Morris, 1987). High angular resolution CO maps, millimeter, infrared and optical spectra suggest that the circumstellar structure of V Hya consists of three kinematic components: a low-velocity disk with radial velocity offsets of $\Delta v \approx \pm$ (8 to 16) km/s from the systemic velocity, a medium-velocity wind with $\Delta v \approx \pm$ 60 km/s, and a high-velocity jet with $\Delta v \approx \pm$ (60 to 200) km/s (Zuckerman & Dyck, 1986; Sahai & Wannier, 1988; Sahai et al., 2009; Lloyd Evans, 1991; Knapp et al., 1997; Olivier et al., 2001; Hirano et al., 2004).

The right panel of Figure 2.20 shows the high-velocity component interferometrically mapped in CO by Hirano et al. (2004), supporting that it comes from an extended, bipolar, and highly collimated outflow. The (projected) opening angle (≈ 25°) of the outflow along the east-west direction does not vary significantly from small (0.”25) to large radii (12.”5). The medium-velocity wind is superimposed and has an opposite velocity vector. This may come from the interaction between the low- and high-velocity component. A newly ejected high-speed jet-like outflow in this star, at a different position angle (due to a possible precession), can be seen in the left panel of Figure 2.15 (page 28) (Sahai et al., 2003).

Not shown in Figure 2.20 is the low-velocity CSE which has a flattened or disk-like shape,

elongated perpendicular along the north-south direction (Tsuji et al., 1988; Kahane et al., 1988, 1996; Sahai et al., 2003). This may enable or enhance the formation of an accretion disk and supports a model in which the jet is driven by an accretion disk around an unseen, compact companion. Within 1" to the star, the ellipticity steadily decreases from 1.2 to 1.0 (Lagadec et al., 2007) and the density structure changes on timescales of months to years (Johnson et al., 1991; Johnson, 1993; Trammell et al., 1994). Images obtained at 9.8 and 11.7 μm (N2 and SiC filters, respectively) by Lagadec et al. (2005) show an additional slightly elongated structure in the south-west direction, tracing the dust emission from material blown away, while the overall structure is roughly spherically symmetric. V Hya is therefore an ideal object to study the transition to a PN via the superwind AGB phase and may give insights why about half of the planetary nebulae show a bipolar structure, while only a very small fraction of AGB CSEs deviate from spherical geometry. It can also be investigated how this is related to a short binary common envelope evolution phase and high speed jets.

With interferometric observations, uniform disk diameters in the H and K-band were determined to $13.0 - 14.5$ mas and a Gaussian FWHM for the dust shell at K-band to (21.2 ± 2.8) mas (van Belle et al., 1999; Millan-Gabet et al., 2003; Ragland et al., 2006) (see Section 5.3). The star has a large infrared excess and strong millimeter molecular line emission, showing that it is losing mass at a fairly high rate. Total mass loss rates were estimated to 2.5×10^{-5} $M_{\odot}yr^{-1}$ (Knapp et al., 1997), 1.0×10^{-6} $M_{\odot}yr^{-1}$ (Barnbaum et al., 1995) and 1.5×10^{-6} $M_{\odot}yr^{-1}$ (Kahane et al., 1996; Knapp et al., 2000) with dust mass loss rates of 2.0 to 5.7×10^{-6} $M_{\odot}yr^{-1}$ (Knapp et al., 1997; Hirano et al., 2004). The abundance of CO is on the order of 9×10^{-4} (Kahane et al., 1996).

Optical spectra of carbon stars are characterized by a set of very closely spaced molecular absorption lines, namely, the vibration-rotation transitions of CN and C_2. Knapp et al. (1997) modeled the dust envelope of V Hya by assuming grains constituted of amorphous carbon with dimensions of 0.2 μm. Barnbaum et al. (1995) speculated that the evolutionary placement on the AGB is in question since V Hya appears to lack ^{99}Tc, a signature of third dredge-up, whose absence suggests that a mass transfer event in the past might be responsible for the enhancement of carbon and s-process elements. Zuckerman & Dyck (1986) discovered the presence of a narrow CO emission feature superposed on a standard broad stellar CO profile, which probably represents the first example of a CO maser ever seen in any interstellar or circumstellar source.

2.4.5 W Hydrae

The O-rich star W Hya, with a spectral type of M7 III, is one of the best observed AGB stars in the southern hemisphere. In particular, a large number of interferometric diameter measurements at visual and infrared wavelengths were carried out (e.g. Ireland et al., 2004a; Woodruff et al., 2009, see Section 5.3). The visual and near-IR diameters of the star W Hya range from about 30 up to 70 mas, correlated to the absorption and emission bands of the radiatively important molecular species. The spectrum of W Hya shows clearly the presence of molecules in the upper atmosphere, with CO, H_2O, OH, CO_2, SO_2 and SiO as the most abundant (besides H_2). Modeling of the spectrum by Justtanont et al. (2004) reveal even the existence of at least three or four different dust species, namely amorphous silicate (emission

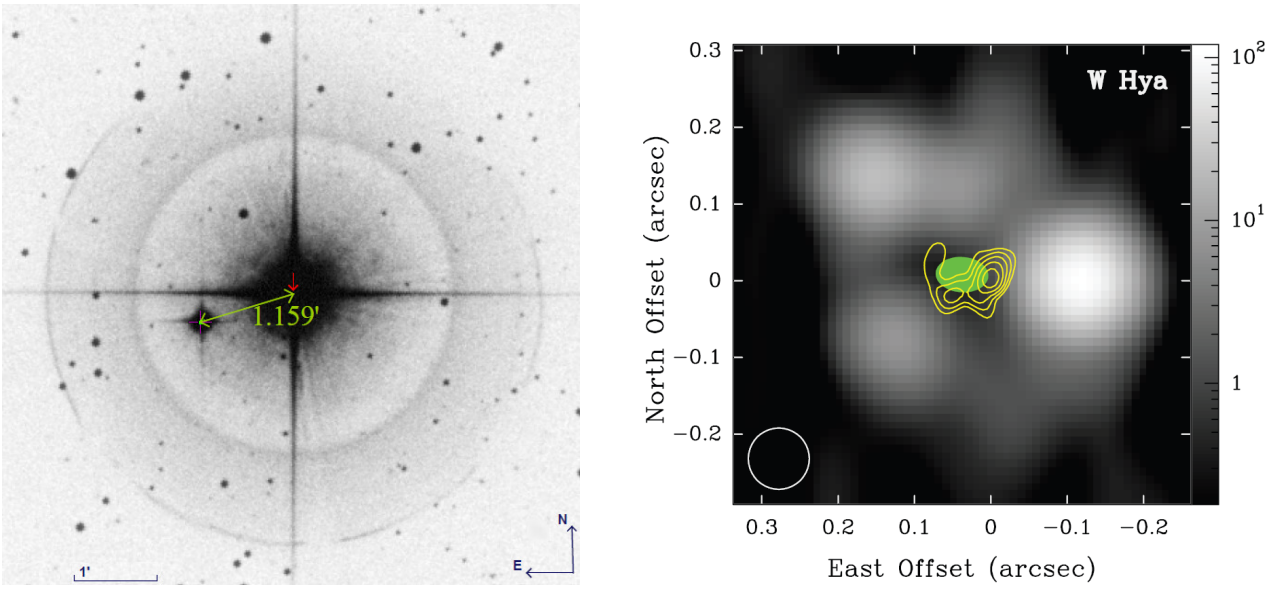

Figure 2.21: *Left:* Target star W Hya with its companion star (Aladin MAMA-R-ESO image). *Right:* W Hya's H_2O maser emission (gray scale) from Reid & Menten (1990), superimposed on SiO maser emission (yellow contours) and radio continuum emission (green ellipse), see Reid & Menten (2007).

features between 10 and 20 μm), compact Al_2O_3 (11 μm), MgFeO (19 μm) and maybe $MgAl_2O_4$ (13 μm, Posch et al., 1999), likely located at different distances from the star. This will be important for interpreting the mid-IR N-band diameters in Section 6.1.

Justtanont et al. (2004, 2005) derived from these spectroscopic observations with ISO[27] a low total mass loss rate of $(2.5 \pm 0.5) \times 10^{-7}$ $M_\odot yr^{-1}$, and a lower limit dust mass loss rate of silicates and Al_2O_3 of about 3×10^{-10} $M_\odot yr^{-1}$, assuming a gas-to-dust ratio of 115. This is consistent with total mass loss estimations from Szymczak et al. (1998) (1×10^{-7} $M_\odot yr^{-1}$), Olofsson et al. (2002) (0.7×10^{-7} $M_\odot yr^{-1}$) and Muller et al. (2008) (5×10^{-7} $M_\odot yr^{-1}$), including the uncertainties. In addition, W Hya is known to have a very extended dusty envelope with a radius of $\approx$ 30 arcsec (Hawkins, 1990).

The abundance of CO is between 2×10^{-4} (Justtanont et al., 2005) and 3×10^{-4} (Ziurys et al., 2009), while the abundance of H_2O is relatively high with a value between 1.5×10^{-3} (Maercker et al., 2009) and $(2.0 \pm 1.0) \times 10^{-3}$ (Justtanont et al., 2005). C-bearing molecules were also detected confirming that shock chemistry is important as well. Abundances determination of HCN range from 9×10^{-7} (Ziurys et al., 2009) to 1×10^{-6} (Muller et al., 2008).

W Hya is classified as a SRa star in the GCVS with a period of 361 days. However, its light curve in recent years seems quite regular (Section 5.1) and its infrared radial velocity curve is more typical of a normal Mira (Hinkle et al., 1984; Gomez Balboa & Lepine, 1986). The derived low dust mass loss rate and pulsation behavior is typically for stars at the beginning of the AGB phase and the transformation from a semi-regular variable to a Mira star. Following Lorenz-Martins & Pompeia (2000), W Hya might be associated to the *intermediate* AGB class concerning their dust species.

[27] http://iso.esac.esa.int/ and Kessler et al. (1996)

W Hya is one of the closest AGB stars. Distance estimations ranging from 78 pc (Knapp et al., 2003, revised Hipparcos value) to 115 pc (Perryman et al., 1997a, Hipparcos value). A more accurate value is obtained by VLBI[28] maser measurements with a value of 98^{+30}_{-18} pc (Vlemmings et al., 2003), while Table 2.5 (page 42) lists a distance of 90 pc, calculated from the PL relation (Whitelock et al., 2008). The mass, luminosity and effective temperature, inferred from modeling and observations, is 1 $M_\odot$, 5400 $L_\odot$ and 2500 K, respectively (Justtanont et al., 2005). W Hya has a wide binary companion with an angular separation of 70 arcsec at a position angle of 110° (epoch 1991, WDS), as shown in the left panel of Figure 2.21.

Complementary maser observations at different wavelengths probe different molecules in the CSE. SiO maser measurements at different epochs were carried out by Miyoshi et al. (1994), Cotton et al. (2004, 2008) and Reid & Menten (2007), resulting in SiO maser ring diameters between 60 and 90 mas. With increasing diameter, masers of H_2O (Reid & Menten, 1990) and OH (Szymczak et al., 1998; Chapman et al., 1994) were detected, besides thermal line emission of HCN (Muller et al., 2008; Ziurys et al., 2009) and CO (Szymczak et al., 1998; Olofsson et al., 2002; Ziurys et al., 2009), consistent with the abundances expected for the corresponding diameters. While the SiO maser originates in the extended atmosphere, the kinematic information of maser emissions of H_2O and OH ($\geq$ 10 stellar radii), and thermal emission of CO (at about 1000 stellar radii), can be used to trace the velocity increase of the wind. At the dust condensation radius the wind starts with a velocity of around (3.6 ± 0.7) km/s and increases until it reaches its terminal velocity of about 7.0 to 8.0 km/s (cf. equation 2.9) (Szymczak et al., 1998; Muller et al., 2008; Maercker et al., 2009; Ziurys et al., 2009) (for a plot see Zubko & Elitzur, 2000).

Past asymmetry determinations of W Hya are not very conclusive, in the sense that many different position angles were reported, ranging from $-20°$ (Szymczak et al., 1998) for the OH maser to $(83 \pm 18)°$ for the radio continuum at 43 GHz (Reid & Menten, 2007) and $(94 \pm 33)°$ (Tuthill et al., 1999) in the visual, while in the near-IR no departures from symmetry could be detected within the uncertainties. The right panel of Figure 2.21 shows asymmetric SiO, H_2O maser and radio continuum emissions of W Hya. A complete overview about detected asymmetries can be found in Section 6.3.

2.4.6 Basic Data

Basic astrometric and photometric data for each star are listed in Table 2.5. In addition, the pulsation period, the pulsation type, effective temperature, luminosity, K-band diameter, and the associated calibrator star for the visibility calibration (Section 4.2.3) is given as well. It should be noted that the magnitudes are mostly averages over the pulsation period, since AGB stars are variable over almost the whole spectrum. The typical error for the given distance is 20% to 30%. Due to the pulsation and angular extension, parallaxes from Hipparcos are very uncertain and the listed distances from the pulsation-luminosity (PL) relation are probably more accurate (cf. equation 2.1) and are used in this work. More exact distances are obtained from VLBI maser emission measurements. The mentioned catalogs can be e.g. found at VizieR[29].

[28] Very Long Baseline Interferometry
[29] http://vizier.u-strasbg.fr/viz-bin/VizieR

Table 2.5: Properties of the Targets. See text for explanations.

Target name	**R Aql** HD 177940 HIP 93820 AAVSO 1901+08 ASAS 190622+0813.8 IRAS 19038+0809	**R Aqr** HD 222800 HIP 117054 AAVSO 2338-15 ASAS 234349-1517.1 IRAS 23412-1533	**R Hya** HD 117287 HIP 65835 AAVSO 1324-22 ASAS 132943-2316.9 IRAS 13269-2301	**V Hya** - HIP 53085 AAVSO 1046-20 ASAS 105137-2115.0 IRAS 10491-2059	**W Hya** HD 120285 HIP 67419 AAVSO 1343-27 ASAS 134902-2822.1 IRAS 13462-2807
Right Ascension α[a]:	$19^h\ 06^m\ 22.25^s$ (286.592717°)	$23^h\ 43^m\ 49.46^s$ (355.956092°)	$13^h\ 29^m\ 42.78^s$ (202.428250°)	$10^h\ 51^m\ 37.26^s$ (162.905229°)	$13^h\ 49^m\ 02.00^s$ (207.258325°)
Declination δ[a]:	+08° 13′ 48.01″ (+8.230003°)	-15° 17′ 04.20″ (-15.284500°)	-23° 16′ 52.79″ (-23.281331°)	-21° 15′ 00.32″ (-21.250089°)	-28° 22′ 03.49″ (-28.367636°)
$\mu_\alpha \cos\delta$[a] (mas/yr):	5.18 ± 1.15	32.98 ± 1.37	-60.73 ± 1.68	-14.21 ± 1.41	-49.05 ± 1.13
μ_δ[a] (mas/yr):	-67.05 ± 0.99	-32.61 ± 1.24	11.01 ± 1.19	2.72 ± 1.14	-59.58 ± 0.84
Distance[b] (pc):	220 ± 40	250 ± 50	130 ± 25	360 ± 70	90 ± 25
Pulsation period[b] (d):	284	387	389	532	361
Pulsation type[d]:	Mira	Mira	Mira	SRa/L	Mira/SRa
Radial velocity[e] (km/s):	32.0 ± 0.9	-22.0 ± 0.9	-10.4 ± 0.9	-15.2 ± 2.0	42.3 ± 2.0
B magnitude[a]:	8.7	10.2	7.7	9.6	8.9
V magnitude[a]:	7.6	8.7	6.4	7.0	7.5
J magnitude[f]:	0.68	-0.16	-1.3	1.6	-1.7
H magnitude[f]:	-0.36	-1.1	-2.2	0.21	-2.7
K magnitude[f]:	-0.83	-1.6	-2.7	-0.69	-3.2
N magnitude[g]:	-2.51	-4.00	-4.00	-3.61	-6.06
N-band flux at 12 μm[g] (Jy):	402 ± 36	1580 ± 60	1590 ± 80	1110 ± 60	4200 ± 210
Spectral classification[h]:	M7 III e var	M7 III pev	M7 III e g	N; C7,5e	M7 III e g
Effective temperature[h] (K):	3000 ± 300	2800 ± 300	2700 ± 300	2650 ± 300	2500 ± 300
Luminosity[h] ($L_\odot$):	3470 ± 500	5000 ± 500	11600 ± 1000	7850 ± 500	5400 ± 500
K band diameter[i] (mas):	11.5 ± 1.4	16.6 ± 3.0	24.5 ± 1.2	14.5 ± 0.3	42.8 ± 3.2
Associated calibrator[j]:	η Sgr, ϵ Peg	30 Psc	2 Cen	α Hya	2 Cen

[a] Hipparcos (Epoch = J1991.25, ICRS, Equinox = J2000) (Perryman & ESA, 1997b); [b] derived from the PL relation, cf. equation 2.1 (Whitelock et al., 2008), errors are approximations; [c] period used for the PL relation in [b] (Whitelock et al., 2008), see Section 5.1.1 for a newer fit of the period; [d] classification from ASAS (Pojmanski et al., 2005) and GCVS (Samus et al., 2009); [e] GCRV (Wilson, 1953); [f] 2MASS (ICRS, Equinox = J2000) (Skrutskie et al., 2006); [g] IRAS (Neugebauer et al., 1984); [h] for references see corresponding Section 2.4.1 to 2.4.5, errors are approximations; [i] this uniform disk angular diameter is equivalent to about 1.2 times the true photospheric diameter (e.g. Millan-Gabet et al., 2005), values are averages from the literature (cf. section 5.3); [j] for calibrator properties see Table 4.3 (page 74)

Chapter 3

Optical Interferometry

Optical interferometry[1] offers the opportunity to observe stars with high resolution. This can be achieved since the current interferometers are able to combine the light from at least two telescopes by holding their relative light path length stable within a few microns. In Section 3.1, the principles of interferometry are recalled, followed by a short discussion how the atmosphere of the Earth influences observations in the infrared (Section 3.2). Section 3.3 describes the MID-infrared Interferometric instrument (MIDI) used in this work.

3.1 Principles of Interferometry

The basic principles of interferometry are addressed here. For a complete introduction to optical interferometry see Lawson (2000a), Quirrenbach (2001) and Monnier (2003). Most of the following content is adapted from these publications and from the proceedings of the Michelson Summer Workshop in 1999[2], the VLTI Summer School in 2008[3], and the theses of Ratzka (2005) and Tristram (2007).

3.1.1 Monochromatic Point Source

An interferometer in astronomy relies on the same optical properties demonstrated in Young's double pinhole experiment (Young, 1804). However, instead of having two pinholes and a screen, two telescopes together with an interferometric instrument are used to create and record the interference pattern. Fig. 3.1 shows the basic layout of such an interferometer. The separation between two telescopes, located at the positions $\vec{x}_A$ and $\vec{x}_B$, is given by the baseline B:

$$\vec{B} = \vec{x}_B - \vec{x}_A. \tag{3.1}$$

Each telescope points at a single celestial point located at a relative position $\vec{S}$ with respect to the middle of the baseline. The pointing direction is given by the unit vector $\vec{s} = \vec{S}/|\vec{S}|$. Assuming that the celestial point source is at sufficient distance, the electromagnetic field can be described as a plane wave. The fields of the monochromatic waves at the position of the telescopes are then given as

$$\vec{E}_A = \vec{E}_{A,0}\, e^{-i\vec{k}\vec{x}_A - i\omega t} \text{ and} \tag{3.2}$$

$$\vec{E}_B = \vec{E}_{B,0}\, e^{-i\vec{k}\vec{x}_B - i\omega t} = \vec{E}_{B,0} e^{-i\vec{k}\vec{x}_A - i\vec{k}\vec{B} - i\omega t}, \tag{3.3}$$

[1] *Optical* is used here in a broad sense, covering the optical and infrared spectral regime.
[2] http://olbin.jpl.nasa.gov/iss1999/
[3] http://www.vlti.org/events/index.php?event=4

where $\vec{k} = k\vec{s} = 2\pi/\lambda \cdot \vec{s} = \omega/c \cdot \vec{s}$ is the wave vector and λ the wavelength. Without loss of generality, the common phase $i\vec{k}\vec{x}_A$ can be omitted, hence

$$\vec{E}_A = \vec{E}_{A,0}\, e^{-i\omega t} \text{ and} \tag{3.4}$$
$$\vec{E}_B = \vec{E}_{B,0}\, e^{-ik\vec{s}\vec{B}} e^{-i\omega t}. \tag{3.5}$$

These equations show that the phase shift between the signal at the two apertures is determined by the difference in optical path, $\vec{s} \cdot \vec{B}$. After passing the apertures, the light is directed via mirrors and delay lines, with total lengths d_A and d_B, respectively, to the detector. This introduces an additional relative phase and the electromagnetic fields, at the place where the beam combination takes places, become:

$$\vec{E}_A = \vec{E}_{A,0}\, e^{-ikd_A} e^{-i\omega t} \tag{3.6}$$
$$\vec{E}_B = \vec{E}_{B,0}\, e^{-ikd_B} e^{-ik\vec{s}\vec{B}} e^{-i\omega t}. \tag{3.7}$$

In contrast to radio interferometers, optical detectors measure only a time-averaged intensity $I = |\vec{E}|^2 = \vec{E}\vec{E}^\star$ of the total electrical field $\vec{E} = \vec{E}_A + \vec{E}_B$:

$$I = (\vec{E}_A + \vec{E}_B) \cdot (\vec{E}_A^\star + \vec{E}_B^\star) \tag{3.8}$$
$$= \vec{E}_{A,0}^2 + \vec{E}_{A,0}\vec{E}_{B,0} e^{ik(d_A - d_B + \vec{s}\vec{B})} + \vec{E}_{A,0}\vec{E}_{B,0} e^{-ik(d_A - d_B + \vec{s}\vec{B})} + \vec{E}_{B,0}^2 \tag{3.9}$$
$$= I_A + I_B + \sqrt{I_A I_B} \cdot 2\cos\left[k(d_A - d_B + \vec{s}\vec{B})\right] \tag{3.10}$$
$$= 2\, I_{\text{tel}}\, (1 + \cos(kd))\,, \tag{3.11}$$

where the identity $2\cos\alpha = e^{i\alpha} + e^{-i\alpha}$ was used. For the last step it has been assumed that the incoming beams has equal intensities $I_{\text{tel}} = I_A = I_B$ and that the relative delay, also called the *optical path difference* (OPD), is given by $d = d_A - d_B + \vec{s}\vec{B}$.

Both, changing the external optical delay, $\vec{s} \cdot \vec{B}$ ($\text{OPD}_{\text{extern}}$), e.g. by changing the pointing of the telescope or the change due to the apparent motion of the source during the night, and the internal optical delay, $d_{AB} = d_A - d_B$ ($\text{OPD}_{\text{intern}}$), e.g. by shifting the so-called optical delay lines (DL), leads to an oscillation of the intensity I. The oscillations are known as interferometric *fringes*.

3.1.2 Resolution of an Interferometer

Applying the Rayleigh criterion to interferometry, a second source at $\vec{S}'$ is resolved, when the peak of the fringe pattern for the first source falls into at least the first minimum of the fringe pattern of the second source. This means that the two fringe pattern are shifted by half a wavelength with respect to each other:

$$k\left(d_{AB} + \vec{s}\vec{B}\right) - k\left(d_{AB} + \vec{s}'\vec{B}\right) \geq \pi\,. \tag{3.12}$$

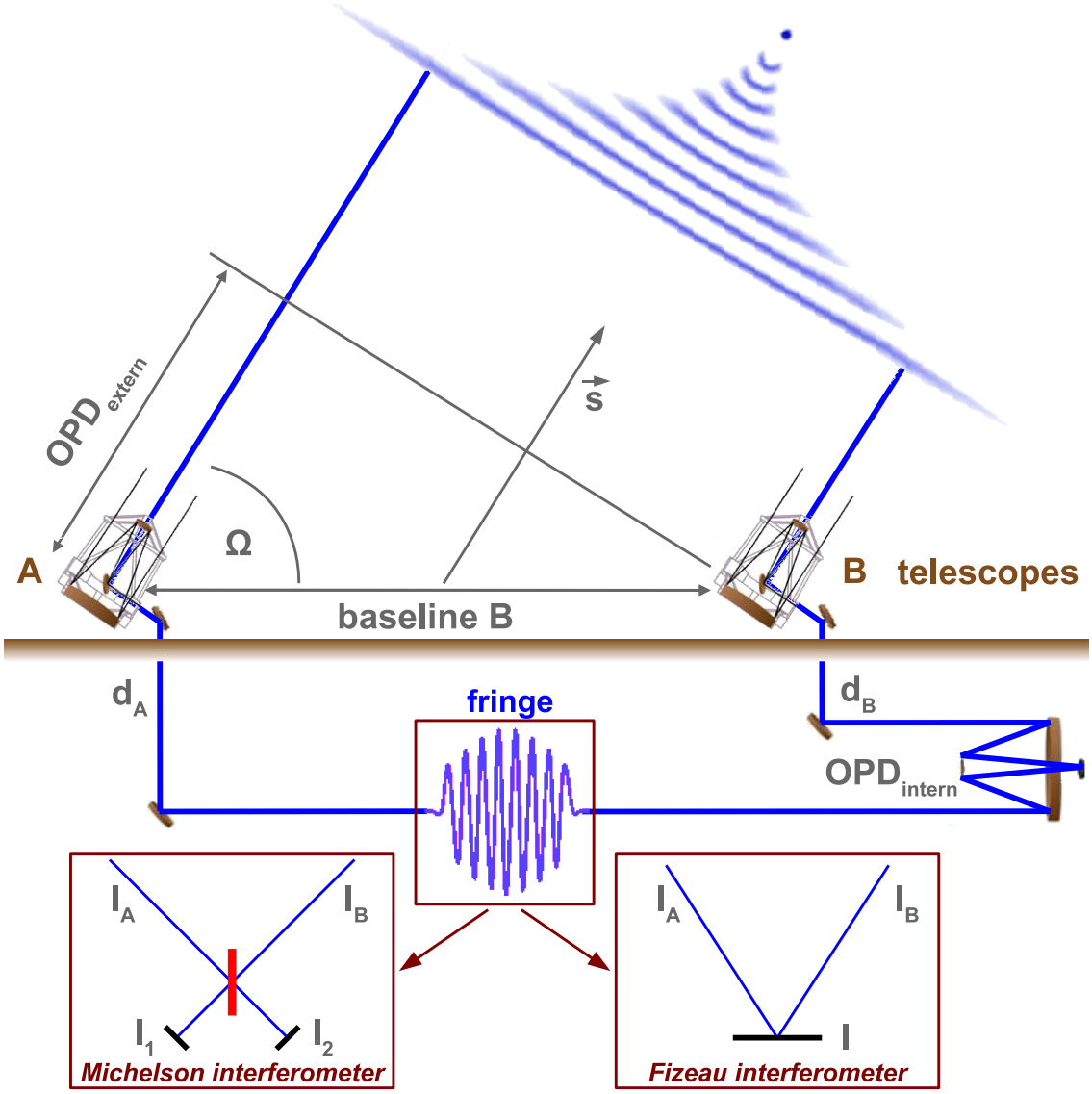

Figure 3.1: Basic layout of an interferometer.

This can be simplified to

$$(\vec{s} - \vec{s}') \cdot \vec{B} \geq \frac{\lambda}{2} \,, \tag{3.13}$$

where the definition of the wave number was used. The left hand side can be rewritten with the *projected baseline* B_{proj}, and the angular separation of the sources α, i.e. the baseline $\vec{B}$ projected on the separation vector $\vec{\alpha} = \vec{s} - \vec{s}'$ and the modulus of the separation vector $\vec{\alpha}$, respectively. Therefore, the resolution[4] of an interferometer is

$$\alpha \geq \frac{\lambda}{2\, B_{\text{proj}}} \,. \tag{3.14}$$

[4]In order to convert the resolution from radians into milli-arcseconds (mas), α must be multiplied with $3600 \cdot 180 \cdot 1000/\pi$.

Alternatively, if the resolution is defined as the inverse of the spatial frequency of the fringe signal, one finds

$$\alpha \geq \frac{\lambda}{B_{\mathrm{proj}}} \, . \tag{3.15}$$

In this form it can be directly compared with the resolution of a single telescope, λ/D, which is determined by the inverse of the highest measurable spatial frequency. The projected baseline B_{proj} of an interferometer thus corresponds to the diameter D of a telescope mirror. The telescopes feeding the interferometer represent in this picture two subapertures located at the edge of a virtual mirror with a diameter B_{proj}. From an observer's point of view it is important to keep in mind that the sensitivity is still limited by the collecting area of the single telescopes.

3.1.3 Beam Combination

Interferometers are divided into two classes according to the method used to combine the beams interferometrically (Traub, 1999). *Image-Plane* or *Fizeau Interferometers* combine the incoming beams, formed by two individual telescopes or two different parts of a mirror, in the image-plane. The fringes are produced by directly focusing the beams onto the detector, very similar to what takes place in Young's experiment.

When dividing a mirror of a telescope into segments, one may think of each pair of segments as an interferometer. Each telescope thus represents an image plane interferometer with a full coverage of the spatial frequencies up to that corresponding to the inverse diffraction limit of the telescope. The diffraction limited point-spread function is a result of the superposition of the different fringe patterns.

Pupil-Plane or *Michelson Interferometers* superimpose the parallel incoming beams by using a beam combiner (half-coated mirror), fiber optics, or similar devices. They are named after Michelson who used a pupil-plane interferometer to measure the speed of light (Michelson & Morley, 1887). The MIDI interferometer (see Section 3.3), used in this study, belongs to this group.

After passing the beam combiner (cf. Figure 3.1), the two outgoing interferometric beams are given by

$$I_1 = \left|\vec{E}_1\right|^2 = \left|\vec{E}_{A,1} + \vec{E}_{B,1} e^{+i\pi/2}\right|^2 \tag{3.16}$$

$$I_2 = \left|\vec{E}_2\right|^2 = \left|\vec{E}_{A,2} + \vec{E}_{B,2} e^{-i\pi/2}\right|^2 \, . \tag{3.17}$$

The phase shifts, $e^{\pm i\pi/2}$, are introduced by the reflection on the half-coated mirror. Further calculations yields

$$I_1 = I_{A,1} + I_{B,1} - 2E_{A,1}E_{B,1}\sin(kd) \tag{3.18}$$

$$I_2 = I_{A,2} + I_{B,2} + 2E_{A,2}E_{B,2}\sin(kd) \, . \tag{3.19}$$

Because the two output beams are complementary, meaning they have the opposite phase, they can be subtracted from each other to determine the interferometric flux $I_{\rm int}$. Under the assumption of equal input intensities ($I_{tel} = I_A = I_B$) and that the beam combiner transmits and reflects exactly 50% ($I_{A,1} = I_{A,2} = I_A/2$ and $I_{B,1} = I_{B,2} = I_B/2$), the intensity becomes

$$\begin{aligned} I_{\rm int} &= I_2 - I_1 && (3.20)\\ &= I_A - I_B + 2\, I_{\rm tel}\, \sin(kd) && (3.21)\\ &= 2\, I_{\rm tel}\, \sin(kd)\,. && (3.22) \end{aligned}$$

This has the additional advantage that all the uncorrelated background flux vanishes in the ideal case and only the correlated interferometric flux remains. This fringe signal is shown in Figure 3.2. The variable d is again the optical path delay between the two incoming beams that can be adjusted by changing the internal delay line.

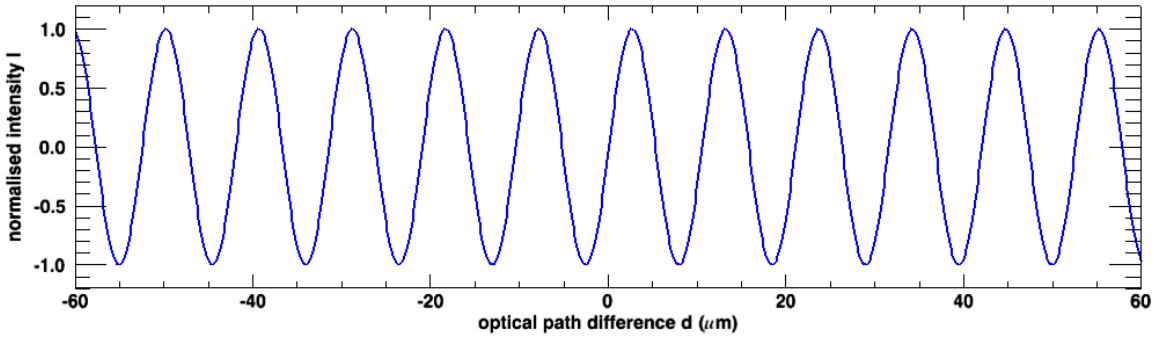

Figure 3.2: Interference pattern for a monochromatic wave at a wavelength of 10.5 μm.

3.1.4 Polychromatic Sources and Coherence Length

In the last sections it has been assumed that the light emitted by an astronomical source is monochromatic. This is obviously not the case for real objects. Astronomical sources emit light in a large wavelength range with a spectral intensity $I_{\rm int}(\lambda)$. Because optical photons (to an extremely good approximation) do not interact with each other, the intensity in (3.22), restricted by the atmospheric and instrumental spectral filter function $\eta(\lambda)$, becomes an integral over all wavelengths,

$$I_{\rm int} = 2 \int I(\lambda)\, \eta(\lambda)\, \sin(kd)\, {\rm d}\lambda\,. \qquad (3.23)$$

Assuming a wavelength-independent intensity and a top hat filter function of width $\Delta\lambda$, centered at λ_0 and defined as

$$\eta(\lambda) = \begin{cases} \eta_0 & \text{if } \lambda_0 - \Delta\lambda/2 < \lambda < \lambda_0 + \Delta\lambda/2 \\ 0 & \text{otherwise} \end{cases}\,, \qquad (3.24)$$

the integration of (3.23) gives

$$I_{\rm int} = 2\,I(\lambda_0)\,\eta_0\,\Delta\lambda\,\frac{\sin\left(\pi\Delta\lambda/\lambda_0^2 d\right)}{\pi\Delta\lambda/\lambda_0^2 d}\,\sin\left(kd\right) \tag{3.25}$$

$$= 2\,I(\lambda_0)\,\eta_0\,\Delta\lambda\,\mathrm{sinc}(\pi d/\Lambda_{\rm coh})\,\sin\left(kd\right)\,, \tag{3.26}$$

with $2\,I(\lambda_0)\,\eta_0\,\Delta\lambda$ the total collected power in the bandpass. The behavior of the intensity with optical path difference is shown in the upper panel of Figure 3.3 (white-light or broad-band fringe) and is equivalent to a superposition of monochromatic fringes shown in the lower panel of Figure 3.3. The result is similar to (3.22) except for the additional modulation by the sinc function. The sinc function is the Fourier transform of the spectral filter function (3.24) and is best described by a characteristic coherence length scale,

$$\Lambda_{\rm coh} \equiv \frac{\lambda_0^2}{\Delta\lambda}\,, \tag{3.27}$$

because the sinc function becomes small for $|\pi d| > \Lambda$. Due to this finite coherence length, fringes in an interferometer can consequently only be recorded, in the bandwidth $\Delta\lambda$ with an efficiency η_0, if the external OPD is compensated by the internal OPD, i.e. fringes are tracked near $d = 0$. If the interferometric signal is dispersed with a spectral resolution of $\mathrm{R} = \lambda_0/\Delta\lambda$, then $\Lambda_{\rm coh} = \mathrm{R}\lambda_0$. For $\mathrm{R} = 30$, $\Lambda_{\rm coh}$ is around 315 μm in the N band[5] ($\lambda_0 = 10.5$ μm).

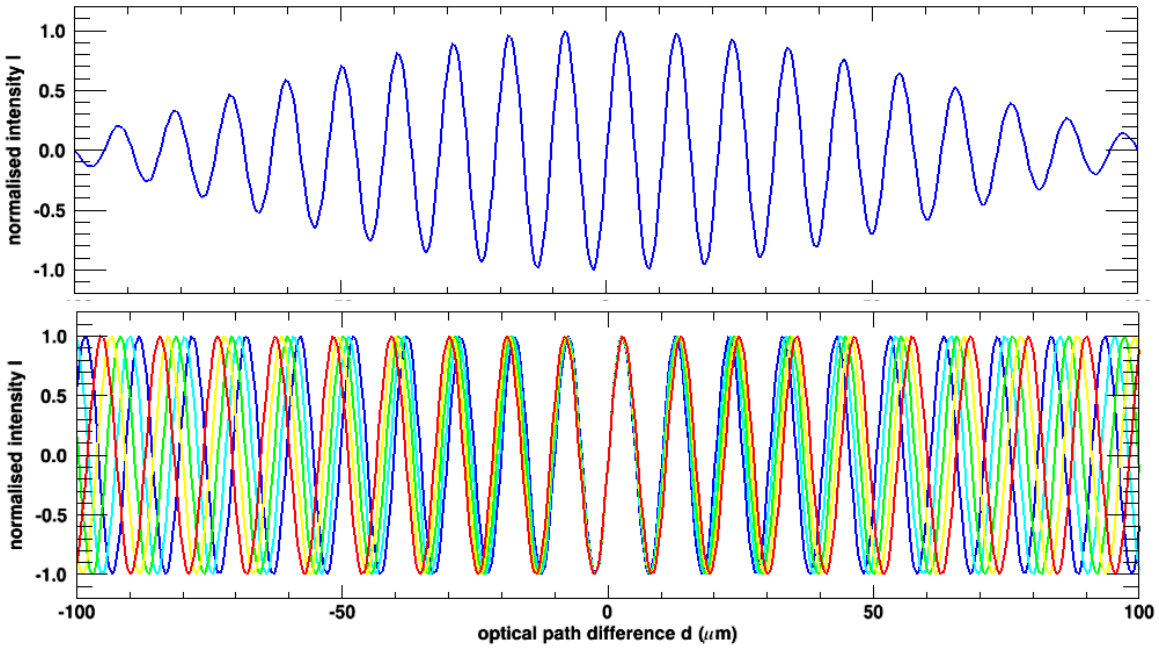

Figure 3.3: *Top:* Interference pattern (white-light or broad-band fringe) for a polychromatic wave with a central wavelength of 10.5 μm and a bandwidth of 8%, corresponding to a coherence length $\Lambda_{\rm coh}$ of 138 μm. *Bottom:* Monochromatic fringes with wavelengths between 10.1 and 10.9 μm forming the upper whitelight fringe.

[5]These are typical numbers for MIDI.

3.1.5 Extended Sources and Visibility

Astronomical sources do not only emit light at different wavelengths, they are not point sources as well. Similar to the polychromatic case, an extended source can be described as a superposition of point sources which are mutually incoherent. With the fraction of light seen through each of the two telescopes

$$f_A = \frac{I_A}{I_A + I_B} \quad \text{and} \quad f_B = \frac{I_B}{I_A + I_B} \tag{3.28}$$

one finds by modifying (3.22)

$$\begin{aligned} I_{\text{int}} &= 2\sqrt{f_A f_B} \int I(\vec{s})\ \sin\left[k(d_{\text{AB}} + \vec{s}\vec{B})\right] \mathrm{d}\vec{s} && (3.29)\\ &= 2\sqrt{f_A f_B} \int I(\vec{s})\ \frac{1}{2i}\left[\ e^{i(kd_{\text{AB}} + k\vec{s}\vec{B})} - e^{-i(kd_{\text{AB}} + k\vec{s}\vec{B})}\ \right] \mathrm{d}\vec{s} && (3.30)\\ &= \sqrt{f_A f_B}\left[\ \frac{1}{i} e^{ikd_{\text{AB}}} \int I(\vec{s})\ e^{ik\vec{s}\vec{B}} \mathrm{d}\vec{s} - \frac{1}{i}\ e^{-ikd_{\text{AB}}} \int I(\vec{s})\ e^{-ik\vec{s}\vec{B}} \mathrm{d}\vec{s}\right]\ . && (3.31) \end{aligned}$$

The two integrals can be interpreted as Fourier transforms of the intensity. With the definition of the wave number k, the phase $\varphi(B_\lambda) = k\vec{s}\vec{B}$ and the spatial frequency B_λ (projected baseline, B_{proj}, measured in units of λ) they can be written as

$$\begin{aligned} \int I(\vec{s})\ e^{+2\pi i \frac{\vec{s}\vec{B}}{\lambda}}\ \mathrm{d}\vec{s} &= \mathcal{V}(+B_\lambda) = |\mathcal{V}(B_\lambda)|\ e^{+i\varphi(B_\lambda)} \ \text{ and} && (3.32)\\ \int I(\vec{s})\ e^{-2\pi i \frac{\vec{s}\vec{B}}{\lambda}}\ \mathrm{d}\vec{s} &= \mathcal{V}(-B_\lambda) = |\mathcal{V}(B_\lambda)|\ e^{-i\varphi(B_\lambda)}\ . && (3.33) \end{aligned}$$

$\mathcal{V}$ is called the *complex visibility*. It has been used that the Fourier transform of real functions, like the intensity distribution I, is hermitic, i.e. the Fourier transform fulfills

$$\mathcal{V}(-\vec{a}) = \mathcal{V}^*(\vec{a}) \quad \text{and} \quad |\mathcal{V}(-\vec{a})| = |\mathcal{V}(\vec{a})|\ . \tag{3.34}$$

This means, if the two telescopes are exchanged, only the phase changes its sign. Inserting (3.32) and (3.33) into (3.31) yields

$$\begin{aligned} I_{\text{int}} &= \sqrt{f_A f_B}\ \left[\frac{1}{i}\ e^{ikd_{\text{AB}}}\ |\mathcal{V}(B_\lambda)|\ e^{i\varphi(B_\lambda)} - \frac{1}{i}\ e^{-ikd_{\text{AB}}}\ |\mathcal{V}(B_\lambda)|\ e^{-i\varphi(B_\lambda)}\right] && (3.35)\\ &= \sqrt{f_A f_B}\ |\mathcal{V}(B_\lambda)|\ \frac{1}{i}\ \left[e^{i(kd_{\text{AB}} + \varphi(B_\lambda))} - e^{-i(kd_{\text{AB}} + \varphi(B_\lambda))}\right] && (3.36)\\ &= 2\ \sqrt{f_A f_B}\ |\mathcal{V}(B_\lambda)|\ \sin\left(kd_{\text{AB}} + \varphi(B_\lambda)\right)\ . && (3.37) \end{aligned}$$

The phase φ shifts the zero-crossing at the maximum of the white-light fringe relative to the zero delay position. A source phase can only be extracted if the instrumental delay and phase can be determined. In the next section it will be seen that the turbulent atmosphere introduces

additional phase shifts and delays, making the recovery of the source phase, and therefore the source morphology, more complicated. By using a *fringe tracker* the additional phases can be compensated. For the data presented here, no external fringe tracker could be used.

Nevertheless, the amplitude of the fringe signal can be determined with sufficiently high accuracy (see Section 4.2). The *normalized visibility* V, which is a real number, is then given by

$$V(B_\lambda) \equiv \frac{|\mathcal{V}(B_\lambda)|}{|\mathcal{V}(0)|}\,, \tag{3.38}$$

and can be determined for unknown phases from the interferometric flux $I_{\rm int}$ via

$$V(B_\lambda) = \frac{|I_{\rm int}|}{2\sqrt{I_A I_B}}\,. \tag{3.39}$$

By definition $V(0) = 1$. The photometric fluxes I_A and I_B have to be measured in addition to the fringe signal. As it will be seen later for MIDI, there are two possibilities, either the photometry is recorded simultaneously or after/before the interferometric observation.

3.1.6 Source Morphologies and Definition of the Coordinate System

As has been shown in the previous section, the normalized visibility $V(B_\lambda)$ is the normalized Fourier transform of the brightness distribution of the source $I(\vec{s})$. This relation is called the *van Cittert-Zernike* theorem. It is hence easy to calculate the expected visibility for an arbitrary baseline and an arbitrary morphology of the source. If (x, y) are orthogonal angular coordinates on the sky with x measured parallel to the projected baseline and y normal to it, then

$$I(x) = \int I(x,y)\,{\rm d}y\,. \tag{3.40}$$

This describes that an interferometer is only sensitive along one dimension, whereas the perpendicular brightness distribution is only seen as integrated intensity.

Interferometric observations are often represented in a two-dimensional coordinate system. The common convention is that the angular coordinates α and β (angular separation relative to the center of the object[6]), describing the brightness distribution in the tangential sky plane, are parallel to the Right Ascension and Declination, respectively. The positive direction of β is to the North (N) and positive direction of α is to the East (E). Polar coordinates are given by the radial coordinate $\rho = \sqrt{\alpha^2 + \beta^2}$, and the position angle (PA, ϑ) is defined as East of North.

In the Fourier plane, coordinates are represented by the spatial frequencies u and v with the same position angle convention and the radial coordinate $r = \sqrt{u^2 + v^2}$. The u and v axes are

[6]Here, the angular separation has to be used and not the difference in sky coordinates, since this is not the same for the declination except for the equator. Note also that the previously defined coordinate system (x, y) is rotated with respect to the (α, β) coordinate system by the position angle ϑ.

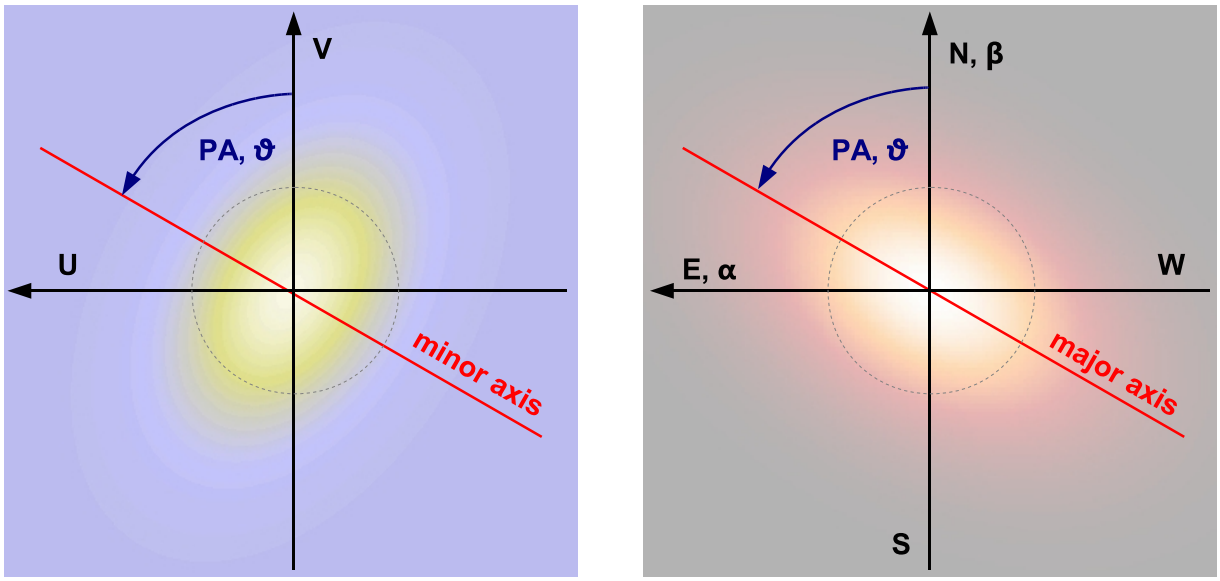

Figure 3.4: Coordinate convention for the Fourier/uv plane (*left*) and sky plane (*right*). The position angle (PA, ϑ) is defined as East (E) of North (N) and corresponds to the major axis of an elliptical model in the sky plane. The East (α) and North (β) direction are parallel to the Right Ascension and Declination, and the u and v direction, respectively. The dashed line shows a circular model for comparison.

parallel to α and β and pointing into the same direction as shown in Figure 3.4. The spatial frequencies are derived via

$$u = U/\lambda = \frac{B \sin\vartheta}{\lambda} \text{ and} \tag{3.41}$$

$$v = V/\lambda = \frac{B \cos\vartheta}{\lambda} \tag{3.42}$$

for a given orientation of the interferometer with respect to the source at the observed wavelength.

Complex structures can be described by convolving the brightness distribution of the astronomical object. However, first size estimations can be obtained with simple intensity functions with only a few free parameters.

For the two-component models used in this study, the relative flux contribution of the first component is given by the parameter ϵ ($0 \leq \epsilon \leq 1$). The total visibility is therefore

$$V_{\text{total}} = A\,|\,\epsilon\,\mathcal{V}_1 + (1-\epsilon)\,\mathcal{V}_2\,|\,, \tag{3.43}$$

where A is the normalization factor. Even for an one-component model, ϵ can be used to account for a not modeled fully resolved brightness distribution. For such an over-resolved component, $|\mathcal{V}_2|$ is equal 0, but its flux, f_2, still contributes to ϵ via $\epsilon = f_1/(f_1 + f_2)$. An over-resolved component could be an extended dust shell.

For the intended search for asymmetries, elliptical models are fitted to the data. An elliptical model is obtained from a circular model by applying a rotation (with an orientation given by the position angle ϑ) and a compression to one of the axes (which becomes the minor axis). The rotation can be achieved by changing the Fourier and sky reference frame via

$$u_\vartheta = u\cos\vartheta - v\sin\vartheta \tag{3.44}$$

$$v_\vartheta = u\sin\vartheta + v\cos\vartheta \tag{3.45}$$

and

$$\alpha_\vartheta = \alpha\cos\vartheta - \beta\sin\vartheta \tag{3.46}$$

$$\beta_\vartheta = \alpha\sin\vartheta + \beta\cos\vartheta, \tag{3.47}$$

respectively.

Applying the compression factor, $\eta = \theta_{\rm min}/\theta_{\rm maj}$, with $\theta_{\rm min}$ the minor diameter and $\theta_{\rm maj}$ the major diameter in Fourier space, yield the new radial variables

$$r_{\vartheta,\eta} = \sqrt{u_\vartheta^2\eta^2 + v_\vartheta^2} \quad \text{and} \tag{3.48}$$

$$\rho_{\vartheta,\eta} = \sqrt{\alpha_\vartheta^2/\eta^2 + \beta_\vartheta^2}\,, \tag{3.49}$$

respectively. For an elliptical model the position angle corresponds to the minor axis in the Fourier plane, while it corresponds to the major axis in the sky plane.

In the following, four basic examples will be discussed (a point source, a binary, a Gaussian distribution and a uniform disk) before the two-component models are introduced. These brightness distributions are all used as models for astronomical sources. Both, the intensity and the visibility for the four example functions are shown in Figure 3.5.

Point Source: A point source of intensity I_0, located at a position a, can be described mathematically by a δ-function:

$$I(x) = I_0\,\delta(a-x)\,. \tag{3.50}$$

The Fourier transform of this function is a constant. The normalized visibility is thus given by

$$V(B_\lambda) \equiv 1\,, \tag{3.51}$$

i.e. it is unity independent of the spatial frequency B_λ.

Binary: A binary is described by two δ-functions. Assuming that the two sources are located at $\pm$a/2, the brightness distribution is

$$I(x) = I_1\,\delta\left(x-\frac{a}{2}\right) + I_2\,\delta\left(x+\frac{a}{2}\right)\,. \tag{3.52}$$

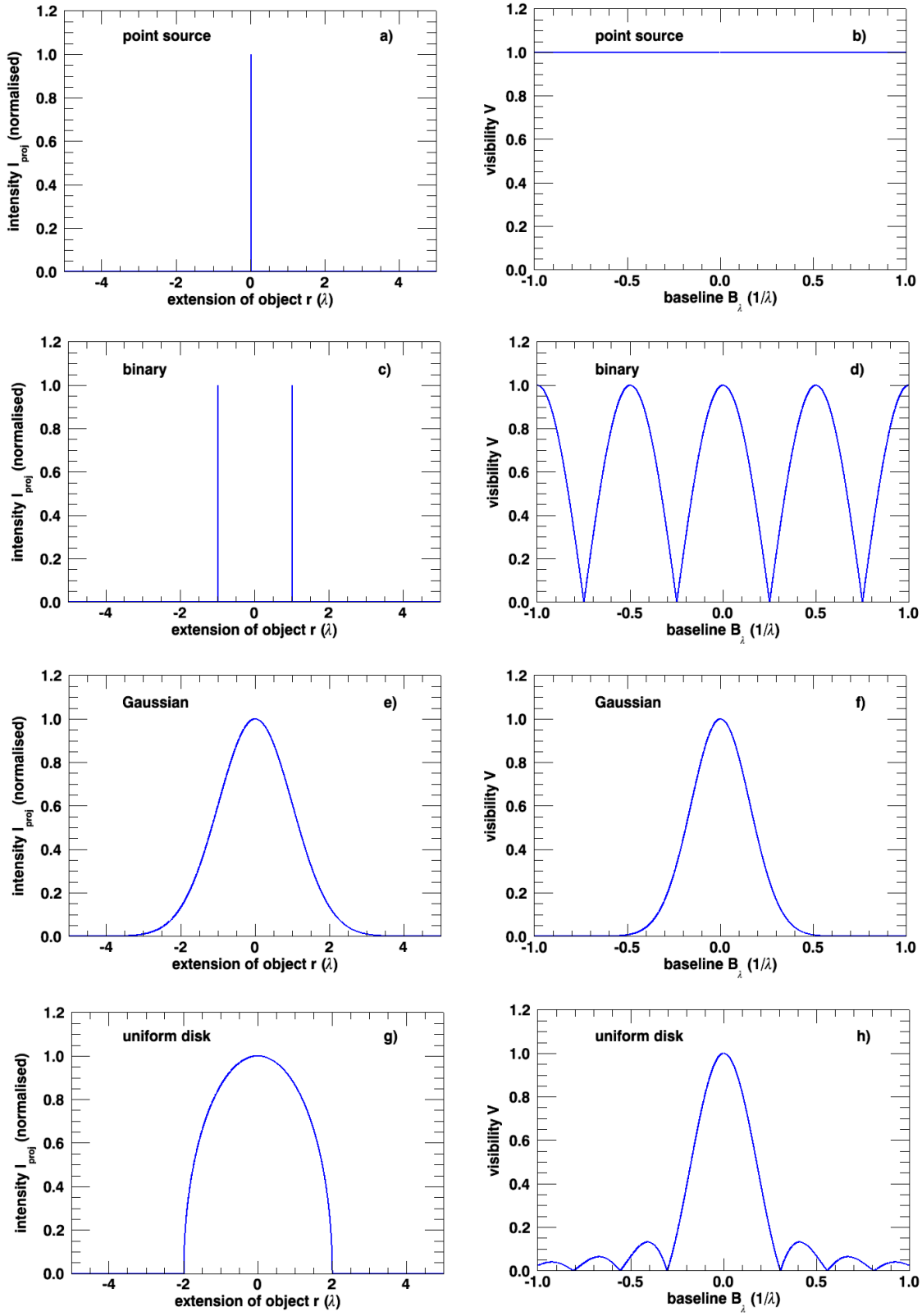

Figure 3.5: Fourier transform examples.

With the flux ratio of the components $f = I_1/I_2$ the normalized visibility is given by

$$V(B_\lambda) = \sqrt{\frac{1 + f^2 + 2f\cos(2\pi a B_\lambda)}{(1+f)^2}} \,. \tag{3.53}$$

The result is an oscillation with a spatial frequency determined by the distance of the two sources. The amplitude of the oscillation depends on the ratio of the intensities.

Gaussian Distribution: Gaussian disks are characterized by their full width at half maximum (FWHM), defined as the width of the disk when measuring at intensity values half of the maximum. In other words, the intensity is reduced to half of the peak value at a distance $\sigma/2$ from the center. Since the integration given in (3.40) preserves the FWHM along the projected baseline, one finds

$$I(x) = I_0\, e^{-\left(\frac{2\sqrt{\ln 2}}{\sigma}x\right)^2} \,. \tag{3.54}$$

The Fourier transform and thus the visibility is also a Gaussian with a reciprocal FWHM, i.e. wide distributions are narrow in Fourier space and vice versa:

$$V(B_\lambda) = e^{-\left(\frac{\pi\sigma}{2\sqrt{\ln 2}}B_\lambda\right)^2} \,. \tag{3.55}$$

Gaussian distributions are often used as an approximation for centrally heated structures like circumstellar shells or disks.

Uniform Disk: Another important morphology is a uniform circular disk of angular diameter θ. In this case, the integrated intensity distribution $I(x)$ (cf. equation 3.40) is a semi-ellipse. The intensity is mathematically described by

$$I(x) = \begin{cases} I_0\sqrt{1-\left(\frac{2x}{\theta}\right)} & \text{if } -\theta/2 < x < \theta/2 \\ 0 & \text{otherwise} \end{cases} \,. \tag{3.56}$$

With the Fourier transform one finds the visibility,

$$V(B_\lambda) = \left|\frac{2\,J_1(\pi\theta B_\lambda)}{\pi\theta B_\lambda}\right| \,, \tag{3.57}$$

where $J_1(x) = (2\pi)^{-1}\int_0^{2\pi}\cos(t - x\sin t)\,\mathrm{d}t$ is the Bessel function of the first kind of order 1. Such a uniform circular disk is the easiest approach to model a resolved star. The function has several roots, where the phase jumps by 2π. It will be later used to determine the diameter of the calibrator stars.

Two-Component Models: The two-component models used in this study are summarized in Table 3.1, listing the number of free parameters (FP), the model name and the name of the star where that model best fitted. A more detailed description with examples is given in Appendix A. In particular, the fully limb-darkened disk (FDD), which is mainly used in this study, is described more precisely. The *relative* models have an additional FP in order to account for an over-resolved component.

Table 3.1: Visibility models used in this study. The *relative* models have an additional free parameter (FP) in order to account for an over-resolved component, see text and equation 3.43.

Section	FP	Model name	Star
A.2	2	(relative) circular uniform disk (UD)	R Aql
A.3	4	(relative) elliptical uniform disk (UD)	
A.4	2	(relative) circular Gaussian (G)	R Aql
A.5	4	(relative) elliptical Gaussian (G)	
A.6	2	(relative) circular fully limb-darkened disk (FDD)	W Hya, R Hya
A.7	4	(relative) elliptical fully limb-darkened disk (FDD)	W Hya, R Hya
A.8	2	circular uniform ring (UR)	
A.9	4	circular uniform disk + circular uniform ring	V Hya
A.10	3	circular uniform disk + circular Gaussian	R Aql, R Aqr, V Hya
A.11	5	circular uniform disk + elliptical Gaussian	
A.12	4	circular FDD + circular uniform ring	V Hya
A.13	3	circular FDD + circular Gaussian	R Aql, R Aqr, V Hya
A.14	5	circular FDD + elliptical Gaussian	
A.15	3	point binary	
A.16	5	uniform disk binary	

3.1.7 Importance of the Phase and Image Reconstruction

For non-circular symmetric objects, phase information can be crucial to recover the morphology of the object. The inverse relation of (3.32),

$$I(\vec{s}) \;=\; \int \mathcal{V}\, e^{-ik\varphi}\, \mathrm{d}\vec{B}\,, \tag{3.58}$$

reconstructs the intensity distribution of the source from visibility measurements. Thus, both the visibility $V(\vec{B}) = |\mathcal{V}(\vec{B})|/|\mathcal{V}(0)|$ and phase $\varphi(\vec{B})$ must be known for a sufficient number of projected baselines $\vec{B}$. Unfortunately, the phase cannot be directly measured in optical interferometry due to the unknown phase introduced by the atmosphere. Differences in the refraction index of the atmosphere and instrumental effects lead to phase shifts $\varphi_{\mathrm{a+i}}$ (see next section). Most of the current two beam interferometers measure only relative phases between different wavelengths at most, whereas normally no phase information is available at all.

There are two possibilities to overcome these problems:

1. By using a phase reference with a known phase $\varphi_{\mathrm{s,ref}}$, the introduced phase can be determined with the observed phase $\varphi_{\mathrm{obs,ref}}$ via $\varphi_{\mathrm{a+i}} = \varphi_{\mathrm{obs,ref}} - \varphi_{\mathrm{s,ref}}$. The reference object can be a nearby unresolved star which experiences the same phase shifts[7]. Applying this to the target the phase of the target $\varphi_{\mathrm{s,target}}$ can be calculated via $\varphi_{\mathrm{s,target}} = \varphi_{\mathrm{obs,target}} - \varphi_{\mathrm{a+i}}$. This method is called phase referencing.

2. If there are at least three telescopes available, a closure phase can be determined. By summing up all relative phases, $\varphi_{\mathrm{obs},ij} = \varphi_{\mathrm{target},ij} + |\varphi_{\mathrm{a+i},j} - \varphi_{\mathrm{a+i},i}|$, between two telescopes ij along a closed ring of three telescopes, the relative atmospheric and instrumental distortions, $|\varphi_{\mathrm{a+i},j} - \varphi_{\mathrm{a+i},i}|$, cancel out. Hence, the final closure phase is given by $\psi_{123} = \varphi_{\mathrm{target},12} + \varphi_{\mathrm{target},23} + \varphi_{\mathrm{target},31}$.

If certain properties of the brightness distribution are assumed, e.g. that the intensity only increases towards the center or that the brightness distribution has certain symmetries, the visibility alone can be used to extract useful information on the source. One should, however, always keep in mind that, without any phase information, important information is lacking.

3.2 Turbulent Infrared Atmosphere

Interferometric observations in the infrared are strongly influenced by the terrestrial atmosphere. A knowledge of the turbulence properties and transmissivity are crucial to overcome these limitations. For a more detailed description see Quirrenbach (1999). Details on observations with the MIDI interferometer are taken from the MIDI user manual[8].

3.2.1 Thermal Infrared

The thermal infrared ranges from about 5 to 30 μm, which is equivalent to a thermal temperature between 100 and 1000 K. The peak of the radiation of a blackbody with a temperature of 300 K is located at about 10 μm. These temperatures are characteristic for the warm dust observed around AGB stars, while the photospheres of these cool stars have temperatures $T > 2000$ K. Stellar light dominates therefore in the visual and near-infrared. The mid-infrared mainly traces photons reprocessed by dusty environments. The dust absorbs ultraviolet and optical radiation and re-emits it in the infrared.

Infrared observations enable the possibility to probe the warm dust itself, but also to look into or through it, since the mass extinction coefficient decreases towards longer wavelengths (Draine & Lee, 1984).

3.2.2 Atmospheric Transmission and Background Emission

Unfortunately, the atmosphere of the Earth is not completely transparent in the infrared regime. The transmission is reduced due to aerosol particles and various molecular species. The most

[7] It means a star within the isoplanatic patch (a few arcsec).
[8] http://www.eso.org/sci/facilities/paranal/instruments/midi/doc/

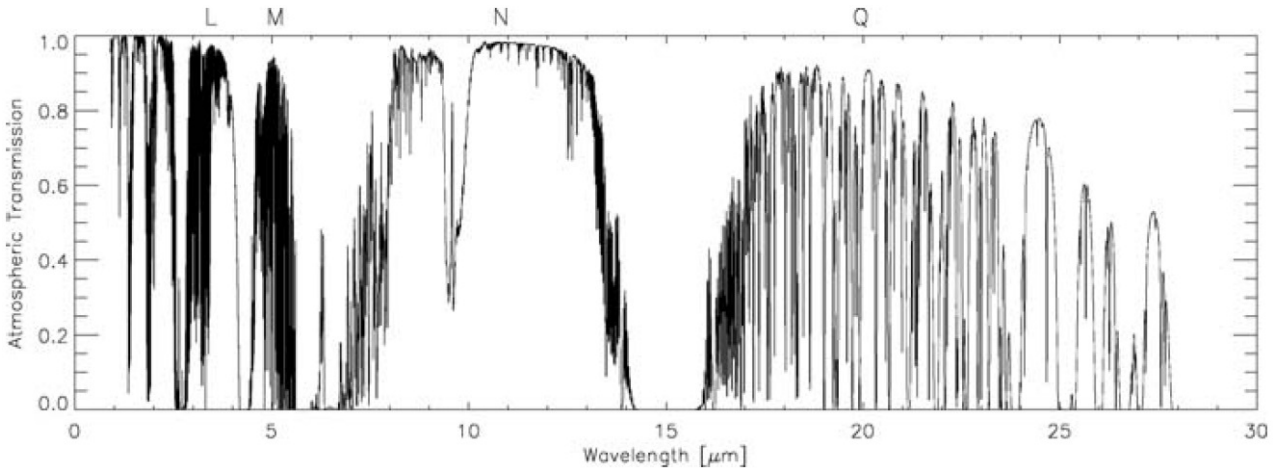

Figure 3.6: Atmospheric transmission in the infrared (Lord, 1992). Labeled are the atmospheric windows (L, M, N and Q) where observations from the ground are possible. Note the ozone absorption feature between 9.3 and 10.0 μm in the N-band.

prominent absorbers are O_3 (9.6 μm), CO_2 (15 μm), H_2O ($\leq$ 7 μm and 25 μm) and CH_4 (7.6 μm), which block large parts of the infrared spectrum. Ground based observations can therefore only be made in atmospheric *windows*. In the thermal infrared two windows exists, the N-band (wavelengths between 7.5 and 14 μm) and the Q-band (16 to 28 μm) as shown in Figure 3.6. Observations can be successfully carried out at extremely dry and high places with a small zenith angle pointing of the telescope.

Many observations are performed above the atmosphere to avoid these problems. A disadvantage, of e.g. IRAS, ISO and Spitzer space missions (Neugebauer et al., 1984; Kessler et al., 1996; Werner et al., 2004), are their limited spatial resolution due to a small mirror size (about 2.5 arcsec at 10 μm for a 1 m mirror). The MIDI interferometer used in this study (see next section) allows to perform high spatial resolution observations and enables the possibility to trace important dust species like silicates. This permits to study the dust condensation, composition, temperature and geometrical distribution in the envelopes of Asymptotic Giant Branch stars.

Since the terrestrial atmosphere radiates mainly in the thermal infrared, a lot of background photons are added to the radiation of the astronomical object. In addition, the mirrors and lenses, needed to collect and direct the light inside the interferometer, are at thermal temperatures as well. For observations with the Auxiliary Telescopes, 24 reflections are necessary before the beam enters the MIDI instrument. This adds many more background photons to the observations, leading to background radiation that is several magnitudes stronger than that of the astronomical object. The overwhelming background restricts the maximal integration time as well, since saturating the detector must be avoided.

This requires the implementation of specific observing and data reduction methods in order to obtain scientifically useful data. A standard procedure is to observe the target and a nearby empty sky position in order to subtract the background. This *chopping* is performed at a high frequency (on the order of 0.5 Hz) to account for the atmospheric variability. An additional advantage is that this sky subtraction removes detector artifacts as well. Employing chopping

is important to obtain accurate photometry, while for the fringe detection it is not necessary as described in Section 3.1.3 (uncorrelated background is removed by subtracting the opposite phased correlated signals).

Furthermore, all optical parts, e.g. windows, filters, and dispersive elements, have to be made of special materials, e.g. gold for the mirror coating (the reflectivity of gold is much higher in the mid-infrared compared to aluminum or silver). Another disadvantage is the limited size and performance of available detectors for the mid-infrared.

3.2.3 Atmospheric Turbulence

Atmospheric turbulence is a major contributor to the difficulties of optical and infrared interferometry from the ground. Rapid atmospheric variations, due to the turbulent movement of different sized atmospheric cells (*eddies*) with different temperatures and densities, lead to a fast relative change of the light path length between collecting telescopes of an interferometer, target color, target brightness and apparent sky location.

The strength of the turbulence can be described by the theory of Kolmogorov. Eddies are arranged hierarchically with an inner scale r_{in} and an outer scale r_{out}, typically between a few millimeters and few tens or hundreds of meters, respectively. The three-dimensional power spectrum is then given for an inertial size distribution of the eddies with their spatial frequency $\vec{\kappa}$ as

$$P(|\vec{\kappa}|) \;\propto\; |\vec{\kappa}|^{-\frac{11}{3}} \,. \tag{3.59}$$

The multi-scale turbulence mixes layers of different temperatures and is thus responsible for inhomogeneities in the air temperature. Fluctuations in the air temperature are essentially inversely proportional to the fluctuations in the air refractive index n. Considering observations of two nearby points, $\vec{x}$ and $\vec{x}+\vec{r}$, the variance of the difference between these two points can be described by the *index structure function*,

$$D_N(\vec{r}) \;=\; \left\langle |n(\vec{x}) - n(\vec{x}+\vec{r})|^2 \right\rangle \;=\; C_N^2 r^{\frac{2}{3}} \,, \tag{3.60}$$

where the index structure coefficient C_N^2 quantifies the local amount of inhomogeneities, $r = |\vec{r}|$ and $\langle\rangle$ represents an ensemble average. $D_N(\vec{r})$ fully describes the statistical properties of the refractive index fluctuations on spatial length scales between r_{in} and r_{out}.

The temporal evolution of the air refraction index can be expressed in a similar way. Assuming that the lifetime of inhomogeneities is much larger than the time it takes to cross the aperture, the turbulence can be modeled by a *frozen* pattern in each single layer (*Taylor hypothesis*). The variance between a time t and a later time $t+\tau$ is then given by the *temporal structure function*,

$$D_N(\tau) \;=\; \left\langle |n(\vec{r},t) - n(\vec{r},t+\tau)|^2 \right\rangle \;=\; C_N^2 \, |\vec{v}\,\tau|^{\frac{2}{3}} \,, \tag{3.61}$$

with $\vec{v}$ the wind speed.

Important for interferometry is, how much relative phase shift is introduced by turbulence and on which time scales this varies. If a wavefront

$$\psi(\vec{x}) \;=\; A\, e^{i\varphi(\vec{x})}\,, \tag{3.62}$$

with amplitude A and phase φ, propagates through a turbulent layer of thickness Δh at a hight h, the variations in the refractive index cause a shift of the phase that can be mathematically described as

$$\Delta\varphi(\vec{x}) \;=\; k \int_h^{h+\Delta h} n(\vec{x}, z)\, \mathrm{d}z\,, \tag{3.63}$$

where $k = 2\pi/\lambda$ is the wave number. The variance of relative differences between different parts of the wavefront can then be described by the *phase structure function*

$$D_\varphi(\vec{r}) \;=\; \left\langle |\varphi(\vec{x}) - \varphi(\vec{x}+\vec{r})|^2 \right\rangle \;=\; 2.914\, k^2\, \Delta h\, C_N^2\, r^{\frac{5}{3}}\,, \tag{3.64}$$

where $r = |\vec{r}|$ and (3.60) was used.

An easy way to quantify this phase variations is via the *Fried parameter*. Equation 3.64 can be rewritten as

$$D_\varphi(r) \;=\; 6.88 \left(\frac{r}{r_0}\right)^{\frac{5}{3}}\,, \tag{3.65}$$

using the definition of the Fried parameter,

$$r_0 \;\equiv\; \left(\frac{0.423\, k^2}{\cos(\zeta)} \int C_N^2(h)\mathrm{d}h\right)^{-\frac{3}{5}}\,, \tag{3.66}$$

with ζ the zenith distance (or $\sec(\zeta)$ the airmass). It has been assumed that in layers which are much thicker than the individual turbulence cells, many independent eddies contribute to the phase shift, which therefore has Gaussian statistics according to the Central Limit Theorem.

The *seeing* described by the Fried parameter quantifies the turbulent atmosphere by one single parameter, which in turn is a function of turbulence strength, zenith angle, and wavelength. Although the size of the turbulence cells spans a range between r_{in} and r_{out}, the atmosphere can be described as a sample of patches of size r_0. Each of these patches has a constant phase. The phases of the various patches are not correlated, i.e. from one patch to another a random phase change occurs. However, a better description of the seeing is given by equation 3.65.

The Fried parameter can also be related to the image quality. The resolution of seeing-limited images, obtained through an atmosphere with turbulence, is the same as the resolution of diffraction-limited images taken with a telescope of diameter r_0. Observations with telescopes much larger than r_0 are seeing-limited, i.e. the resolution is proportional to λ/r_0, whereas observations with telescopes smaller than r_0 are essentially diffraction-limited, i.e. the resolution is proportional to λ/D. Most of the distortions originate from the first few tens to hundreds of meters above the telescope.

An advantage of observing in the mid-infrared (around 10 μm) is the relatively large value of r_0 compared to optical wavelengths. Since r_0 scales with the wavelength λ in the following way

$$r_0 \propto \lambda^{\frac{6}{5}} , \tag{3.67}$$

as can be seen from (3.66), diffraction limited observations are much easier to achieve. An interferometer works only correctly if the wavefronts from the individual telescopes are coherent, i.e. have phase variances not larger than 1 rad^2 over an aperture of r_0 (Fried, 1965; Noll, 1976). For 0.8 arcsec seeing in the visible, r_0 is approximately 0.2 m in the visible, but 4.6 m in the infrared. No adaptive optics, except for simple tip-tilt corrections, are therefore necessary for Auxiliary Telescope observations (diameter = 1.8 m, see next section). It should be noted that at any given site r_0 varies dramatically from night to night and on time scales down to minutes and seconds.

According to Taylors hypothesis, the crossing time of a turbulence pattern is given as

$$\tau_0 \equiv \frac{r_0}{v} \propto \lambda^{\frac{6}{5}} . \tag{3.68}$$

A long exposure, i.e. an exposure with an integration time much longer than the *coherence time* τ_0 averages over the atmospheric random process, and the ratio between the Fried parameter and the telescope diameter determines whether the image is diffraction-limited or seeing-limited. In addition, an exposure with an integration time much shorter than τ_0 can always reveal diffraction-limited information.

The coherence time sets fundamental limits for interferometers, since the time for integrating a fringe signal must be shorter than the coherence time. Otherwise it will cause a smearing of the fringe if no fringe tracker is installed. Consequently, it restricts the sensitivity and limiting magnitude. The correlation time of the atmosphere is typically milliseconds in the visible and increases to hundreds of milliseconds in the mid-IR.

Another effect concerning the photometry is *scintillation*. Atmospheric interference effects, due to refraction and diffraction of light, cause fluctuations in the brightness of the source. Since these effects are highly chromatic, the brightness varies with wavelength. This is most apparent near the horizon but averages out for long exposure times. Scintillation is less important in the mid-infrared where fluctuations of sky emission ("sky noise") dominates.

3.3 MIDI at the VLTI

The MID-infrared Interferometric instrument (MIDI) is one of the interferometric instruments operated at the Very Large Telescope Interferometer (VLTI). The VLTI is located on the top of the 2635 m high *Cerro Paranal* at 24°40' S and 70°25' W in the Atacama desert. The mountain is located about 130 km south of the city of Antofagasta in the coastal mountain range and lies only 12 km from the Pacific ocean. The specific climatic conditions make the site one of the driest[9] locations on Earth. The exceptional aridity makes the atmosphere very transparent at infrared wavelengths.

[9]The median precipitable water vapor at e.g. Paranal/Andes Mountains is on the order of 1 to 2 mm H_2O (http://www.eso.org/sci/facilities/paranal/site/paranal.html).

The observatory is built and operated by the European Southern Observatory (ESO), an intergovernmental organization for astronomical research. A comprehensive description of the VLTI and its subsystems can be found in the VLT White Book (ESO, 2003).

3.3.1 VLTI Environment

The VLTI consists of 4 Unit Telescopes (UTs) and 4 Auxiliary Telescopes (ATs) (Figure 3.7). The UTs are fixed and have a primary mirror diameter of 8.2 m, while the ATs are movable with a primary mirror diameter of 1.8 m. This means that their light collecting area is only 5% of that of a unit telescope. The UTs are used for single dish observations most of the time, while the ATs are dedicated to interferometric observations only. Ground baseline lengths for the UTs are between 47 and 130 m with all 6 possible baselines. The ATs can be moved to 30 different locations in order to allow different baseline configurations with ground baseline lengths between 8 and 200 m[10].

Figure 3.7: The VLTI telescopes. Four unit telescopes (UT1 to UT4) and four auxiliary telescopes in the front can be seen (Image courtesy of ESO).

MIDI can combine either the light of two UTs or two ATs. Existing and upcoming instruments will use up to 4 telescopes at once. Figure 3.8 shows the location of the UT telescopes and the possible locations of the AT telescopes. The ATs are equipped with a tip-tilt corrector (STRAP[11]) to compensate atmospheric distortions of the wavefront and to guide the target. For UT observations the adaptive optics system MACAO is used. Although seeing effects in the mid-infrared are not as severe as in the near-infrared or optical, the STRAP systems guarantee

[10]Not all configurations are offered so far.
[11]System for Tip-tilt Removal with Avalanche Photodiodes

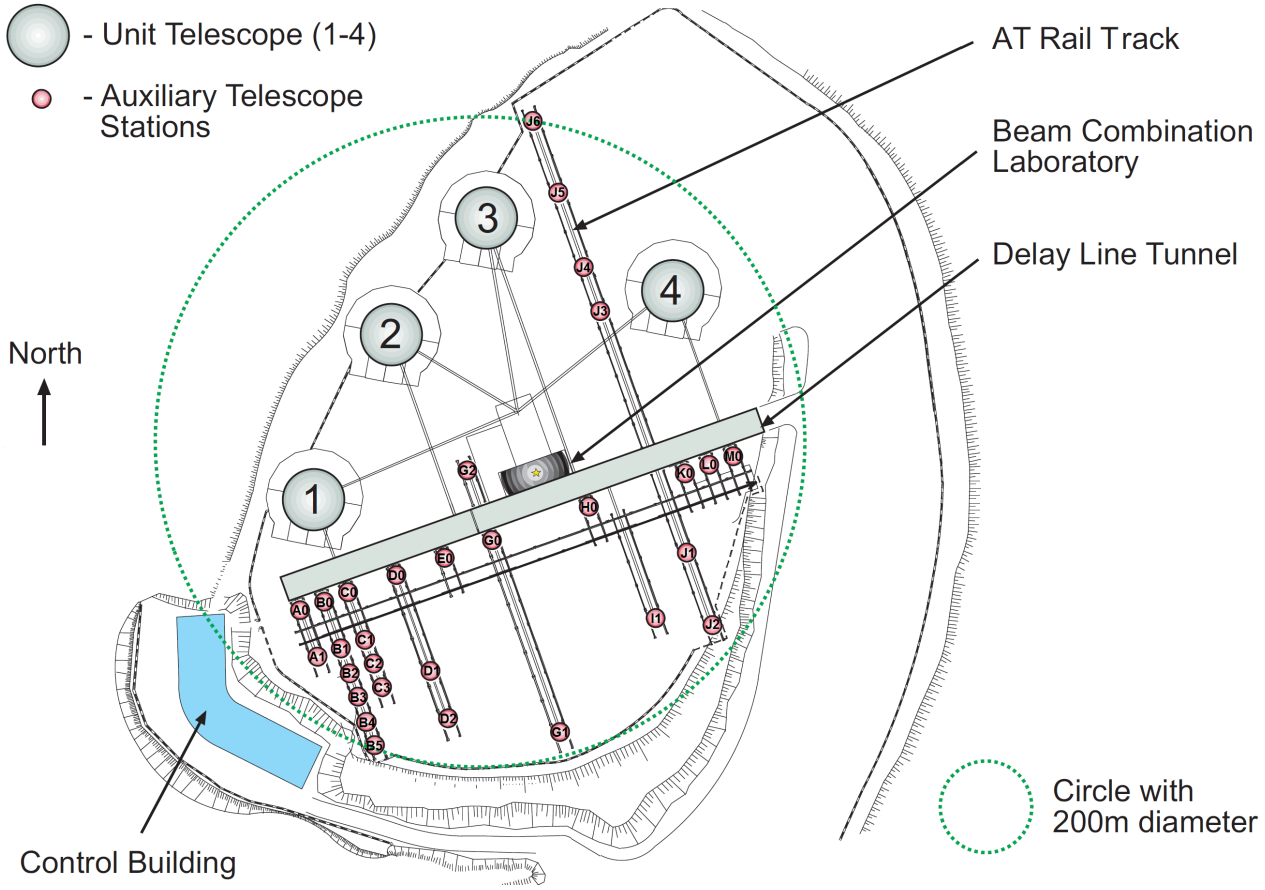

Figure 3.8: Layout of the VLTI and location of the individual telescope stations. The Unit Telescopes (UTs) are labeled with $1-4$. The Auxiliary Telescopes (ATs) can be moved to any of the stations represented by red dots (Image adapted from Glindemann et al., 2000).

diffraction limited images even for fair seeing conditions. They also ensure the stability of the source position in the beam, which is necessary for a good overlap in the interferometric instrument.

After passing the ATs, the light is redirected through delay lines to compensate the OPD difference between the two telescopes. One delay line is fixed, whereas the other continuously moves to compensate for apparent sidereal motion. Figure 3.9 shows the light path (dark blue) from the delay line tunnel (maximum length is 168 m) to the MIDI instrument in the VLTI laboratory. A variable curvature mirror (VCM) is installed on the carriages of the delay line reflector system to relay the pupil, optimize the field of view (FOV) and reduce the thermal background of the VLTI optics in the sense that they are independent of the AT location and delay line position.

In order to correct the image drift introduced inside the VLTI, the InfraRed Image Sensor (IRIS) simultaneously measures the tilt of the beams. IRIS guarantees therefore the correct alignment of the beams during the observations. IRIS normally operates in K-band for MIDI operations and allows to skip the acquisition imaging, reducing considerably the execution overheads. For specific observations fringes can be tracked with the external fringe tracker FINITO, with the purpose to compensate at high rate the atmospheric differential fluctuations and integrate the

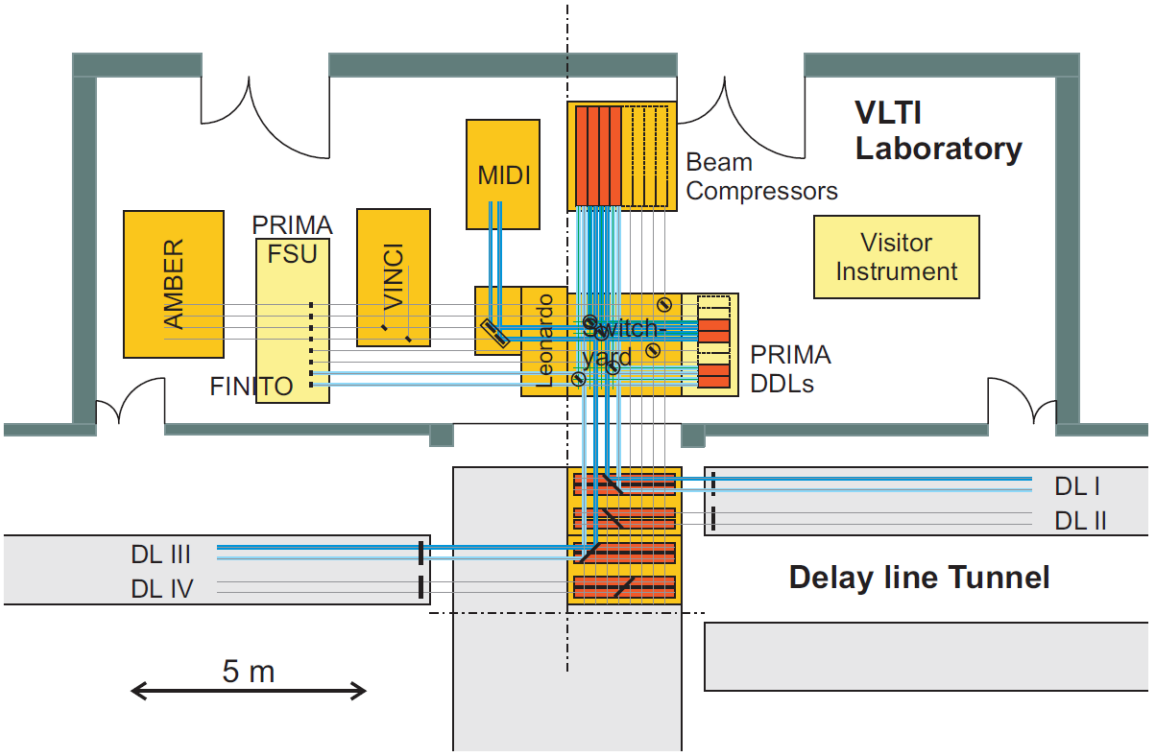

Figure 3.9: The interferometric laboratory at the VLTI (Image adapted from Glindemann et al., 2000).

fringe signal longer. This requires a high correlated flux in the H-band.

3.3.2 MIDI Instrument

The MID-infrared Interferometric instrument is a two-beam Michelson-type interferometer producing dispersed fringes in the N-band in a wavelength range from 8 to 13 μm (Leinert et al., 2003). MIDI was built by a consortium of institutes from Germany, France and the Netherlands. First fringes with the UTs were obtained on 12$^{\text{nd}}$ December, 2002, and MIDI is offered to the worldwide community of astronomers for observations in service mode or in visitor mode since 1$^{\text{st}}$ September, 2003. MIDI is composed of two main parts, the warm optics on the MIDI table and the cold optics in the cryostat. Figure 3.10 shows both parts integrated at the VLTI laboratory.

On the warm optical bench (at ambient temperature) the two incoming beams (beam A and B) are directed to two small delay lines. The piezo driven mirrors can compensate for up to 200 μm optical path delay. This ensures a fast compensation of external delay changes. In addition, one of the Piezo stages is able to move by up to 55 mm. Calibration devices are mounted on the warm optical bench as well. A blackbody can be moved into the optical path and the light from a CO_2 test laser (λ=10.6 μm) can also be fed to the instrument.

Due to the dominating thermal radiation at 10 μm from the environment most of the instrument optics are cooled to cryogenic temperatures. The cold optical bench, located in a dewar, is

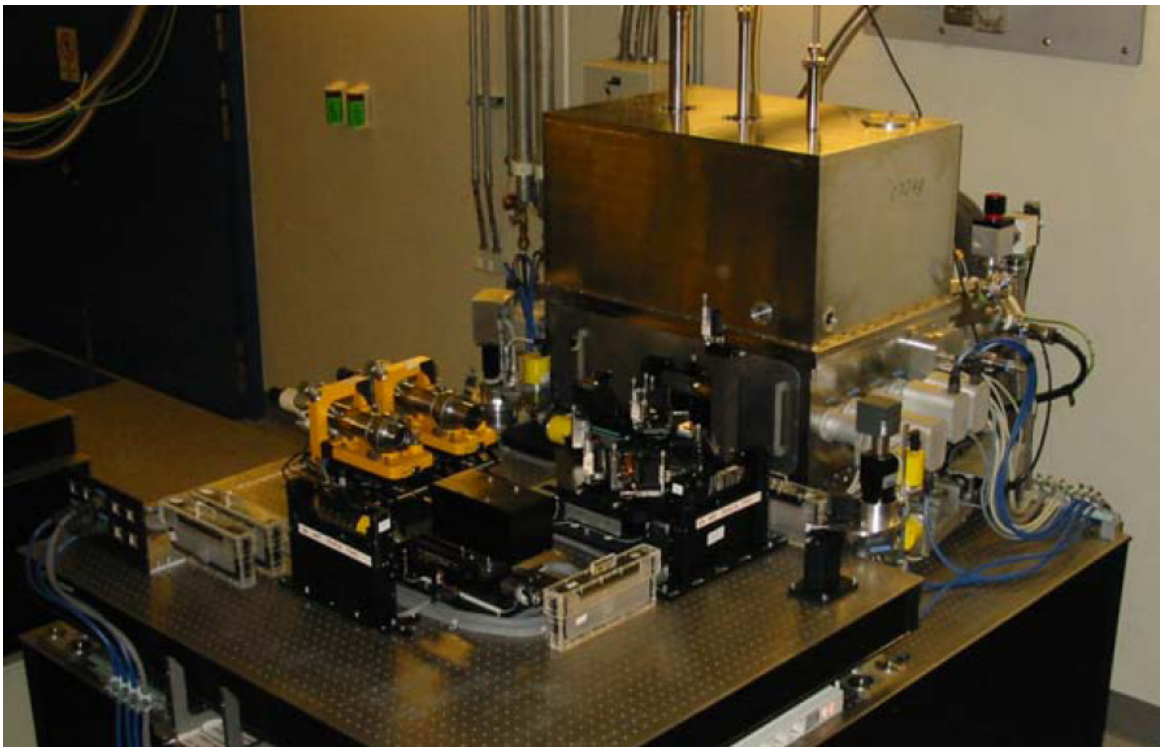

Figure 3.10: MIDI in the interferometric laboratory. The box in the background is the dewar containing the cold optical bench, while the optical devices of the warm optical bench are located in the front. Both benches can be adjusted to ensure a sufficient alignment of the instrument. (Image courtesy of ESO)

cooled down to a temperature of (40 ± 5) K with liquid nitrogen and helium, while the detector is cooled to an even lower temperature of 4 K. The dewar is evacuated to allow the cooling, but with the disadvantage to introduce vibrations by the closed cycle coolers.

Figure 3.11 shows a sketch of the cold optical layout. The two light beams enter the dewar through an entrance window made of ZnSe (zinc selenide) which provides a good transmission between 0.6 μm and 18 μm. A shutter behind it can cover one of the beams. The light passes then the pupil stop and the field stop. The two stops are designed to cut out the background and improve the image quality. Before the light beams reach the beam combiner, photometric beam splitter plates can be inserted in order to extract about 30% of the light for a simultaneous recording of the photometry (see below). This diverted light is directly sent to the detector.

The beam combiner combines the light and produces two interfered beams with opposite phase (cf. equation 3.22). The combiner consists of a half-transparent ZnSe plate on which the telescope beams are superimposed with nominally 50% of beam A being transmitted and nominally 50% of beam B being reflected. The remaining light, 50% reflection of beam A and 50% transmission of beam B, is superimposed as well. The light from these two interferometric channels (channel 1 and 2) and the light from the possible two photometric channels are then filtered and dispersed. Two different dispersive elements can be used, either the NaCl-Ge PRISM with a spectral resolution of R = 30 or the KRS5 (thallium bromoiodide) GRISM with R = 230 (both values for $\lambda = 10.6$ μm). The dispersion allows determinations of visibilities at different

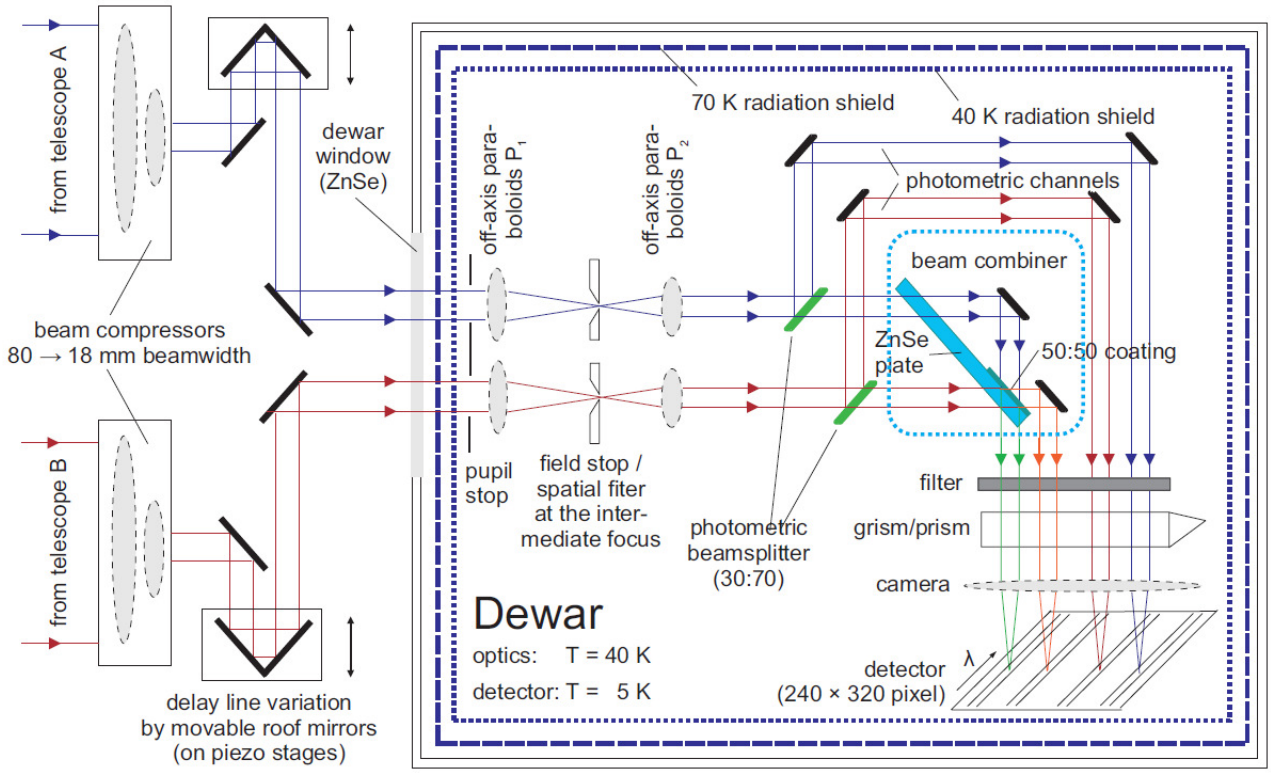

Figure 3.11: Schematic sketch of the optical layout of the warm and cold optical bench of MIDI. (Image courtesy of U. Graser, MPIA)

spectral channels within the N-band and to increase the detector integration time by spreading the light over a larger detector zone, avoiding its saturation. This is possible as long as the integration time is below the atmospheric coherence time of about 100 ms in the mid-infrared.

Finally, the light can be focused onto the detector with two different cameras. The field camera is used for imaging when no dispersive element is inserted into the light path, while the spectral camera is used for dispersed signals. The detector is a 320 × 240 pixel Raytheon Si:As Impurity Band Conduction (IBC) array with a peak quantum efficiency of 34%. The detector is divided into 16 channels and the pixels have a physical size of 50 × 50 μm. The time required to read out the full detector in the standard integrate-then-read mode is about 6 ms. However, in most cases only sub-arrays are integrated and a windowed readout with shorter readout time is used as well as a software windowing afterwards to reduce the amount of data. The minimum integration time is 0.2 ms.

Two main observation modes are available with MIDI, namely `HIGH-SENS` and `SCI-PHOT`. In `HIGH-SENS` (high-sensitivity) mode no photometric beam splitters are inserted in the light beam and the complete light from both telescopes interferes. This allows to measure visibilities of faint sources, but requires to record photometry before or afterwards, i.e. by closing shutter A first and then B after opening A again. Due to changes in the transmission of the turbulent atmosphere between both observations, the typical visibility errors are on the order of 10%.

The `SCI-PHOT` (science-photometry) mode, with the photometric beam splitters inserted, has the advantage that the interferometric and photometric signals are recorded simultaneously and

in principle no additional photometry is needed. On the other hand, this requires the knowledge of the exact instrumental light split ratios or point spread function (PSF) mapping behaviors between interferometric and photometric channels. They can be obtained by recording *additional* photometry, as will be described in Section 4.1. Since the signals are recorded under the same atmospheric conditions, visibilities with errors as low as 1 to 5% can be achieved for bright sources with the UTs. Due to instrumental uncertainties and a not fully verified reduction procedure this is unfortunately not easily achieved at the moment.

Figure 3.12 shows a detector read out of a `SCI-PHOT` observation with the GRISM. As can be seen, the flux spectra in the outer photometric channels, PA and PB, are curved due to the internal optics, while the interferometric spectra in the inner interferometric channels, I1 and I2, are almost a straight line. The dispersion direction is horizontal with increasing wavelength from the left (8 μm) to the right (13 μm). If compared with Figure 3.11, it is obvious that the physical arrangement of the channels is different from the sketch.

Table 3.2 lists the available observation setups for MIDI, while Table 3.3 shows the limiting magnitudes of MIDI for different observation modes. The values refer to the photometric flux. Fringe tracking is still possible for lower correlated flux, i.e. for extended sources with a correlated flux of at least 50% of the listed values (10% with the external fringe tracker FINITO). The course of an observation, as proceeded for the observations of the targets in this study, is described in the next chapter. More details on MIDI can be found in the user manual[12] and in Ratzka (2005). It should already be mentioned that a second source with known properties, the calibrator, must be observed with the same setup to calibrate the photometry, the visibility and the differential phase for instrumental effects.

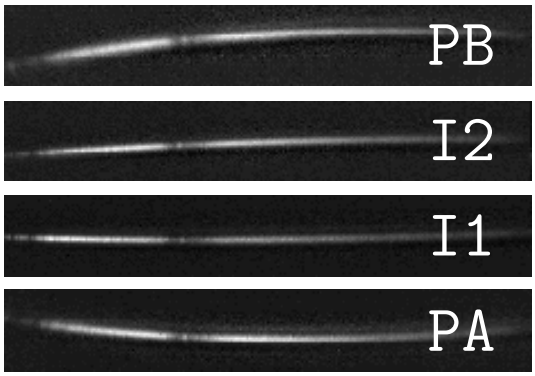

Figure 3.12: The MIDI optical channels. Shown are the outputs of the photometric channels from telescope A and B (PA and PB) as well as the interferometric channels (I1 and I2) for an observation in `SCI-PHOT` mode with the GRISM (see next chapter for details).

[12] http://www.eso.org/sci/facilities/paranal/instruments/midi/doc/

Table 3.2: Observation setups available with MIDI as well as some properties.

Observation mode:	`HIGH-SENS` or `SCI-PHOT`
Dispersive element:	GRISM or PRISM
Spectral filters[a]:	N-band, SiC, N8.7, [ArIII], [SIV], [NeII] and N11.3
Fringe tracking mode[b]:	dispersed or white
Field of view (FOV):	0.52 arcsec (UTs), 2.29 arcsec (ATs)
Chopping frequency[c]:	0.306 Hz (GRISM), 0.545 Hz (PRISM), 0.5 Hz (AQU)
Fringe scan length[d]:	80 μm
Noise level[e]:	0.3 Jy (UTs), 6 Jy (ATs)

[a] For the acquisition the N8.7 and for the observations the N-band filter is commonly used.

[b] The dispersed group delay tracking mode is the standard mode, while the white mode (field/astrometry mode) is only interesting when it is known that the scientific target consists of a cluster of several not connected sources in a narrow field-of-view.

[c] Chopping is enabled for photometric recording, interferometric `SCI-PHOT` recording and acquisition (AQU) imaging, while it is off for interferometric `HIGH-SENS` recording.

[d] The fringe is scanned by changing the OPD by the given amount with the MIDI piezos.

[e] This value refers to `HIGH-SENS` PRISM observations. In order to obtain a signal to noise (S/N) of 10, the source has to be as bright as 3 Jy for UTs or 60 Jy for ATs. For other setups it scales as the limiting flux values given in Table 3.3.

Table 3.3: Limiting N-band magnitudes of MIDI for different observation modes published by ESO. Note that in `SCI-PHOT` mode the actual limits are higher, 15 Jy for UTs and 200 Jy for ATs with the PRISM, concerning the currently available reduction software (cf. Section 4.2.1).

Telescope	Mode	Disperser	Limiting Magnitude	Limiting Flux
UT	`HIGH-SENS`	PRISM	4.0	1 Jy
UT	`HIGH-SENS`	GRISM	2.8	3 Jy
UT	`SCI-PHOT`	PRISM	3.2	2 Jy
UT	`SCI-PHOT`	GRISM	2.0	6 Jy
AT	`HIGH-SENS`	PRISM	0.74	20 Jy
AT	`HIGH-SENS`	GRISM	0.31	30 Jy
AT	`SCI-PHOT`	PRISM	0.00	40 Jy
AT	`SCI-PHOT`	GRISM	-0.44	60 Jy

Chapter 4

Observation and Data Reduction

In order to accomplish the proposed goals from Chapter 1 a dedicated target selection and observation strategy is needed as well as an adequate data reduction. Both aspects are covered in this chapter.

4.1 Observation Procedure

4.1.1 Target Selection and Observation Strategy

The objects studied in this work were already described in Section 2.4, including a listing of important properties. There are different reasons for choosing R Aql, R Aqr, R Hya, V Hya and W Hya. On the observational side, there are constrains concerning the observability. The stars have to be observable from the VLTI, i.e. their declination δ has to be below $+25°$. They must also be bright enough in the mid-infrared to be detectable with MIDI using the ATs. Consequently, one selection criterion was their 10 μm brightness. In order to resolve the circumstellar envelope (CSE), the surrounding warm molecular layers and the underlying stellar disk with MIDI, the targets should be located relative close with respect to the sun. Assuming a typical diameter of an AGB star of 1 to 10 AU, the stars should be within a few 100 pc, if baselines[1] between 10 and 100 m are used.

The number of potential targets is mainly reduced by the above observational constrains. Additional considerations concern the two-dimensional uv-coverage. There are two basic possibilities to obtain a well sampled uv-plane in order to search for asymmetries. It can be either achieved by changing the orientation of the baseline on earth by changing the telescope positions or by taking advantage of earth rotation. The latter requires a favorable declination of the target.

On the scientific side, there are fewer restrictions. The targets are chosen to cover different chemistries, evolution stages and mass loss rates. About 30 targets remain after applying the instrumental constrains (see the MIDI consortium proposal for all potential feasible stars, MIDI Science Group, 2003). From this sample five stars were selected to carry out detailed observations. R Aql, R Aqr, R Hya and W Hya are O-rich AGB stars, while V Hya is a late C-rich AGB star with a fast collimated wind (Whitelock & Feast, 2000; Loup et al., 1993). R Aqr is a symbiotic system and W Hya exhibits a low mass lost rate (cf. Section 2.4).

The observations concentrated on a relative small number of stars to obtain a fair number of visibility points to sample the uv-plane as well as the pulsation phase. The immediate objective is to identify molecules and dust which are present in the layer above the photosphere, and which have absorption features in the mid-IR, causing the diameter to vary across the N-band.

[1] For convenience, *baseline* refers always to the projected baseline if not stated otherwise.

In order to study the photosphere, close molecular and dust layers, it is necessary to sample the visibility around the first lobe to constrain such a layer model. Visibility points at short baselines are also required to measure the contribution of surrounding dust. Observations at several orientations can be used to establish whether the sources are elongated and which component (dust shell, molecular layer or photosphere) shows an elongation.

The AGB circumstellar environment is affected by the stellar pulsations. From infrared spectroscopy, it is already known that there is no simple relation between the spatial distribution of different molecules and the pulsation phase. Monitoring the stars regularly over a few pulsation cycles is therefore mandatory to study the dynamic behavior, in particular the variation in the distribution of the close warm layers of dust and molecules. Due to the fact that typical periods of AGB stars are on the order of one year and that in general a star is not visible throughout a whole year, it can be difficult to fulfill this requirement.

In order to identify molecules and dust species, the mid-infrared fringes are spectrally dispersed. The high spectral resolution GRISM mode of MIDI is of advantage, but introduces additional problems in the reduction process (e.g. the photometric channels are unfavorably illuminated). Therefore, observations were mainly executed with the PRISM. High visibility accuracies are possible by observing the correlated and uncorrelated flux at the same time. Since the targets are bright enough, the `SCI-PHOT` mode could be used.

The observation strategy can be summarized as follows:

- study only a few stars in great detail
- use long baselines to resolve the photosphere and close layers of molecules and dust
- use short baselines to measure the contribution of surrounding dust
- ensure a good uv-coverage to search for asymmetries
- cover a few pulsation cycles to detect dynamical spatial variations of the layers
- disperse the light to identify the dust and molecule species
- use the `SCI-PHOT` mode to obtain high accuracy visibilities

The observations are carried out in the framework of a Guaranteed Time Observation (GTO) program. Institutes contributing to an instrument for ESO telescopes get a reward on guaranteed time for observations on that instrument. For the MIDI instrument a total time of 450 hours on ATs were allocated for the proposed study of late-type stars. This means that 450 visibility measurements could be made over a dedicated time (1 hour is required to obtain 1 visibility measurement, see next section). Unfortunately some hours were lost due to a not fully working VLTI and a not verified observation procedure at the beginning. In semester[2] 75 and 76, the VCM (for FOV corrections, see Section 3.3.1) was not operating, and until the end of semester 78 no additional photometry were recorded. Without additional photometry the light split ratios between interferometric and photometric channels cannot be calibrated.

[2]ESO divides a year into 2 semesters, ranging from 1st April to 30th September and 1st October to 31st March. Semester 75 corresponds to the year 2005 and semester 76 to the year 2005/06.

The next two sections describe how the observations of semester 79 to 83 were prepared and executed with MIDI. Table 4.1 gives an overview of the course of observations, including the ESO program ID under which the stars were observed. The complete observation log of all five stars can be found in Appendix B. It should be noted that observations were still ongoing at the time of writing this thesis, and that observations not executed in a specific semester are shifted to the next semester. Probably with the end of semester 85 the whole program will be completed. Before the begin of semester 79, other late-type stars, namely Betelgeuse, R Leo, π1 Gru, R Scl and Vx Sgr, were observed as well, but were later excluded to concentrate on fewer stars with better observability.

Table 4.1: Overview of the course of observations used for this study. Given are the number of visibility measurements obtained with MIDI in `SCI-PHOT` mode for each of the five stars. Note that for the last two semesters the observation program was still ongoing. See Appendix B for a complete observation log.

Semester[a]	Program ID	Disperser	R Aql	R Aqr	R Hya	V Hya	W Hya
79	079.D-0140	GRISM	11	10	18	8	22
80	080.D-0005	PRISM	6	10	16	26	17
81	081.D-0198	PRISM	15	7	16	8	18
82	082.D-0641	PRISM	0	4	12	20	14
83	083.D-0294	PRISM	8	8	10	1	12

[a] Semester 79 = 1st April, 2007 to 30th September, 2007; Semester 80 = 1st October, 2007 to 31st March, 2008; Semester 81 = 1st April, 2008 to 30th September, 2008; Semester 82 = 1st October, 2008 to 31st March, 2009; and Semester 83 = 1st April, 2009 to 30th September, 2009.

4.1.2 Observation Preparation

With the above boundary conditions the observations could be prepared. Two basic tasks were carried out in order to define an observation. First an appropriate baseline must be selected, and second, an adequate calibrator star had to be found. For both tasks dedicated ESO web interfaces[3] are available to search for and to verify the best selection. For a short review see Percheron (2008). With the Visibility Calculator (VisCal), the visibility, projected baseline and uv-coverage can be explored in addition to observability and pointing restrictions. The Calibrator Selector (CalVin) can be used to find a suitable calibrator and to check its interferometric properties.

The selected baselines used in this study are given in Table 4.2 and are visualized in Figure 4.1. The table lists the proposal identifier name (an arbitrary letter) and the corresponding AT station configuration with its physical ground length and position angle (PA, East of North) on Paranal. The resolution is calculated with equation 3.14 for the given ground length at a wavelength of 10 μm. Several instrumental restrictions have to be kept in mind while choosing

[3] http://www.eso.org/observing/etc/

Table 4.2: AT configurations used for the observations in this study. The resolution corresponds to the ground length at 10 μm. Note that for observations only the projection of the baseline and the position angle (PA) on the sky is relevant.

Name	AT stations	Ground length[a]	Ground PA[a]	Resolution
A	E0-G0	16.006 m	71.020°	64 mas
B	G0-H0	31.998 m	70.998°	32 mas
B*	A0-D0	32.011 m	71.014°	32 mas
C	E0-H0	48.004 m	71.005°	21 mas
D	D0-H0	64.005 m	71.012°	16 mas
E	D0-G1	71.557 m	134.443°	14 mas
F	H0-G1	71.555 m	7.576°	14 mas

[a] from http://www.eso.org/sci/facilities/paranal/telescopes/vlti/configuration/index.html.
* B* was used only a few times and has almost the same properties as B.

the baseline. The pointing can be limited due to the shadowing from the UTs and due to the fact that the maximum delay line path difference cannot be more than 105 m.

Calibrator stars are needed to calibrate the visibility spectra, photometric spectra and differential phases of the targets. A good calibrator should be unresolved at the given baseline, i.e. $V_{\rm theor} = 1$, or the diameter should be known in order to estimate $V_{\rm theor}$ with an uniform disk model. Diameters for calibrators are estimated from available photometry using model fitting or by direct interferometric measurements. The transfer function (TF) of the system can then be calculated via

$$\mathrm{TF} = \frac{V_{\rm meas}}{V_{\rm theor}}\,, \tag{4.1}$$

where $V_{\rm meas}$ is the measured visibility with the instrument. The mid-infrared flux, needed for the photometric calibration, is obtained from space observatories like IRAS[4] or MSX[5]. The calibrator should be bright in the recorded wavelength, and should be observed close in time and angular separation in order to experience similar atmospheric conditions. In addition, the calibrator should have a similar spectral type without spectral features. This ensures that the instrumental response is the same for both objects with identical instrumental setup, and that the diameter of the calibrator is wavelength independent. The current CalVin database consists of about 400 calibrator stars usable for mid-infrared observations. The selection is based on a list of Cohen et al. (1999). The database is constantly updated and cleaned of bad calibrators. Exclusions can be due to multiplicity, variability or an infrared excess. Therefore a quality flag is assigned to each entry where 1 designates a good calibrator and 3 a bad calibrator.

Table 4.3 (page 74) lists the selected calibrators used in this study. Given are astrometric data as well as several photometric magnitudes. The angular diameters are from different sources. In this study the bold values from the CalVin database are used. Other sources can list different

[4] http://irsa.ipac.caltech.edu/Missions/iras.html
[5] http://irsa.ipac.caltech.edu/Missions/msx.html

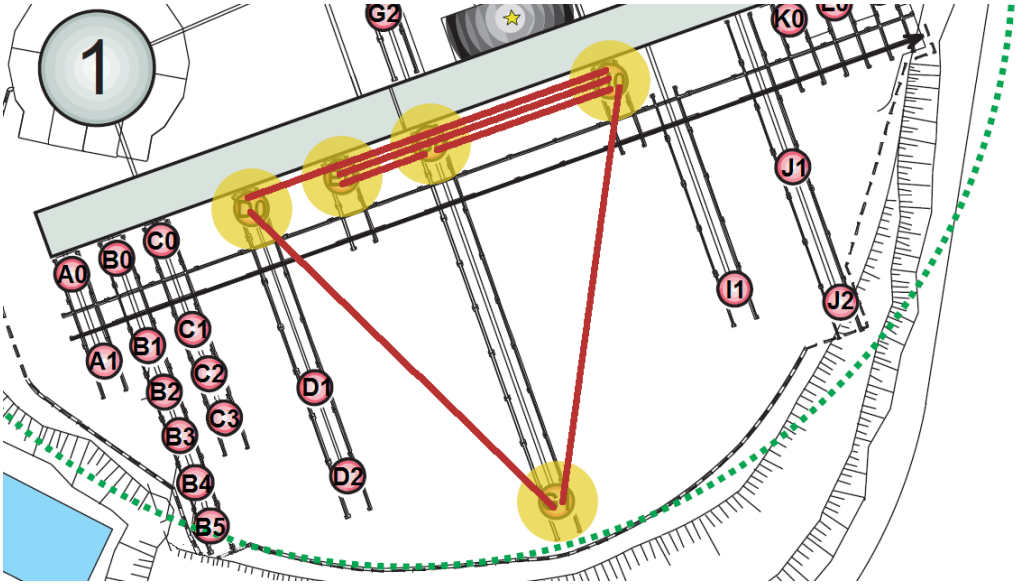

Figure 4.1: Part of Figure 3.8. The used AT stations are marked with yellow circles and the baseline configurations used are connected be red lines (see Table 4.2 for details).

diameters obtained with other methods. These differences might come from not modeled or not understood calibrator properties. As can be seen from the quality flag, 2 Cen is not one of the best calibrators. The quality flag of 2 means that the object can be variable within a certain range or the photometry and diameter values are less accurate. 2 Cen, 30 Psc and α Hya are variable stars with a low visual amplitude on the order of $0.1 - 0.6$ mag.

The last row lists the associated targets for which the calibrator is used. The angular separation between calibrator and target is given in brackets and shows that they are located relatively far away from each other. This results from the low number of available calibrators, but is fortunately not a big concern in the mid-infrared. Only for calibrating the photometry the different airmass has to be taken into account. The visibility is not affected since both, the correlated and uncorrelated flux, changes proportional with airmass. The calibration of the differential phase is mainly affected by the time difference between calibrator and target observation and not by their angular distance.

Nevertheless, observations need to be carried out under good seeing conditions (typical $\leq 1.4''$) and a clear sky. Both is necessary to have a long coherence time in order to obtain fringes and to reduce the infrared background. The moon does not influence the measurements and observations can be done at full moon. Only for the guiding at visual wavelength, the moon should be not to close to the target to avoid straylight, i.e. the separation should be larger than $10°$.

Table 4.3: Properties of the Calibrators.

Calibrator name	η **Sgr** HD 167618	ϵ **Peg** HD 206778	**30 Psc** HD 224935	α **Hya** HD 81797	**2 Cen** HD 120323
Right Ascension α[a]:	$18^h\ 17^m\ 37.64^s$ (274.406833°)	$21^h\ 44^m\ 11.16^s$ (326.046492°)	$00^h\ 01^m\ 57.62^s$ (0.490083°)	$09^h\ 27^m\ 35.24^s$ (141.896833°)	$13^h\ 49^m\ 26.72^s$ (207.361333°)
Declination δ[a]:	$-36°\ 45'\ 42.00''$ (−36.761667°)	$+09°\ 52'\ 30.00''$ (+9.875000°)	$-06°\ 00'\ 50.70''$ (−6.014083°)	$-08°\ 39'\ 31.00''$ (−8.658611°)	$-34°\ 27'\ 02.70''$ (−34.450750°)
$\mu_\alpha \cos\delta$[a] (mas/yr):	−129.27 ± 1.05	30.02 ± 1.12	46.62 ± 1.09	−14.49 ± 0.89	−42.59 ± 0.88
μ_δ[a] (mas/yr):	−166.61 ± 0.60	1.38 ± 0.49	−41.32 ± 0.44	33.25 ± 0.63	−59.87 ± 0.64
Parallax[a] (mas):	21.87 ± 0.92	4.85 ± 0.84	7.86 ± 0.94	18.40 ± 0.78	18.39 ± 0.74
B magnitude[a]:	4.682 ± 0.004	3.900 ± 0.003	6.001 ± 0.006	3.430 ± 0.003	5.710 ± 0.007
V magnitude[a]:	3.100 ± 0.004	2.380 ± 0.004	4.370 ± 0.005	1.990 ± 0.004	4.190 ± 0.007
J magnitude[b]:	−0.424 ± 0.192	-0.117 ± 0.166	0.623 ± 0.164	-0.256 ± 0.147	−0.578 ± 0.155
H magnitude[b]:	−1.394 ± 0.266	-0.750 ± 0.192	-0.238 ± 0.190	-0.990 ± 0.192	−1.501 ± 0.226
K magnitude[b]:	−1.633 ± 0.388	-0.860 ± 0.220	-0.399 ± 0.218	-1.127 ± 0.208	−1.793 ± 0.292
N magnitude[c]:	−1.82	−1.04	−0.85	−1.49	−2.02
N-band flux at 12 μm[c] (Jy):	213 Jy	104 Jy	87 Jy	157 Jy	256 Jy
Spectral classification[a]:	M2 III	K2 Ib var	M3 III	K3 III	M5 III
Angular diameter[d] (mas):	11.33 ± 0.04	8.38 ± 0.09	7.24 ± 0.03	9.05 ± 0.07	9.16 ± 0.07
Angular diameter[c] (mas):	**11.66 ± 0.04**	**7.59 ± 0.05**	**7.24 ± 0.03**	**9.14 ± 0.05**	**13.25 ± 0.06**
Quality flag[c]:	1	1	1	1	2
Associated target[e]:	R Aql (46.4°)	R Aql (42.8°)	R Aqr (10.3°)	V Hya (23.8°)	W Hya (6.1°) R Hya (12.0°)

[a] Hipparcos (Epoch = J1991.25, ICRS, Equinox = J2000) (Perryman & ESA, 1997b); [b] 2MASS (ICRS, Equinox = J2000) (Skrutskie et al., 2006); [c] ESO CalVin database (cf. Section 4.1.2); [d] MIA/EWS database (cf. Section 4.2); [e] the angular separation between calibrator and target is given in brackets

All observations are executed in service mode, i.e. the personnel at Paranal observatory observes the targets and calibrators without the need for visiting scientists to go there. Single observations are prepared with P2PP[6] as observation blocks (OBs) before sending the observation request. All described relevant scientific and instrumental information are specified in such an OB. It also permits to define specific sidereal time intervals to ensure to some degree a good time coverage of the pulsation cycle. In addition, finding charts are attached as well to clearly identify the target. Altogether, the chosen baselines, calibrators and time intervals match basically the requirements needed to fulfill the proposed strategy from Section 4.1.1.

4.1.3 MIDI Observation Procedure

The VLTI is a very complex system, consisting of the telescopes, delay lines and the interferometric instrument. All subsystems have to work perfectly together to obtain visibilities. Even though the details are not of importance here, the general observation procedure is described in this section in order to point out some practical instrumental limitations and to understand the scientific data obtained. After the submission of the target list, the observations are carried out as specified in the corresponding OBs. In order to obtain one measurement, one hour of observation is required. It includes overheads from the acquisition procedure, and the recording of the interferometric and photometric data for the target and the calibrator.

Since the used `SCI-PHOT` mode with MIDI includes already the needed measurements of the correlated and uncorrelated flux to calculate the visibility (cf. equation 3.39), the additional photometry is only recorded to calibrate the relative throughputs of all channels. As already mentioned in the previous section, the calibrator is needed to account for instrumental visibility losses, to obtain absolute flux values and to calibrate the differential phase. The described following procedures are done for the target *and* the calibrator.

4.1.3.1 Acquisition

With the start of executing an OB, the AT telescopes start to move until the correct pointing position with respect to the object is reached. At the same time one of the delay lines moves to the expected zero-OPD position, calculated from the sidereal trajectories. After starting the smooth slewing of the delay line, and the coudé-guiding with the STRAP units[7], the object can be seen in the FOV[8] of MIDI in imaging mode. In this work, the objects themselves are used as guide stars, whereas a nearby star could also be used in other cases. The MIDI setup for the imaging mode can be seen in the left panel of Figure 4.2. In this setup, no slit, photometric beam splitter, beam combiner and dispersive element is placed in the beams. The light goes only through the N8.7 filter before the camera images the object on the detector.

In order to ensure the beam interference later, the images from both beams must be correctly aligned. This is either guaranteed by using the IRIS guiding system (the default mode, see Section 3.3.1) or by using the MIDI acquisition image setup. IRIS brings the photocenter of

[6]Phase II Proposal Preparation tool: http://www.eso.org/sci/observing/phase2/P2PP/P2PPTool.html

[7]The STRAP is also responsible for the tip-tilt corrections, the lowest order of wavefront-distortions introduced by the atmospheric turbulence.

[8]The VCM ensures a stable field of view (FOV).

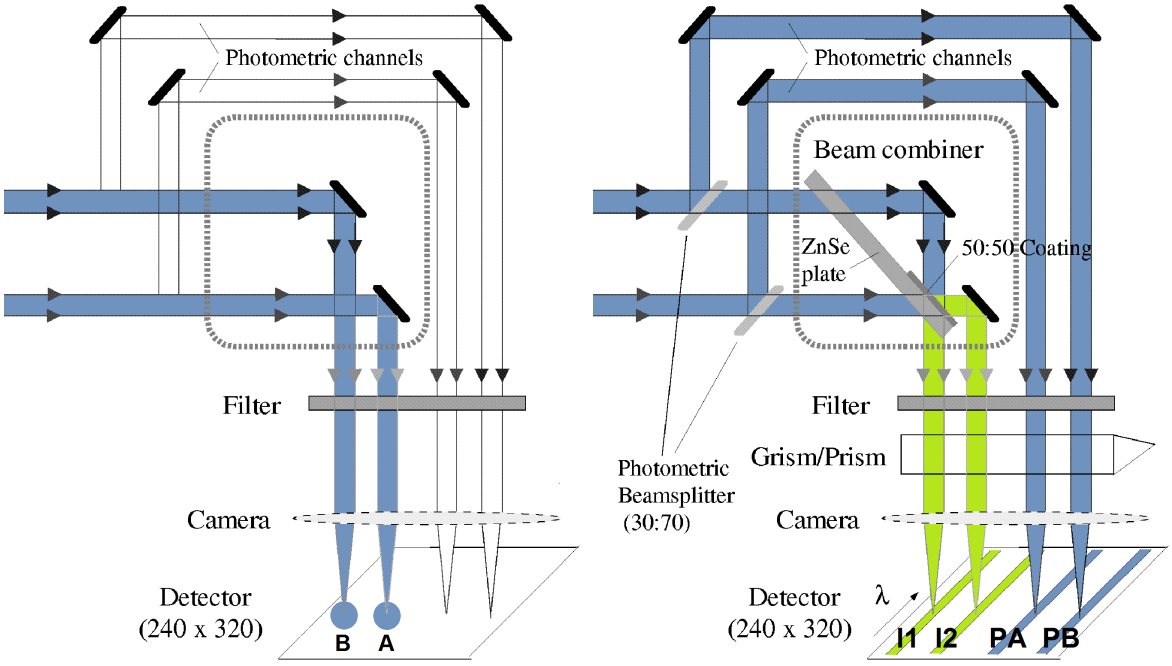

Figure 4.2: MIDI setup in acquisition *(left)* and `SCI-PHOT` *(right)* mode.

the object onto a reference pixel and sends corrections to the telescopes. Acquisition images are only taken if the target is too faint for IRIS. However, some acquisition exposures were recorded for the calibrators and bright stars studied in this work. Figure 4.3 illustrates how these mid-infrared images look.

The top images are for the target W Hya, while the bottom images show the calibrator 2 Cen. These observations were taken in 15th August, 2009. In order to eliminate the background radiation from the delay line tunnel (bright outer rim), the mirrors and the atmosphere (less bright inner area) chopping is performed at a frequency of 0.5 Hz and an amplitude of 15 arcsec with the secondary mirror. The left images show the averaged on-source frames, the middle images the averaged off-source frames (nearby empty sky position) and the right images the subtraction of both. It can be seen from the figure that the background is so high that 2 Cen is only visible after taking the difference. The detector integration time (DIT) is typically 3.5 ms. 1000 frames with this DIT are combined to increase the signal-to-noise ratio.

4.1.3.2 Fringe Recording

The previous procedure led to a delay line arrangement near zero OPD and achieved a good beam overlap. The next step is to find the exact zero OPD position. The right panel of Figure 4.2 shows the MIDI setup for the fringe search and `SCI-PHOT` recording mode. The slit, the photometric beam splitters, the beam combiner and the PRISM or GRISM are now inserted into the light path, and the broad N-band filter is used instead of the N8.7 filter. Only four subarrays, the two interferometric channels I1 and I2 (spectrally dispersed interferograms of opposite phase) and the two photometric channels PA and PB (spectrally dispersed photometry), on the detector are read out. The read out window sizes are 171 × 41 and 261 × 40

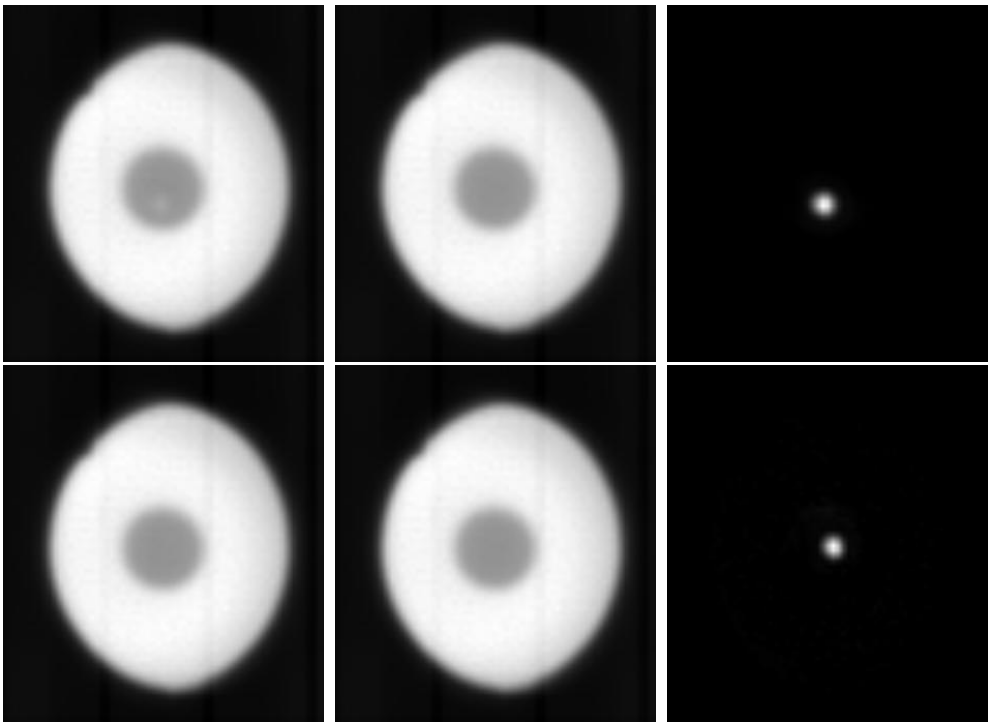

Figure 4.3: Acquisition images of W Hya *(top)* and 2 Cen *(bottom)*. From left to right the averaged on-source, off-source and difference image is shown. 2 Cen is only clearly visible after taking the difference. The image size is 62 × 69 pixel.

pixels for the PRISM and the GRISM, respectively. The relationship between the wavelength λ in μm and the detector pixel on MIDI with the PRISM and GRISM is given by

$$\lambda_{\mathrm{prism}}(X) = -1.539^{-4} \cdot X^2 + 9.491^{-3} \cdot X + 15.451905 \text{ and} \quad (4.2)$$

$$\lambda_{\mathrm{grism}}(X) = -1.21122^{-6} \cdot X^2 + 0.0231223 \cdot X + 7.54423\,, \quad (4.3)$$

respectively[9]. X designates the pixel position, where 1 refers to the left edge column and 320 to the right edge column of the whole detector. The exact location of the read out windows has to be taken from the observation files, since this changed slightly over the years. In order to find the fringes, the OPD is scanned with the MIDI piezo-mounted mirrors on the warm optical bench and the VLTI delay lines. The search range is a few mm around the expected zero OPD given by the empirical OPD model. Under normal circumstances the obtained position is stable for hours within a fraction of a millimeter.

After this determination of the real zero OPD position, MIDI scans several times the broad-band fringe (white light fringe covering the whole N-band) by modulating the OPD with the piezos alone. This is necessary to enhance the signal-to-noise ratio by basically adding up all scans in the reduction process later (Section 4.2). The OPD scan length is about 80 μm. Figure 4.4 shows such a complete interferometric observation sequence, while Figure 4.5 shows a more detailed part of it. In total 200 consecutive scans, each consisting of 40 exposures, are performed. With an exposure time of 18 ms for the PRISM or 36 ms for the GRISM the

[9] as described in the MIDI user manual

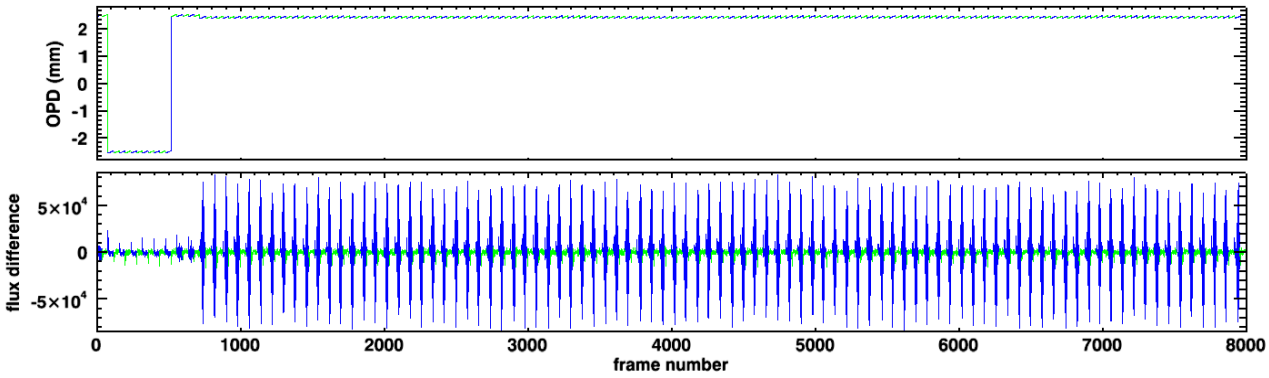

Figure 4.4: Complete SCI-PHOT observation sequence. The upper plot shows the OPD against frame number. The sawtooth OPD change due to the 200 scans as well as the large OPD offset at the beginning for the determination of the background noise is visible. The lower plot illustrates that only for on-target scans (blue) broad-band fringes are detected while for off-target scans (green) no fringes are detected. The flux difference is the difference between both interferometric channels, which have opposite phase. See Figure 4.5 for a detailed view.

recording of the 8000 frames takes about 3.1 min or 5.4 min, respectively. This includes an overhead of 5 ms per frame.

In contrast to HIGH-SENS observations, chopping is performed during SCI-PHOT observations to remove the background from the simultaneously recorded photometry. Every second scan, the telescope points to a nearby sky position and no fringes are recorded. The synchronization with the scans leads to a chopping frequency of 0.545 Hz and 0.306 Hz for the PRISM and the GRISM, respectively. This does not affect the internal fringe tracking which stabilizes the path difference.

MIDI uses group delay measurements to correct the OPD shifts introduced by the sidereal motion and the atmosphere by sending this information to the VLTI delay lines. The group delay is estimated from the spectral information of the dispersed fringes. With this method, it is possible to determine the direction where the white-light fringe can be found by analyzing several frames within a scan (cf. Figure 4.5d). This allows for bright stars to distinguish whether the signal is tracked at real zero OPD or at a sidelobe. A better tracking could be performed with an external fringe tracker, operating at a shorter wavelength, if appropriate.

4.1.3.3 Additional Photometry

The additional photometry, needed to calibrate the light mapping ratios between interferometric and photometric channels, are obtained be closing alternatively the shutter of telescope beam A or beam B, and keeping the optical set up the same. This is shown in Figure 4.6. With this procedure the ratios I1/PA, I2/PA, I1/PB and I2/PB as function of wavelength are determined. Chopping is still enabled to remove the background. The chopping frequency and integration time is the same as for the fringe recording. The only difference is that fewer frames are recorded (4000 frames per beam before P80 and 2000 frames with beginning of P80).

As will be seen in the next section, the correct determination of the photometry is crucial to

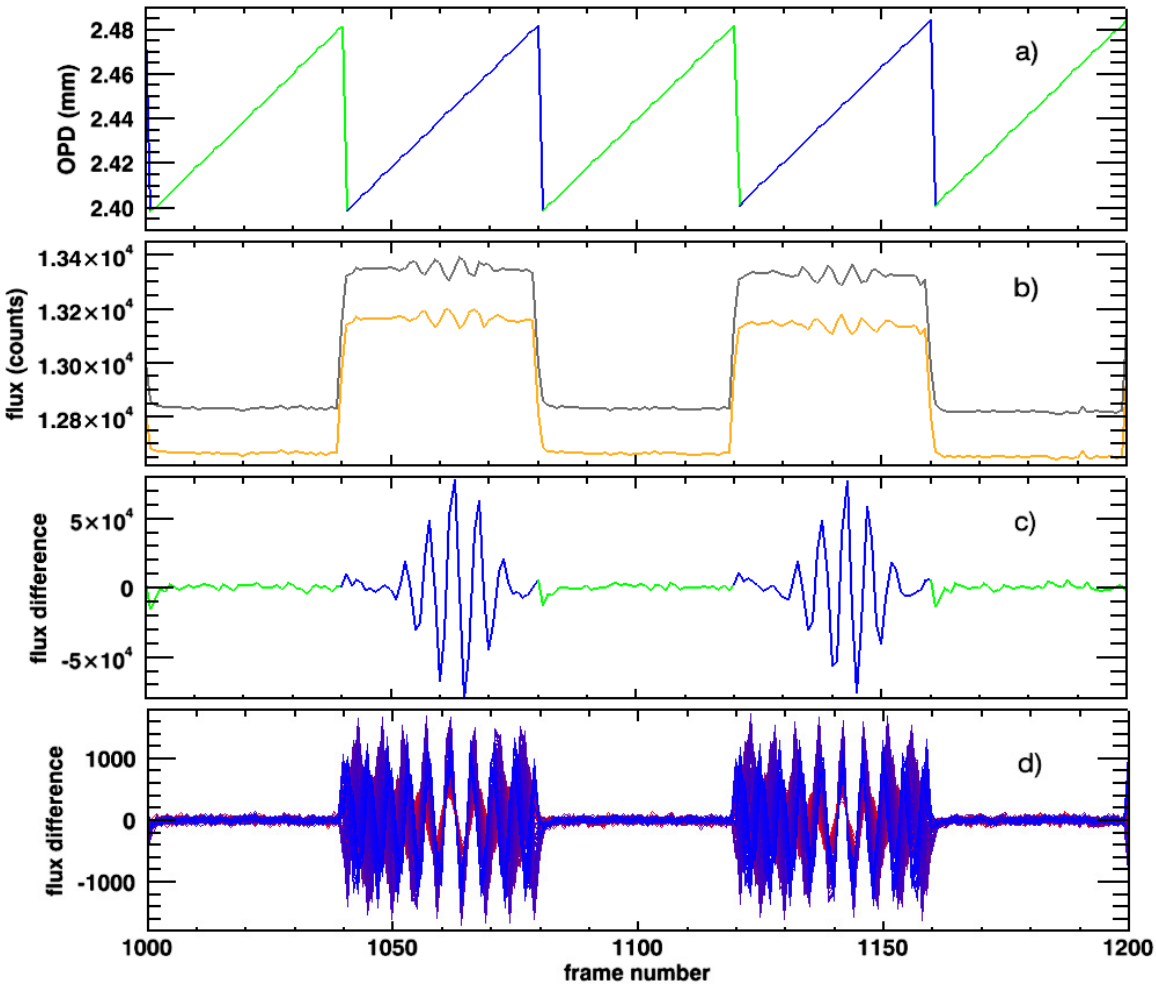

Figure 4.5: 5 from 200 scans of a whole SCI-PHOT observation sequence (W Hya observed on 2009-04-24, total scan length: 5×80 μm). *a:* shows the sawtooth OPD scans with green off-target and blue on-target. In this example the real zero-OPD is found about 2.44 mm offset the estimated OPD. *b:* presents the fluxes of both interferometric channels (I1 and I2). It is obvious that the background is very high at both chopping states and the fringes of both channels have opposite phase. *c:* illustrates the difference of the throughput corrected interferometric channels of *b*. The broad-band fringe is clearly visible while the background is removed. The flux of all wavelengths from *d* are just added up. The coherence length, Λ_{coh}, of the broad-band fringe is 20 μm (equation 3.27). *d:* Dispersed fringes. The fringes of 80 wavelengths between 8 (blue) and 13 μm (red) are shown. Only for real zero-OPD the maxima coincide (for a zero source phase and no relative dispersion, cf. Figure 3.3). Since the coherence length with the used PRISM is about 300 μm, the fringe for each wavelength is detected throughout the whole scanning range, while for the sum in *c* it is not.

obtain accurate visibilities. Even though the chopping removes most of the background, some remains and has to be determined somehow else. The fact that the observations presented in this work were obtained in SCI-PHOT mode makes this less severe, but does not eliminate this.

As described, the interferometric observation itself takes only a few minutes. Most of the allocated time of 30 minutes is used for the telescope setup, acquisition, photometry recording

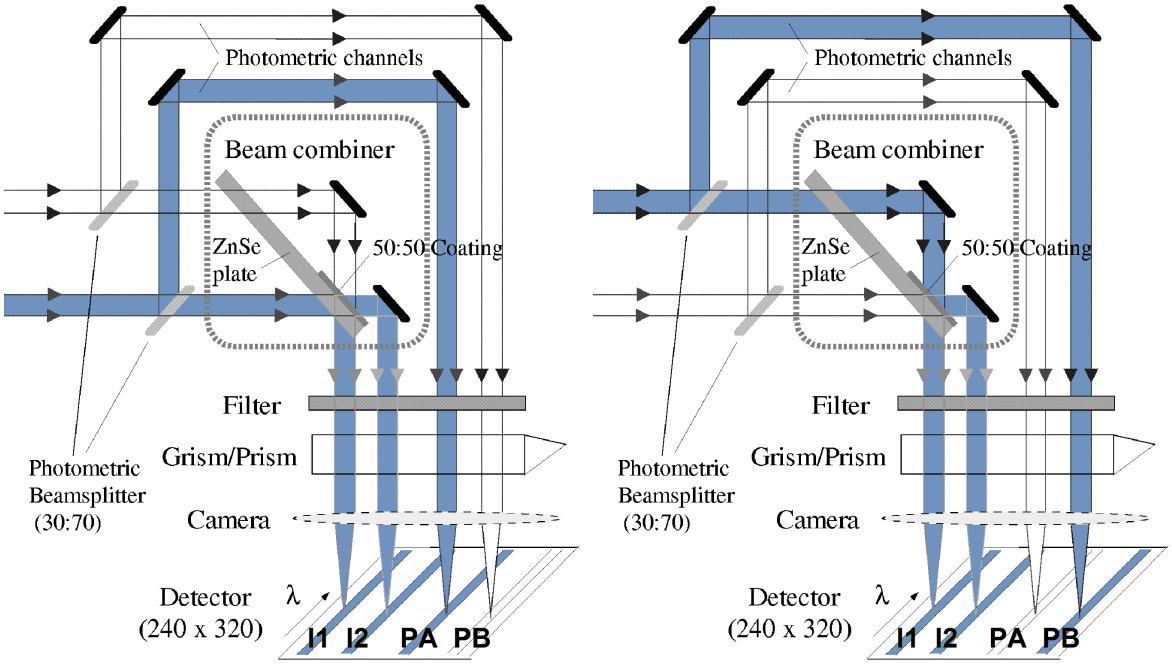

Figure 4.6: MIDI setup in photometry mode. If the shutter for beam B is closed only I1, I2 and PA are illuminated *(left)*, while for closed beam A channel PB is exposed instead of PA *(right)*. Note that the interferometric channels do not record fringes, they detect a photometric spectrum as well.

and data handling[10]. In addition to the science target a calibrator star is observed. The total time allocation for one calibrated visibility spectrum, photometric spectrum and differential phase spectrum is hence on the order of one hour.

4.2 MIA/EWS SCI-PHOT Reduction

The standard `MIA+EWS`[11] (version 1.6) (MIDI Interactive Analyses + Expert Work Station) data reduction package (Köhler, 2005; Jaffe, 2004, respectively) with additional routines for processing `SCI-PHOT` data (Walter Jaffe, private communication) is used. The software runs on the commercial data visualization and analyses platform `IDL`[12] (Interactive Data Language). Most of the computationally intensive data processing is carried out by C routines. The MIDI data are stored in OIFITS files (Optical Interferometry Flexible Image Transport System, Pauls et al., 2005). `MIA` and `EWS` use different methods to estimate the visibility spectrum, while the photometric spectrum is obtained in a similar way.

`MIA` determines the fringe amplitude incoherently with a power spectrum analysis. As described in the previous section, the broad-band fringe is scanned by modulating the internal OPD. Each

[10]Due to the many short exposures, the data amount generated by MIDI is large. One hour of observation results in about 1 GByte data split into 100 MByte files.
[11]http://www.strw.leidenuniv.nl/~koehler/MIDI
[12]http://www.ittvis.com/ProductServices/IDL.aspx

fringe scan is Fourier transformed from delay space into frequency space in order to calculate the power spectrum and obtain an average squared amplitude of the fringe. Filtering ensures the integration of the power inside the correct frequency interval. After averaging the total power of all scans and subtracting an estimate of the noise level (Colavita, 1999), obtained from the offset OPD interval at the beginning of the interferometric recording, the squared visibility, V^2, is calculated by using the photometric flux. No phase information can be extracted with this method.

`EWS` on the other hand uses a coherent method. It takes advantage of the fact that the fringes are dispersed with the PRISM or GRISM. Since the N-band is relatively broad ($\Delta\nu/\nu \approx 0.7$) and the background noise is primarily photon noise (Poisson distributed) instead of read-out noise, the fringes can be measured in frequency space rather than in OPD space. The OPD, which is the sum of the variable known instrumental delay and the unknown atmospheric delay, can be estimated from the rapidly measured spectra without loss of signal to noise for each frame. Thus, the OPD is measured from a single exposure and the coherence time does not need to be longer than this. This exploits the same method used for the group delay tracking mentioned above.

After reducing all frames to the same OPD, they are added coherently. In contrast to the incoherent averaging, the major advantage is that the noise in the sum has nearly zero mean and the complex visibility can be estimated directly. Thus, it is usually not necessary to subtract an estimate of the system noise from the visibility. In addition to the visibility V, this method estimates a differential phase φ as well.

The `SCI-PHOT` reduction can be split into three main steps, which are associated with the call of three routines inside `EWS` (`EWS` + the additional `SCI-PHOT` routines). The names of the routines and the reduction steps are:

1. spCrossCal determines the mapping behavior between interferometric and photometric channels from the additional photometry
2. spPipe estimates the instrumental visibility, photometry and phases for the target *and* the calibrator from the interferometric observation
3. spCalVis calibrates the target visibility, photometry and phase using the calibrator estimates

The following sections describe the `SCI-PHOT` reduction with `EWS` in detail. Example plots are given for the observation of W Hya on 2009-04-24, using the calibrator 2 Cen, to illustrate the different steps.

4.2.1 Cross Coupling Coefficient Determination

In SCI-PHOT mode, the interferometric channels (I1 and I2) and photometric channels (PA and PB) are illuminated at the same time. In order to get an estimate of the uncorrelated flux in the interferometric channels from the simultaneous photometric fluxes in the photometric channels the appropriate multiplication factor (cross coupling coefficient κ) has to be known, i.e. it is necessary to determine how much light goes into each channel. More exactly, the mapping of

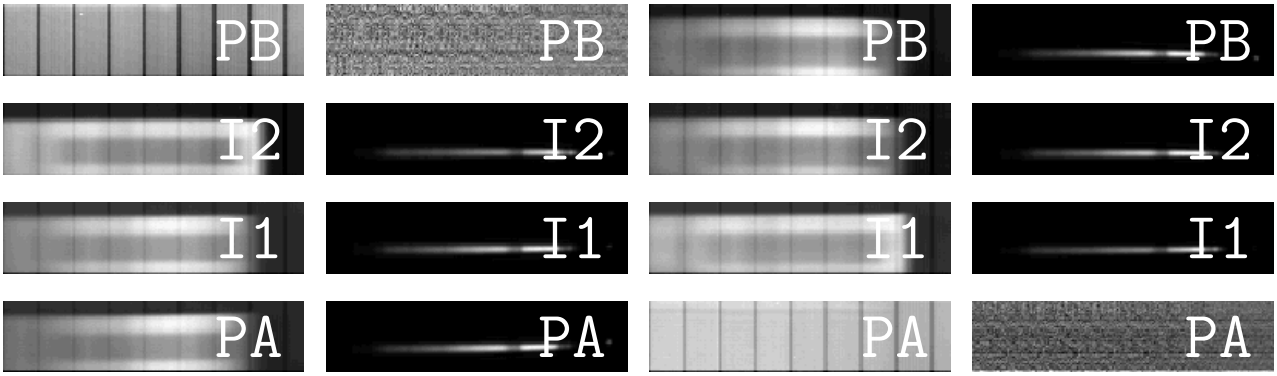

Figure 4.7: Averaged sky and averaged unchopped photometric spectra for all four channels. The *left eight* panels show the A open case whereas the *right eight* panels show the B open case. The left column for each case are the averaged sky frames. The spectra with the ozone absorption feature is only visible after sky subtraction on the right column for each case. For the closed channel only detector dark current and noise can be seen.

the photometric channel to the interferometric channel needs to be calculated, including the determination of the point spread function (PSF) along the perpendicular spectral direction at each wavelength and the relative shift of the spectrum. This allows in the next step to calculate the instrumental visibility from the uncorrelated and correlated flux at the position of the interferometric channel.

The additional photometry, recorded before or after the actual interferometric observation, is used to extract the exact wavelength dependent light split ratios. As shown in Figure 4.6, the ratios I1/PA and I2/PA can be determined if A is open and the ratios I1/PB and I2/PB can be determined if B is open. In the ideal case, 30% of the flux goes into the photometric channel and 70% into the interferometric channels, and due to the beam combiner, 35% of the light reaches therefore each interferometric channel. If this is also true for each wavelength the split ratio would be 1.17. The real case is different and the following things need to be considered to obtain a good calibration of the mapping.

For a proper work of the spCrossCal routine, photometric data from a very bright source are needed[13], i.e. for this work the photometry of the brighter target is always used. In principle it does not matter if the photometry is taken from the target or calibrator observation, and it should be even sufficient if this calibration is done for one dataset per night. In order to check for consistency and stability, the photometry of each target-calibrator pair is used to extract the mapping behavior.

Concerning the splitting of the light between photometric and interferometric channels, and the generally relatively faint calibrators, it is advisable to observe with the PRISM to ensure that the routines work appropriately. GRISM data from the same object have a lower source flux per pixel due to the larger dispersion on the detector array. In addition, the GRISM spectra in the photometric channels are much more curved as a result of the optical layout (cf. Figure 3.12), making the whole calibration process more error prone. With the longer integration time in GRISM mode, more temporal decorrelation of the interferometric signal is expected as well,

[13]As mentioned in Table 3.3, the flux should be greater than 15 Jy for UTs and 200 Jy for ATs (PRISM).

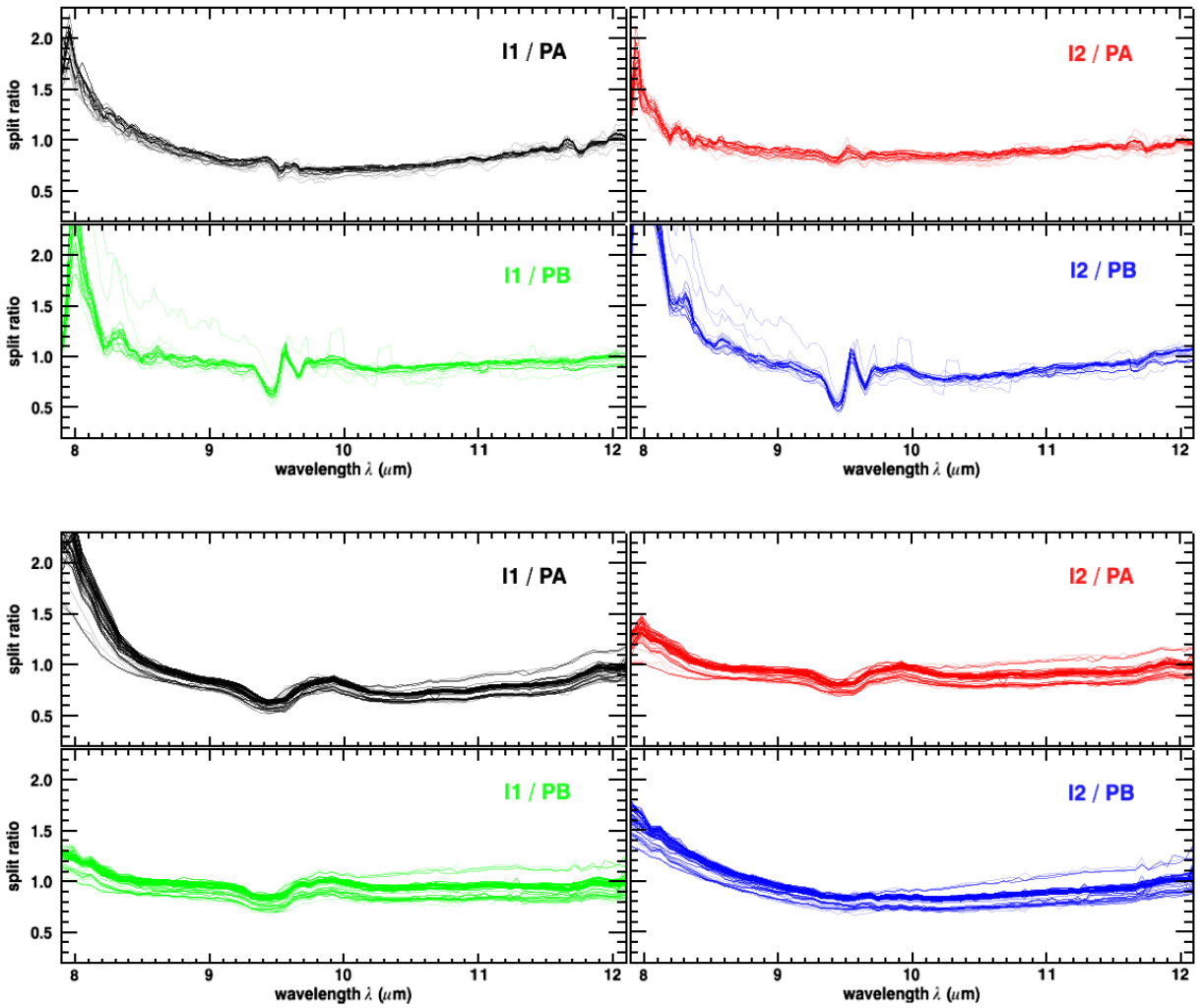

Figure 4.8: The four cross coupling coefficients (I1/PA, I2/PA, I1/PB and I2/PB) for GRISM (*top*) and PRISM (*bottom*) observations as function of wavelength. Shown are all 75 determinations (22 GRISM and 53 PRISM) for the 75 observations of W Hya. Clearly, PRISM observations are more stable.

degrading the final visibility further.

The first thing spCrossCal does is to unchop the A open and B open photometric data using the subroutine `oirChopPhotoImages`. The subtraction of the average of the on-source frames by the average of the off-source frames removes most of the overwhelming mid-infrared background. Figure 4.7 shows for both shutter states the sky frames and the unchopped frames. In these detector read-out examples only the good frames are averaged.

In the next important step, the subroutine `spCross` fits point spread functions (PSF) to each channel to obtain wavelengths dependent photometric masks. The PSFs are the Fourier transforms of the masks for every wavelength bin. Cross coupling coefficients are calculated by comparing these PSFs. Figure 4.8 shows all cross coupling coefficients obtained for one of the target stars. These numbers indicate the split ratios but do not reflect the complete mapping

behavior, since the wavelength dependent PSF and shift of the spectrum has to be known as well. The actual photometric PSF masks and shifts are used later on. The cross coupling coefficients are smoother with wavelength and more stable with time for PRISM observations compared to GRISM observations. This is due to the better optical light propagation inside the instrument.

In order to fit the PSFs correctly, the remaining background, not subtracted by the unchopping, has to be determined and removed. Remaining background comes from short term variations of the high sky background and instrumental imperfections. Hence, the subroutine `spFindTunnel` has to distinguish between sky, tunnel and source flux, and has to know the slit position. This changes with AT position, projected baseline and pointing, and causes in the end problems in the calibration process, since too high or too low uncorrelated or correlated fluxes can lead to high uncertainties and even unphysical visibilities (lower than 0 or higher than 1). This is one of the largest error sources, resulting in uncertainties for the final visibility and photometric spectrum on the order of typically 10% and 30%, respectively. It is also important to note that the fitting of the masks and their correct application to the photometry and interferometry of the target and the calibrator can cause errors.

4.2.2 Instrumental Photometry, Phase and Visibility Estimation

In the second main step, the instrumental visibility, photometry and phase for the target *and* calibrator are estimated from the interferometric observation. Therefore, all steps described in the following are performed on the target *and* calibrator interferometric data (AB open chopped fringe tracking data), i.e. the routine spPipe is executed two times in total. After unchopping the data two important reduction steps are performed. First, the flux in the photometric channels is used to calculate the uncorrelated flux with the previously obtained mapping behavior and a photometric spectrum. Second, the flux in the interferometric channels is coherently added in a certain way to obtain the correlated flux and differential phase.

4.2.2.1 Uncorrelated Flux and Photometry

As in Section 4.2.1, the unchopping is done with the subroutine `oirChopPhotoImages`. The difference is now that fringe data are unchopped as well. This reduces the number of frames from 8000 to 3900, always including the removal of the frame between the two chopping states. The averaged results are shown in the left column of Figure 4.9. The averaged fringe data (I1 and I2) obtained in this step are not used, since the average is done over fringes with different OPDs, i.e. they are not coherently added. They are only shown for completeness.

In the next step the subroutine `spMaskTrackMask` compares the position of the current spectra in channel PA and PB with the previously processed photometric PA and PB spectrum (Section 4.2.1). It constructs from the measured shifts four new masks for each channel as shown in the right column of Figure 4.9. Each shifted photometric mask matches then the current pointing position. The remaining background is removed by the same procedure as described in the previous section. This contributes with the same order of magnitude to the uncertainties.

The subroutine `sci2Hi` determines now from the PA and PB channels the hypothetical un-

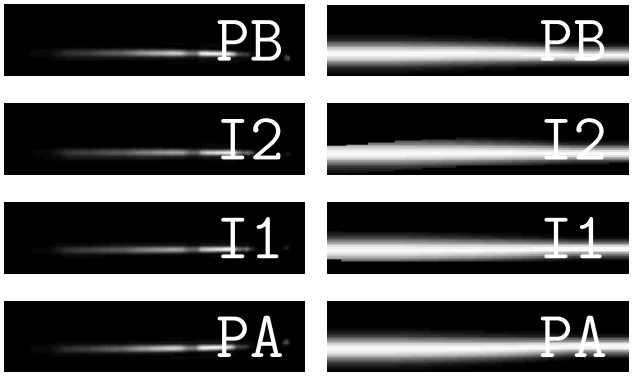

Figure 4.9: The *left four* panels show the averaged unchopped SCI-PHOT AB open data for all four channels. The data are simultaneously recorded as shown in Figure 4.2. The *right four* panels display the constructed final masks for each channel, see text.

correlated flux in the interferometric channels I1 and I2. It basically converts the SCI-PHOT photometry images into HIGH-SENSE photometry images by projecting the PA and PB photometric channels to the I1 and I2 interferometric channels by applying the previously obtained mapping behavior.

In order to do this, the previously obtained photometric PA and PB PSFs, shifted according to the determined pointing, is fitted to the corresponding current PA and PB channel at each wavelength. The resulting PA and PB spectrum is then multiplied be the wavelength dependent cross coupling coefficients to obtain an estimate of the photometric flux in the interferometric channels. This step includes a wavelength shift as well in order to correct for differences in the wavelength scale between each channel.

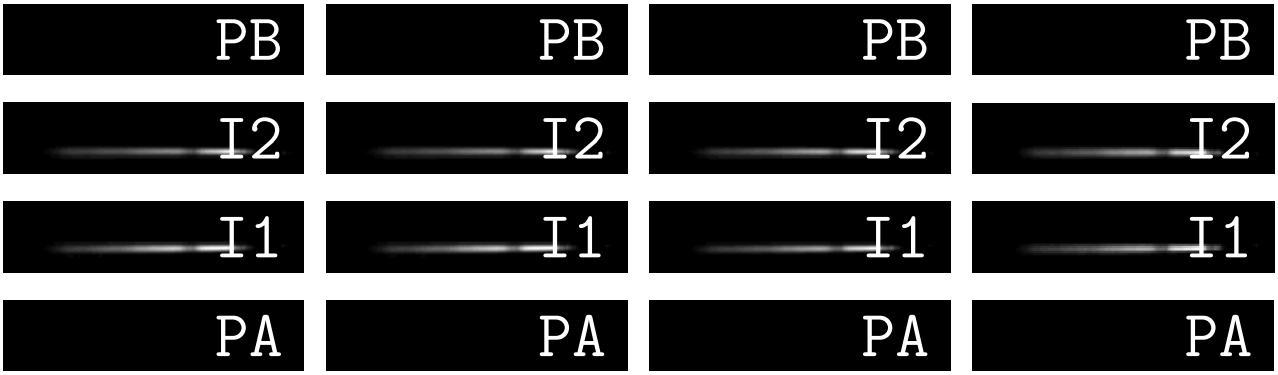

Figure 4.10: The *first* and *second column* show the predicted photometry $I2_A$, $I1_A$ and $I2_B$, $I1_B$ in the two interferometric channels in the middle, respectively. The *third column* gives an estimate of the photometric fluxes $I1_A$+$I1_B$ and $I2_A$+$I2_B$ in the interferometric channels, while the *fourth column* gives the geometric mean images $\sqrt{I1_A I1_B}$ and $\sqrt{I2_A I2_B}$ (uncorrelated fluxes).

This process can be described as

$$\begin{aligned} \mathrm{I1}_A(\lambda) &= \mathrm{I1/PA}(\lambda) \cdot \mathrm{PA}(\lambda) \cdot \mathrm{PSF}_{\mathrm{I1}} && (4.4)\\ \mathrm{I1}_B(\lambda) &= \mathrm{I1/PB}(\lambda) \cdot \mathrm{PB}(\lambda) \cdot \mathrm{PSF}_{\mathrm{I1}} && (4.5)\\ \mathrm{I2}_A(\lambda) &= \mathrm{I2/PA}(\lambda) \cdot \mathrm{PA}(\lambda) \cdot \mathrm{PSF}_{\mathrm{I2}} && (4.6)\\ \mathrm{I2}_B(\lambda) &= \mathrm{I2/PB}(\lambda) \cdot \mathrm{PB}(\lambda) \cdot \mathrm{PSF}_{\mathrm{I2}}\,, && (4.7) \end{aligned}$$

where $\mathrm{I1}_A$, $\mathrm{I1}_B$, $\mathrm{I2}_A$ and $\mathrm{I2}_B$ are the predicted images of PA and PB in channel I1 and I2. In this step, each image is multiplied by the previously obtained photometric $\mathrm{PSF}_{\mathrm{I1}}$ or $\mathrm{PSF}_{\mathrm{I2}}$ (Section 4.2.1) as well. This produces a very sharp image, but introduces additional errors, since the correct overlap cannot always be achieved perfectly. The left two columns in Figure 4.10 show the predicted photometric spectra in the interferometric channels.

For the estimation of the instrumental photometric flux the predicted images in each channel are summed. The resulting $\mathrm{I1}_A$+$\mathrm{I1}_B$ and $\mathrm{I2}_A$+$\mathrm{I2}_B$ images are shown in the third column of Figure 4.10. The actual instrumental photometric spectrum is obtained by averaging the result from both channels and applying the corresponding PSF to each wavelength column. The final instrumental photometric spectrum $I_{\mathrm{inst}}(\lambda)$ is shown in Figure 4.13a (page 93) for the target and calibrator example.

The uncorrelated flux in each interferometric channel is instead given by the geometric mean images $\sqrt{\mathrm{I1}_A\mathrm{I1}_B}$ and $\sqrt{\mathrm{I2}_A\mathrm{I2}_B}$ (cf. equation 3.11). This accounts for inequalities in each image. The geometric mean images are optionally corrected for lost fine spectral structure data. This is sometimes necessary due to the poor optics of the photometric channels and a therefore poorer spectral resolution in the corners of the detector.

4.2.2.2 Correlated Flux and Differential Phase

After determining the uncorrelated flux in the previous section, the next step is the calculation of the correlated flux. Its determination is very similar to the `HIGH-SENS` case and uses the same subroutine `midiVisPipe`. Only the last steps are different. In principle, for each frame the real delay, originating from the known scanning process and the unknown atmospheric contribution, is determined. This is used to de-rotate each frame in order to coherently add all frames. With this approach a high signal to noise ratio for the correlated flux spectrum can be achieved. This is described in the following in detail.

The first step is to compress the interferometric data in each interferometric channel. This is done with the subroutine `oir1dCompressData`. The signal in each of the 3900 frames is multiplied by the corresponding mask shown in Figure 4.9. The masks act as spatial weighting functions. They suppresses the noise signal above and below the spectrum. After applying the masks the pixels values along the direction perpendicular to the dispersion are summed up to get one dimensional spectra. After this, all spectra are stacked together to get a two dimensional image with frame number in horizontal direction (equivalent to a time direction) and wavelength in vertical direction.

In the second step, the subroutine `oirFormFringes` is used to subtract the two interferometric channels from each other. Since the two channels are 180° out of phase, the amplitude of

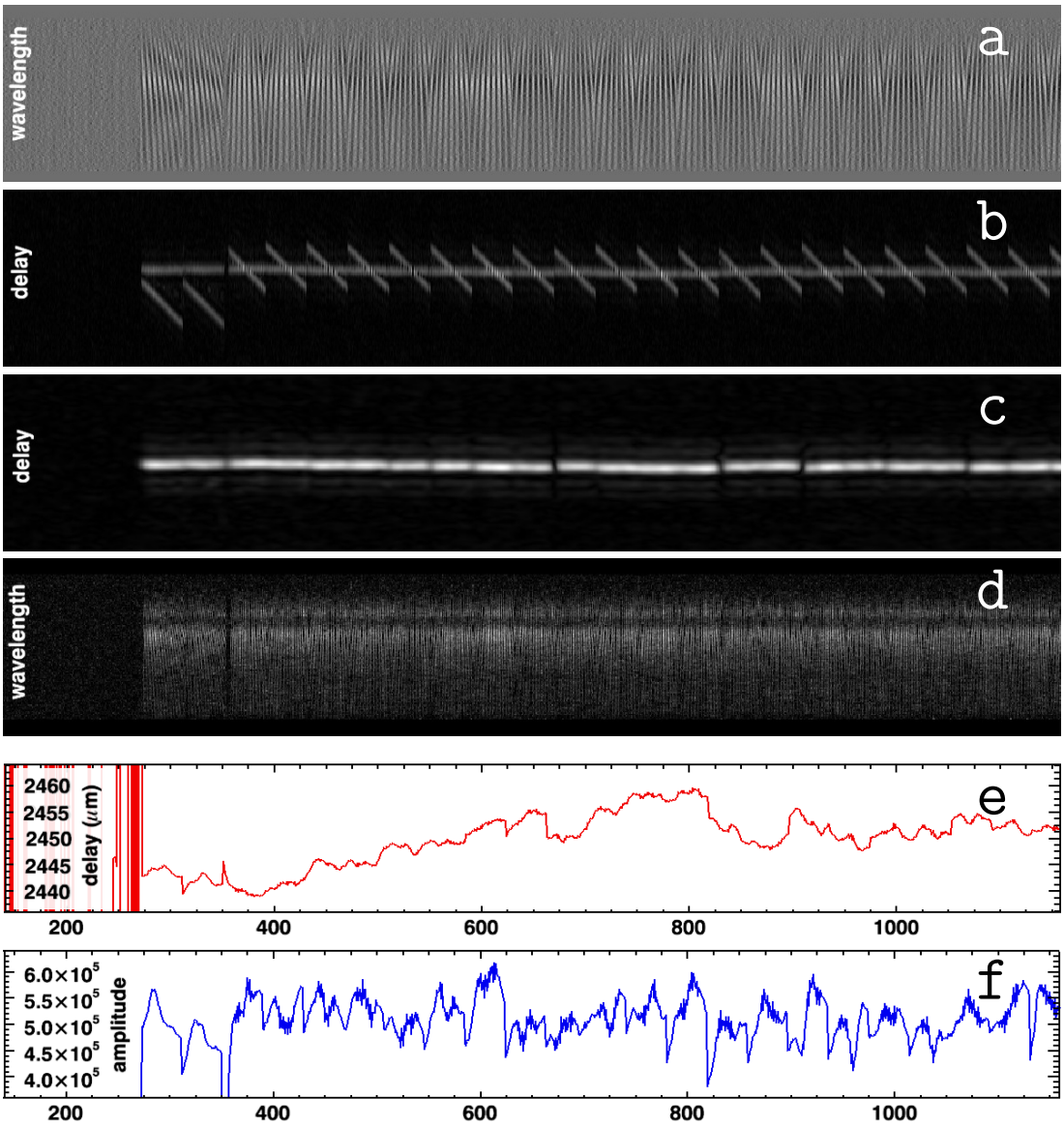

Figure 4.11: Steps in the group delay analysis. Shown are about 1000 frames. The first 100 frames correspond to the large OPD offset part. All graphs are plotted over frame number, which is equivalent to a time axis (1 frame ≡ 18/36 ms [PRISM/GRISM]). *a:* Stacked interferograms after compression, subtraction and high pass filtering. The vertical direction corresponds to the wavelength (fringes are dispersed). *b:* Delay function of the fringe packets. The movement of the peak, modulated by twice the instrumental delay, can be seen clearly, while the peak with the remaining atmospheric delay stays almost constant. *c:* In time direction smoothed version of *b*. The unwanted sideband is strongly suppressed, while the other peak remains. *d:* Absolute value of the fringe spectra after removal of instrumental delay, atmospheric delay and the constant phase shift by refraction of water vapor. *e and f:* The determined atmospheric delay, d_{atm}, and peak amplitude from *c* as function of frame number.

the spectrally dispersed fringes double, while most of the remaining background is removed (about 90%). This assumes that the wavelength channels are sufficiently aligned. At this point, a high-pass filter (boxcar filter) is applied as well. The remaining sky and instrumental

background varies very slowly[14] compared to the fringes. By smoothing the values along the frame number direction, and subtracting this smoothed version from the original version, the residual background can be highly suppressed. The default smooth value is 50 frames, which is acceptable for stable atmospheric conditions and strong sources. Only for very weak sources and fast varying background the value should be set lower. It is important to note that a too low value could remove some of the interferometric signal, which would result in a lower signal-to-noise ratio. The same value has to be used for the calibrator and target.

The output of these steps is displayed in Figure 4.11a. About 1000 frames are shown. The first 100 frames are the part where the OPD is offset by a large amount and where therefore no fringes are recorded. The MIDI scans of the fringes (about 22 are shown) over zero OPD is also clearly visible by the changing structure of the wavelength dependent fringe pattern. At zero OPD the fringes at all wavelengths are at their maximum (if the source phase is zero and no relative atmospheric dispersion is introduced). Except for the first two scans this happens always in the middle of each scan (scan length is now 39 frames).

As shown in equation 3.37, this output can be described as

$$I_{\mathrm{int}} = 2\sqrt{f_A f_B}\ |\mathcal{V}(k)|\ \sin\left(k d_{\mathrm{tot}} + \varphi\right), \tag{4.8}$$

with $\mathcal{V}(k)$ the unnormalized complex visibility and $f_{A,B} = I_{A,B}/(I_A + I_B)$. The delay $d_{\mathrm{tot}} = d_{\mathrm{ins}} + d_{\mathrm{atm}}$ is composed of the known instrumental delay $d_{\mathrm{ins}} = d = d_{\mathrm{A}} - d_{\mathrm{B}} + \vec{s}\vec{B}$ and the unknown atmospheric delay d_{atm}. The differential phase $\varphi = \varphi_{\mathrm{s}} + \varphi_{\mathrm{i}} + \varphi_{\mathrm{a}}$ consists of the desired source phase φ_{s}, the unknown instrumental phase φ_{i} and the also unknown atmospheric phase φ_{a}, which originates mainly from water vapor. The phase terms are in general wavelength dependent as well.

In order to remove the instrumental OPD, d_{ins}, each frame is multiplied by $\exp\left(-ikd_{\mathrm{ins}}\right)$,

$$I_{\mathrm{rot}} = I_{\mathrm{int}}\, e^{-ikd_{\mathrm{ins}}} \tag{4.9}$$

$$= 2\sqrt{f_A f_B}\ |\mathcal{V}(k)|\ \frac{1}{i}\ \left(e^{ikd_{\mathrm{atm}}+i\varphi} - e^{-ik(d_{\mathrm{atm}}+2d_{\mathrm{ins}})-i\varphi}\right), \tag{4.10}$$

with the subroutine `oirRotateInsOPD`. This operation corresponds to a rotation in the complex plane with the result that I_{rot} is now complex data. In the first exponential function the instrumental term is removed, while it is with a factor of two present in the second. The group delay can be determined from these data by Fourier transform from the frequency domain to the delay domain (Lawson et al., 2000b). The delay function $F(D)$, calculated with the subroutine `oirGroupDelay`, is then given by

$$F(D) = \int I_{\mathrm{rot}}\, e^{-ikD}\mathrm{d}k \tag{4.11}$$

$$= 2\sqrt{f_A f_B}\ |\mathcal{V}(k)|\ \frac{1}{i}\ \left[\delta(d_{\mathrm{atm}} - D)e^{i\varphi} - (d_{\mathrm{atm}} + 2d_{\mathrm{ins}} + D)e^{-i\varphi}\right]. \tag{4.12}$$

This is true for an infinitely broad band and a constant visibility over the wavelength range. With a finite band or a variable visibility the delta peaks will be broader and will depend on the form of $\sqrt{f_A f_B}\ |\mathcal{V}(k)|$.

[14] The variation is on the order of the coherence time of about 1 to 2 seconds.

Since the MIDI beam-combiner has only two output phases, it is essentially a cosine correlator, meaning that the group delay has two peaks. The absolute value of the delay function is shown in Figure 4.11b. Visible are two bright peaks in each frame. One of them is almost stationary with frame number due to only small changes in the delay, $d_{\rm atm}$, introduced by the atmosphere. The other peak oscillates rapidly due to the modulation of the instrumental delay, $2d_{\rm ins}$, with the MIDI piezo mirrors. Variations in the overall amplitude are mainly caused by drifts in the image overlap of the two telescopes.

The unwanted sideband is strongly suppressed and the other peak remains if the data are smoothed in time direction. In addition, the signal to noise is increased as can be inferred from Figure 4.11c. The smoothing is performed with a Gaussian kernel with a sigma set to a default value of 4 frames. For weak sources and stable atmospheric conditions this value should be chosen higher, but should not exceed the coherence time. The position of the remaining peak (basically the brightest spot in delay direction of each frame) corresponds to the atmospheric delay. Figure 4.11e and f shows the determined group delay $d_{\rm atm}$ and peak amplitude as function of frame number, respectively. With this information, the instrumental and atmospheric delay can be removed from the original interferometric signal in the following.

In `HIGH-SENS` (HS) mode the differential interferometric output of equation 4.8 is de-rotated via

$$I_{\rm rot,HS} = I_{\rm int}\, e^{-ik(d_{\rm ins}+d_{\rm atm})} \tag{4.13}$$

$$= 2\sqrt{f_A f_B}\ |\mathcal{V}(k)|\ \frac{1}{i}\ \left(e^{i\varphi} - e^{-i2k(d_{\rm atm}+d_{\rm ins})-i\varphi}\right) \tag{4.14}$$

by the subroutine `oirRotateGroupDelay`. In addition, the linear phase shift, induced by the varying index of refraction of water vapor, $\varphi_{\rm a} = a\lambda + b$, is estimated and eliminated as well by subtracting it from the complex visibility. The result is shown in Figure 4.11d. After rejecting frames with too large optical path differences or large group delay jumps the remaining data are averaged coherently along the time direction with the subroutine `oirAverageVis`. This suppresses the rapidly varying second exponential term again and gives the correlated flux spectrum $I_{\rm corr}$,

$$I_{\rm corr,HS} = |I_{\rm coh=avg}| \tag{4.15}$$

$$= |2\sqrt{f_A f_B}\ \mathcal{V}(k)\ \frac{1}{i}\ e^{i\varphi_{\rm inst}}| \tag{4.16}$$

$$= 2\sqrt{f_A f_B}\ |\mathcal{V}(k)|\,, \tag{4.17}$$

and the differential phase, $\varphi_{\rm inst}(\lambda)$, corrected for water vapor. The remaining differential phase still includes the instrumental phase in addition to the true source phase. The differential instrumental phase $\varphi_{\rm inst}(\lambda)$ is the only final result used in this step and is shown in Figure 4.13c (page 93) for the target and calibrator example.

In `SCI-PHOT` (SP) mode the calculation of the correlated flux is done in a different way. The instrumental and atmospheric delay is removed from the original uncompressed interferometric data for each interferometric channel *separately*. The subroutine `oirFormFringes` applies to each pixel value of all 3900 unchopped interferometric images the high pass filter in order to suppress the sky and instrumental background not removed by the unchopping. It also

eliminates any constant interferometric source terms (cf. equation 3.19). At this point no advantage is taken from the 180° phase shift between both channels.

Each image is then de-rotated with `oirRotateGroupDelay`, i.e. each pixel of each image is multiplied with $\exp[-ik(d_{\rm ins} + d_{\rm atm})]$. The interferometric output is thus given for each channel by

$$I_{\rm rot,1,SP} = -\sqrt{f_A f_B}\ |\mathcal{V}(k)|\ \frac{1}{i}\ \left(e^{i\varphi} - e^{-i2k(d_{\rm atm}+d_{\rm ins})-i\varphi}\right) \text{ and} \quad (4.18)$$

$$I_{\rm rot,2,SP} = +\sqrt{f_A f_B}\ |\mathcal{V}(k)|\ \frac{1}{i}\ \left(e^{i\varphi} - e^{-i2k(d_{\rm atm}+d_{\rm ins})-i\varphi}\right), \quad (4.19)$$

respectively. The linear phase shift due to water vapor is eliminated using its determination from the previous `HIGH-SENS` step.

The coherent averaging is performed with the subroutine `oirMeanRMS` in order to obtain a two-dimensional map of the correlated flux in each interferometric channel. The correlated flux images are calculated from the coherently averaged maps via

$$I_{\rm corr,1,SP} = |I_{\rm coh=avg}| = \sqrt{f_A f_B}\ |\mathcal{V}(k)| \text{ and} \quad (4.20)$$

$$I_{\rm corr,2,SP} = |I_{\rm coh=avg}| = \sqrt{f_A f_B}\ |\mathcal{V}(k)|, \quad (4.21)$$

respectively. Figure 4.12 shows the real and imaginary parts of the coherently averaged images. In the ideal case, each interferometric channel contains the same total correlated flux, which is half the amount of the combined correlated flux of the `HIGH-SENS` mode.

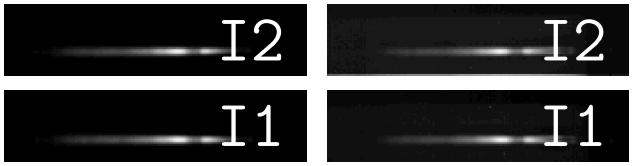

Figure 4.12: Coherent averaged images. *Left* the real and *right* the imaginary parts of the coherently averaged image for each interferometric channel.

The final step is the estimation of the instrumental visibility from the correlated flux ($I_{\rm rot,1,SP}$ and $I_{\rm rot,2,SP}$) and the uncorrelated flux ($\sqrt{\mathrm{I1}_A \mathrm{I1}_B}$ and $\sqrt{\mathrm{I2}_A \mathrm{I2}_B}$, calculated in Section 4.2.2.1). For each wavelength bin λ[15] and each interferometric channel the subroutine `spVis` calculates the instrumental visibility via

$$V_{\rm inst,1}(\lambda) = \frac{I_{\rm corr,1,SP}(\lambda)}{\sqrt{\mathrm{I1}_A(\lambda)\ \mathrm{I1}_B(\lambda)}} \text{ and} \quad (4.22)$$

$$V_{\rm inst,2}(\lambda) = \frac{I_{\rm corr,2,SP}(\lambda)}{\sqrt{\mathrm{I2}_A(\lambda)\ \mathrm{I2}_B(\lambda)}}, \quad (4.23)$$

respectively. In other words, the routine searches for the number which when multiplied by the geometric mean PSF profile of a specific wavelength bin, best fits the correlated signal

[15]The pixel column perpendicular to the dispersion direction, i.e. the vertical direction in Figure 4.12.

PSF profile in the corresponding wavelength bin. The subroutine removes a potential linear background in the uncorrelated flux as well. Both instrumental visibility spectra are then averaged. The final instrumental visibility spectrum, $V_{\rm inst}(\lambda)$, is shown in Figure 4.13e (page 93) for the target and calibrator example.

4.2.3 Photometry, Phase and Visibility Calibration

In the previous sections the instrumental photometry $I_{\rm inst,tar/cal}(\lambda)$ (page 86), instrumental differential phase $\varphi_{\rm inst,tar/cal}(\lambda)$ (page 89) and instrumental visibility $V_{\rm inst,tar/cal}(\lambda)$ (page 91) were estimated for the target (tar) and the calibrator (cal). They are shown in the left column of Figure 4.13. The calibrated quantities for the target are calculated by spCalVis processing the quantities obtained for the calibrator. In order to do this, the flux and angular size of the calibrator has to be known. Both are listed in Table 4.3 (page 74) for the calibrators used in this study. The calibration technique presumes that the instrument behaves very similarly for the target and calibrator observations.

The calibrated flux is estimated by assuming that the spectrum of the calibrator looks close enough to the Rayleigh-Jeans part of a blackbody. With the known flux of the calibrator, $F_{10\mu{\rm m,cal}}$ at 10 μm, e.g. obtained from an IRAS 12 μm flux measurement by scaling with $(12/10)^2$, the calibrated flux is given by

$$I_{\rm calib,tar}(\lambda) \;=\; F_{10\,\mu{\rm m,cal}} \left(\frac{10}{\lambda}\right)^2 \frac{I_{\rm inst,tar}(\lambda)}{I_{\rm inst,cal}(\lambda)}\,. \tag{4.24}$$

If the complete N-band spectrum for the calibrator is known, e.g. from ISO[16] data or a template spectrum database like the one of Cohen et al. (1999), it can be directly scaled up without assuming a Rayleigh-Jeans law. The large flux difference between target and calibrator, and the described difficulties to remove the background reliably for AT observations, results in a uncertainty for the calibrated flux of about 30%. In particular beyond 12 μm, difficulties in the calibration process are notable. In this range, the flux of the calibrator gets too low. Figure 4.13b shows the calibrated flux spectrum for the example.

The instrumental differential phase of the target still includes phases introduced by the instrument. In order to extract the true target phase the instrumental differential phase of the calibrator is subtracted from it. It assumes that the calibrator has no intrinsic phase, i.e. the brightness distribution of the calibrator is point-symmetric. The target phase is then given by

$$\varphi_{\rm calib,tar}(\lambda) \;=\; \varphi_{\rm inst,tar}(\lambda) - \varphi_{\rm inst,cal}(\lambda) \bmod 360^\circ. \tag{4.25}$$

An example of $\varphi_{\rm calib,tar}(\lambda)$ is shown in Figure 4.13d. Two important facts influence the accuracy of this measurement. First, the linear fit to the index of refraction of water vapor does not remove its contribution completely. Second, the water vapor content in the atmosphere varies between target and calibrator observation too fast so that it cannot be assumed constant. Therefore, deviations of 20° to 30° around zero are expected due to these facts. Thus, the existence of a non-zero target phase should be only considered if $\varphi_{\rm calib,tar}(\lambda)$ is larger than 40°.

[16] http://iso.esac.esa.int/ and Kessler et al. (1996)

The visibility of the target can be calculated with the transfer function $V_{\mathrm{TF}}(\lambda)$, obtained from the calibrator measurement. If the calibrator is resolved by the interferometer, i.e. if its theoretical visibility, $V_{\mathrm{theo,cal}}$, is not equal 1, the transfer function has to be corrected. By assuming a wavelength independent uniform disk diameter for the calibrator (cf. equation 3.57), the transfer function can be calculated via

$$V_{\mathrm{TF}}(\lambda) \;=\; \frac{V_{\mathrm{inst,cal}}(\lambda)}{V_{\mathrm{theo,cal}}(\lambda)}\,. \tag{4.26}$$

The true visibility spectrum of the object is then simply given by

$$V_{\mathrm{calib,tar}}(\lambda) \;=\; \frac{V_{\mathrm{inst,tar}}(\lambda)}{V_{\mathrm{TF}}(\lambda)} \;=\; V_{\mathrm{theo,cal}}\,\frac{V_{\mathrm{inst,tar}}(\lambda)}{V_{\mathrm{inst,cal}}(\lambda)}\,. \tag{4.27}$$

Typical uncertainties are on the order of 10%. This is mainly due to the mentioned difficulties of the background determination and removal during the calculation of the uncorrelated flux. Thus, the photometry is the most limiting factor in getting good visibilities for AT observations. However, with an improved reduction, which would make it necessary to invest more time in improving the reduction software, visibility errors of less than 10% should be possible in `SCI-PHOT` mode even with ATs, exceeding the performance of `HIGH-SENS` observations.

The calculation of a reliable error for an individual observation is a difficult issue. A widely used way is to calibrate the target with several calibrators and look at the scatter of the results. This requires that several calibrators were observed in the same mode with similar air masses and atmospheric conditions. This is in most cases not completely fulfilled and therefore the visibility errors in the next chapter should be considered as indicative values.

Figure 4.13f shows the calibrated visibility for the example. It can be noticed again that beyond 12 μm the visibility of the calibrator exhibits a random behavior due to the low signal to noise ratio in this range. This happens for most of the calibrators used in this study. It shows sometimes even large spikes or visibilities far from being physical. For this reason the wavelength range between 12 and 13 μm is excluded for the model fitting and interpretation in this study.

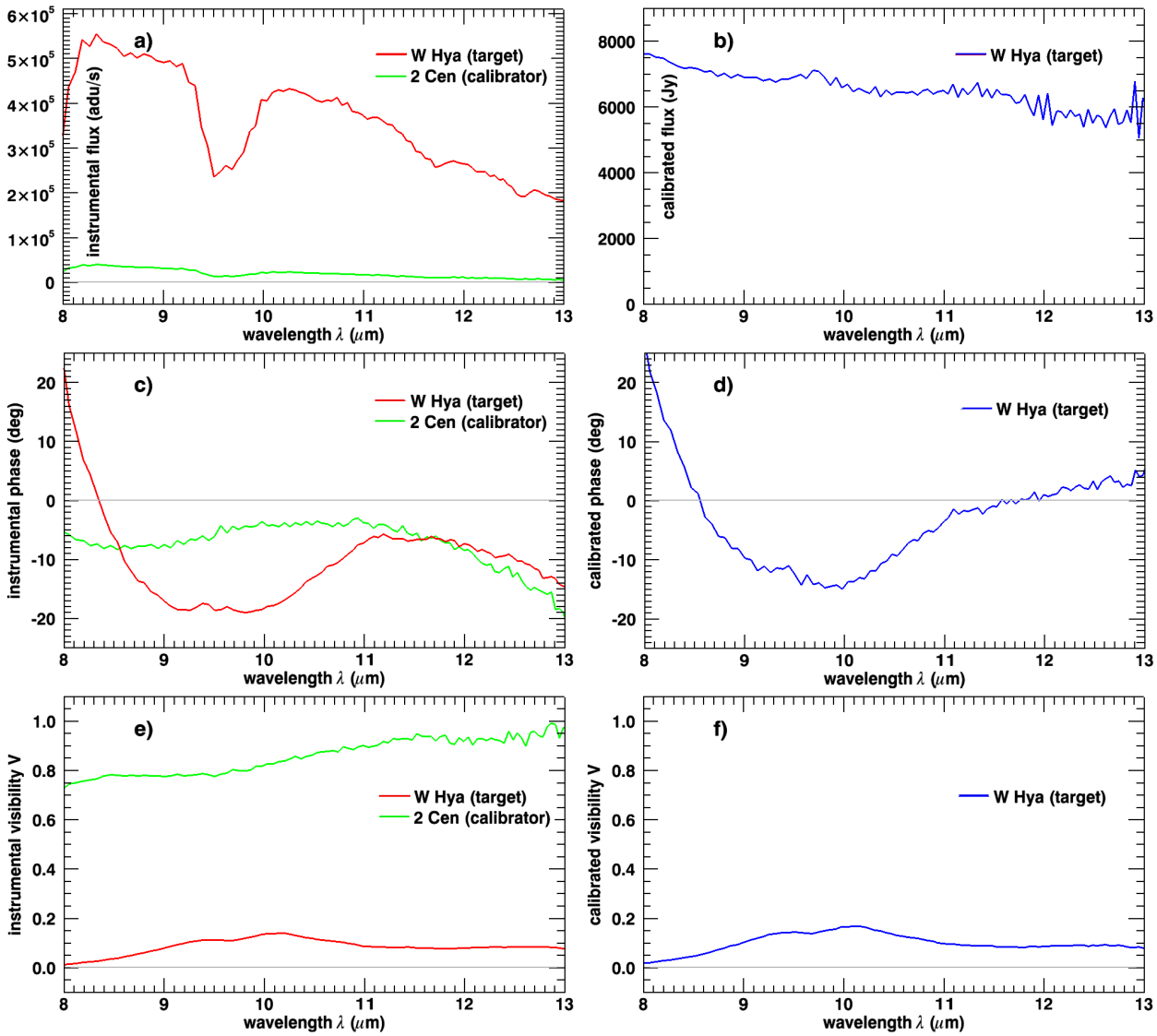

Figure 4.13: Instrumental *(left column)* and calibrated *(right column)* photometry, differential phase and visibility *(from top to bottom)*. The results shown are from observations of W Hya and 2 Cen (2009-04-24). *a and b:* The telluric ozone feature is clearly visible in the spectrum at around 9.8 μm. It almost disappears after the calibration. *c and d:* The remaining large phase shifts due to water vapor are clearly visible. No intrinsic target phase can be extracted here. *e and f:* Clearly, the target is resolved over the whole N-band, i.e. the visibility is below one.

Chapter 5

Results and Modeling

This chapter presents the light curves, spectra and visibilities as well as the results of the different visibility models applied to each of the five observed stars. The results of the visibility modeling are discussed in the next chapter.

5.1 Light Curves and Spectra

5.1.1 Light Curves

In order to assign a pulsation phase to the observations, visual data from the American Association of Variable Star Observers (AAVSO[1]) and the All Sky Automated Survey (ASAS[2], Pojmanski et al., 2005) are used. After binning the AAVSO data into 10 day bins a simple sinusoid[3] is fitted to the AAVSO and ASAS data set over a period of about ten years ($2000-2010$). The resulting periods P, Julian Dates of maximum brightness T_0 (defined as phase 0.0), mean visual magnitudes V_0 and visual semi-amplitudes $V_{\rm ampl}$ are given in Table 5.1. The given errors are estimates evaluated from the fitting process. The uncertainties for T_0 and V_0 are of the same order as the uncertainties for the period and the semi-amplitude, respectively. Note that V Hya has two periods and the longer period is taken from Knapp et al. (1999).

Table 5.1: Visual light curve data.

Target	P days	T_0 JD	V_0 mag	$V_{\rm ampl}$ mag
R Aql	271 ± 4	2452910	8.30	1.80 ± 0.15
R Aqr	390 ± 5	2452480	8.75	2.75 ± 0.20
R Hya	374 ± 5	2453231	6.95	1.95 ± 0.15
V Hya	529 ± 10	2450045	8.50	1.50 ± 0.10
	6160 ± 400	2446937	8.50	3.50 ± 0.50
W Hya	388 ± 5	2452922	7.56	1.41 ± 0.10

For each star the photometric data as well as the fit is plotted in figures 5.1 to 5.5 versus time and versus visual phase, covering the period of the MIDI observations. The MIDI observations are included as tick marks above the curve, color-coded by phase in the upper panel and position angle in the lower panel. This allows to recognize different distributions of position

[1] http://www.aavso.org/
[2] http://www.astrouw.edu.pl/asas/
[3] $V(t) = V_{\rm ampl} \sin[2\pi(t - T_0)/P] + V_0$

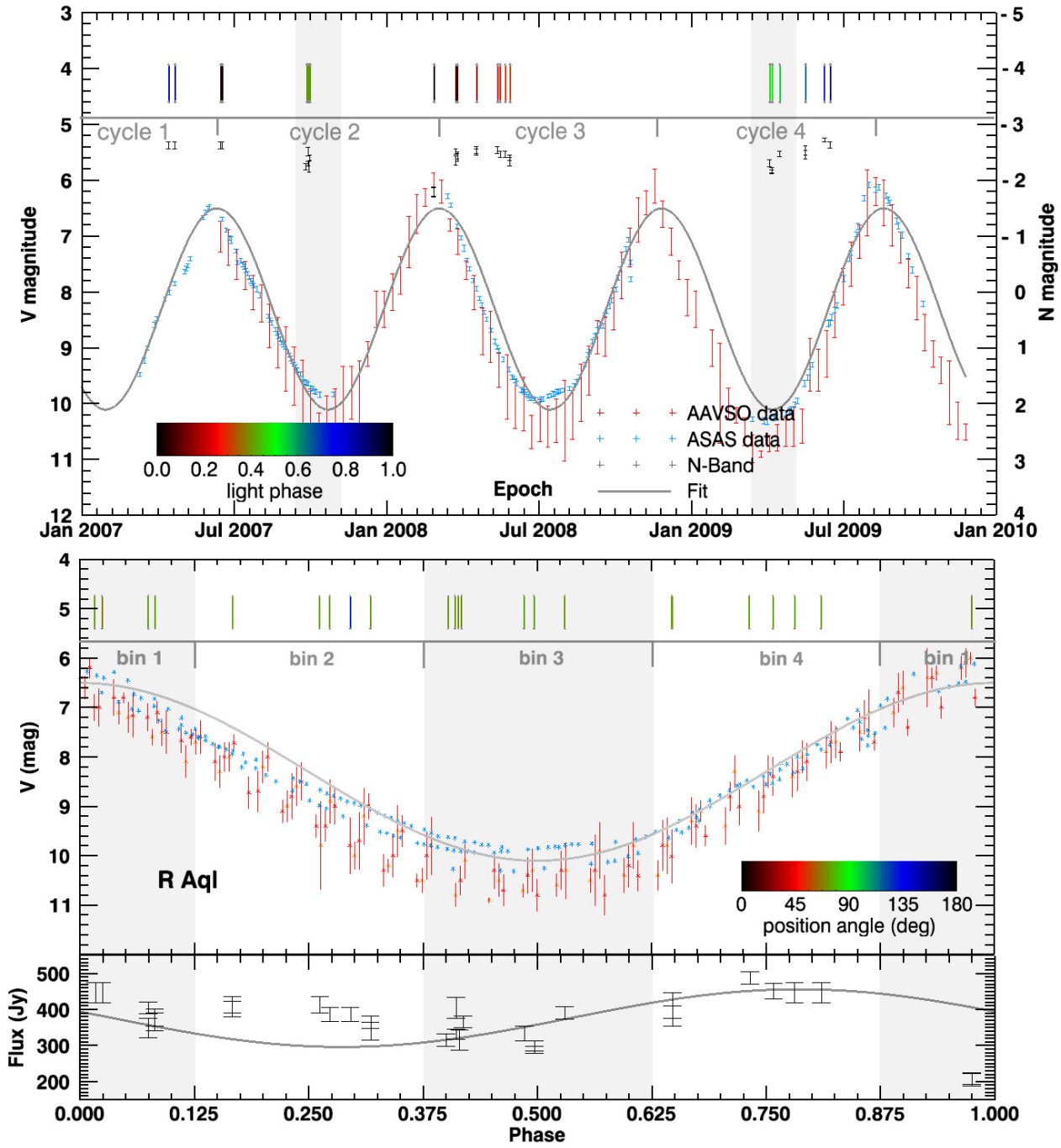

Figure 5.1: The visual light curve of R Aql. *Top:* Plotted against time. *Bottom:* Plotted against visual phase. In addition, the lower panel shows the flux obtained with MIDI at around 12 μm. See text.

angles throughout the pulsation cycle. The N-band magnitude[4] is shown directly below the tick marks with the magnitude scale given on the right in the upper panel. The data within the shaded regions are used for cycle-to-cycle and intracycle studies.

[4]Only the flux in the wavelength range between 11.5 and 12.5 μm is averaged and converted to magnitudes.

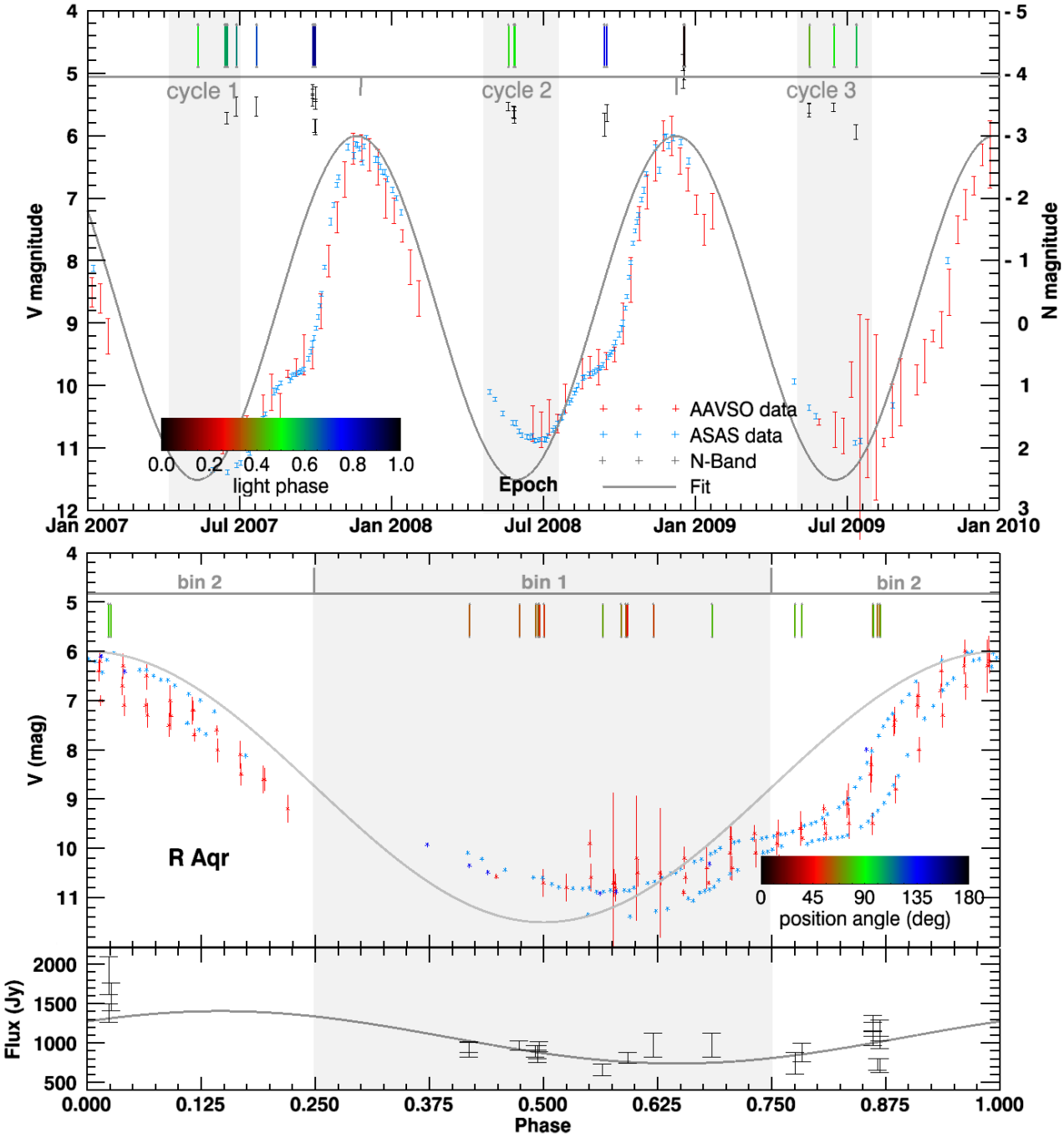

Figure 5.2: Same as Figure 5.1 except for R Aqr.

In addition, the mid-IR fluxes obtained with MIDI are shown in the lower panels. Only the averaged flux between 11.5 and 12.5 μm is plotted in order to be comparable with observations made with other instruments. As mentioned in the previous chapter, the MIDI fluxes are strongly error-prone due to difficulties in the reduction removing instrumental imperfections, and the large sky background which is varying on short time scales. For this reason, the errors are assumed to be high. However, a clear phase dependence is detectable in each of the phase-

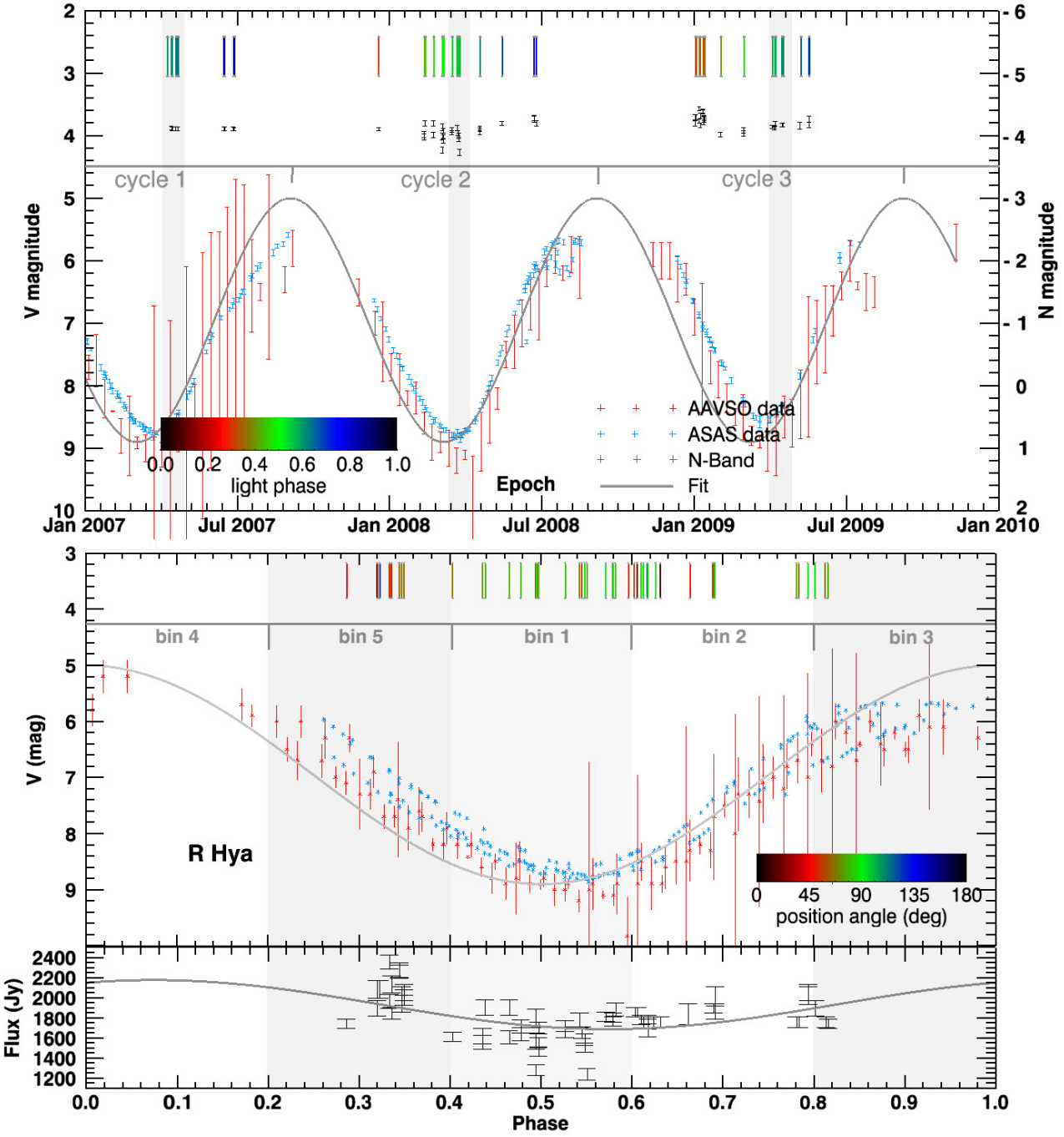

Figure 5.3: Same as Figure 5.1 except for R Hya.

folded plots. The results of the fits are summarized in Table 5.2. The table gives the relative phase shifts of the mid-IR maximum with respect to the visual light curves, the mean N-band fluxes N_0 and the semi-amplitudes N_{ampl}.

Even if the mid-IR amplitudes are much smaller than the visual ones (cf. the visual magnitudes in the upper plots), flux variations are still on the order of 10% to 30% for the Mira variables in this sample. The Mira R Aqr and the semiregular variable V Hya, which is the only C-rich

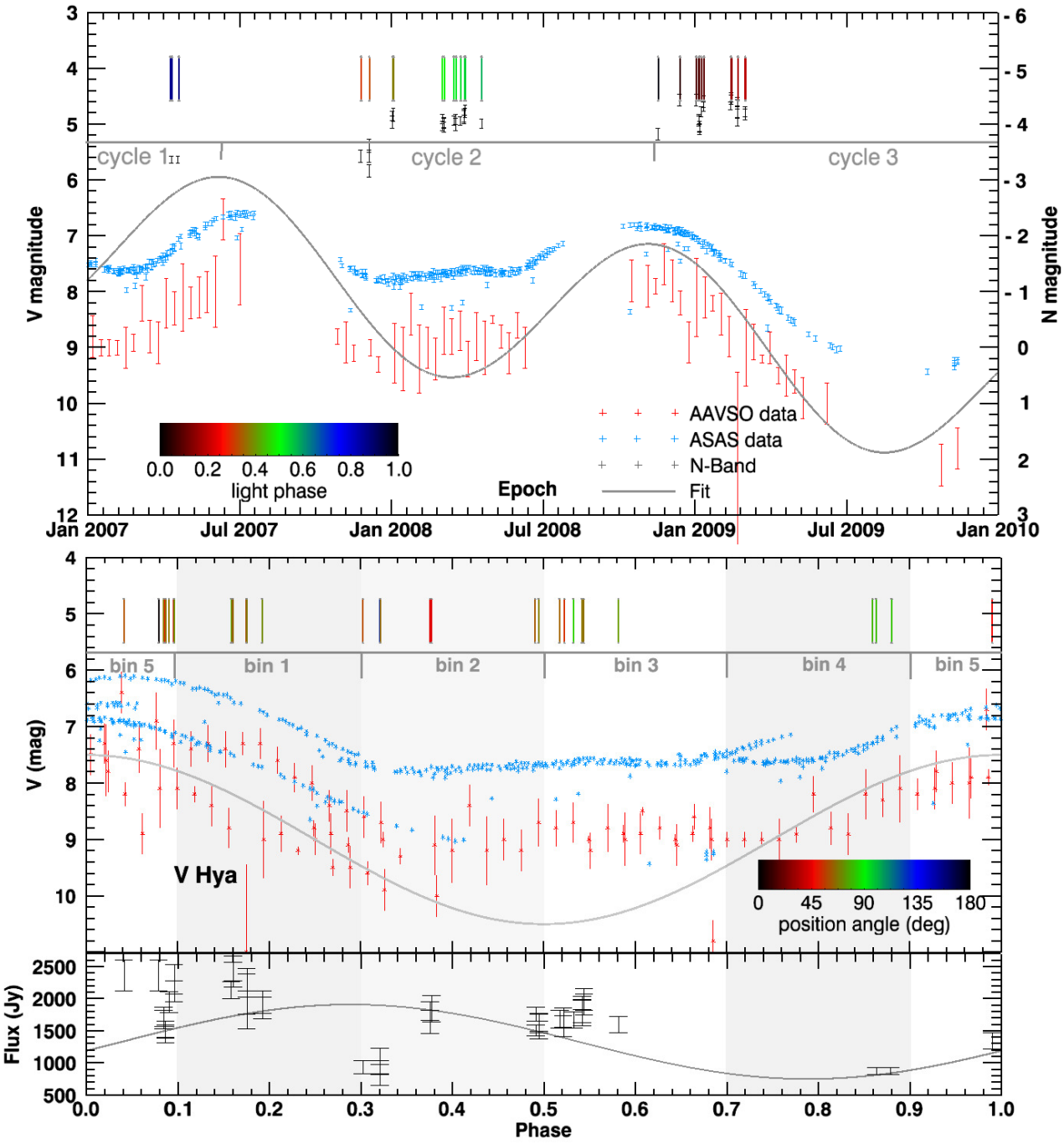

Figure 5.4: Same as Figure 5.1 except for V Hya.

star in the sample, show the highest amplitudes. Both systems are close binary systems and contain a large amount of circumstellar material. This might be the reason for their large amplitudes (see also below). Except for R Aql, the mid-IR maximum[5] occurs always after the visual maximum at on average phase 0.15 ± 0.05, which is consistent with observations of other AGB stars (e.g. Smith et al., 2006, and references therein). This is understandable since the

[5]The mid-IR flux is the sum of the mid-IR radiation of the star and the circumstellar dust.

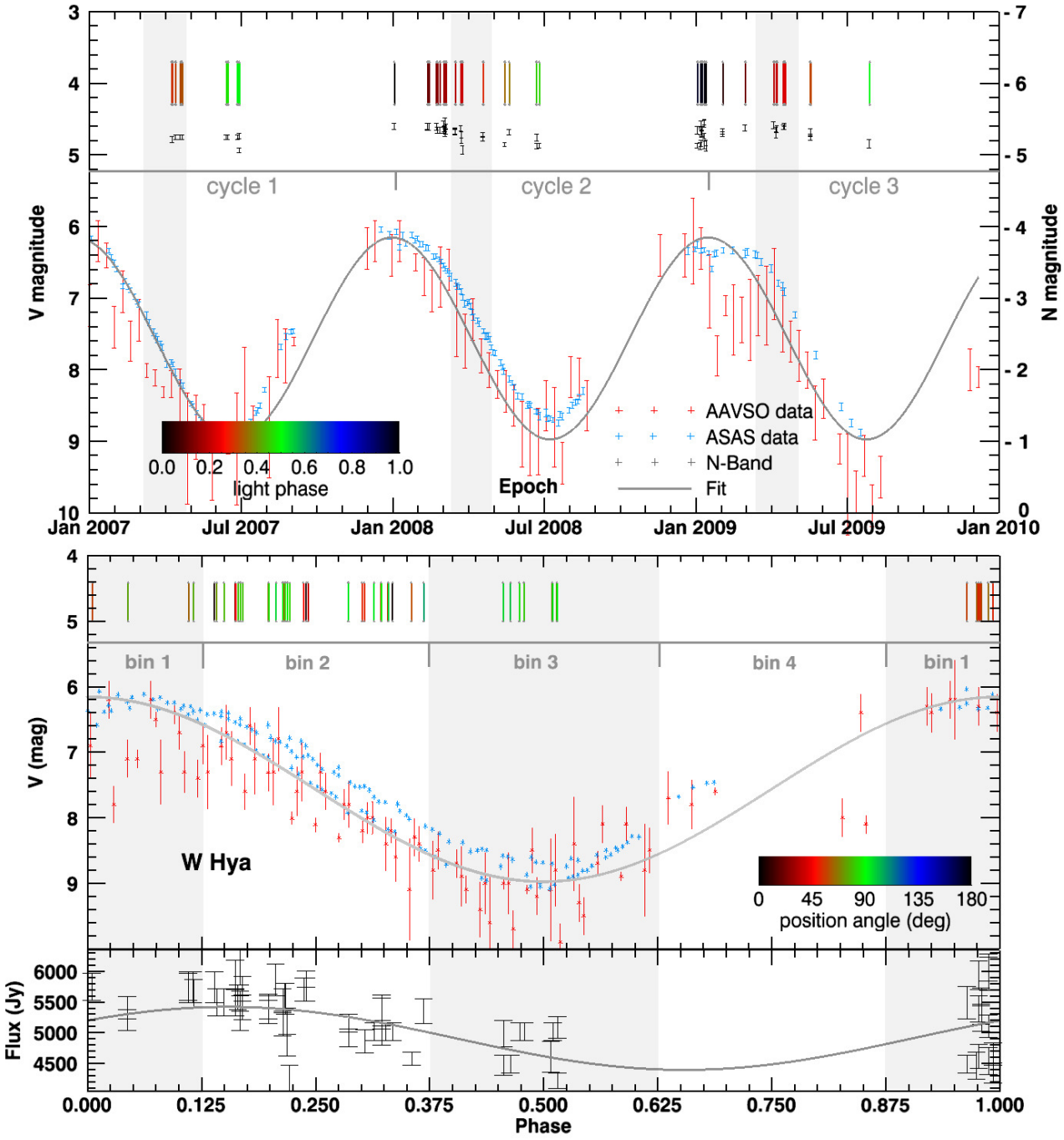

Figure 5.5: Same as Figure 5.1 except for W Hya.

dust needs time to heat up in order to radiate at thermal wavelengths. Nevertheless, the AT photometric accuracy of MIDI is very low. Therefore, these values should be taken with care and the trends should only be seen as indicative. For this reason, all data are interpreted with respect to the visual light curve instead of the mid-IR light curve. It should also be kept in mind that folding consecutive cycles into one cycle might not always be appropriate, since the pulsation is not strictly regular. The non-regularity can clearly be inferred from the plots. In

Table 5.2: MIDI mid-IR light curve data.

Target	phase shift	N_0 Jy	$N_{\rm ampl}$ Jy
R Aql	-0.21 ± 0.05	377 ± 50	80 ± 50 (21%)
R Aqr	$+0.15 \pm 0.05$	1080 ± 100	330 ± 50 (31%)
R Hya	$+0.08 \pm 0.05$	1930 ± 200	240 ± 50 (12%)
V Hya	$+0.29 \pm 0.05$	1330 ± 200	580 ± 200 (44%)
W Hya	$+0.15 \pm 0.05$	4910 ± 200	510 ± 100 (10%)

addition, cycle-to-cycle variations may have influences as well.

However, similar flux variations have been reported for other AGB stars by Ohnaka (private communication; preliminary results for R Car, R Cnc and Z Pub) and Karovicova (private communication; preliminary result for RR Aql) for MIDI AT observations, and by Wittkowski et al. (2007) (O-rich Mira S Ori) and Ohnaka et al. (2007) (C-rich Mira V Oph) for MIDI UT observations. Therefore, three conclusions can be drawn. First, mid-IR flux variations are common and are not negligible. Second, these variations are even detectable with MIDI AT observations. Third, the flux amplitude is related to the dust content in the system, i.e. it is probably connected to the mass loss rate as well.

R Aql: R Aql shows only a very small variation in the mid-IR by eye, suggesting that the amplitude could be overestimated, and it is even consistent with no variation at all. This is probably the reason why a mid IR maximum before the visual maximum is obtained. Due to the paucity of data points, which are spread over four pulsation cycles, the folding into one cycle might smear out the true mid-IR flux variation as well. However, the data cover the whole pulsation cycle and intracycle variations will be investigated, even if cycle-to-cycle comparison is difficult for this target. Observations are always done at almost the same position angle implying that asymmetries cannot be analyzed.

R Aqr: The data for R Aqr are sparsely sampled over the three consecutive cycles as well, but cycle-to-cycle studies will be possible. On the other hand, the observations at the same phase during each cycle have the disadvantage that the phase coverage is unfavorable, and only two bins can be used for an intracycle analysis. The fit to the mid-IR light curve is robust and the flux variation of about 30% seems to be real. Even though the mass loss rate is low, the orbiting dust in this symbiotic system has probably also the effect of increasing the mid-IR flux amplitude. The observational constraints led to measurements at similar position angles preventing a study of asymmetries for this star.

R Hya: R Hya has a very smooth and regular visual light curve over the last decade. MIDI observations were only possible around minimum light, since the period of R Hya is close to one year and at maximum light the star is not observable from Paranal. As a result, the mid-IR light curve could not be well constrained and the observed flux variation is relatively small, only

on the order of 10%. However, this might be related to the present low mass loss rate as well. The unfavorable phase coverage has as additional consequence that effectively only 3 of the 5 phase bins can be used for intracycle studies. On the other hand, R Hya is a good target for cycle-to-cycle investigations. Position angles are well distributed, even over the phase, making a study of asymmetries feasible.

V Hya: Since V Hya displays two superimposed visual periods, an assignment of a visual phase is not an adequate description. Even if the short period is Mira-like the cause and influence of the long secondary period is unknown. Due to the fact that observations are not repeated at the same phase in consecutive cycles it is obvious that no cycle-to-cycle investigation can be done for this target. Since altogether the measurements are well distributed in phase an intracycle study will be conducted. The position angle distribution seems to be good, but the projected baselines are unfavorable. Thus, departures from symmetries cannot be analyzed properly.

The mid-IR fluxes vary with a high amplitude and a large scatter, resulting in a fit which is not very robust. Many aspects are probably the reason for the large and varying mid-IR flux. In C-stars the production of carbonaceous dust is more effective, and hence more material can be heated. The fact that V Hya is probably a common envelope system with a lot of surrounding dust provides an additional explanation. However, V Hya's evolutionary status as post AGB star, exhibiting the superwind phase with a fast and dense mass loss, might be the main reason for the varying mid-IR flux.

W Hya: Two things are notable here. First, the pulsation phase is not equally sampled due to the observability of the star and a pulsation period on the order of one year (this is also true for the AAVSO and ASAS sampling). Second, the position angles are not well distributed over the pulsation period. Around maximum light, position angles are approximately 45°, while around minimum light, position angles are approximately 90°. Only at intermediate phases the position angle distribution is more uniform. This will be important later while studying asymmetries and pulsation dependencies. The mid-IR and visual light curves are very stable with only moderate amplitudes. For the mid-IR, this might be related to the low mass loss rate, while for the visual it can be attributed to the early evolutionary stage[6]. Since W Hya and R Hya are fairly nearby, both stars have high absolute mid-IR fluxes.

5.1.2 Spectra

For all stars in the sample a spectral energy distribution (SED) plot is prepared in order to compare the measured mid-IR N-band spectra of MIDI with values in the literature. For each star, all obtained calibrated photometric MIDI spectra are median averaged and scaled with the 12 μm IRAS flux corrected for reddening effects (cf. equation 4.24). They are shown in figures 5.6 to 5.10. The uncertainties are given by the standard deviation. Even if this averaging over all pulsation phases and cycles might be questionable (at least for V Hya), it is not of importance here, since the spectra are not used for any modeling. In addition to

[6]Which on the other hand implies a low mass loss rate.

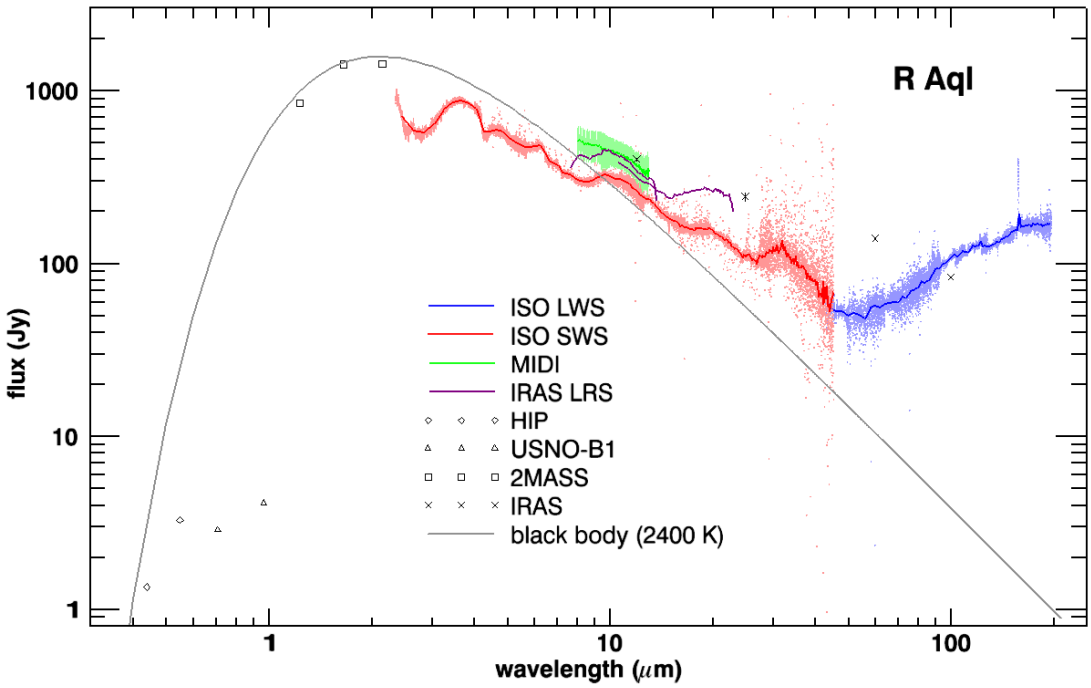

Figure 5.6: The spectral energy distribution of R Aql.

fully scientifically verified spectra from ISO[7] and IRAS[8], photometric data from HIPPARCOS, USNO-B1, 2MASS and IRAS, not corrected for reddening effects, are plotted as well. A blackbody curve is over-plotted as guidance. Due to the infrared excess, strong metallic oxide line and molecule absorption at shorter wavelengths, and dust extinction, it is not expected that a blackbody curve fits the spectral data in an appropriate way.

The Infrared Astronomical Satellite (IRAS), launched in 1983, was a spacecraft with a telescope mounted in a liquid helium cooled cryostat. The telescope had a focal length of 5.5 m and a 0.57 m aperture. The mirrors were made of beryllium and cooled to approximately 4 K. The focal plane assembly contained the survey detectors, visible star sensors for position reconstruction, a Low Resolution Spectrometer (LRS) and a Chopped Photometric Channel (CPC). The focal plane assembly was located at the Cassegrain focus of the telescope and was cooled to about 3 K. The two LRS spectra, available for some of the stars in the sample, covered the wavelength range from $8-13$ μm and $11-23$ μm, had a slit widths of 5.0 and 7.5 arcmin, and used a detector made of Si:Ga and Si:As, respectively. The spectral resolution was 14 to 35 for both LRS.

The Infrared Space Observatory (ISO), with a mission period from 1995 to 1998, was equipped with two spectrometers (SWS and LWS), a camera (ISOCAM), and an imaging photo-polarimeter (ISOPHOT) which together covered wavelengths from 2.5 to around 240 μm with spatial resolutions ranging from 1.5 arcsec (at the shortest wavelengths) to 90 arcsec (at the longest wavelengths). Its 60 cm diameter telescope was cooled by superfluid liquid helium to temperatures of $2-4$ K. For most of the stars in the sample, Short and Long Wavelength Spectrometer (SWS and LWS) spectra are available. The SWS and LWS covered the wavelength range from

[7]http://iso.esac.esa.int/ida/
[8]http://irsa.ipac.caltech.edu/Missions/iras.html

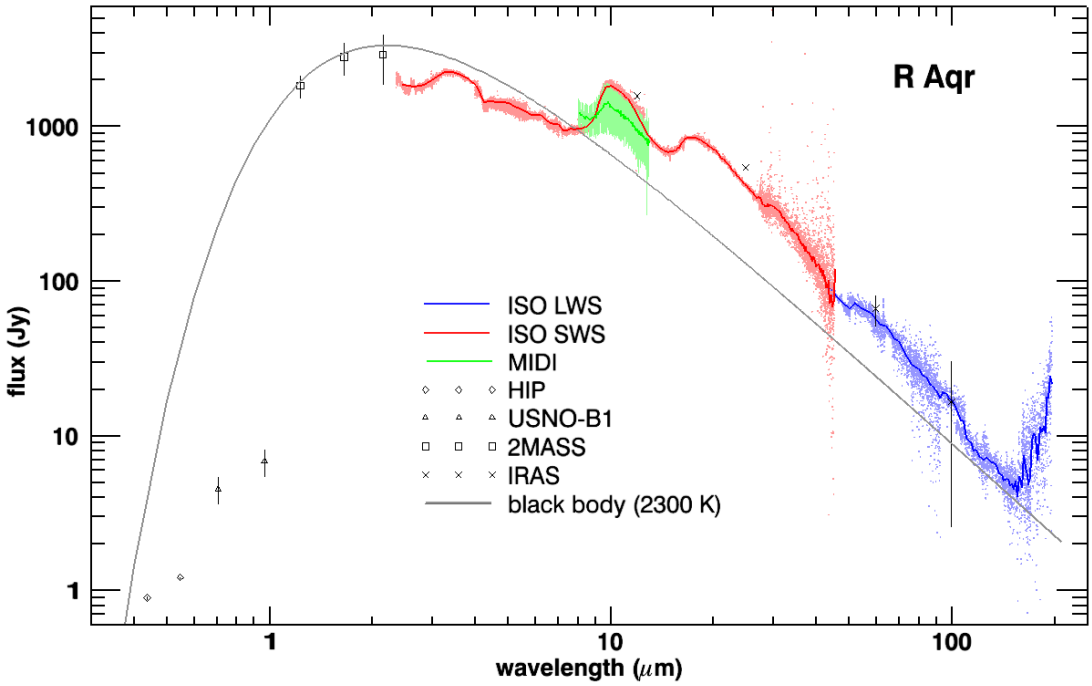

Figure 5.7: The spectral energy distribution of R Aqr.

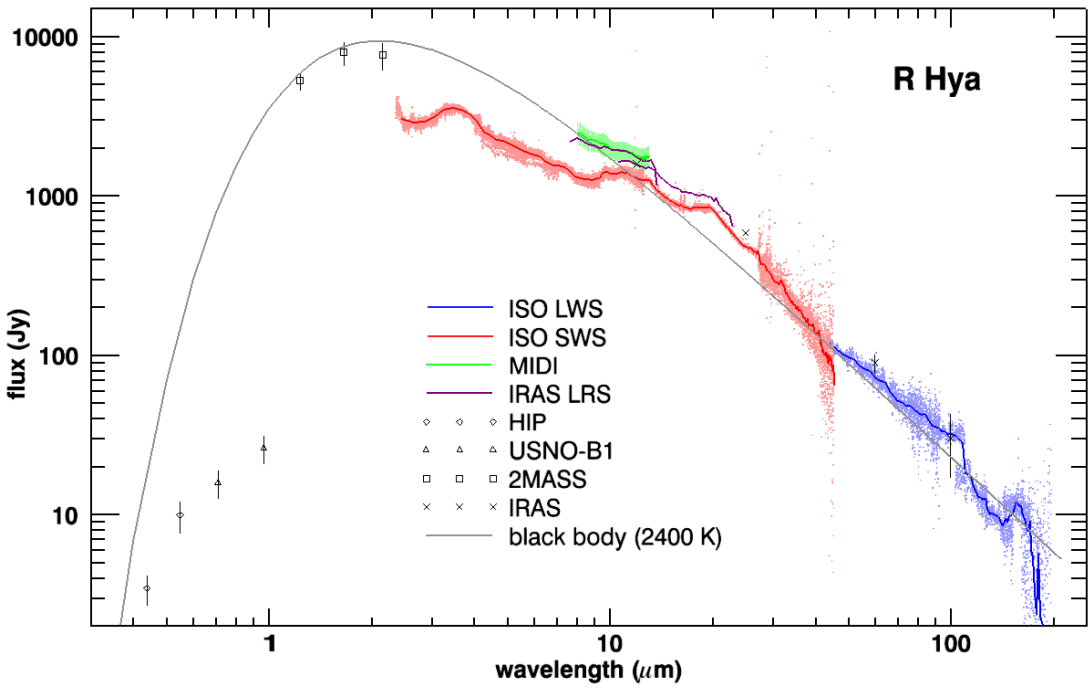

Figure 5.8: The spectral energy distribution of R Hya.

$2.38-45.2$ μm and $43-197$ μm, with a spectral resolution of 1000 to 2000 and 200, respectively. The spatial resolution was between 14 and 33 arcsec for the SWS and 1.65 arcmin for the LWS.

The ISO spectrum of the O-rich stars (R Aql, R Aqr, R Hya and W Hya) is mainly dominated by absorption bands of H_2O between $2.5-3.0$ μm (stretching mode) and $5.0-8.0$ μm (bending

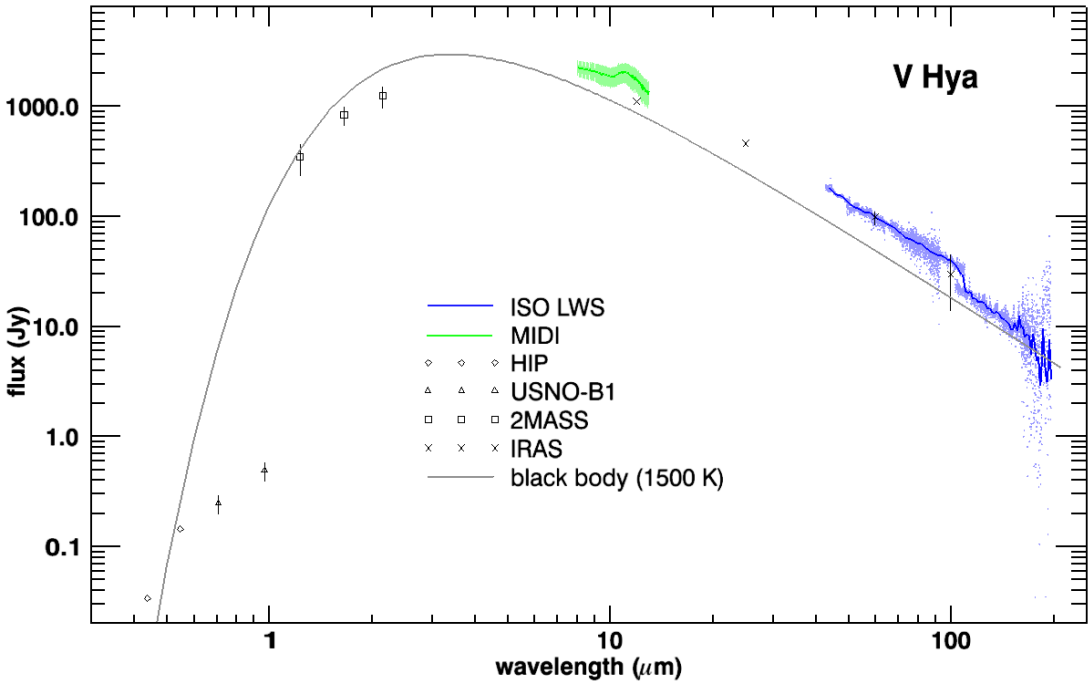

Figure 5.9: The spectral energy distribution of V Hya.

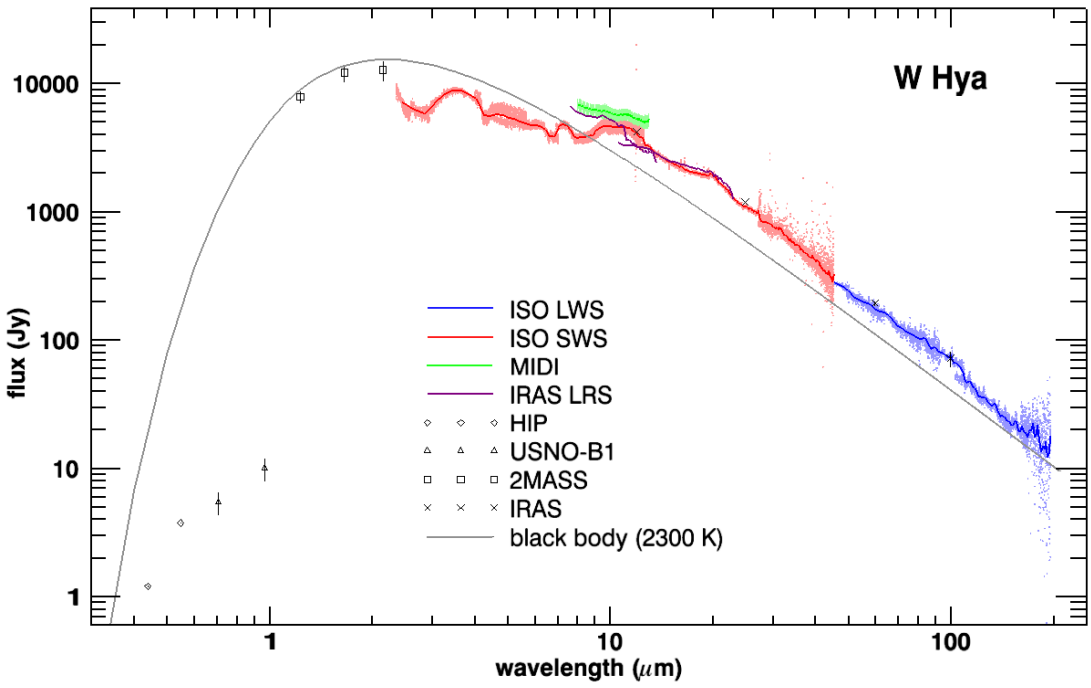

Figure 5.10: The spectral energy distribution of W Hya.

mode), and an SiO absorption band between 8 and 9 μm ($\nu = 1-0$). Distinct absorption lines of CO at around 2.4 μm, OH at $2.9-4.0$ μm, CO_2 at 4.25 μm and SO_2 at 7.4 μm can be seen in the spectra of some of the stars. From temperature investigations (e.g. Justtanont et al., 2004, for W Hya) it can be derived that these absorptions originate from different molecular layers

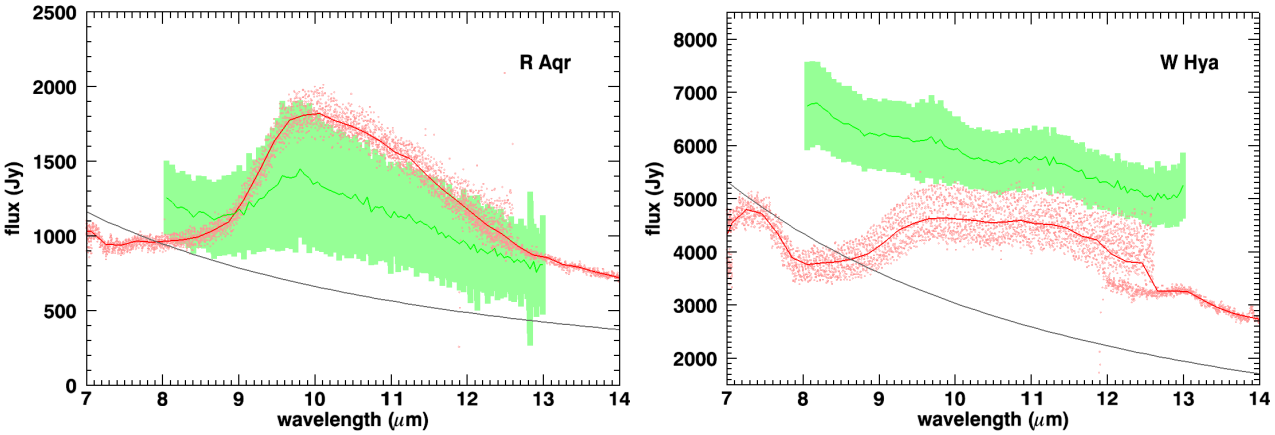

Figure 5.11: N-band SEDs of R Aqr (*left*) and W Hya (*right*), see text.

in the circumstellar shell. OH, CO and CO_2 absorption bands arise mainly from a hot (about 3000 K), dense region very close to the stellar photosphere, where H_2O is still photodissociated by shocks. H_2O and CO_2 absorption bands originate from a layer with a temperature of 1000 K, i.e. a molecular layer (molsphere) further out. Since CO is present in the whole circumstellar environment, it can be traced by the presence of different excitation levels. The fundamental band originates from cool regions while the overtone bands come from the hotter regions close to or from the pulsating atmosphere. The SiO molecule absorption arises in the same region where the H_2O molecular shell exists and where SiO is still not bound in dust grains.

All O-rich stars in the sample show dust emission in their ISO spectrum with different peculiarities. The features between 10 and 20 μm are a combination of emission from amorphous silicates at around 10 μm, compact Al_2O_3 at around 11 μm and MgFeO at around 19 μm. Regarding the 13 μm emission feature, e.g. seen in R Hya and weakly in W Hya, it is still under debate whether it comes from spinel ($MgAl_2O_4$) (Posch et al., 1999) or aluminum oxide (Onaka et al., 1989). Except for the 13 μm feature, Justtanont et al. (2004) obtained a satisfactory fit to all observed emission features in W Hya with the three other species. While R Hya shows similar emissions as W Hya, the 13 μm feature is missing in R Aql and R Aqr. Sloan & Price (1998b) classified O-rich envelopes according to their dust emission. They defined three large emission categories: broad oxygen-rich dust emission (SE1-2), structured silicate emission (SE3-6), and classic narrow silicate emission (SE7-8)[9]. The last column of Table 5.3 gives the classification obtained for the stars in the sample.

If the MIDI spectra are compared with the ISO spectra, it becomes obvious that the silicate emission is not detected except for R Aqr. Figure 5.11 shows a more detailed view of the SEDs of R Aqr and W Hya in the N-band. In the MIDI spectrum of W Hya, a weak emission of Al_2O_3 at around 11 μm is present, while no silicate feature at around 10 μm can be seen[10]. In contrast, the broad silicate emission at around 10 μm is very prominent in R Aqr. This behavior can be attributed to instrumental characteristics. ISO has a much larger field of view (FOV) compared to MIDI. With a small FOV of about 1 to 2 arcsec (cf. Table 3.2)[11], the

[9] A corrected flux ratio is the basis for the SE index: $SE = 10 \cdot F_{11}/F_{12} - 7.5$.

[10] Fluctuations between 9.3 and 10 μm are caused by difficulties in the reduction due to the telluric ozone feature, and flux measurements beyond 12 μm are probably not well calibrated.

[11] The exact value depends on the used baseline, the slit/mask position and other instrumental specifications.

emission of the extended silicate dust shell is not observed with MIDI.

This applies to the nearby stars R Hya and W Hya. R Aql and R Aqr are located further away and have nearly the same distance. Therefore, both stars should both either show or not show the silicate dust emission feature, but this apparent contradiction can be solved. In Section 5.2.4 it will be seen that the dust shell around R Aqr is much closer due to the fact that R Aqr is a symbiotic system containing a large amount of dust (see also the interpretation in Section 6.1.1). A calibration problem for R Hya and W Hya can certainly be ruled out, since the spectrum of the calibrator, 2 Cen, shows no silicate emission feature in the MIDI spectrum (even if it is weakly present in the ISO spectrum).

However, this non-detection allows it to derive a lower limit for the inner boundary of the silicate dust shell. Assuming a conservative value of the FOV of 1 arcsec, the main emission of the silicate dust shell originates in regions with diameters larger than 220 AU, 130 AU and 90 AU in R Aql, R Hya and W Hya, respectively. Even for R Aqr it can be speculated that silicate dust must exist further out, at a region with a diameter larger than 250 AU, since MIDI catches not the whole silicate dust emission.

V Hya is the only carbon star in the sample. From ISO, only the LWS spectrum is available, which does not show any significant spectral features. On the other hand, the MIDI spectrum shows very clearly the dust emission of SiC at 11.3 μm. Amorphous carbon, which makes up most of the dust, is basically featureless. Both dust species have in C-rich stars typically inner dust shell radii of about 2.5 photospheric radii with a temperature of about 1500 K (e.g. Ohnaka et al., 2007). Molecular shells of C_2H_2 (bands at $8-9$ μm and $11-14$ μm) and HCN (bands at $7-8$ μm and $11-13$ μm) at different distances and temperatures from the star might be present as well, but are not seen in the low resolution MIDI spectrum of V Hya. In the scheme of Sloan et al. (1998a), V Hya is categorized as Red, meaning that a strong continuum increase in intensity toward longer wavelengths is superposed on the dust features.

Table 5.3: Epochs and phases of the ISO spectra and classification from Sloan et al. (1998a) and Sloan & Price (1998b), see text.

Target	SWS		LWS		Classification
R Aql	1996-09-27	0.57	1996-10-01	0.58	SE5
R Aqr	1996-06-04	0.25	1996-05-16	0.20	SE7
R Hya	1996-08-02	0.16	1996-02-07	0.68	SE2t
V Hya			1996-07-01	0.42	Red
W Hya	1996-02-07	0.78	1996-02-14	0.80	SE8

The absolute flux values, but also the strengths of the spectral features, in particular the water bands, depend strongly on the pulsation state of the star. Therefore, Table 5.3 lists the visual light phase at the time the ISO spectra were taken. Unfortunately, the IRAS point source catalog does not list the epoch of observation[12], so that the MIDI spectra (scaled with the 12 μm IRAS flux) cannot be set in relation to the ISO spectra. In particular, the relative shift in intensity cannot be investigated satisfactorily. However, the offsets between the ISO SWS,

[12]Probably because many observations are averaged.

the IRAS SWS and the MIDI spectrum can easily be understood in terms of the flux variation due to pulsation. In this context, it should be kept in mind that the MIDI spectra are averages over different pulsation phases and cycles. Consequently, the spectral features are averages as well, or only represent a certain phase range.

5.2 Visibility Modeling

5.2.1 Overview of Observational Data

All five targets were observed several times over the course of semesters 79 to 83. From the observation logs in Appendix B it can be seen that for R Aql, R Aqr, R Hya, V Hya and W Hya, 32 of 40, 26 of 39, 64 of 72, 48 of 63 and 75 of 83 observations could be adequately reduced, respectively. Rejected are observations where the reduction process failed or unphysical visibilities arose due to bad environmental conditions. Due to the low N-band flux of the calibrator of R Aqr (cf. Table 4.3, page 74), this star is in particular affected, and one third of the data could not be reduced satisfactorily with the current software.

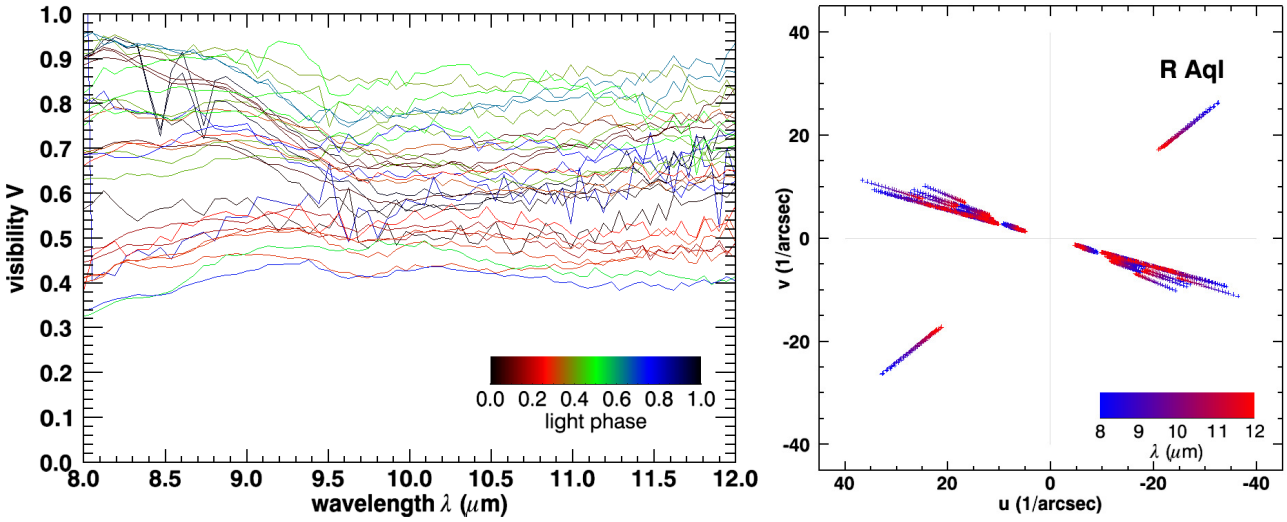

Figure 5.12: Visibilities and uv-coverage of R Aql for all 32 data sets used. *Left:* Visibilities data versus wavelength, color-coded by visual light phase. Errors are omitted for clarity, but given in sections 5.2.3 to 5.2.7. *Right:* Plot of the uv-coverage. The visibility spectra are binned into 25 wavelengths and are color-coded accordingly. Due to the 180° degeneracy, data are plotted twice (cf. equation 3.34).

At the nights where more than one calibrator observation were executed, the nearest calibrators in time were used to calculate a median calibrated visibility. The errors are given by the standard deviation of the calibrated visibilities. In addition, it was necessary to exclude measurements at wavelengths beyond 12 μm due to too low fluxes and a therefore not consistent reduction (see Section 4.2.3 for details). The GRISM data from period 79 are interpolated to the PRISM grid, and the wavelength range between 8 and 12 μm is binned from originally 94 wavelength bins into 25 wavelength bins to allow a faster computation of the model fits.

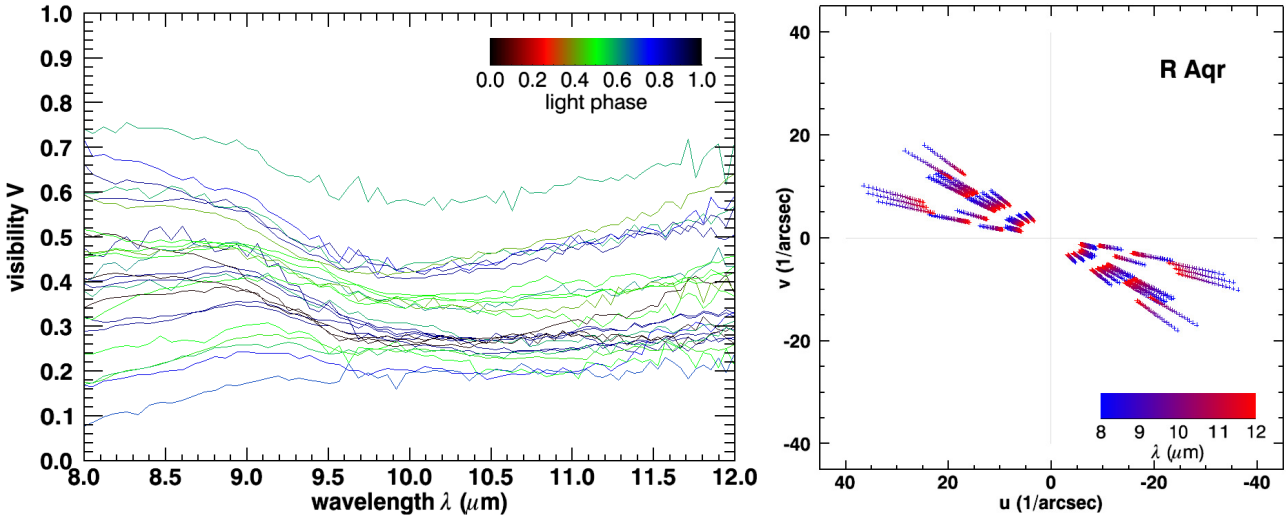

Figure 5.13: Same as Figure 5.12, except for R Aqr (26 data sets used).

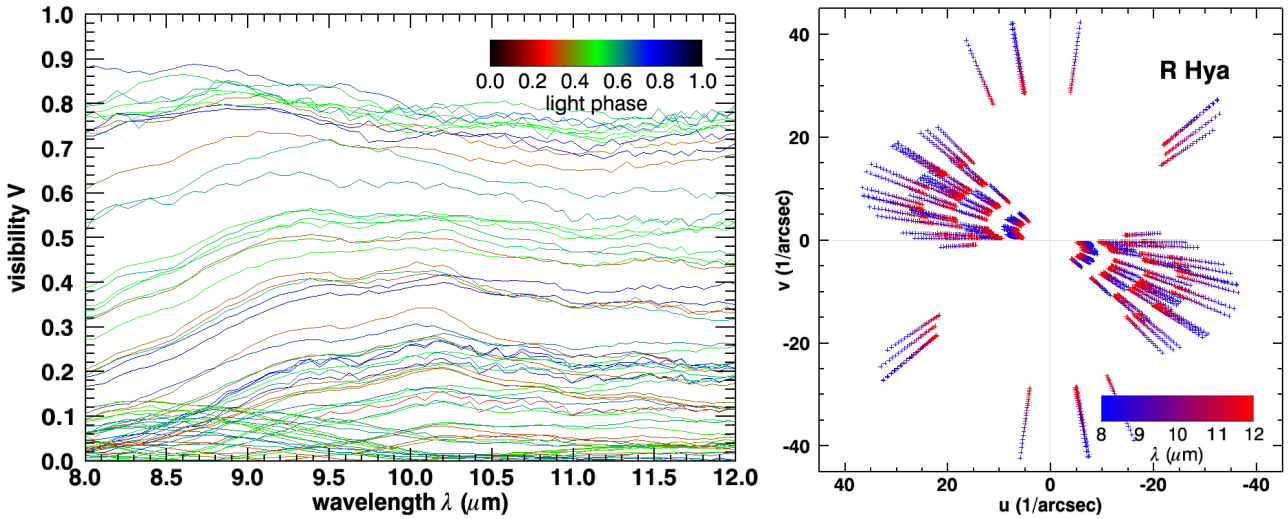

Figure 5.14: Same as Figure 5.12, except for R Hya (64 data sets used).

Within each wavelength bin a mean visibility and error is calculated. For the fits presented later on, it was always checked that this approach does not mask any additional features, with the result that in all cases the shapes of the wavelength dependent parameters are not altered significantly.

In order to avoid the problem of underestimating the error and to allocate an error to visibilities where only one calibrator observation exists, all available visibility errors within the same wavelength bin are averaged. The result is then assigned to *all* visibilities within this wavelength bin (*this* visibility error is given in the result tables and is shown in the corresponding plots later on).

Assuming the same error for all measurements within a wavelength bin improves the model fits as well. In a fitting method based on a chi-square technique (next section), all visibility points are then represented with the same significance. In the case that each value has another

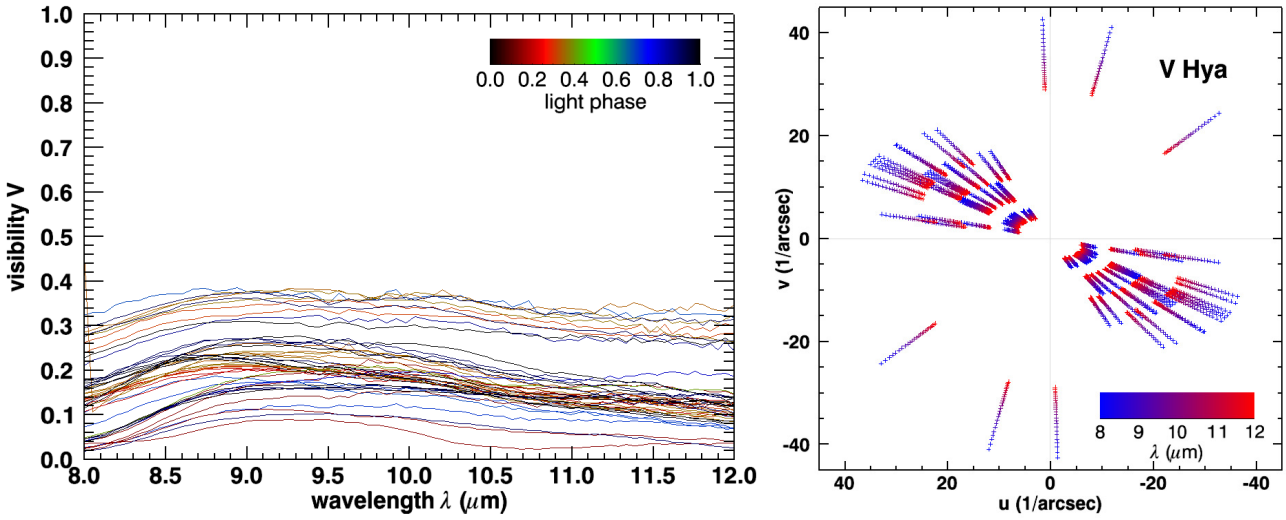

Figure 5.15: Same as Figure 5.12, except for V Hya (48 data sets used).

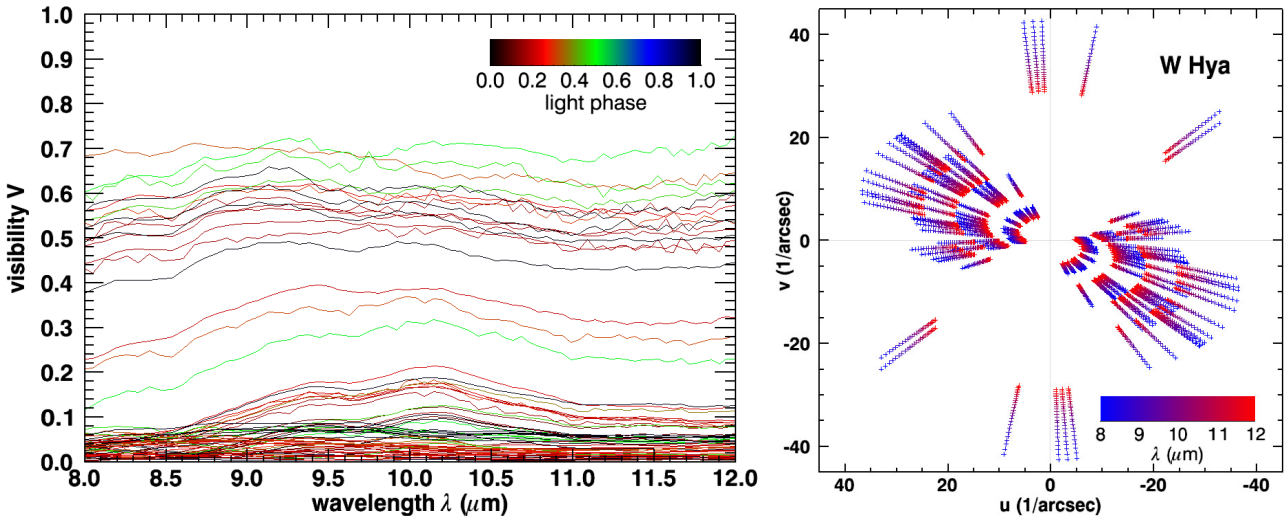

Figure 5.16: Same as Figure 5.12, except for W Hya (75 data sets used).

uncertainty, values with higher errors are underrepresented while values with low errors are overrepresented. Consequently, higher visibilities, with in general higher absolute errors, are not weighted accordingly, and the importance of lower visibilities, at in general higher spatial frequencies with lower absolute errors, are overestimated. Only the equal weighting ensures that over the whole spatial frequency range a model fits all data well, assuming that all measurements are equally significant.

The uv-coverage and the final calibrated visibility curves are shown in figures 5.12 to 5.16. The central wavelengths and assigned visibility errors are given in the individual sections for each star (Sections 5.2.3 to 5.2.7). The six different baseline configurations of AT pairs (cf. Figure 4.1, page 73) resulted in projected baselines between 11 and 72 m and a wide range of position angles (PA, ϑ; East of North). It is important to note again that different spatial frequencies (projected baseline divided by wavelength) probe different regions, i.e. high spatial frequencies are sensitive to small regions and low spatial frequencies to more extended structures. From the uv-coverage

it can be inferred that only for R Hya and W Hya departures from circular symmetry can be studied. In this respect, V Hya is a special case as will be discussed in Section 5.2.6. The shape of the visibility curves will be interpreted in combination with the discussion of the results of the visibility modeling in the next chapter.

5.2.2 Modeling and Fit Method

The most straight-forward way of interpreting sparsely sampled interferometric data (visibilities) is by fitting the Fourier transform of an assumed brightness distribution of the object. Simple size estimations can be obtained by elementary models with only few free parameters. The visibility functions used in the following sections were described in Section 3.1.6 and are listed in Appendix A. As mentioned in the introduction, the definition of a diameter is difficult because of its strong wavelength dependence as well as of intracycle and possible long-term cycle-to-cycle variations (e.g. Haniff et al., 1995) expected from models (e.g. Hofmann et al., 1998). On the other hand, the size and its wavelength dependent shape can tell which layer of the atmosphere is actually observed and which chemical and physical mechanisms are responsible. The existence of molecular layers results in an extended atmosphere and temperature structure around late-type stars. Therefore, no sharp transition between star and circumstellar environment exists and limb darkening effects/center to limb variations are very pronounced. An outcome of the modeling will be that a fully limb-darkened disk model fits the data better compared to an uniform disk model.

The best model parameters in this work are derived by performing the Levenberg-Marquardt least-squares minimization procedure programmed for the interactive data language IDL as `MPFIT` by C. B. Markwardt[13]. It is based on χ^2-statistics, where the reduced $\chi^2_{\mathrm{r},\lambda}$ for the best-fit model is estimated from

$$\chi^2_{\mathrm{r},\lambda} = \frac{\chi^2_{\mathrm{min},\lambda}}{N-p}\,, \tag{5.1}$$

with N the number of observational constraints (number of observations) and p the number of adjustable parameters (number of free model parameters, FP). $\chi^2_{\mathrm{min},\lambda}$ is the minimum chi square obtained in the model runs, which is calculated for each wavelength bin λ *separately* with

$$\chi^2_{\mathrm{min},\lambda} = \sum_{i=1}^{N} \frac{(V_{\mathrm{mod},i}(\lambda) - V_{\mathrm{obs},i}(\lambda))^2}{\sigma_i^2}\,, \tag{5.2}$$

where σ_i are the calibration uncertainties, and $V(\lambda)_{\mathrm{mod},i}$ and $V(\lambda)_{\mathrm{obs},i}$ are the visibilities of the model and measurement, respectively. As previously mentioned, the visibility error, σ_i, is assumed to be constant for all visibilities within the same wavelength bin. Consequently, even though the errors represent a reasonable uncertainty estimation, the chi-square values are only interpretable in a relative sense. For this reason, the given $\chi^2_{\mathrm{r},\lambda}$ values are only used to compare different models.

[13] http://cow.physics.wisc.edu/∼craigm/idl/idl.html

In order to avoid the problem of running into local minima and to check for degeneracies, a global grid search was implemented. This is done in a way that the least-squares minimization operates always between two grid points in each parameter, while going through the whole parameter space. Formal $1\,\sigma$ parameter errors were computed by taking the difference between the best fit value and the value given at the lowest (non-reduced) χ^2 plus one ($\chi^2_{\mathrm{min},\lambda} + 1$). This is only an approximation, since the χ^2 values are not Gaussian distributed. In order to get a more appropriate parameter error, the visibility errors are scaled to a value yielding a reduced chi-square of one. Besides this, the final parameter errors are always a multiple of, and never smaller than the smallest grid distance.

5.2.3 R Aql

The 32 visibility measurements of R Aql are plotted for one example wavelength bin (bin 8, 9.4 μm) versus spatial frequency (projected baseline divided by wavelength) in the left panel of Figure 5.17. It appears that the individual measurements have a high scatter, and there are two reasons for this. First, the low N-band flux of the target and the calibrator causes a low signal-to-noise ratio of the fringe signal (this is the main reason), and second, the plot contains observations made at different pulsation phases and pulsation cycles. The data are color-coded by visual light phase. This reveals that observations at visual maximum have in general lower visibilities as at visual minimum. However, this trend is very weak. From the right panel of Figure 5.12 (page 108) it is clear that a possible intrinsic asymmetry of the star does not have any influence on the scatter, since all data were obtained at a similar position angle around 70° (assuming that a possible asymmetric appearance is not variable on a comparable time scale).

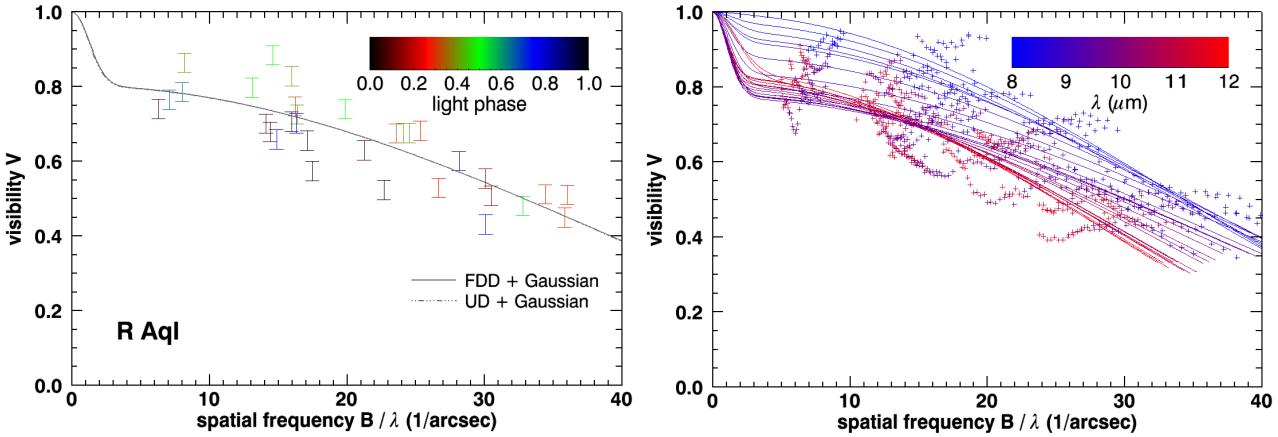

Figure 5.17: *Left:* Fit of a circular fully limb-darkened (FDD) + circular Gaussian (model A.13) and a circular uniform disk (UD) + circular Gaussian (model A.10) to the 32 visibility measurements of R Aql at wavelength bin 8 (9.4 μm). Both models are not distinguishable. Data, taken over all phases and position angles, are plotted versus spatial frequency and are color-coded by visual light phase. *Right:* Same as left, but for all 25 wavelength bins of model A.13. See Table 5.4 and Figure 5.18 for the obtained fit parameters.

Model: The distribution of the visibilities suggests that an over-resolved component contributes to the total visibility, since at low spatial frequencies the values are significantly below

Table 5.4: Model fit results for R Aql: circular fully limb-darkened (FDD) + circular Gaussian (model A.13) and circular uniform disk (UD) + circular Gaussian (model A.10).

		circular FDD + circular Gaussian				circular UD + circular Gaussian			
λ (μm)	ΔV[a]	$\theta_{\rm FDD}$ (mas)	Flux $\epsilon_{\rm FDD}$	$\theta_{\rm G}$ (mas)	$\chi^2_{\rm r}$	$\theta_{\rm UD}$ (mas)	Flux $\epsilon_{\rm UD}$	$\theta_{\rm G}$ (mas)	$\chi^2_{\rm r}$
8.12	0.034	23.1 ± 1.5	0.99 ± 0.02	234 ± 188	4.8	20.4 ± 1.5	0.99 ± 0.02	236 ± 186	4.9
8.33	0.033	22.7 ± 1.5	0.97 ± 0.02	274 ± 148	5.2	20.1 ± 1.5	0.97 ± 0.02	276 ± 146	5.2
8.54	0.031	22.7 ± 1.5	0.95 ± 0.02	268 ± 154	3.9	20.1 ± 1.5	0.95 ± 0.02	258 ± 164	3.9
8.71	0.031	22.2 ± 1.5	0.93 ± 0.02	296 ± 126	3.6	19.6 ± 1.5	0.93 ± 0.02	276 ± 146	3.6
8.87	0.031	21.6 ± 1.5	0.92 ± 0.02	286 ± 136	3.6	19.2 ± 1.5	0.92 ± 0.02	286 ± 136	3.6
9.07	0.029	21.1 ± 1.5	0.88 ± 0.02	302 ± 120	4.3	18.7 ± 1.5	0.88 ± 0.02	316 ± 106	4.3
9.26	0.029	20.5 ± 1.5	0.84 ± 0.02	294 ± 128	5.2	18.2 ± 1.5	0.84 ± 0.02	324 ± 106	5.2
9.45	0.026	20.3 ± 2.0	0.80 ± 0.02	302 ± 120	6.9	18.1 ± 1.5	0.80 ± 0.06	310 ± 112	6.9
9.63	0.028	21.1 ± 1.5	0.78 ± 0.02	340 ± 122	5.5	18.7 ± 1.5	0.78 ± 0.02	314 ± 108	5.5
9.78	0.027	21.4 ± 2.0	0.78 ± 0.06	324 ± 106	7.1	19.0 ± 2.0	0.78 ± 0.02	328 ± 110	7.1
9.92	0.027	21.3 ± 2.0	0.77 ± 0.02	338 ± 120	6.7	18.9 ± 2.0	0.77 ± 0.02	338 ± 120	6.7
10.09	0.027	21.4 ± 2.0	0.78 ± 0.06	357 ± 138	7.8	19.0 ± 2.0	0.78 ± 0.06	358 ± 140	7.8
10.26	0.026	21.9 ± 2.0	0.78 ± 0.06	362 ± 144	7.9	19.4 ± 2.0	0.78 ± 0.06	336 ± 118	7.9
10.42	0.029	22.6 ± 2.0	0.78 ± 0.06	350 ± 132	6.2	20.1 ± 2.0	0.78 ± 0.06	368 ± 150	6.2
10.58	0.031	23.6 ± 2.0	0.79 ± 0.02	350 ± 132	5.0	21.0 ± 2.0	0.79 ± 0.02	354 ± 134	5.0
10.71	0.030	24.2 ± 1.5	0.80 ± 0.02	378 ± 160	5.4	21.5 ± 2.0	0.79 ± 0.02	364 ± 146	5.5
10.84	0.030	24.8 ± 2.0	0.80 ± 0.06	368 ± 150	4.7	22.0 ± 1.5	0.80 ± 0.06	358 ± 140	4.7
10.99	0.030	26.1 ± 1.5	0.81 ± 0.02	366 ± 148	4.8	23.2 ± 1.5	0.81 ± 0.02	362 ± 144	4.8
11.14	0.027	26.7 ± 1.5	0.82 ± 0.06	354 ± 136	5.4	23.7 ± 1.5	0.82 ± 0.02	360 ± 142	5.4
11.29	0.031	26.9 ± 2.0	0.83 ± 0.02	382 ± 164	3.9	23.8 ± 1.5	0.82 ± 0.02	396 ± 178	3.9
11.43	0.030	26.2 ± 1.5	0.81 ± 0.02	372 ± 154	4.5	23.2 ± 1.5	0.81 ± 0.02	380 ± 162	4.5
11.55	0.029	26.4 ± 2.0	0.81 ± 0.02	406 ± 188	5.1	23.5 ± 2.0	0.81 ± 0.02	392 ± 174	5.1
11.67	0.026	27.5 ± 2.0	0.83 ± 0.02	376 ± 158	5.7	24.4 ± 2.0	0.83 ± 0.02	394 ± 176	5.8
11.81	0.029	27.3 ± 2.0	0.83 ± 0.02	219 ± 200	4.5	24.2 ± 1.5	0.83 ± 0.02	219 ± 202	4.5
11.95	0.029	27.8 ± 2.0	0.84 ± 0.06	219 ± 202	4.3	24.7 ± 1.5	0.84 ± 0.02	219 ± 202	4.4

[a] This is the mean visibility error used for the corresponding wavelength bin (see Section 5.2.1).

one. An over-resolved silicate dust shell, which is is seen in the ISO spectrum and is expected in AGB stars, could be the most compelling reason. The brightness distribution of a dust shell is in a simple model best represented by a Gaussian. However, from the plot it is clear that such an over-resolved structure cannot be well constrained due to the lack of measurements at very low spatial frequencies near zero.

In contrast, the diameter of the star, or better the molecular sphere probed at the observational wavelength, is much better constrained. Even though the first zero is not present, the clear decline with increasing spatial frequency makes it possible to fit a circular fully limb-darkened (FDD) or circular uniform (UD) disk to the data. Since the exact behavior around a possible first zero and the following second lobe is unknown, it is impossible to choose the best model among the above two. A UD is in general best suited for a first diameter estimation of a star and is therefore often used in the literature. However, the investigation of the O-rich stars R Hya and W Hya, presented in later sections, suggests that an equally simple FDD describes the observed molecular shells in O-rich stars much better in the mid-IR.

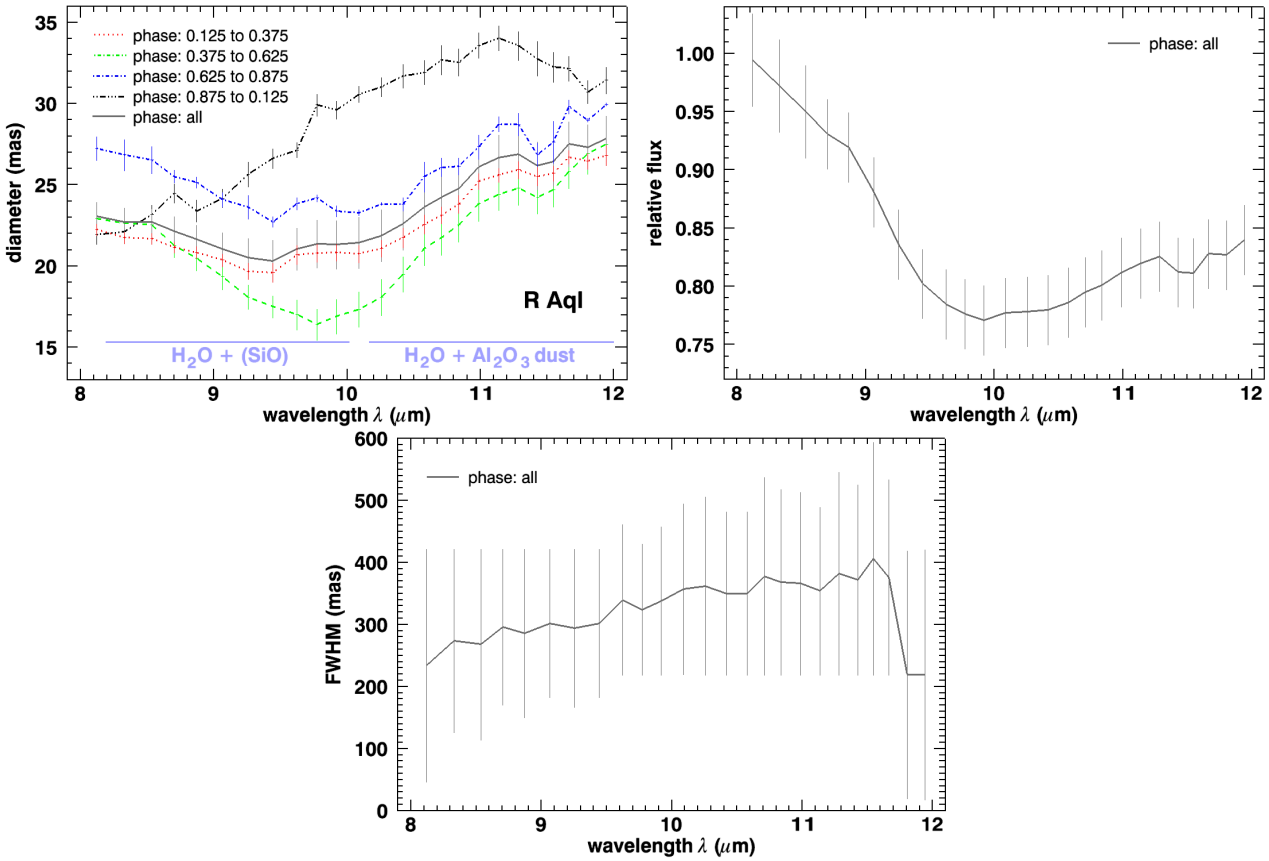

Figure 5.18: Plot of the A.13 model parameters from Table 5.4 for R Aql. *Top left:* The fully limb-darkened disk diameter, θ_{FDD}, is given as function of wavelength. The solid gray line shows the fit to all 32 measurements and the other lines the fits to subsequent pulsation phase bins. *Top right:* The relative flux, ϵ_{FDD}, of the fully limb-darkened disk obtained for the fit to the full data set. These flux values are fixed for the fit of the FDD to subsequent pulsation phase bins. *Bottom:* The Gaussian FWHM, θ_{G}, for the fit to the full data set. This parameter was not fitted for subsequent pulsation phases.

Fit: The fits of these two-component models, a circular FDD + circular Gaussian (model A.13) and a circular UD + circular Gaussian (model A.10), to the data are shown in the left panel of Figure 5.17 as well. The best-fit parameters for both models are given in Table 5.4 for all 25 wavelength bins. Formal errors are computed as mentioned in Section 5.2.2, while the listed mean visibility errors are derived as described in Section 5.2.1. A comparison of the reduced chi square values, χ^2_{r}, validates that both models are not distinguishable and the high error of the Gaussian FWHM confirms that θ_{G} is not well constrained. A residual analysis shows that for each wavelength bin on average about 75% of the measurements are inside the $3\,\sigma$ range.

The right panel of Figure 5.17 displays the fit of the favored FDD + Gaussian model to all 25 wavelength bins. The turning point at around 2.5 arcsec^{-1} stays at almost the same spatial frequency, while the visibility at that point goes down with increasing wavelength. This shows that the FWHM diameter, θ_{G}, increases and the relative flux contribution, ϵ_{FDD}, of the FDD decreases with increasing wavelength. The increasingly steep slope with increasing wavelength (at high spatial frequencies), resulting in a first zero at lower spatial frequency (not shown),

indicates that overall the FDD diameter, $\theta_{\rm FDD}$, increases as well. This behavior is more exactly shown in the three parameter plots in Figure 5.18.

From these panels it can be seen that $\theta_{\rm FDD}$ actually decreases slightly from (23.1 ± 1.5) mas to (21.3 ± 2.0) mas, going from 8 μm to 10 μm, before it increases again to its highest value of (27.8 ± 2.0) mas at 12 μm. This corresponds to a relative increase, $\theta_{12\mu{\rm m}}/\theta_{10\mu{\rm m}}$, of (31 ± 15)% in the longer wavelength regime. The diameter increase from about 21 mas to about 28 mas is equivalent to an increase from 4.6 AU to 6.2 AU at the assumed distance of R Aql. The molecules and close dust species causing this shape are already indicated inside the corresponding plot, but will be discussed further in the next chapter. In contrast, the relative flux decreases from (0.99 ± 0.02) to (0.80 ± 0.02) going to longer wavelengths, reflecting the increased flux contribution from the colder surrounding silicate dust shell (the over-resolved component).

The Gaussian FWHM on the other hand steadily increases from about (230 ± 150) mas to about (400 ± 150) mas, consistent with increasingly cool parts of the dust shell probed with increasing wavelength. This is equivalent to an increase from 51 AU to 88 AU and sets the characteristic silicate dust shell radius at 10 μm at a distance of about 16 ± 6 times the layer radius. This high ratio is probably a result of the not well constrained Gaussian and is only a lower limit. The analysis of the spectrum has already shown that the dust shell is even larger, with an inner dust condensation diameter larger than 220 AU.

Intracycle variations: The pulsation cycle is divided into 4 bins as shown in Figure 5.1 (page 96), and each observation is assigned to the corresponding phase bin. Bins 1, 2, 3 and 4 consist of 8, 9, 9 and 6 observations with phase ranges of $0.875 - 0.125$, $0.125 - 0.375$, $0.375 - 0.625$ and $0.625 - 0.875$, respectively. Bin 1 contains observations at visual maximum and bin 3 observations at visual minimum. A FDD is fitted to the data for each bin with the relative flux fixed to the value obtained for the full data set (model A.6). This compensates for fewer measurements by having fewer free parameters. The Gaussian FWHM is not fitted for subsequent pulsation phases, since this parameter cannot be reasonably constrained.

As can be inferred from the upper left panel of Figure 5.18, the FDD diameter is on average[14] (5.5 ± 2.3) mas larger at visual maximum and on average (2.2 ± 2.6) mas smaller at visual minimum if compared with the averaged full data set diameter. This trend was already anticipated above by having lower visibilities at visual maximum and higher visibilities at visual minimum. In bin 2 and 4, the diameters are close to the mean value being on average (0.8 ± 1.9) mas smaller and (2.3 ± 2.8) mas larger, respectively. Altogether, this results in a consistent sinusoidal variation. The diameter difference between visual maximum and minimum corresponds to a variation of (36 ± 14)%. Except for the bin at visual maximum, the shapes are very similar. This exception is unusual if compared with the other stars investigated in later sections, but not surprising if one takes into account that the visibility measurements for R Aql have a comparatively high uncertainty.

Cycle-to-cycle variations: R Aql was observed over four consecutive pulsations cycles. The small overlap of observations at similar phases allows only to use data from cycle 2 and 4 to study cycle-to-cycle variations. At both cycles, data between phases 0.40 and 0.55 are used.

[14]The average across the N-band spectral regime (8 to 12 μm). See discussion in Section 6.2.

These regions are shaded in the upper panel of Figure 5.1 (page 96). The ranges of cycle 2 and 4 contain 5 and 4 observations, respectively. A circular FDD (model A.6) is fitted to these observations, while the relative flux is fixed to the value obtained for the full data set.

The FDD diameter of cycle 2 is on average about (4.2 ± 3.2) mas below the diameter of the full data set. From cycle 2 to cycle 4, the diameter increased on average by (3.5 ± 4.4) mas, while the wavelength dependent shape does not change notably. This is equivalent to an increase of (18 ± 23)%. However, regarding the uncertainties this is not significant for cycle-to-cycle variations due to pulsation instabilities in R Aql.

5.2.4 R Aqr

The 26 visibility measurements of R Aqr are plotted for one example wavelength bin (bin 8, 9.4 μm) versus spatial frequency in the left panel of Figure 5.17. As for R Aql, the individual measurements have a high scatter, which is in this case primarily due to the low N-band flux of the calibrator. The data are color-coded by visual light phase. The phase coverage is very narrow, and no clear systematics are obvious, only that at visual minimum the visibilities are slightly higher than at post-minimum. From the right panel of Figure 5.13 (page 109) it can be inferred that an intrinsic asymmetry of the star has no significant influence, since all data were obtained at a narrow position angle range between 60° and 80°.

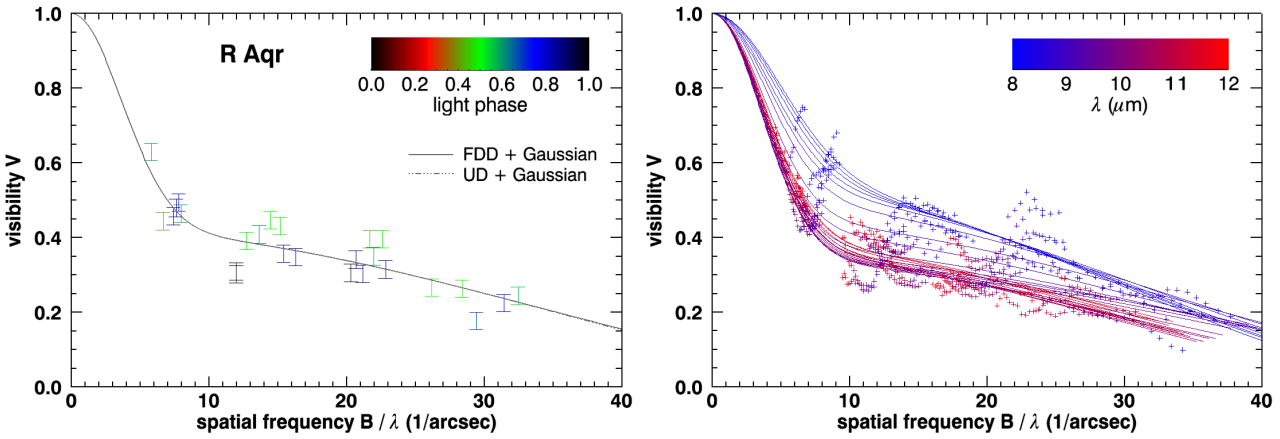

Figure 5.19: *Left:* Fit of a circular fully limb-darkened (FDD) + circular Gaussian (model A.13) and a circular uniform disk (UD) + circular Gaussian (model A.10) to the 26 visibility measurements of R Aqr at wavelength bin 8 (9.4 μm). Both models are not distinguishable. Data, taken over all phases and position angles, are plotted versus spatial frequency and are color-coded by visual light phase. *Right:* Same as left, but for all 25 wavelength bins of model A.13. See Table 5.5 and Figure 5.20 for the obtained fit parameters.

Model: The distribution of the visibilities suggests that two components contribute to the total visibility, since at spatial frequencies shortward 9 arcsec^{-1} the visibilities are getting clearly increasingly higher. This can be well described with a Gaussian brightness distribution representing a silicate dust shell. In comparison to R Aql, this dust shell is much better

Table 5.5: Model fit results for R Aqr: circular fully limb-darkened (FDD) + circular Gaussian (model A.13) and circular uniform disk (UD) + circular Gaussian (model A.10).

		circular FDD + circular Gaussian				circular UD + circular Gaussian			
λ (μm)	ΔV[a]	θ_{FDD} (mas)	Flux ϵ_{FDD}	θ_{G} (mas)	χ^2_{r}	θ_{UD} (mas)	Flux ϵ_{UD}	θ_{G} (mas)	χ^2_{r}
8.12	0.025	27.4 ± 2.5	0.57 ± 0.03	78 ± 12	4.9	24.2 ± 2.0	0.56 ± 0.03	78 ± 11	4.9
8.33	0.026	26.8 ± 2.5	0.56 ± 0.09	81 ± 10	4.9	23.7 ± 2.0	0.55 ± 0.09	80 ± 11	4.8
8.54	0.025	26.6 ± 2.5	0.55 ± 0.09	85 ± 11	5.4	23.5 ± 2.0	0.55 ± 0.03	84 ± 12	5.4
8.71	0.024	26.2 ± 2.0	0.55 ± 0.03	90 ± 12	4.7	23.2 ± 2.0	0.55 ± 0.03	90 ± 13	4.7
8.87	0.022	25.2 ± 2.0	0.54 ± 0.03	94 ± 11	5.1	22.4 ± 2.0	0.53 ± 0.03	94 ± 12	5.1
9.07	0.023	24.2 ± 2.5	0.50 ± 0.03	97 ± 11	4.4	21.5 ± 2.0	0.50 ± 0.03	97 ± 11	4.4
9.26	0.021	22.9 ± 3.0	0.45 ± 0.03	102 ± 11	5.4	20.4 ± 2.5	0.45 ± 0.03	101 ± 10	5.3
9.45	0.023	23.3 ± 3.5	0.42 ± 0.03	104 ± 10	4.4	20.7 ± 2.5	0.42 ± 0.03	104 ± 10	4.4
9.63	0.025	22.5 ± 3.5	0.38 ± 0.03	104 ± 8	3.6	20.0 ± 3.0	0.38 ± 0.03	104 ± 9	3.6
9.78	0.020	21.8 ± 3.5	0.36 ± 0.03	104 ± 7	4.6	19.4 ± 3.5	0.36 ± 0.03	104 ± 7	4.6
9.92	0.019	20.9 ± 3.5	0.35 ± 0.03	105 ± 8	4.8	18.6 ± 3.0	0.35 ± 0.03	105 ± 8	4.8
10.09	0.017	21.5 ± 3.5	0.35 ± 0.03	106 ± 7	5.3	19.2 ± 3.0	0.35 ± 0.03	106 ± 7	5.3
10.26	0.017	22.2 ± 3.5	0.34 ± 0.03	105 ± 7	5.8	19.7 ± 3.0	0.34 ± 0.03	105 ± 7	5.8
10.42	0.018	24.0 ± 3.5	0.34 ± 0.03	105 ± 6	4.9	21.4 ± 3.5	0.34 ± 0.03	105 ± 7	4.9
10.58	0.021	25.4 ± 3.5	0.35 ± 0.03	106 ± 7	3.1	22.5 ± 3.0	0.35 ± 0.03	106 ± 6	3.1
10.71	0.019	25.9 ± 3.5	0.36 ± 0.03	105 ± 6	4.3	23.0 ± 3.0	0.36 ± 0.03	105 ± 6	4.3
10.84	0.020	27.0 ± 3.5	0.36 ± 0.03	104 ± 7	3.8	24.0 ± 3.0	0.36 ± 0.03	104 ± 6	3.9
10.99	0.019	27.6 ± 3.0	0.37 ± 0.03	104 ± 6	4.1	24.5 ± 3.0	0.37 ± 0.03	104 ± 6	4.1
11.14	0.022	26.9 ± 3.5	0.37 ± 0.03	104 ± 7	2.8	23.9 ± 3.0	0.37 ± 0.03	104 ± 6	2.8
11.29	0.018	26.6 ± 3.5	0.37 ± 0.03	103 ± 6	5.0	23.6 ± 3.5	0.37 ± 0.03	103 ± 7	5.0
11.43	0.022	26.6 ± 4.0	0.37 ± 0.03	101 ± 7	3.7	23.6 ± 3.5	0.37 ± 0.03	101 ± 6	3.7
11.55	0.022	24.6 ± 4.5	0.37 ± 0.03	102 ± 7	4.0	21.8 ± 4.5	0.37 ± 0.03	101 ± 7	4.0
11.67	0.022	26.1 ± 4.5	0.39 ± 0.03	101 ± 7	4.2	23.2 ± 4.0	0.38 ± 0.03	101 ± 7	4.2
11.81	0.029	27.4 ± 4.5	0.40 ± 0.03	101 ± 7	2.7	24.3 ± 4.0	0.40 ± 0.03	100 ± 8	2.7
11.95	0.032	26.0 ± 5.5	0.39 ± 0.03	99 ± 7	2.8	23.1 ± 5.0	0.39 ± 0.03	99 ± 7	2.8

[a] This is the mean visibility error used for the corresponding wavelength bin (see Section 5.2.1).

constrained. However, additional measurements at very low spatial frequencies could verify the trend suggested by the given points.

As for R Aql, the diameter of the molecular layer/star can be fitted by a circular fully limb-darkened (FDD) or circular uniform (UD) disk. Again, a decision between both models cannot be made due to not knowing the exact behavior around the first zero and second lobe. However, a FDD is preferred as for R Aql, since it represents the molecular layers in a better way.

Fit: The fits of these two-component models, a circular FDD + circular Gaussian (model A.13) and a circular UD + circular Gaussian (model A.10), to the data are shown in the left panel of Figure 5.19. The best-fit parameters for both models are given in Table 5.5 for all 25 wavelength bins. Formal errors are computed as mentioned in Section 5.2.2, while the listed mean visibility errors are derived as described in Section 5.2.1. A comparison of the reduced chi square values, χ^2_{r}, validates that both models are not distinguishable and the relatively low errors of the Gaussian FWHMs confirm that θ_{G} is much better constrained. A residual analysis shows that for each wavelength bin on average more than 80% of the measurements are inside

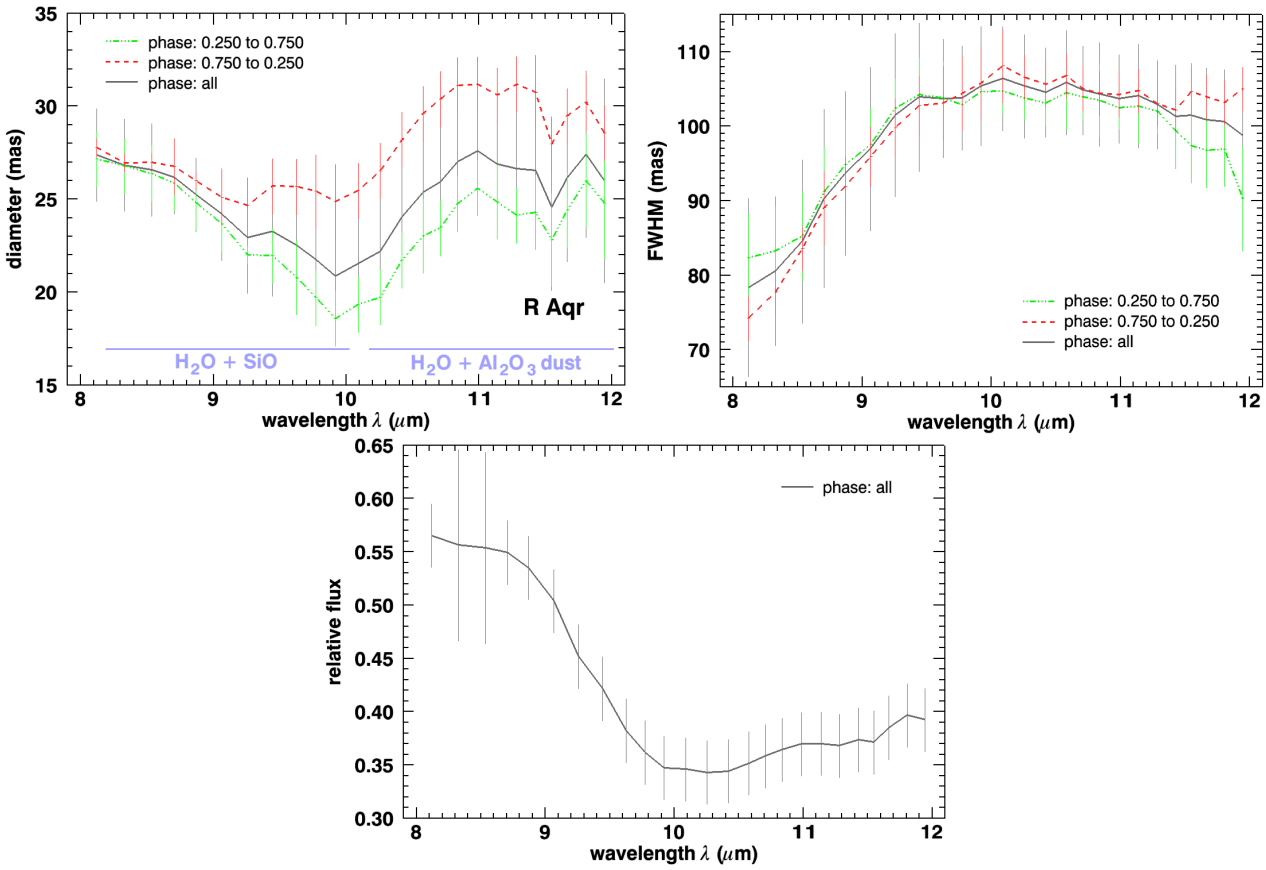

Figure 5.20: Plot of the A.13 model parameters from Table 5.5 for R Aqr. *Top:* The fully limb-darkened disk diameter, θ_{FDD}, (*left*) and Gaussian FWHM, θ_{G}, (*right*) are given as function of wavelength. The solid gray lines show the fit to all 26 measurements and the other lines the fits to subsequent pulsation phase bins. *Bottom:* The relative flux, ϵ_{FDD}, of the fully limb-darkened disk obtained for the fit to the full data set. These flux values are fixed for the fit of the FDD + Gaussian to subsequent pulsation phase bins.

the $3\,\sigma$ range.

The right panel of Figure 5.19 displays the fit of the favored FDD + Gaussian model to all 25 wavelength bins. The turning point at around 9 arcsec^{-1} stays at almost the same spatial frequency, while the visibility at that point goes down with increasing wavelength. This shows that the FWHM diameter, θ_{G}, increases and the relative flux contribution, ϵ_{FDD}, of the FDD decreases with increasing wavelength. The gradient of the curve at higher spatial frequencies (> 9 arcsec^{-1}) changes from a high to a low and again to a high value with increasing wavelength. This means that the first zero lies first at a low then at a high and then again at a low spatial frequency (not shown). The consequence is that with increasing wavelength the FDD diameter, θ_{FDD}, is first high then low and then high again. This behavior is more exactly shown in the three parameter plots in Figure 5.20.

From these panels it can be seen that θ_{FDD} decreases from (27.4 ± 2.5) mas to (20.9 ± 3.5) mas, going from 8 μm to 10 μm, before it increases again to a value of (26.0 ± 5.5) mas at 12 μm. This corresponds to a relative increase, $\theta_{12\mu\mathrm{m}}/\theta_{10\mu\mathrm{m}}$, of $(24 \pm 34)\%$ in the longer wavelength

regime. The diameter increase from about 21 mas to about 26 mas is equivalent to an increase from 5.3 AU to 6.5 AU at the distance of R Aqr. The molecules and close dust species causing this shape are already indicated inside the plot, but will be discussed further in the next chapter. In contrast, the relative flux decreases from (0.57 ± 0.03) to (0.39 ± 0.03) going to longer wavelengths, reflecting the increased flux contribution from the colder surrounding silicate dust shell. In contrast to R Aql, the mid-IR flux contribution of the star/molecule layer is considerably lower because of the large amount of dust bound in the symbiotic system.

The Gaussian FWHM on the other hand increases steadily from (78 ± 12) mas to (104 ± 7) mas between 8 and 10 μm, consistent with the increasingly cold parts of the dust shell probed with increasing wavelength, and stays around this value between 10 and 12 μm. This is equivalent to an increase from 20 AU to 26 AU and sets the characteristic silicate dust shell radius at 10 μm at a distance of about 5.0 ± 0.9 times the layer radius. This ratio is at the lower end expected for O-rich AGB stars.

The constant or even slightly declining FWHM at wavelengths longward 10 μm could be a hint that the dust shell is truncated due to the gravitation conditions set by the the WD in the CSE (cf. Section 2.4.2). With the sudden decline of the dust density, cold dust in outer regions, probed by wavelength longer than 10 μm, does not exist and can therefore not be detected. This would be also consistent with the low mass loss rate reported for R Aqr. However, this truncation would be contradictory to the finding that the MIDI spectrum suggests silicate dust at larger radii as well. Therefore, the following explanation might be preferred. At longer wavelengths (> 10 μm), regions closer to the star contribute more to the total dust emission traced with MIDI, since these wavelengths are outside the very strong silicate emission feature coming from the extended dust shell, and therefore an apparently lower dust shell diameter is measured.

Intracycle variations: Due to only few observations and a not optimal phase coverage the pulsation cycle could only be divided into 2 bins as shown in Figure 5.2 (page 97). Bin 1 (14 observations), corresponding to observations at visual minimum, and bin 2 (12 observations), corresponding to observations at visual maximum, have phase ranges of $0.25 - 0.72$ and $0.75 - 0.25$, respectively. For both bins the FDD + Gaussian model is fitted with the relative flux fixed to the value obtained for the full data set (model A.13). In contrast to R Aql, the Gaussian FWHM could be well fitted for each subsequent pulsation phase.

As can be deduced from the upper left panel of Figure 5.20, the FDD diameter is on average (2.9 ± 3.9) mas larger at visual maximum and on average (1.5 ± 3.9) mas smaller at visual minimum, if compared with the diameter obtained for the full data set. This is unfortunately not significant due to high uncertainties, except maybe for the longer wavelength regime. The diameter difference between visual maximum and minimum corresponds to a change by (19 ± 17)%. The shapes are very similar, except that at shorter wavelengths the apparent diameters are almost identical. The large FWHM diameter of the dust shell does not change fundamentally on the short pulsation time scale as expected (upper right panel of Figure 5.20), in particular, since the geometry of the silicate dust shell is more dependent on the entire system rather the Mira alone.

Cycle-to-cycle variations: R Aqr was observed over three consecutive pulsations cycles. At each cycle, data at minimum light between phases 0.4 and 0.6 are used to search for cycle-to-cycle variations. These three regions are shaded in the upper panel of Figure 5.2 (page 97). The ranges contain only 5, 4 and 4 observations, respectively, and have therefore only moderate spatial frequency coverages. A circular FDD + Gaussian (model A.13) is fitted to these data points, while the relative flux is fixed to the value obtained for the full data set. The fit to cycle 1 and 3 give acceptable results, while for cycle 2 the Gaussian could not be reasonably constrained due to having no data points at low spatial frequencies.

At cycle 1, the FDD diameter was on average (1.2 ± 6.0) mas below the diameter obtained for the full data set. From cycle 1 to cycle 2 and from cycle 2 to cycle 3, the diameter steadily decreased on average by (3.2 ± 7.9) mas and (3.7 ± 9.8) mas, respectively. This total change by (25 ± 31)% is relatively large compared to R Aql. The Gaussian FWHM increased from cycle 1 to cycle 3 by (25 ± 29) mas, i.e. (27 ± 32)%. This increase might be caused by the additional thermal radiation from the accretion disk of the WD companion, which is located within the dust shell at a distance of around 50 mas[15]. From cycle 1 to cycle 3, the separation vector of the embedded compact emission region and the AGB star becomes parallel to the unchanged baseline orientation, and MIDI gets sensitive to that separated emission (compare Figure 2.16 on page 29 with Figure 5.13 on page 109). This results in an increased Gaussian FWHM, but also in a decreasing FDD diameter due to the lower flux contribution of the layer+star. However, the uncertainties are very high and therefore this change is neither very significant nor representative. The overall shape of the diameter and the Gaussian as function of wavelength does not change notably throughout the cycles.

5.2.5 R Hya

The 64 visibility measurements of R Hya are plotted for one example wavelength bin (bin 8, 9.4 μm) versus spatial frequency in the left panel of Figure 5.21. The relatively high flux of the target and the calibrator entails a comparatively small scatter in the visibility measurements. However, there is still a considerable spread due to including observations obtained at different pulsations phases, pulsation cycles and position angles, and it still reflects uncertainties in the reduction process. The plot shows the data color-coded by visual light phase. It is notable that in the first lobe observations at pre-minimum (red points) lie systematically under the observations done at minimum and post-minimum (green and blue points), if measurements at similar spatial frequencies are compared.

Model: After the first zero at around 31 arcsec^{-1}, the visibilities in the second lobe, which is only partly covered by the observations, remain low. This indicates that a uniform disk (UD) is not a good model representing the data, because it would give a higher second lobe in Fourier space. This gets more obvious if compared with W Hya later in Section 5.2.7. Due to the clear detection of the second lobe, a Gaussian is not appropriate either. Only a model which takes an extended atmosphere into account, exhibiting limb darkening, can fit the data properly. The simplest possibility with only few free parameters and a low second lobe is a fully limb-darkened disk (FDD). In order to account for the flux contribution of an extended silicate dust shell, the

[15]The average Gaussian FWHM, obtained for the full data set, is approximately 100 mas.

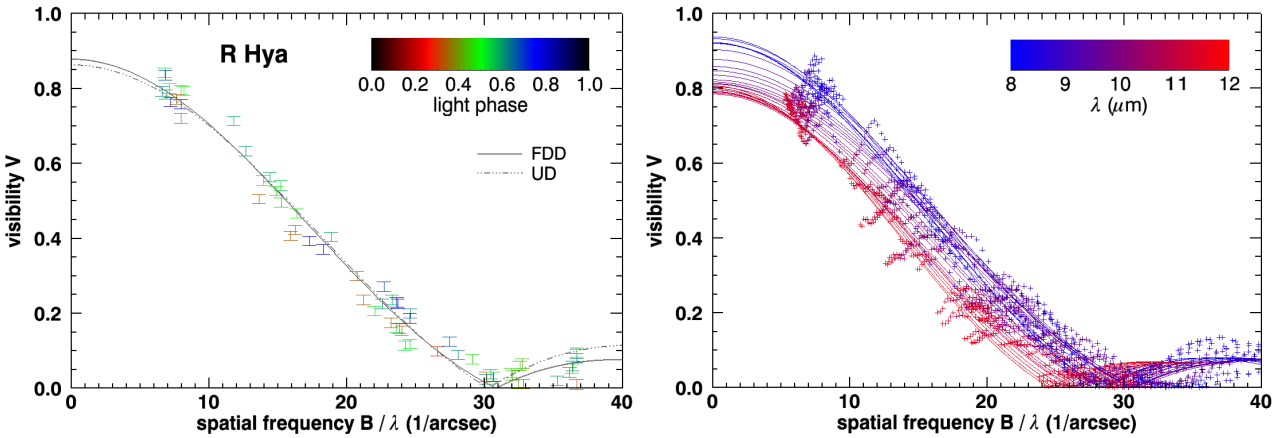

Figure 5.21: *Left:* Fit of a circular fully limb-darkened (FDD) and circular uniform disk (UD) (model A.6 and A.2) to the 64 visibility measurements of R Hya at wavelength bin 8 (9.4 μm). Data, taken over all phases and position angles, are plotted versus spatial frequency and are color-coded by visual light phase. The FDD model fits the data at higher spatial frequencies better. *Right:* Same as left, but for all 25 wavelength bins of model A.6. See Table 5.6 and Figure 5.22 for the obtained fit parameters.

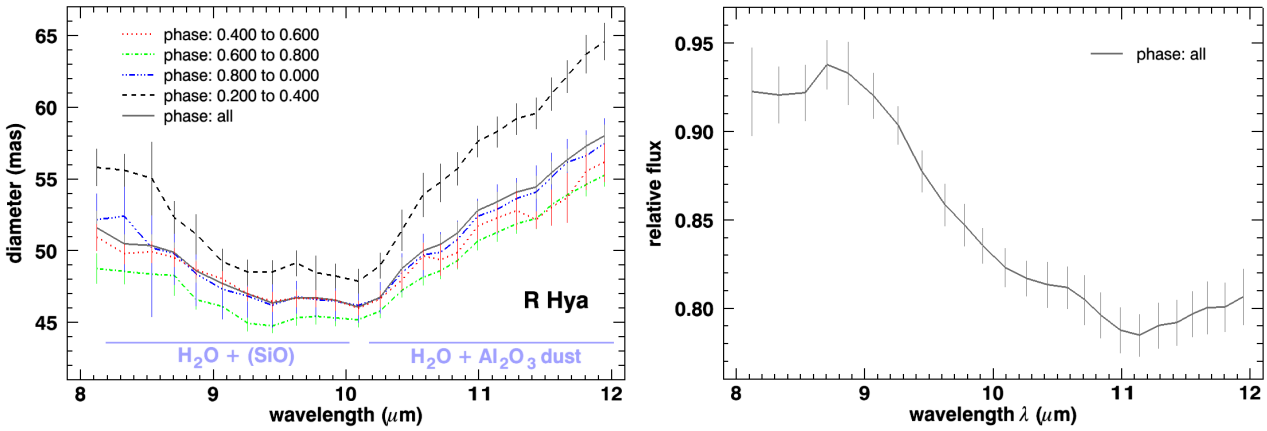

Figure 5.22: Plot of the A.6 model parameters from Table 5.6 for R Hya. *Left:* The fully limb-darkened disk diameter, θ_{FDD}, is given as function of wavelength. The solid gray line shows the fit to all 64 measurements and the other lines the fits to subsequent pulsation phase bins. *Right:* The relative flux, ϵ_{FDD}, of the fully limb-darkened disk obtained for the fit to the full data set. These flux values are fixed for the fit of the FDD to subsequent pulsation phase bins.

visibility function is not forced to be 1 at zero spatial frequency. A Gaussian, representing the dust shell, cannot be constrained by interferometry due to the lack of measurements at very low spatial frequencies (a lower limit is obtained from the limited FOV, cf. Section 5.1.2).

Circular Fit: In addition to the fit of a circular FDD (model A.6), a circular UD (model A.2) is shown in the left panel of Figure 5.21. The second lobe is better fitted with a FDD, but this is not as significant as for W Hya. However, a comparison of the reduced chi square values, χ^2_{r}, in Table 5.6 confirms that a FDD is a better representation of the brightness distribution of

Table 5.6: Model fit results for R Hya: circular fully limb-darkened and circular uniform disk (model A.6 and A.2).

		circular FDD			circular UD		
λ (μm)	ΔV[a]	$\theta_{\rm FDD}$ (mas)	Flux $\epsilon_{\rm FDD}$	$\chi^2_{\rm r}$	$\theta_{\rm UD}$ (mas)	Flux $\epsilon_{\rm UD}$	$\chi^2_{\rm r}$
8.12	0.012	51.6 ± 1.2	0.92 ± 0.03	13	45.6 ± 1.2	0.91 ± 0.02	19
8.33	0.012	50.5 ± 0.7	0.92 ± 0.02	13	43.4 ± 1.2	0.89 ± 0.03	18
8.54	0.012	50.4 ± 0.8	0.92 ± 0.02	14	43.2 ± 0.8	0.89 ± 0.02	19
8.71	0.011	49.9 ± 0.7	0.94 ± 0.01	13	42.9 ± 0.6	0.91 ± 0.02	18
8.87	0.011	48.6 ± 0.8	0.93 ± 0.02	12	42.1 ± 0.6	0.91 ± 0.02	17
9.07	0.012	47.7 ± 0.5	0.92 ± 0.01	10	41.1 ± 0.6	0.90 ± 0.01	13
9.26	0.011	47.0 ± 0.5	0.90 ± 0.01	9	40.5 ± 0.6	0.88 ± 0.01	11
9.45	0.013	46.4 ± 0.6	0.88 ± 0.01	7	40.3 ± 0.6	0.86 ± 0.02	9
9.63	0.011	46.8 ± 0.6	0.86 ± 0.01	9	40.3 ± 0.6	0.84 ± 0.01	11
9.78	0.011	46.7 ± 0.5	0.85 ± 0.01	9	40.3 ± 0.6	0.83 ± 0.01	11
9.92	0.011	46.6 ± 0.6	0.84 ± 0.01	8	40.3 ± 0.6	0.82 ± 0.01	10
10.09	0.011	46.1 ± 0.5	0.82 ± 0.01	8	40.3 ± 0.6	0.81 ± 0.01	10
10.26	0.011	46.8 ± 0.5	0.82 ± 0.01	9	40.9 ± 0.8	0.81 ± 0.01	11
10.42	0.009	48.8 ± 0.8	0.81 ± 0.01	14	42.2 ± 0.6	0.80 ± 0.01	18
10.58	0.009	50.0 ± 0.6	0.81 ± 0.01	16	43.2 ± 0.6	0.79 ± 0.01	21
10.71	0.010	50.5 ± 0.7	0.80 ± 0.01	16	43.7 ± 0.6	0.79 ± 0.01	20
10.84	0.009	51.3 ± 0.8	0.80 ± 0.01	19	44.3 ± 0.6	0.78 ± 0.01	24
10.99	0.008	52.8 ± 0.7	0.79 ± 0.01	21	45.5 ± 0.6	0.77 ± 0.01	28
11.14	0.008	53.4 ± 0.7	0.78 ± 0.01	21	46.0 ± 0.8	0.77 ± 0.02	27
11.29	0.010	54.1 ± 0.7	0.79 ± 0.01	16	46.6 ± 0.8	0.77 ± 0.01	21
11.43	0.011	54.4 ± 0.8	0.79 ± 0.01	13	46.9 ± 0.8	0.77 ± 0.01	16
11.55	0.011	55.5 ± 0.8	0.80 ± 0.01	14	47.8 ± 0.8	0.78 ± 0.01	17
11.67	0.011	56.3 ± 0.8	0.80 ± 0.02	15	48.5 ± 1.0	0.78 ± 0.02	19
11.81	0.008	57.3 ± 0.8	0.80 ± 0.01	29	49.3 ± 1.2	0.78 ± 0.02	37
11.95	0.007	58.0 ± 0.8	0.81 ± 0.02	40	49.9 ± 1.0	0.79 ± 0.02	51

[a] This is the mean visibility error used for the corresponding wavelength bin (see Section 5.2.1).

R Hya. In addition to the best-fit parameters of the circular FDD, Table 5.6 lists the parameters for the circular UD for all 25 wavelength bins as well. They are given in order to compare with values from the literature.

Formal errors are computed as mentioned in Section 5.2.2, while the listed mean visibility errors are derived as described in Section 5.2.1. A residual analysis shows that for each wavelength bin on average about 60% of the measurements are inside the $3\,\sigma$ range. This low value is due to using rather low uncertainties for the visibilities and the fact that this fit does not account for the scatter of the data due to pulsation influences.

The right panel of Figure 5.21 displays the fit to all 25 wavelength bins. Clearly, the first zero shifts to lower spatial frequencies with increasing wavelength, i.e. the FDD diameter, $\theta_{\rm FDD}$, increases with increasing wavelength. At the same time the relative flux contribution, $\epsilon_{\rm FDD}$, of the FDD decreases. This behavior is more exactly shown in the two parameter plots in Figure 5.22.

From these panels it can be derived that $\theta_{\rm FDD}$ actually decreases from (51.6 ± 1.2) mas to (46.6 ± 0.6) mas between 8 and 10 μm, while it gradual increases again at wavelengths longer

than 10 μm, to reach (58.0 $\pm$ 0.8) mas at 12 μm. This corresponds to a relative increase, $\theta_{12\mu m}/\theta_{10\mu m}$, of (24 $\pm$ 2)% in the longer wavelength regime. The diameter increase from 47 mas to 58 mas is equivalent to an increase from 6.1 AU to 7.5 AU at the distance of R Hya. The molecules and close dust species causing this shape are already indicated inside the plot, but will be discussed further in the next chapter. In contrast, the relative flux decreases from (0.92 $\pm$ 0.03) to (0.80 $\pm$ 0.02), reflecting the increased flux contribution from the colder surrounding silicate dust shell detected with longer wavelengths.

Elliptical Fit: A detailed investigation of R Hya shows that asymmetries cannot be studied conclusively, despite the fact that the uv-coverage appears sufficient. A closer look at the uv-coverage, shown in the right panel of Figure 5.16 (page 110), reveals that almost all observations lie in a narrow position angle range between 45° and 90°. Only a few measurements were made at other position angles, and they are unfortunately all located at high spatial frequencies. By only using the data in the narrow position angle range a model cannot be well constrained, and the inclusion of the high spatial frequency points, which are located in the second lobe, makes a model very uncertain and extremely dependent on these points.

In order to get at least an estimation on how strong a possible asymmetry for R Hya is, a simple elliptical FDD[16] (model A.7) is fitted to the measurements in the first lobe, i.e. only the points within the narrow position angle range are considered for the fit. This has also the advantage that only observations are used which were taken at similar visual light phases and are located in a comparatively narrow spatial frequency range.

The fit to the data did not reveal any signs of an elliptical asymmetry. The diameter difference between major and minor axis is on average below the measurement uncertainty. Thus, this result is consistent with no asymmetry at all. However, one should keep in mind that the model was fitted to data with an unfavorable uv-coverage. In comparison, a departure from symmetry will be deduced for W Hya.

Intracycle variations: The pulsation cycle is divided into 5 bins as shown in Figure 5.3 (page 98), and each observation is assigned to the corresponding phase bin. Bins 1, 2, 3 and 5 consist of 27, 20, 3 and 14 observations with phase ranges of $0.4-0.6$, $0.6-0.8$, $0.8-0.0$ and $0.2-0.4$, respectively. There are no observations for bin 4 with a phase range of $0.0-0.2$. Bin 1 contains observations at visual minimum, while no observations were made at visual maximum due to the observational constrains. Only bin 3 provides some pre-maximum measurements.

A circular FDD fit (model A.6) gives the largest diameter for post-maximum (bin 5) with on average (3.7 $\pm$ 1.4) mas above the full data set value. The smallest diameter is obtained at post-minimum (bin 2), with on average (1.9 $\pm$ 1.0) mas below the full data set value. The intermediate bins 1 and 3 are in between, with on average (0.8 $\pm$ 1.1) mas and (0.1 $\pm$ 1.9) mas below the full data set value, respectively. Altogether, this results again in a consistent sinusoidal behavior with a positive delay between maximum diameter and visual maximum. The diameter difference between visual maximum and minimum is (5.6 $\pm$ 1.7) mas. This corresponds to a change by (12 $\pm$ 3)%. Since there are no observations at visual maximum, this value is most probably only a lower limit.

[16]The derivation of an elliptical model from a circular symmetric model can be found in Section 3.1.6.

The individual wavelength dependent trends can be seen in the left panel of Figure 5.22. As can be inferred from the plot, the shapes for each subsequent phase bin are very similar, indicating that the probed different layers at different wavelength behave similarly. The relative flux was fixed to the value obtained for the full data set (shown in the right panel of Figure 5.22). If the flux is not fixed no different insights arise. The diameter values have only a higher scatter.

Cycle-to-cycle variations: R Hya was observed over three consecutive pulsations cycles. At each cycle, data in a small phase range between 0.53 and 0.61 are used to search for cycle-to-cycle variations. These three regions are shaded in the upper panel of Figure 5.3 (page 98) and contain 6, 11 and 7 observations, respectively. Each range consists of data with a sufficient spatial frequency coverage. A circular FDD (model A.6) is fitted to these observations, while the relative flux is fixed to the value obtained for the full data set.

At cycle 1, the FDD diameter was on average (2.4 ± 1.3) mas below the diameter obtained for the full data set. From cycle 1 to cycle 2, the diameter increased on average by (2.5 ± 1.4) mas, and from cycle 2 to cycle 3, θ_{FDD} decreased on average by (1.9 ± 2.0) mas. This means that the maximal variation due to cycle-to-cycle instabilities of the pulsation is on the order of $(5 \pm 3)\%$. The wavelength dependent shape of the diameter does not change notably between cycles. This variation is small but reliable, in particular, since the selected observations constrain the fit of the FDD very reasonably and only a small phase range is used. This allowed also to fit the FDD without fixing the flux values, but no significant differences were notable except for a higher scatter.

5.2.6 V Hya

The 48 visibility measurements of V Hya are plotted for two example wavelength bins (bin 3 at 9.4 μm and bin 20 at 11.3 μm) versus spatial frequency in the upper row of Figure 5.23. Since the target and the calibrator have a comparatively high flux, the scatter in the visibility measurements is acceptable. However, there is a considerable spread notably at higher spatial frequencies. This is due to including observations recorded at different pulsations phases, pulsation cycles and position angles, but can also in particular be attributed to the presence of the temporal and spatially changing high velocity outflows (cf. Section 2.4.4). Both plots show the data color-coded by visual light phase. There are no obvious systematic trends regarding the visual light phase.

Model: A model consistent of two components is necessary to describe the distribution of the visibility measurements. One component is needed to explain the moderate decrease of the visibilities from 10 to 40 arcsec^{-1}. As for the previous stars this could be either a uniform disk (UD) or a fully limb-darkened disk (FDD). Since the second lobe of both models is at much higher spatial frequency, not covered by the observations, these models cannot be distinguished. Since C-rich stars have probably molecular shells as well, the FDD will be preferred in the following.

The second component is essential to account for the points with high visibilities at spatial frequencies around 7 arcsec^{-1}. Similar to O-rich stars, a Gaussian, representing an amorphous

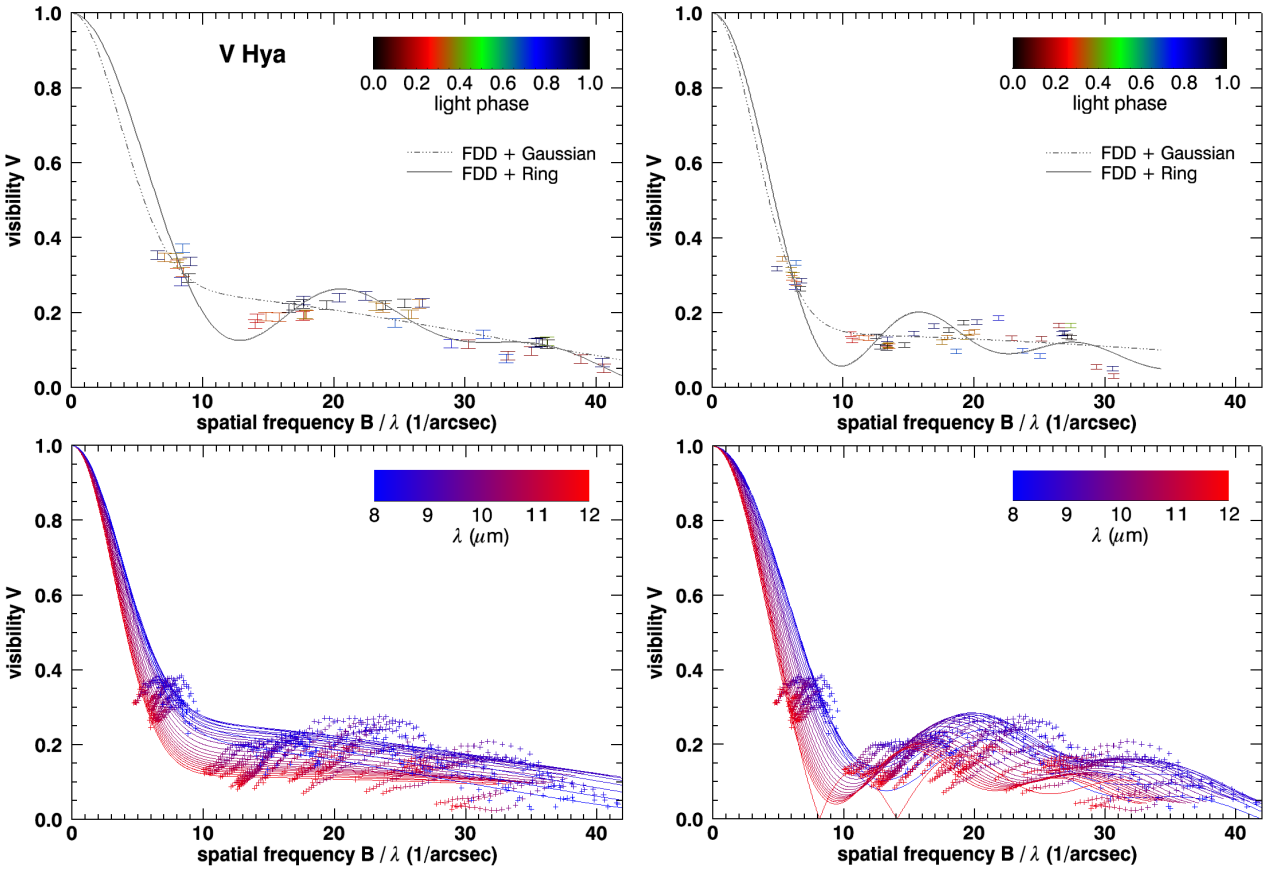

Figure 5.23: *Top:* Fit of a circular fully limb-darkened disk (FDD) + circular Gaussian (model A.13) and a circular fully limb-darkened disk (FDD) + circular uniform ring (model A.12) to the 48 visibility measurements of V Hya at wavelength bin 3 (8.5 μm, *left*) and bin 20 (11.3 μm, *right*). Data, taken over all phases and position angles, are plotted versus spatial frequency and are color-coded by visual light phase. The FDD + ring model fits the observations better at shorter wavelengths, while the FDD + Gaussian model is more suitable at longer wavelengths. *Bottom:* Same as upper, but for all 25 wavelength bins of model A.13 *(left)* and model A.12 *(right)*. See Table 5.7 and Figure 5.24 for the obtained fit parameters.

carbon (AMC) dust shell, could be an adequate function. However, the sinusoidal visibility variation between 10 and 20 arcsec^{-1} (upper left panel of Figure 5.23) suggests a brightness distribution with steep edges. A uniform circular ring with a sharp inner and outer edge could be a proper function describing a dust shell and a sinusoidal modulation. Since the sinusoidal effect is only weak at longer wavelength, as can be inferred from the upper right plot of Figure 5.23, the dust shell is better represented by a Gaussian in this wavelength range. Therefore, both models can be used, each for the appropriate wavelength regime. Due to the lack of measurements at very low spatial frequencies the boundaries of the ring and the Gaussian are less well constrained, respectively.

Circular Fit: The fits of a circular FDD + circular Gaussian (model A.13) and a circular FDD + circular uniform ring (model A.12) are shown in the two plots in the upper row of Figure 5.23. At shorter wavelengths the FDD + ring fits apparently better (left), while at

Table 5.7: Model fit results for V Hya: circular fully limb-darkened disk (FDD) + circular Gaussian (model A.13) and circular fully limb-darkened disk (FDD) + circular uniform ring (model A.12).

		circular FDD + circular Gaussian				circular FDD + circular ring				
λ (μm)	ΔV^{a}	$\theta_{\rm FDD}$ (mas)	Flux $\epsilon_{\rm FDD}$	$\theta_{\rm G}$ (mas)	$\chi^2_{\rm r}$	$\theta_{\rm FDD}$ (mas)	Flux $\epsilon_{\rm FDD}$	$\theta_{\rm r,in}$ (mas)	$\theta_{\rm r,out}$ (mas)	$\chi^2_{\rm r}$
8.12	0.011	28.5 ± 2.0	0.22 ± 0.03	99 ± 6	8	35.3 ± 2.0	0.32 ± 0.04	51 ± 4	124 ± 6	14
8.33	0.011	26.5 ± 2.0	0.25 ± 0.03	100 ± 7	8	31.9 ± 2.0	0.33 ± 0.04	49 ± 4	125 ± 6	12
8.54	0.012	24.5 ± 2.0	0.26 ± 0.03	101 ± 5	8	30.0 ± 2.0	0.34 ± 0.04	50 ± 4	127 ± 6	12
8.71	0.011	22.9 ± 2.0	0.27 ± 0.01	101 ± 5	9	28.7 ± 2.0	0.35 ± 0.04	51 ± 4	129 ± 6	12
8.87	0.011	21.8 ± 2.0	0.27 ± 0.01	102 ± 5	10	27.9 ± 2.0	0.35 ± 0.04	51 ± 4	131 ± 6	12
9.07	0.011	21.0 ± 2.0	0.27 ± 0.03	102 ± 5	11	27.7 ± 2.0	0.35 ± 0.04	51 ± 4	133 ± 6	15
9.26	0.010	20.4 ± 2.5	0.26 ± 0.03	102 ± 4	13	27.7 ± 2.0	0.34 ± 0.04	51 ± 4	135 ± 6	17
9.45	0.010	20.2 ± 2.5	0.25 ± 0.01	103 ± 5	14	27.9 ± 2.0	0.34 ± 0.04	51 ± 4	138 ± 6	20
9.63	0.009	19.8 ± 3.0	0.24 ± 0.03	105 ± 5	18	28.1 ± 2.0	0.33 ± 0.04	52 ± 4	140 ± 6	26
9.78	0.009	19.2 ± 3.0	0.23 ± 0.03	105 ± 5	19	28.1 ± 2.0	0.32 ± 0.04	51 ± 4	143 ± 6	29
9.92	0.008	19.3 ± 3.5	0.23 ± 0.03	105 ± 4	20	28.6 ± 2.0	0.32 ± 0.04	51 ± 4	145 ± 6	30
10.09	0.008	19.8 ± 3.5	0.22 ± 0.01	105 ± 4	25	29.3 ± 2.0	0.31 ± 0.04	50 ± 4	147 ± 6	39
10.26	0.007	20.4 ± 3.5	0.21 ± 0.01	106 ± 4	26	30.4 ± 2.0	0.30 ± 0.04	50 ± 4	149 ± 6	41
10.42	0.006	20.6 ± 3.5	0.20 ± 0.03	107 ± 4	33	31.0 ± 2.0	0.29 ± 0.04	49 ± 4	152 ± 6	56
10.58	0.006	20.6 ± 3.5	0.18 ± 0.03	108 ± 5	35	31.0 ± 2.0	0.27 ± 0.04	46 ± 4	155 ± 6	65
10.71	0.007	20.6 ± 4.0	0.17 ± 0.03	109 ± 5	29	31.1 ± 2.0	0.26 ± 0.04	44 ± 4	157 ± 6	57
10.84	0.006	19.8 ± 4.5	0.17 ± 0.03	111 ± 4	36	30.7 ± 2.0	0.25 ± 0.04	43 ± 4	160 ± 6	73
10.99	0.005	19.2 ± 4.5	0.16 ± 0.01	112 ± 4	41	30.4 ± 2.0	0.24 ± 0.04	41 ± 4	162 ± 6	85
11.14	0.006	18.1 ± 5.5	0.15 ± 0.01	113 ± 4	37	29.2 ± 2.0	0.22 ± 0.04	37 ± 4	165 ± 6	77
11.29	0.006	17.5 ± 6.0	0.15 ± 0.03	114 ± 3	33	28.6 ± 2.0	0.21 ± 0.04	34 ± 4	167 ± 6	70
11.43	0.006	16.9 ± 5.5	0.14 ± 0.01	115 ± 4	33	27.7 ± 2.0	0.20 ± 0.04	29 ± 4	169 ± 6	71
11.55	0.006	16.3 ± 5.0	0.14 ± 0.03	115 ± 5	33	27.8 ± 2.0	0.19 ± 0.04	28 ± 4	171 ± 6	73
11.67	0.006	16.8 ± 5.5	0.13 ± 0.01	117 ± 4	30	28.8 ± 2.0	0.19 ± 0.04	28 ± 4	173 ± 6	69
11.81	0.006	15.0 ± 6.5	0.12 ± 0.03	117 ± 4	34	28.9 ± 2.0	0.18 ± 0.04	28 ± 4	175 ± 6	79
11.95	0.007	14.9 ± 6.5	0.12 ± 0.01	117 ± 4	30	25.5 ± 2.0	0.13 ± 0.04	64 ± 4	146 ± 6	70

[a] This is the mean visibility error used for the corresponding wavelength bin (see Section 5.2.1).

longer wavelengths the FDD + Gaussian seems better (right). However, a comparison of the reduced chi square values, $\chi^2_{\rm r}$, in Table 5.7 reveals that the FDD + Gaussian model is actually the best representation across the whole N-band. Nevertheless, the $\chi^2_{\rm r}$ is very similar between 8 and 9 μm for both models.

The best-fit parameters of both models are given in Table 5.7 for all 25 wavelength bins. Formal errors are computed as mentioned in Section 5.2.2, while the listed mean visibility errors are derived as described in Section 5.2.1. A residual analysis shows that for each wavelength bin on average only half of the measurements are inside the $3\,\sigma$ range. This low value is due to using rather low uncertainties for the visibilities at each wavelength bin and the high scatter of the data at high spatial frequencies. A reduced chi-square investigation of the free parameters verified that no degeneracies are present.

In the lower row of Figure 5.23, the fits to all 25 wavelength bins are shown for both models. The increasingly steep decrease of the Gaussian and ring component at low spatial frequencies (< 10 arcsec^{-1}) with increasing wavelength shows that this component is more extended at

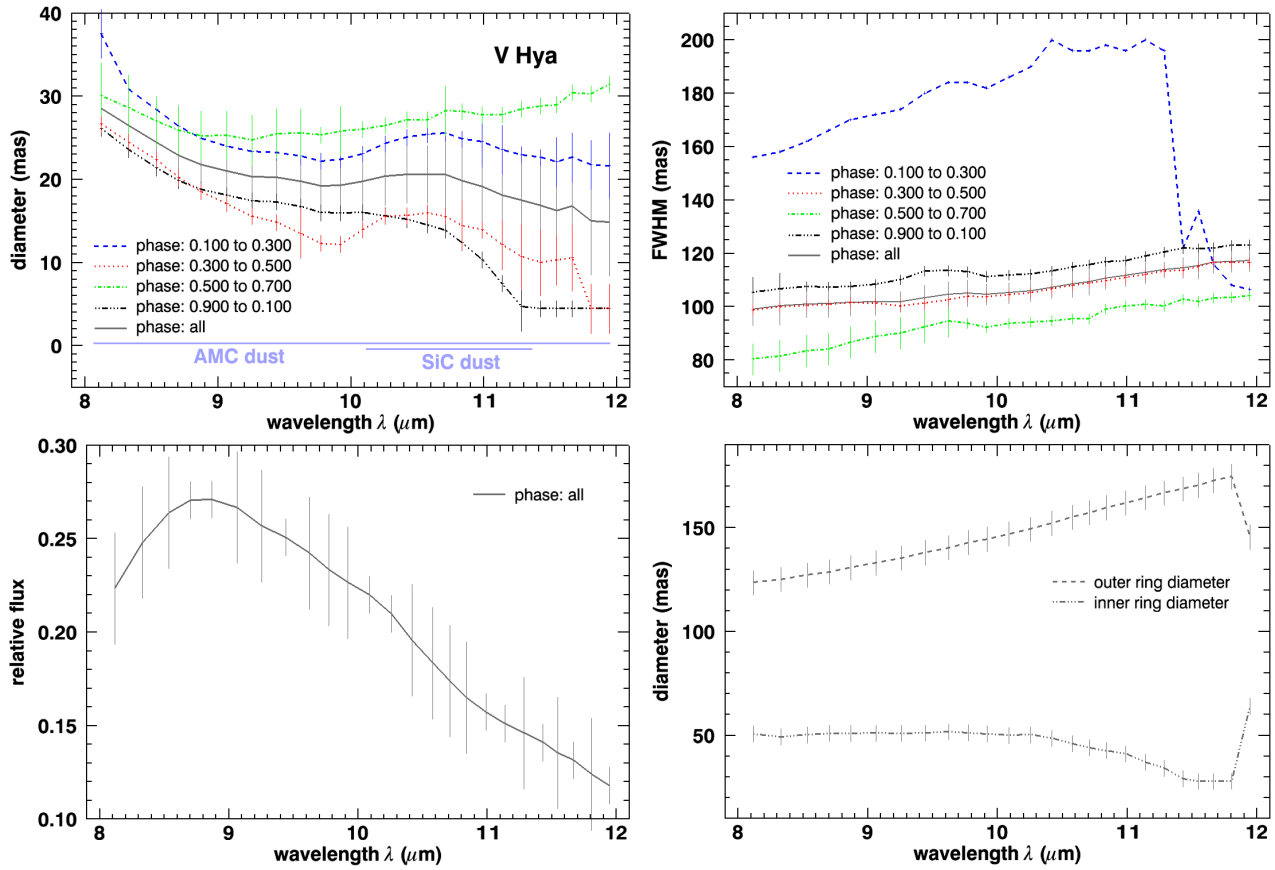

Figure 5.24: Plot of the A.13 model parameters from Table 5.7 for V Hya. *Top:* The fully limb-darkened disk diameter, θ_{FDD}, (*left*) and Gaussian FWHM, θ_{G}, (*right*) are given as function of wavelength. The solid gray lines show the fit to all 48 measurements and the other lines the fits to subsequent pulsation phase bins. *Bottom left:* The relative flux, ϵ_{FDD}, of the fully limb-darkened disk obtained for the fit to the full data set. These flux values are fixed for the fit of the FDD + Gaussian to subsequent pulsation phase bins. *Bottom right:* The inner and outer ring diameters, $\theta_{\mathrm{r,in}}$ and $\theta_{\mathrm{r,out}}$, of model A.12, obtained for the fit to the full data set.

longer wavelengths, respectively. In contrast, the slope of the FDD component for the star/layer decreases with increasing wavelength, yielding that the FDD diameter, θ_{FDD}, decreases. At the same time the relative flux contribution, ϵ_{FDD}, of the FDD decreases as well. This behavior is more exactly shown in the parameter plots in Figure 5.24. The upper plots and the lower left plot refer to model A.13, while the lower right plot shows the inner and outer ring diameter, $\theta_{\mathrm{r,in}}$ and $\theta_{\mathrm{r,out}}$, of model A.12.

It can be inferred from these figures that θ_{FDD} decreases from (28.5 ± 2.0) mas to (14.9 ± 6.5) mas between 8 and 12 μm with a maximum at around 10.6 μm. This corresponds to a relative decrease $\theta_{12\mu\mathrm{m}}/\theta_{8\mu\mathrm{m}}$ of (48 ± 24)%. V Hya is the only C-star in the sample and the only star exhibiting a strong diameter decrease from short to long wavelengths in the N-band. The diameter decrease from 28.5 mas to 14.9 mas is equivalent to a decrease from 10.3 AU to 5.4 AU at the distance of V Hya. The molecules and close dust species causing this shape are already indicated inside the plot, but will be discussed further in the next chapter.

The relative flux decreases from a maximum of (0.27 ± 0.03) at 8.8 μm to (0.12 ± 0.02) at 12 μm, reflecting the increased flux contribution from the colder surrounding amorphous carbon dust shell detected at longer wavelengths. This is similar to the O-rich stars in the sample. As for R Aqr, the flux contribution of the molecule layer/star is considerably lower. This is probably again related to the large amount of dust bound in this system.

The Gaussian FWHM, θ_G, on the other hand steadily increases from (99 ± 6) mas to (117 ± 4) mas between 8 and 12 μm, consistent with the colder parts of the dust shell probed with increasing wavelength. This is equivalent to an increase from 36 AU to 42 AU and sets the characteristic AMC dust shell radius at 10 μm at a distance of about 5.4 ± 1.0 times the layer radius. This dust condensation radius is at a similar distance as for the O-rich star R Aqr. The increase of θ_G with longer wavelengths is consistent with the results for the FDD + ring model. The lower right panel of Figure 5.24 shows that the outer ring diameter increases with increasing wavelength as well. Notable is also that the inner ring diameter approaches the FDD diameter at longer wavelengths. This explains why a Gaussian model fits better this wavelength region, since there is no gap anymore between FDD and ring component.

Elliptical Fit: The uv-coverage of V Hya does not allow a very precise study of asymmetric features (cf. right panel of Figure 5.15, page 110). The uv-plane is even less well sampled compared to R Hya. Observations were mainly made in a narrow position angle range between 45° and 80°, and only a few measurements were obtained at other position angles. As for R Hya, a model cannot be well constrained.

With the spatial frequency coverage of V Hya it was possible to fit a circular FDD for the star/layer and a Gaussian for the dust shell to the observed visibilities. Hence, this could also allow to study asymmetries in both components. Unfortunately, there are not enough measurements at different position angles at low spatial frequencies (around 10 arcsec^{-1}) in order to fit an elliptical Gaussian (model A.5). Even a fit of an elliptical FDD (model A.7) to the visibility data onward 10 arcsec^{-1} is not conclusive due to the high scatter of the measurements in this part. A simultaneous fit to both components is not successful as well, since the fit depends strongly on either the low or high spatial frequency component. Therefore, neither a positive detection nor a negative detection of a departure from symmetry can be concluded for V Hya.

Intracycle variations: The pulsation cycle is divided into 5 bins as shown in Figure 5.4, and each observation is assigned to the corresponding phase bin. Bins 1, 2, 3, 4 and 5 consist of 8, 16, 4, 3 and 17 observations with phase ranges of 0.1−0.3, 0.3−0.5, 0.5−0.7, 0.7−0.9 and 0.9−0.1, respectively. Bin 5 refers to observations at visual maximum and bin 2 and 3 to observations at visual minimum. A FDD + Gaussian is fitted to each of the bins with the relative flux fixed to the value obtained for the full data set (model A.13). No fit could be obtained for bin 4. Even for the other bins, it is problematic to fit the above model. Either points at low spatial frequencies are missing, i.e. the Gaussian could not be constrained satisfactorily, or there are not enough points at high spatial frequencies, i.e. the FDD could not be fitted adequately. This applies in particular to phase bins 1 and 5.

Even though the resulting shapes are similar, the behavior of the layer/stellar diameter is not consistent. If compared with the diameter for the full data set, the fit to bin 1 and bin 3

resulted in a larger diameter, and the fit to bin 2 and bin 5 in a smaller diameter. This is shown in the upper left panel of Figure 5.24. This unusual behavior is probably also caused, in addition to the unfavorable spatial frequency coverage, by the presence of a secondary long period. For this reason only an approximation is given in the following. Assuming that the fits give at least a rough estimate of the diameter variation then the FDD diameter is on average (4.6 ± 6.3) mas larger at visual maximum (bin 1) and on average (5.4 ± 6.5) mas smaller at visual minimum (bin 2). The diameter difference between visual maximum and minimum corresponds to a maximal change of (70 ± 40)%. This presupposes that the diameter is higher at visual maximum and lower at visual minimum, which need not be true concerning the inconsistencies and the large errors.

The Gaussian FWHM is simultaneously fitted to the subsequent visual phases bins. For the reasons mentioned above, phase bin 1 and 4 were excluded. The remaining three phase bins (2, 3 and 5) show a consistent behavior in the sense that at pre-minimum the FWHM diameter is similar to the FWHM obtained for the full data set, and that at post-minimum θ_G is smaller, and at visual maximum θ_G is larger (upper right panel of Figure 5.24). This means that the dust shell traced with MIDI appears smaller after visual minimum, and its size changed by (20 ± 6)%. However, the uncertainties are high and this conclusion might be not true. The fit of a FDD + ring to the subsequent visual phase bins gave no clear results, since the ring diameters could not be constrained reasonably.

Cycle-to-cycle variations: V Hya was observed over three consecutive pulsations cycles. The difficult spatial frequency coverage and the fact that the overlap of observations with similar visual light phases are negligible, no cycle-to-cycle investigations can be performed. Unfortunately, this prevents a study of a possible influence of the secondary long period as well.

5.2.7 W Hya

The 75 visibility measurements of W Hya are plotted for one example wavelength bin (bin 6, 9.1 μm) versus spatial frequency in the upper row of Figure 5.25. As for R Hya, the relatively high flux of the target and the calibrator entails a comparatively small scatter in the visibility measurements. However, there is still a considerable spread due to including observations obtained at different pulsations phases, pulsation cycles and position angles, and it still reflects some uncertainties in the reduction process. The upper left plot shows the data color-coded by visual light phase, while the upper right plot shows the data color-coded by position angle. In both plots systematically displaced distributions are notable. In the upper left panel, observations at visual maximum (dark points) have lower visibilities than these at pre-minimum (red points), if measurements with similar spatial frequencies are compared. However, this trend is very weak. In comparison, the displacement of the two distributions with different position angles is significant in the upper right panel.

Model: After the first zero, the visibilities in the second lobe at around 24 arcsec^{-1} remain low. This indicates that a uniform disk (UD) with a constant brightness distribution up to the edge of the disk cannot be applied to the data. An UD would give a higher second lobe in Fourier

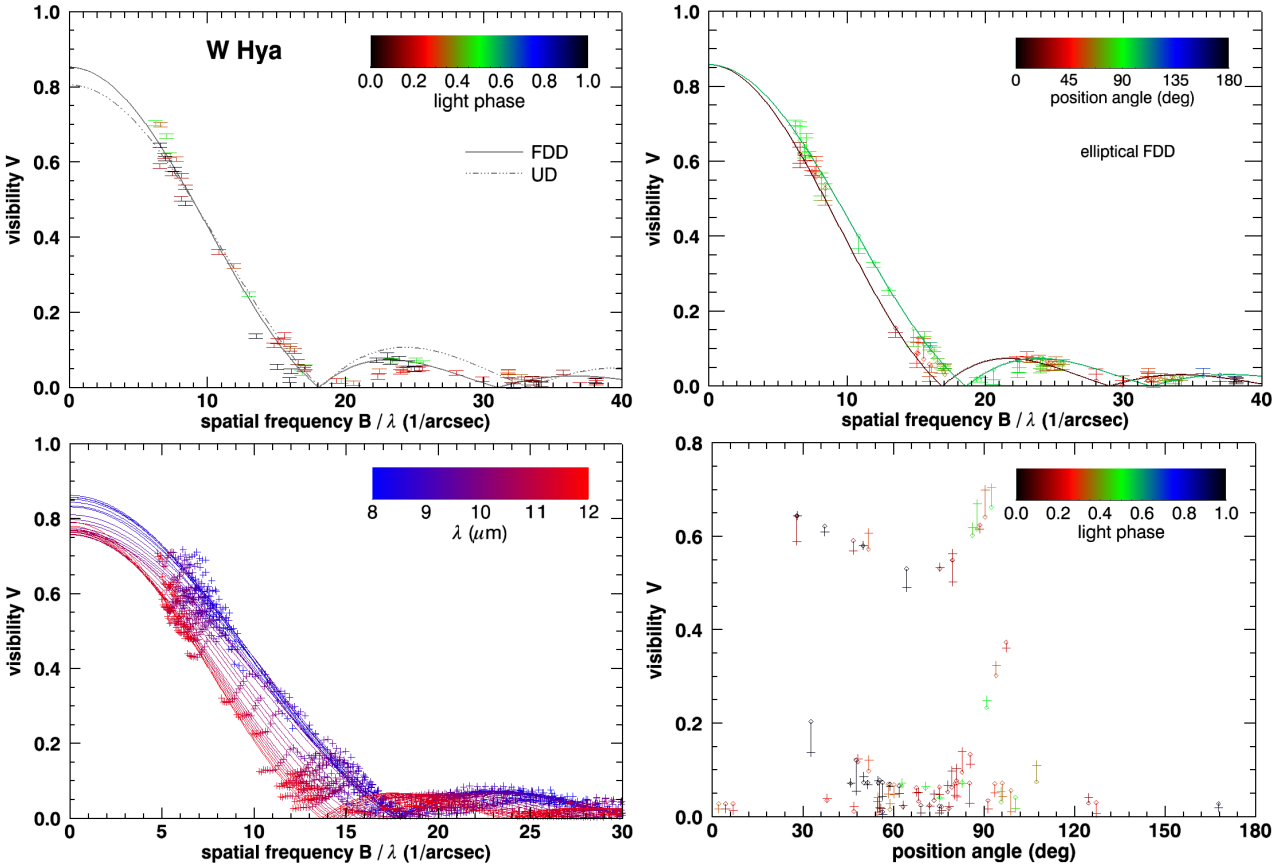

Figure 5.25: *Top:* Fit of a circular fully limb-darkened disk (FDD), circular uniform disk (UD) (model A.6 and A.2, *left*) and elliptical fully limb-darkened disk (model A.7, *right*) to the 75 visibility measurements of W Hya at wavelength bin 6 (9.1 μm). Data, taken over all phases and position angles, are plotted versus spatial frequency and are color-coded by visual light phase (*left*) and position angle (*right*). Clearly, the UD model does not fit the observations well, while the circular FDD describes the data reasonably well. However, the best fit is obtained with an elliptical FDD. The model fit to a given measurement is represented as an open circle and is connected by a line with the corresponding observational point. Both, the fits along the minor and major axis are included. *Bottom left:* Same as upper left, but for all 25 wavelength bins of model A.6. See Table 5.8 and Figure 5.26 for the obtained fit parameters. *Bottom right:* Visibility versus position angle for wavelength bin 6. Measurements (crosses) are connected with their corresponding circular FDD model points (open circles) showing that there is a systematic shift in the difference by going from 0° to 90°.

space. On the other hand, a simple Gaussian is not appropriate either, since a second lobe is clearly detected. Only a model which takes an extended atmosphere into account, resulting in limb-darkening, can fit the data properly. As for R Hya, the simplest possibility with only a few free parameters and a low second lobe is a fully limb-darkened disk (FDD). In order to account for a flux contribution of an extended silicate dust shell, the visibility function is not forced to be 1 at zero spatial frequency. It applies also to W Hya that a Gaussian, representing a dust shell, cannot be constrained by interferometry due to the lack of measurements at very low spatial frequencies (a lower limit is obtained from the limited FOV, cf. Section 5.1.2).

Table 5.8: Model fit results for W Hya: circular and elliptical fully limb-darkened disk (model A.6 and A.7).

		circular FDD			elliptical FDD				
λ (μm)	ΔV^{a}	θ_{FDD} (mas)	Flux ϵ_{FDD}	χ^2_{r}	$\theta_{\mathrm{maj,FDD}}$ (mas)	Axis Ratio η	PA ϑ (°)	Flux ϵ_{FDD}	χ^2_{r}
8.12	0.007	81.0 ± 1.0	0.86 ± 0.02	13	92.5 ± 5.0	0.87 ± 0.07	−1 ± 4	0.89 ± 0.03	11
8.33	0.007	79.9 ± 1.2	0.84 ± 0.01	13	88.4 ± 5.0	0.89 ± 0.08	6 ± 4	0.87 ± 0.03	11
8.54	0.006	80.8 ± 1.0	0.83 ± 0.01	15	89.3 ± 5.0	0.89 ± 0.07	−1 ± 4	0.84 ± 0.03	13
8.71	0.006	80.9 ± 1.6	0.86 ± 0.02	17	90.5 ± 5.0	0.86 ± 0.07	−1 ± 4	0.86 ± 0.03	13
8.87	0.006	79.6 ± 1.0	0.86 ± 0.01	17	84.9 ± 5.0	0.91 ± 0.08	14 ± 4	0.86 ± 0.03	13
9.07	0.006	79.2 ± 1.0	0.85 ± 0.01	18	85.3 ± 5.0	0.89 ± 0.08	15 ± 4	0.86 ± 0.03	13
9.26	0.006	78.0 ± 1.0	0.83 ± 0.02	23	85.1 ± 5.0	0.88 ± 0.08	18 ± 4	0.85 ± 0.03	16
9.45	0.006	77.9 ± 1.2	0.81 ± 0.02	22	87.5 ± 5.0	0.86 ± 0.08	13 ± 4	0.83 ± 0.03	15
9.63	0.006	79.6 ± 1.2	0.80 ± 0.02	25	89.4 ± 5.0	0.85 ± 0.07	14 ± 4	0.81 ± 0.03	17
9.78	0.006	79.8 ± 1.2	0.79 ± 0.02	27	90.5 ± 5.0	0.84 ± 0.07	14 ± 4	0.81 ± 0.03	18
9.92	0.006	79.0 ± 1.2	0.78 ± 0.01	27	89.7 ± 5.0	0.85 ± 0.07	3 ± 4	0.78 ± 0.03	20
10.09	0.005	78.8 ± 1.0	0.77 ± 0.01	31	89.7 ± 5.0	0.85 ± 0.07	3 ± 4	0.78 ± 0.03	23
10.26	0.005	80.4 ± 1.0	0.76 ± 0.01	38	91.5 ± 5.0	0.85 ± 0.07	5 ± 4	0.77 ± 0.03	27
10.42	0.005	84.5 ± 1.4	0.77 ± 0.01	47	93.7 ± 5.0	0.86 ± 0.07	13 ± 4	0.77 ± 0.03	34
10.58	0.005	87.3 ± 1.4	0.77 ± 0.02	45	98.1 ± 5.0	0.84 ± 0.07	15 ± 4	0.78 ± 0.03	30
10.71	0.005	89.2 ± 1.4	0.77 ± 0.01	40	99.6 ± 5.0	0.85 ± 0.07	15 ± 4	0.78 ± 0.03	28
10.84	0.005	91.2 ± 1.2	0.76 ± 0.01	42	102.2 ± 5.0	0.86 ± 0.06	11 ± 4	0.77 ± 0.03	28
10.99	0.004	94.8 ± 1.4	0.76 ± 0.01	46	104.5 ± 5.0	0.86 ± 0.06	15 ± 4	0.76 ± 0.03	31
11.14	0.004	96.3 ± 1.2	0.76 ± 0.01	51	105.7 ± 5.0	0.87 ± 0.06	14 ± 4	0.77 ± 0.03	35
11.29	0.004	97.8 ± 1.2	0.77 ± 0.01	44	106.8 ± 5.0	0.88 ± 0.06	15 ± 4	0.77 ± 0.03	31
11.43	0.005	98.9 ± 1.4	0.76 ± 0.01	35	108.2 ± 5.0	0.87 ± 0.06	15 ± 4	0.77 ± 0.03	25
11.55	0.005	100.5 ± 1.4	0.77 ± 0.01	42	109.8 ± 5.0	0.88 ± 0.06	14 ± 4	0.78 ± 0.03	31
11.67	0.005	101.6 ± 1.4	0.77 ± 0.01	34	110.8 ± 5.0	0.88 ± 0.06	15 ± 4	0.78 ± 0.03	24
11.81	0.004	103.4 ± 1.4	0.78 ± 0.02	53	112.3 ± 5.0	0.88 ± 0.06	16 ± 4	0.79 ± 0.03	39
11.95	0.004	104.7 ± 1.2	0.79 ± 0.01	55	113.2 ± 5.0	0.88 ± 0.06	19 ± 4	0.80 ± 0.03	39

[a] This is the mean visibility error used for the corresponding wavelength bin (see Section 5.2.1).

Circular Fit: In addition to a fit of the circular FDD (model A.6), a circular UD (model A.2) is shown in the upper left panel of Figure 5.25 as well. Clearly, the second lobe is better fitted by a FDD. A comparison of the reduced chi square values, χ^2_{r}, validates that a UD is not a good representation of the brightness distribution of W Hya. This, together with the result for R Hya, verifies that the assumption of using a FDD for R Aql and R Aqr is reasonable. V Hya is not a oxygen-rich star and therefore it should not be assumed a priori that this applies as well, even if it was used for this star.

The best-fit parameters of the circular FDD are given in Table 5.8 for all 25 wavelength bins. Formal errors are computed as mentioned in Section 5.2.2, while the listed mean visibility errors are derived as described in Section 5.2.1. A residual analysis shows that for each wavelength bin on average about 60% of the measurements are inside the $3\,\sigma$ range. This low value is due to using rather low uncertainties for the visibilities and the fact that this fit does not account for the scatter of the data due to pulsation influences.

The lower left panel of Figure 5.25 displays the fit to all 25 wavelength bins. As for R Hya, the first zero shifts clearly to lower spatial frequencies with increasing wavelength, i.e. the

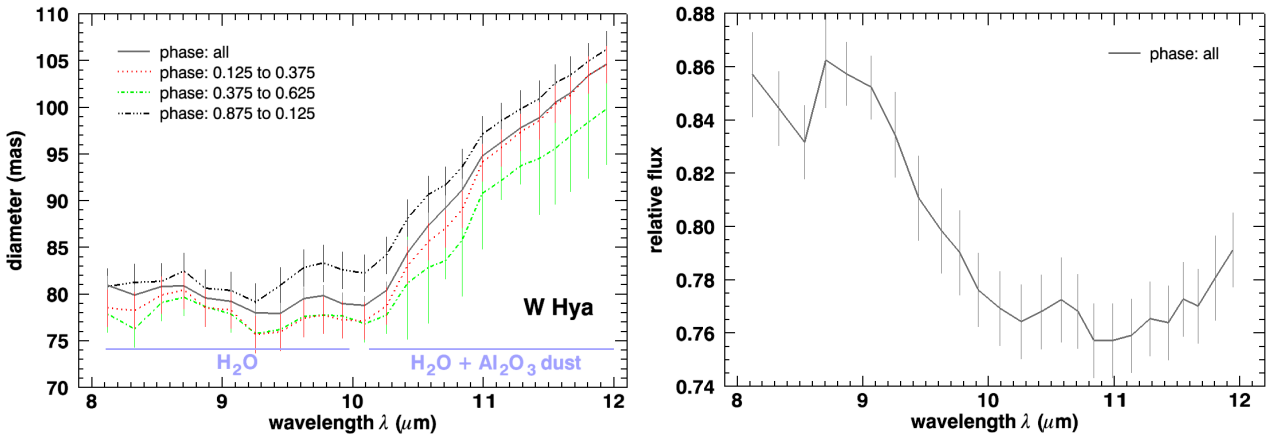

Figure 5.26: Plot of the A.6 model parameters from Table 5.8 for W Hya. *Left:* The fully limb-darkened disk diameter, $\theta_{\rm FDD}$, is given as function of wavelength. The solid gray line shows the fit to all 75 measurements and the other lines the fits to subsequent pulsation phase bins. *Right:* The relative flux, $\epsilon_{\rm FDD}$, of the fully limb-darkened disk obtained for the fit to the full data set. These flux values are fixed for the fit of the FDD to subsequent pulsation phase bins.

FDD diameter, $\theta_{\rm FDD}$, increases with increasing wavelength. At the same time the relative flux contribution, $\epsilon_{\rm FDD}$, of the FDD decreases. This behavior is more exactly shown in the two parameter plots in Figure 5.26.

From these panels it can be derived that $\theta_{\rm FDD}$ actually stays constant at a value of about (80 ± 1.2) mas between 8 and 10 μm, while it gradual increases at wavelengths longer than 10 μm to reach (105 ± 1.2) mas at 12 μm. The diameter increase in the longer wavelength part corresponds to a relative increase, $\theta_{12\mu{\rm m}}/\theta_{10\mu{\rm m}}$, of (31 ± 3)%. This increase from 80 mas to 105 mas is equivalent to an increase from 7.1 AU to 9.5 AU at the distance of W Hya. The molecules and close dust species causing this shape are already indicated inside the plot, but will be discussed further in the next chapter. In contrast, the relative flux decreases from (0.85 ± 0.02) to about (0.77 ± 0.02), reflecting the increased flux contribution from the colder surrounding silicate dust shell going to longer wavelengths.

Elliptical Fit: In order to study asymmetries, the application of elliptical models give first indications as shown for R Hya. An alternative approach is to fit a circular model with a number of spots offset from the center. Since this requires more boundary conditions, a physical indication, and an in general better uv-coverage as for W Hya (cf. right panel of Figure 5.16, page 110), only an elliptical FDD is fitted to the data. Another reason is that a dependence on the visual light phase brings already additional complexity into the model (see below). The presence of an asymmetry could already be inferred from the lower right panel of Figure 5.25, where the visibilities of the observations and the visibilities of a circular FDD are compared as function of position angle. Obviously, the difference between both quantities changes its sign going from 0° to 90°. This can be even noticed for the low visibilities in the plot. The location of these measurements in the increasing part of the second lobe (18 to 24 arcsec^{-1}) leads to the expected inverse systematic.

Since observations at similar pulsation phases were conducted at similar position angles, the

effect of measuring different star/layer diameters, due to asymmetry and due to pulsation is unfortunately not easy to disentangle for W Hya. At visual minimum, the position angle (PA) range is about 80° to 100° (green tick marks in the visual light phase plot, lower panel of Figure 5.5, page 100). At these position angles the visibilities are higher than expected for a circular FDD, i.e. a smaller diameter is observed. At visual maximum, the PA range is about 50° to 60° (red tick marks in the visual light phase plot) with the result of getting lower visibilities as expected for a circular FDD, i.e. a larger diameter. This trend is also notable by comparing the two upper panels of Figure 5.25. In the first lobe the measurements at visual maximum (dark points in the left panel), which are located systematically under the other points, referring to the red points with position angles of 50° to 60° in the right panel.

This follows if all 75 observations over all 3 pulsation cycles are included in the study. A careful analysis, as described below, reveals the presence of both effects in W Hya, with the result that the diameter variation due to an elliptical asymmetry and due to a pulsation dependence is on the same order of magnitude.

Studying asymmetric features requires a good angular uv-coverage at each projected baseline length obtained within a reasonable time. For this reason, the elliptical FDD (model A.7) is fitted to subsets of the full data set, which have similar spatial frequencies and a small visual light phase range at a certain pulsation cycle. For all these configurations the resulting fits show a similar non-uniformity with comparable position angles and axis ratios. The fit was repeated for the full data set to obtain an overall departure from symmetry and to have a more reliable uncertainty estimation, since the subsets have a high scatter and can contain discordant values due to fewer observations used. The similar results for each subset show that at least for W Hya the ellipticity is to the first order stable over few years, over a certain angular extension and not dependent on the pulsation phase. Therefore, the parameters obtained for the full data set, as stated in Table 5.8, are reliable.

In that table, the major diameters, $\theta_{\mathrm{maj,FDD}}$, the axis ratios, η, the position angles, ϑ, and the relative fluxes, ϵ_{FDD}, are given for all wavelength bins. The mean ϑ and the mean η over the full wavelength range is $(11.2 \pm 6.2)^\circ$ and (0.87 ± 0.07), respectively. Compared to the circular FDD, the fluxes are identical within the errors as expected, while the reduced chi square estimates gave lower values, thus indicating a slightly better model. The upper right panel of Figure 5.25 presents the fit of the elliptical FDD to the data for wavelength bin 6 (9.07 μm). The visibility model curves for the minor and mayor axis are drawn together with the data points, showing that the perpendicular axes fit the measurements at the corresponding position angles.

However, the parameter errors are most probably underestimated because of the high number of free parameters in combination with not negligible uncertainties in the data. In particular, the PA estimation is not very well constrained, and the error might be more on the order of 15° to 20°, if compared with all fitted subsets. Hence, the derived numbers are more indicative rather than completely determined, and a non-departure from symmetry cannot be ruled out completely. The investigation of the differential phases obtained with MIDI are unfortunately not conclusive, since they are smaller than the assumed errors (cf. Section 4.2.3). It can only be deduced that a departure from point-symmetry cannot be very high[17].

[17] An elliptical FDD is a point-symmetric function, thus this kind of asymmetry can never be detected with the differential phases of MIDI.

Intracycle variations: The pulsation cycle is divided into 4 bins as shown in Figure 5.5 (page 100), and each observation is assigned to the corresponding phase bin. Bins 1, 2 and 3 consist of 23, 42 and 10 observations with phase ranges of $0.875 - 0.125$, $0.125 - 0.375$ and $0.375 - 0.625$, respectively. There are no observations for bin 4 with a phase range of $0.625 - 0.875$. Bin 1 contains observations at visual maximum and bin 3 observations at visual minimum.

In order to estimate a light phase dependent angular diameter in the presence of a position angle dependence, the projected baseline values of the input data are shifted in a way that the elliptical model transforms into a circular model. The derived parameters from the elliptical FFD fit are used for this shearing. Due to this arbitrary shift the fitted absolute diameter values are not meaningful and only differences with respect to a fit of a circular FDD to the full sheared data set are given.

A fit of a circular FDD (model A.6) to the sheared data of the intermediate phase bin (bin 2) gives an on average (1.2 ± 2.3) mas smaller diameter. The difference between maximum phase, with an on average (2.2 ± 2.3) mas greater diameter, and minimum phase, with an on average (3.2 ± 3.7) mas smaller diameter, is (5.4 ± 1.8) mas. This corresponds to a percentage change of $(6 \pm 2)\%$. Having an apparently larger diameter at visual maximum and an apparently smaller diameter at visual minimum is therefore common for all four oxygen-rich stars investigated in this study.

The individual wavelength dependent trends can be seen in the left panel of Figure 5.26. As can be inferred from the plot, the shapes for each subsequent phase bin are very similar, indicating again that the different layers probed at different wavelength behave similarly. The relative flux was fixed to the value obtained for the complete data set (shown on the right panel of Figure 5.26).

Cycle-to-cycle variations: W Hya was observed over three consecutive pulsation cycles. At each cycle, data between phase 0.2 and 0.4 are used to search for cycle-to-cycle variations. These three ranges are shaded in the upper panel of Figure 5.5 (page 100). The ranges contain 8, 8 and 11 observations, respectively, and have a sufficient spatial frequency coverage. A circular FDD (model A.6) is fitted to these observations (sheared as described above), while the relative flux is fixed to the value obtained for the full data set. This compensates for fewer measurements and avoids the problem to be too dependent on fewer points at low spatial frequencies (< 10 arcsec^{-1}).

Cycle 1 and 2 give similar diameters, with values on average of about (3.0 ± 2.5) mas below the diameter obtained for the full data set. The diameter for cycle 3 is marginally higher, being on average (1.5 ± 3.0) mas above the full data set value. This means that the maximal variation due to cycle-to-cycle instabilities of the pulsation is on the order of $(5 \pm 4)\%$, and therefore very similar to R Hya. However, regarding the uncertainties this is only marginally significant for W Hya. The wavelength dependent shape of the diameter does not change notably between cycles.

5.3 Wavelength Dependence of the Diameter

This section sets the previously obtained FDD diameters in relation to diameters measured at other wavelengths. Figures 5.27 to 5.31 show interferometric angular diameter determinations reported from various authors from the visual to the mid-IR ($0.5 - 15$ μm). They are obtained by fitting a Gaussian (G, green), a uniform disk (UD, red) or a fully limb-darkened disk (FDD, blue) to the data. A conversion between the models is not performed, since the various diameter determinations depend on the spatial frequency coverage[18]. The information on visual phases and position angles (if applicable) of these observations can be found in Table 5.9 (page 140).

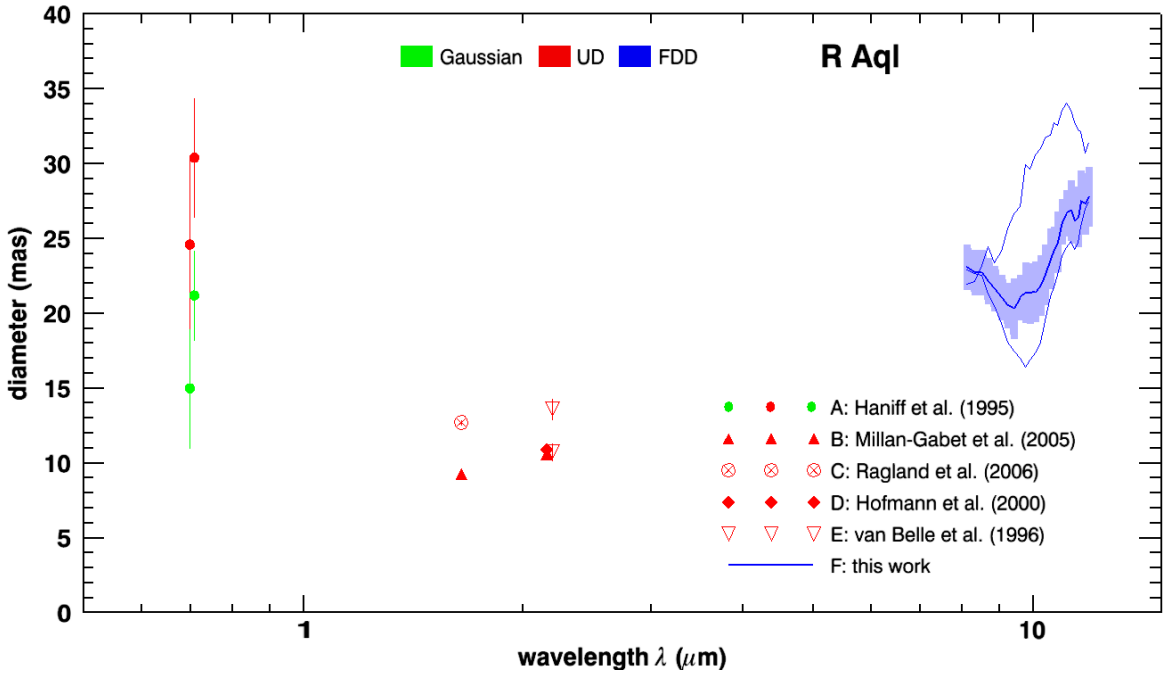

Figure 5.27: Diameter measurements of R Aql over a wide wavelength range reported by various authors. In addition to the N-band diameter obtained for the full data set (thick blue line) in this work, diameters for maximum (upper thin blue line) and minimum visual phase (lower thin blue line) are given as well. See Table 5.9 (page 140) for more details.

In addition to the FDD diameter, derived for the fit to the full data set in this study, the diameter trend at visual maximum (upper curve) and visual minimum (lover curve) is plotted for each star as well. The observed apparent diameter changes dramatically within the given wavelength range due to the strong wavelength dependent opacity of the atmospheric constituents (Baschek et al., 1991; Scholz, 2001). This can best be seen in the plots of the O-rich stars R Hya and W Hya (Figures 5.29 and 5.31). Diameter measurements over a large wavelength range are available for this two stars. In the optical, the measured diameters are sensitive to TiO bands. The largest variations are around the strongest bands at 712 nm and 670 nm with apparent diameter enlargements of up to a factor of 2.

For R Hya and W Hya it is notable that the diameters from Ireland et al. (2004a) are systematically larger compared to the diameters obtained by Haniff et al. (1995) and Tuthill et al.

[18]Empirical conversion factors are approximately: FDD $\approx$ 1.15 UD $\approx$ 1.68 FWHM.

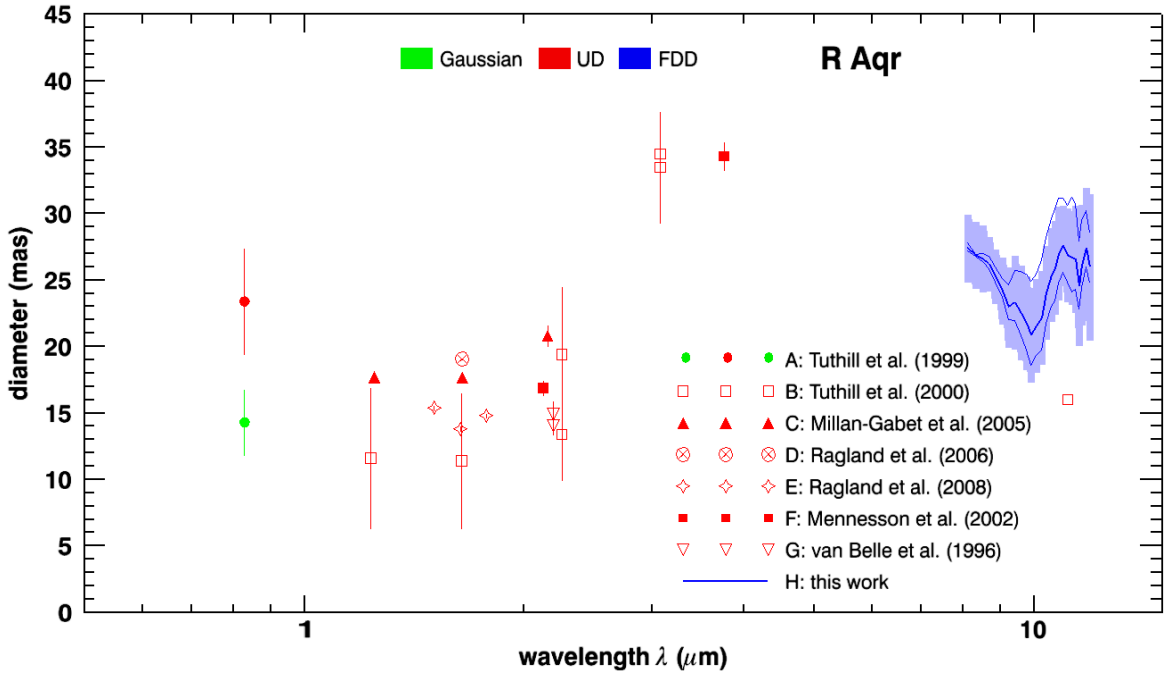

Figure 5.28: Same as Figure 5.27, except for R Aqr. See Table 5.9 for more details.

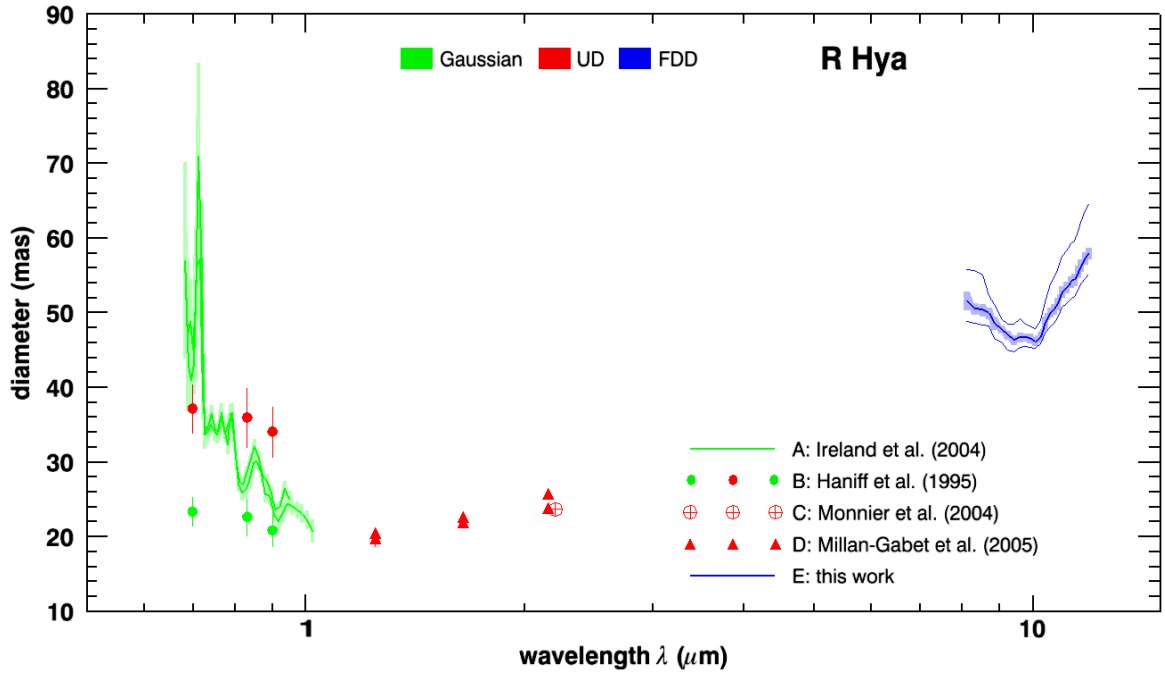

Figure 5.29: Same as Figure 5.27, except for R Hya. See Table 5.9 for more details.

(1999), respectively. Since both stars were observed by Ireland et al. (2004a) at around visual minimum and by the other authors at around visual maximum, this may imply that significant dust production occurs near minimum (Ireland et al., 2004a). Ireland et al. (2004a) suggested that the large increase in apparent diameter towards the blue is caused from light scattered by dust.

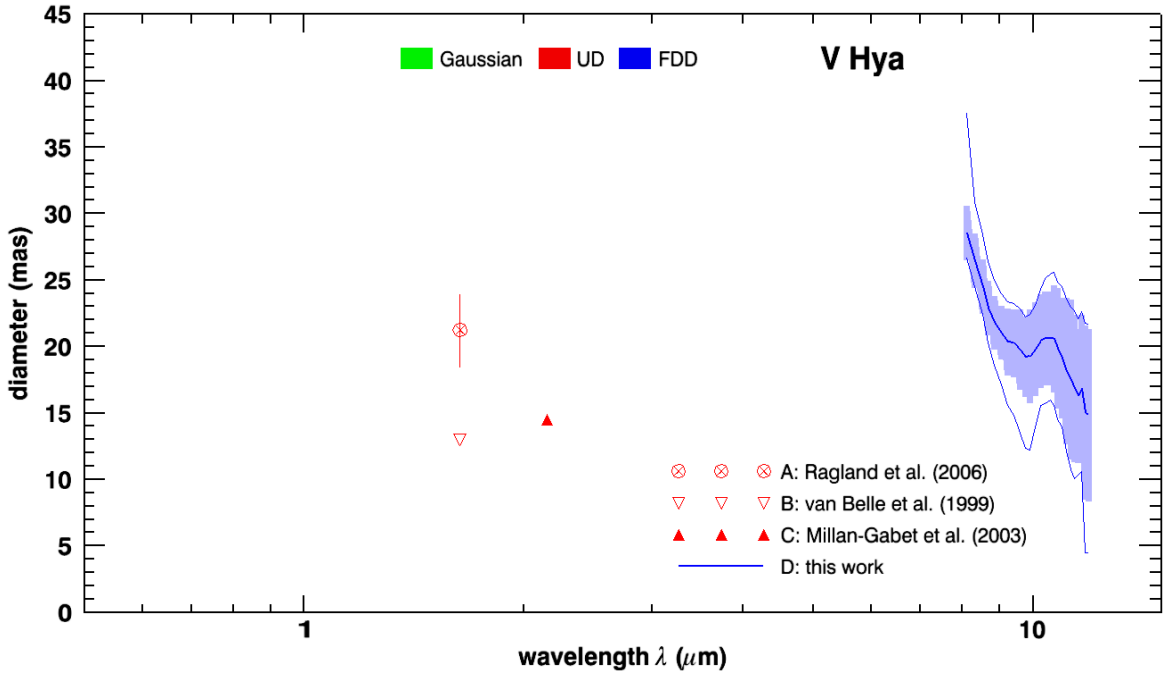

Figure 5.30: Same as Figure 5.27, except for V Hya. See Table 5.9 for more details.

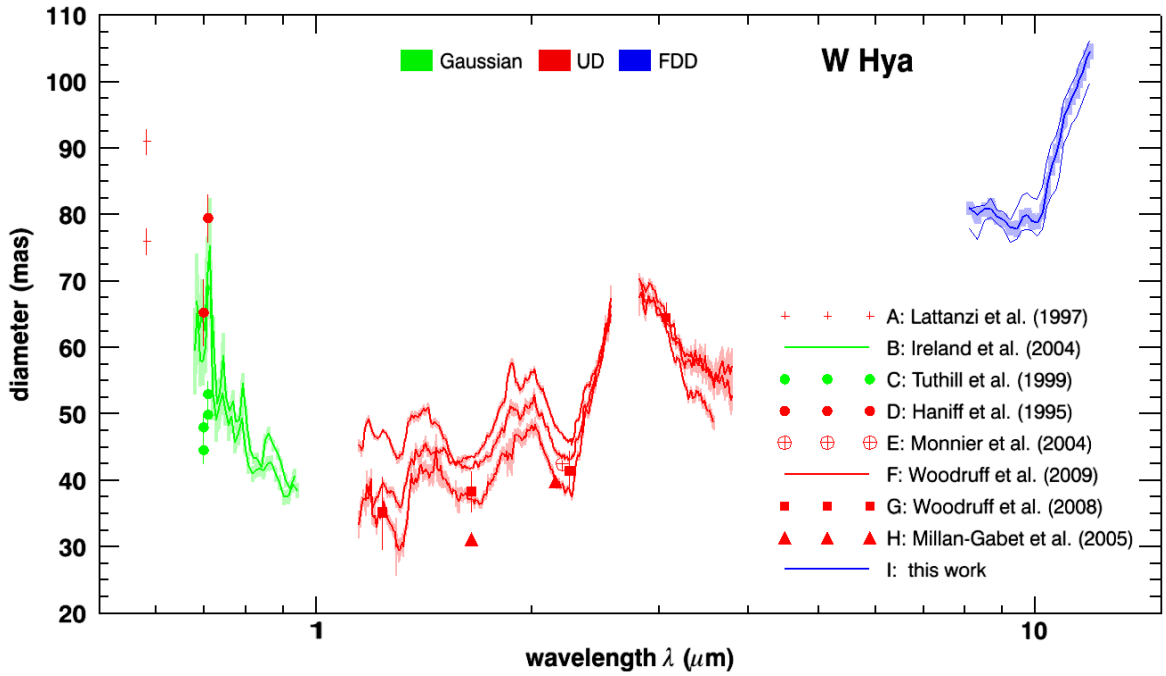

Figure 5.31: Same as Figure 5.27, except for W Hya. See Table 5.9 for more details.

In the near-IR, predominantly H_2O and CO in different layers are responsible for the wavelength dependence of the diameter (cf. Section 2.2.2 and 5.1.2). Most of the observations were conducted at J, H and K band (1.25, 1.65 and 2.16 μm, respectively). For R Aqr measurements at L-band (3.8 μm) are available as well. It can be again inferred from Figure 5.31 that also in the near-IR diameters vary by a factor of 2, and that there is a complex diameter dependence

on pulsation cycle and pulsation phase (cf. Woodruff et al., 2009). This has been reported for a large number of AGB stars (e.g. Weiner et al., 2003).

V Hya is the only carbon star in the sample. Unfortunately, only H and K-band observations are published. Diameter determinations for C-stars in these bands are mainly influenced by the presence of molecular shells consisting of C_2H_2, HCN, CN and CO (Paladini et al., 2009). The shapes of the N-band diameters will be discussed in the next chapter in detail.

Since the emission comes from multiple layers and contaminations by nearby continuum emission has a strong influence, the filter bandwidth of the observation plays a significant role. However, a reasonable estimation for the true photospheric diameter of an AGB star can be obtained from uniform disk measurements at K-Band. The K-band diameter is approximately 1.2 times the true photospheric diameter (e.g. Millan-Gabet et al., 2005).

Maser observations of different molecules give additional diameter constraints. SiO and H_2O masers probe inner regions where the molecule spheres are present and the dust formation takes place, while OH masers trace wind regions further out (cf. Section 2.2.2). Both, the K-band and SiO maser diameters are therefore important in the next chapter for the interpretation of the size of the mid-IR diameters obtained in this work. They will also be given in the following.

R Aql: There are four measurements at K-band by the authors given in Table 5.9. The average of all results in a diameter, $\theta_{\mathrm{UD},2.2\mu\mathrm{m}}$, of (11.5 ± 1.4) mas, where the error is obtained from the standard deviation. This corresponds to a N-band to K-band ratio, $\theta_{\mathrm{FDD},10\mu\mathrm{m}}/\theta_{\mathrm{UD},2.2\mu\mathrm{m}}$, of 1.9 ± 0.3. Ring diameters for SiO masers were measured by the authors given in Section 2.4.1 at 43.1 and 42.8 GHz. The average of these diameters is (24.2 ± 2.7) mas, which gives a ratio, $\theta_{\mathrm{SiO}}/\theta_{\mathrm{FDD},10\mu\mathrm{m}}$, of 1.1 ± 0.2, meaning that the FDD and SiO diameters are similar. The H_2O maser ring diameter at 22 GHz were determined to about 330 mas (Lane et al., 1987).

R Aqr: A lot of diameter measurements at single wavelengths are available for R Aqr. The average of all diameters at K-band of the authors given in Table 5.9 is (16.6 ± 3.0) mas. This gives a ratio, $\theta_{\mathrm{FDD},10\mu\mathrm{m}}/\theta_{\mathrm{UD},2.2\mu\mathrm{m}}$, of 1.3 ± 0.3, which is much smaller compared to the ratio obtained for R Aql. From Figure 5.28, it is notable that the diameters at 3.1 and 3.8 μm are more than two times larger compared to the near-IR, and even higher compared to the N-band. This indicates that probably an extended halo of OH is present above the atmospheric layers. The ionizing radiation of the compact close companion might be the reason for the occurrence of OH molecules so close to the Mira. However, the specific opacity characteristics of H_2O and CO or the existence of hot circumstellar dust could be an alternative reason (Tuthill et al., 2000). These effects might have also influences in the K-band and mid-IR and could be the reason for the small N-band to K-band ratio as well (see discussion in the next chapter).

The given diameter at 11.15 μm is unfortunately only the photospheric diameter used for the radiative modeling by Tuthill et al. (2000). This value is consistent with the K-band diameters, but can therefore not be compared with the MIDI measurements, since MIDI traces the molecular spheres. SiO maser ring diameters, as given by the authors in Section 2.4.2, average to (31.7 ± 1.2) mas. Hence, the corresponding SiO maser to N-band ratio, $\theta_{\mathrm{SiO}}/\theta_{\mathrm{FDD},10\mu\mathrm{m}}$, is 1.5 ± 0.3 and larger compared R Aql. However, if the SiO ring diameter is set in relation to the K-band diameter it becomes clear that the SiO maser is located at a similar distance to

the star as for R Aql.

R Hya: Ireland et al. (2004a) measured diameters between 0.7 and 1.0 μm at two different position angles (123° and 72°), but could not derive any departure from symmetry. The three K-band diameter measurements by the authors given in Table 5.9 average to (24.5 ± 1.2) mas. This corresponds to a N-band to K-band ratio, $\theta_{\mathrm{FDD},10\mu\mathrm{m}}/\theta_{\mathrm{UD},2.2\mu\mathrm{m}}$, of 1.9 ± 0.1. Ring diameters of masers have not been published for R Hya so far.

V Hya: Only one diameter measurement at K-band is available for V Hya. Millan-Gabet et al. (2003) fitted a UD + Gaussian model to the visibilities obtained at 2.2 μm. This resulted in an UD diameter of (14.5 ± 0.3) mas with a total flux contribution of 0.63 ± 0.02. The Gaussian FWHM were constrained to (35 ± 3) mas. This gives ratios, $\theta_{\mathrm{FDD},10\mu\mathrm{m}}/\theta_{\mathrm{UD},2.2\mu\mathrm{m}}$ and $\theta_{\mathrm{G},10\mu\mathrm{m}}/\theta_{\mathrm{G},2.2\mu\mathrm{m}}$, of 1.3 ± 0.2 and 3.0 ± 0.3, respectively. Since at K-band hotter circumstellar material is probed, it is reasonable that the ratio of the Gaussian FWHMs is comparatively high.

However, the ratio of the molecular layer FDD to K-band UD is similar to R Aqr. This could be again related to the fact that both stars are close binary system with a large dust content. Since V Hya displays a completely different chemistry, this could be just a coincidence. The high sublimation temperature of amorphous carbon (compared to silicate dust in O-rich stars) leads in general to a closer and more intensive dust production in C-rich star. Diameter measurements of close maser emission regions have not been published for this star so far.

W Hya: Gaussian diameters between 0.7 and 1.0 μm were measured by Ireland et al. (2004a) at two position angles (120° and 252°). Even if there is a small trend notable in Figure 5.31, the authors concluded that this is not significant, since a departure from symmetry was below the uncertainties of the measurement. The near-IR curves by Woodruff et al. (2009) show very clearly how strong the diameter depends on the pulsation phase. The gap at around 2.7 μm originates from telluric contaminations. In comparison to R Aqr, the diameters are relatively small between 3 and 4 μm. It is also obvious that at K-band the curve has a minimum. The average of all diameters at 2.2 μm of the authors given in Table 5.9 is (42.8 ± 3.5) mas. This gives a ratio, $\theta_{\mathrm{FDD},10\mu\mathrm{m}}/\theta_{\mathrm{UD},2.2\mu\mathrm{m}}$, of 1.8 ± 0.2 and validates the ratios obtained for R Aql and R Hya. R Aqr and V Hya have different ratios for the reasons mentioned above.

Ring diameters for SiO masers were measured by the authors given in Section 2.4.5. The average of these diameters is (77.3 ± 10.5) mas, which gives a ratio, $\theta_{\mathrm{SiO}}/\theta_{\mathrm{FDD},10\mu\mathrm{m}}$, of 1.0 ± 0.1. This is consistent with the ratios obtained for R Aql and R Aqr. H_2O maser ring diameters for W Hya are on the order of 300 mas, while OH maser ring diameters at 1665 and 1667 MHz were determined to about 700 and 1130 mas, respectively.

Table 5.9: Details of the diameter measurements presented in figures 5.27 to 5.31 for all targets. Given are the models (G = Gaussian, UD = uniform disk and FDD = fully limb-darkened disk), the phases and the position angles (PA) if applicable. The phase refer to the phase determined by the author.

R Aql: Author	Model	Phase	Comments
A: Haniff et al. (1995)	UD+G	0.06	UD and Gaussian at 700 and 710 nm
B: Millan-Gabet et al. (2005)	UD	0.90	UD diameter for the H and K band
C: Ragland et al. (2006)	UD	0.70	UD diameter for the H band
D: Hofmann et al. (2000)	UD	0.17	UD diameter for the K band
E: van Belle et al. (1996)	UD	0.90 & 0.31	upper for phase 0.31 & lower for phase 0.90 (K band)
F: this work	FDD	0.00 & 0.50	full data set (middle) & max/min light (upper/lower)
R Aqr: Author	Model	Phase	Comments
A: Tuthill et al. (1999)	UD+G	–	UD and Gaussian at 830 nm
B: Tuthill et al. (2000)	UD	0.12 & 0.68	phase 0.68 for upper/lower point at 2.2/3.1 μm
C: Millan-Gabet et al. (2005)	UD	0.40	UD diameter for the J, H and K band
D: Ragland et al. (2006)	UD	0.30	UD diameter for the H band
E: Ragland et al. (2008)	UD	$0.60 - 1.11$	UD diameters around the H band at different phases
F: Mennesson et al. (2002)	UD	0.41 & 0.51	UD diameter for the K and L band
G: van Belle et al. (1996)	UD	0.34 & 0.57	upper for phase 0.34 & lower for phase 0.57 (K band)
H: this work	FDD	0.00 & 0.50	full data set (middle) & max/min light (upper/lower)
R Hya: Author	Model	Phase	Comments
A: Ireland et al. (2004a)	G	0.62	upper for PA 123° & lower for PA 72°
B: Haniff et al. (1995)	UD+G	0.28	UD and Gaussian at 700, 833 and 902 nm
C: Monnier et al. (2004)	UD	0.50	UD diameter for the K band
D: Millan-Gabet et al. (2005)	UD	0.80	UD diameters for the J, H and K band
E: this work	FDD	0.00 & 0.50	full data set (middle) & max/min light (upper/lower)
V Hya: Author	Model	Phase	Comments
A: Ragland et al. (2006)	UD	0.10	UD diameter for the H band
B: van Belle et al. (1999)	UD	0.00	UD diameter for the H band
C: Millan-Gabet et al. (2003)	UD	–	UD diameter for the K band
D: this work	FDD	0.00 & 0.50	full data set (middle) & max/min light (upper/lower)
W Hya: Author	Model	Phase	Comments
A: Lattanzi et al. (1997)	UD	0.64	perpendicular axes ($\eta \approx 0.86$, PA $\approx 143°$, 583 nm)
B: Ireland et al. (2004a)	G	0.44	upper curve for PA 120° and lower curve for PA 252°
C: Haniff et al. (1995)	UD	0.04	UD diameter at 700 and 710 nm
D: Tuthill et al. (1999)	G	0.04	elliptical G at 700 and 710 nm ($\eta \approx 0.94$, PA $\approx 93°$)
E: Monnier et al. (2004)	UD	0.50	UD reported as a bad fit to the data (K band)
F: Woodruff et al. (2009)	UD	$0.58 - 1.53$	phase 0.58 (middle), 0.79 (lower) and 1.53 (upper)
G: Woodruff et al. (2008)	UD	$0.50 - 1.00$	mean of multiple measurements in given phase range
H: Millan-Gabet et al. (2005)	UD	0.60	UD diameter for the H and K band
I: this work	FDD	0.00 & 0.50	full data set (middle) & max/min light (upper/lower)

Chapter 6

Interpretation and Discussion

In the previous chapter the mid-IR light curves, the spectra and the results from the visibility modeling (star/layer and dust shell diameters) were presented and set in relation to diameters obtained at other wavelengths by other authors and to the visual light curves. In addition, asymmetries were investigated. Table 6.1 summarizes all important results obtained in the last chapter.

The results are interpreted and discussed in this chapter. In particular, the wavelength dependence of the fully limb-darkened disk diameter is studied in more detail. General conclusions will be derived for oxygen and carbon-rich stars concerning their molecular shells, dust production, intracycle and cycle-to-cycle variations, and asymmetries.

6.1 Diameter as Function of Wavelength

The obtained angular diameter as function of wavelength in the N-band is significantly different between the four O-rich stars and the one C-rich star in the sample. R Aql, R Aqr, R Hya and W Hya show a moderate to low diameter decrease from 8 to 10 μm and a strong diameter increase from 10 to 12 μm, while on overall the diameter of V Hya strictly decreases from 8 to 12 μm (cf. figures 5.18, 5.20, 5.22, 5.26 and 5.24, respectively). Since different constituents cause this different shape, both underlying chemistries are studied separately in the following.

6.1.1 O-rich AGB stars

The spectra in Section 5.1.2 have shown that molecules are present in the atmosphere of the stars. The most abundant of these molecules are CO, H_2O and SiO besides H_2. In the N-band, between 8 and 13 μm, strong pure-rotation lines of H_2O are expected. SiO exhibits fundamental bands between 8 and 10 μm (see e.g. Decin, 2000). Modeling of W Hya by Justtanont et al. (2004) revealed the existence of at least three different dust species, namely amorphous silicate, Al_2O_3 and MgFeO, which are likely located at different distances from the star, and are detected in the mid-IR through their thermal dust emission. In particular, Al_2O_3 provides significant opacity for wavelengths longwards of 10 μm (Begemann et al., 1997) and can survive at high temperatures.

Quasi-static, warm and dense molecular layers close to the star, at typically $2 - 3$ $R_\star$[1], are detected for O-rich (e.g. Mennesson et al., 2002; Perrin et al., 2004; Ireland et al., 2004d; Woodruff et al., 2004; Fedele et al., 2005) and C-rich (e.g. Hron et al., 1998; Ohnaka et al., 2007)

[1] $R_\star$ is the photospheric radius and typically about 20% smaller compared to the K-band radius (cf. e.g. Millan-Gabet et al., 2005).

Table 6.1: Summary of the results.

Target:	R Aql	R Aqr	R Hya	V Hya	W Hya
Type:	Mira	Mira	Mira	SRa/IR	Mira/SRa
Chemistry:	O-rich	O-rich	O-rich	C-rich	O-rich
Best model:	FDD + Gaussian (A.13)	FDD + Gaussian (A.13)	FDD (A.6)	FDD + Gaussian (A.13)	FDD (A.6)
ϵ_{FDD} layer[a]	0.77 ± 0.02	0.35 ± 0.03	0.84 ± 0.01	0.23 ± 0.03	0.78 ± 0.01
θ_{FDD} layer[a] (mas):	21.3 ± 2.0 (4.7 AU)	20.9 ± 3.5 (5.2 AU)	46.6 ± 0.6 (6.1 AU)	19.3 ± 3.5 (6.9 AU)	79.0 ± 1.2 (7.1 AU)
θ_{G} dust[a] (mas):	338 ± 120 (74 AU)	105 ± 8 (26.3 AU)	> 1000[d] (> 130 AU)	105 ± 4 (37.8 AU)	> 1000[d] (> 90 AU)
Alternative model:	UD + Gaussian (A.10)	UD + Gaussian (A.10)	–	FDD + Ring[b] (A.12)	–
$\theta_{\mathrm{FDD},12\mu\mathrm{m}}/\theta_{\mathrm{FDD},10\mu\mathrm{m}}$:	(31 ± 15)%	(24 ± 34)%	(24 ± 2)%	(−48 ± 24)%[c]	(31 ± 3)%
$\theta_{\mathrm{FDD},10\mu\mathrm{m}}/\theta_{\mathrm{UD},2.2\mu\mathrm{m}}$:	1.9 ± 0.3	1.3 ± 0.3	1.9 ± 0.1	1.3 ± 0.2	1.8 ± 0.2
$\theta_{\mathrm{SiO}}/\theta_{\mathrm{FDD},10\mu\mathrm{m}}$:	1.1 ± 0.2	1.5 ± 0.3[e]	–	–	1.0 ± 0.1
$\theta_{\mathrm{G},10\mu\mathrm{m}}/\theta_{\mathrm{FDD},10\mu\mathrm{m}}$:	16 ± 6	5.0 ± 0.9	> 21[d]	5.4 ± 1.0	> 13[d]
Intracycle variation, $\theta_{\mathrm{FDD,max}}/\theta_{\mathrm{FDD,min}}$:	(36 ± 14)%	(19 ± 17)%	$>$ (12 ± 3)%	$<$ (70 ± 40)%	(6 ± 2)%
Cycle-to-cycle variation:	–	–	(5 ± 3)%	–	(5 ± 4)%
Asymmetry:	–	–	no	?	yes

[a] at 10 μm (exactly 9.92 μm); [b] other possible models are: UD + Gaussian (model A.10) and UD + Ring (model A.9); [c] given is $\theta_{\mathrm{FDD},12\mu\mathrm{m}}/\theta_{\mathrm{FDD},8\mu\mathrm{m}}$, this is the only star with a declining diameter (cf. Section 6.1.2); [d] lower limits of the dust diameter (not Gaussian) for R Hya and W Hya are obtained from FOV restrictions (cf. Section 5.1.2); [e] if the SiO ring diameter is compared with the K-band diameter, it becomes clear that the SiO maser is located at a similar distance from the star as for the other stars in the sample

AGB stars, as well as for RSG stars (e.g. Perrin et al., 2007). These layers were introduced before to explain spectroscopic observations (e.g. Hinkle & Barnes, 1979; Tsuji et al., 1997; Yamamura et al., 1999). In particular, the Mira RR Sco (Ohnaka et al., 2005), the Mira S Ori (Wittkowski et al., 2007) and the RSG star α Orionis (Betelgeuse) (Perrin et al., 2007) show a very similar diameter behavior throughout the N-band. Their UD diameters are shown in Figure 6.1. Since α Orionis is a RSG star, only specific aspects of this star will be used for a comparison.

Comparison: If the wavelength dependence of the diameters of RR Sco and S Ori across the N-band is compared with the shapes obtained in this work (lower right panel of Figure 6.1), it can be proposed that probably in all these stars similar constituents and mechanism are

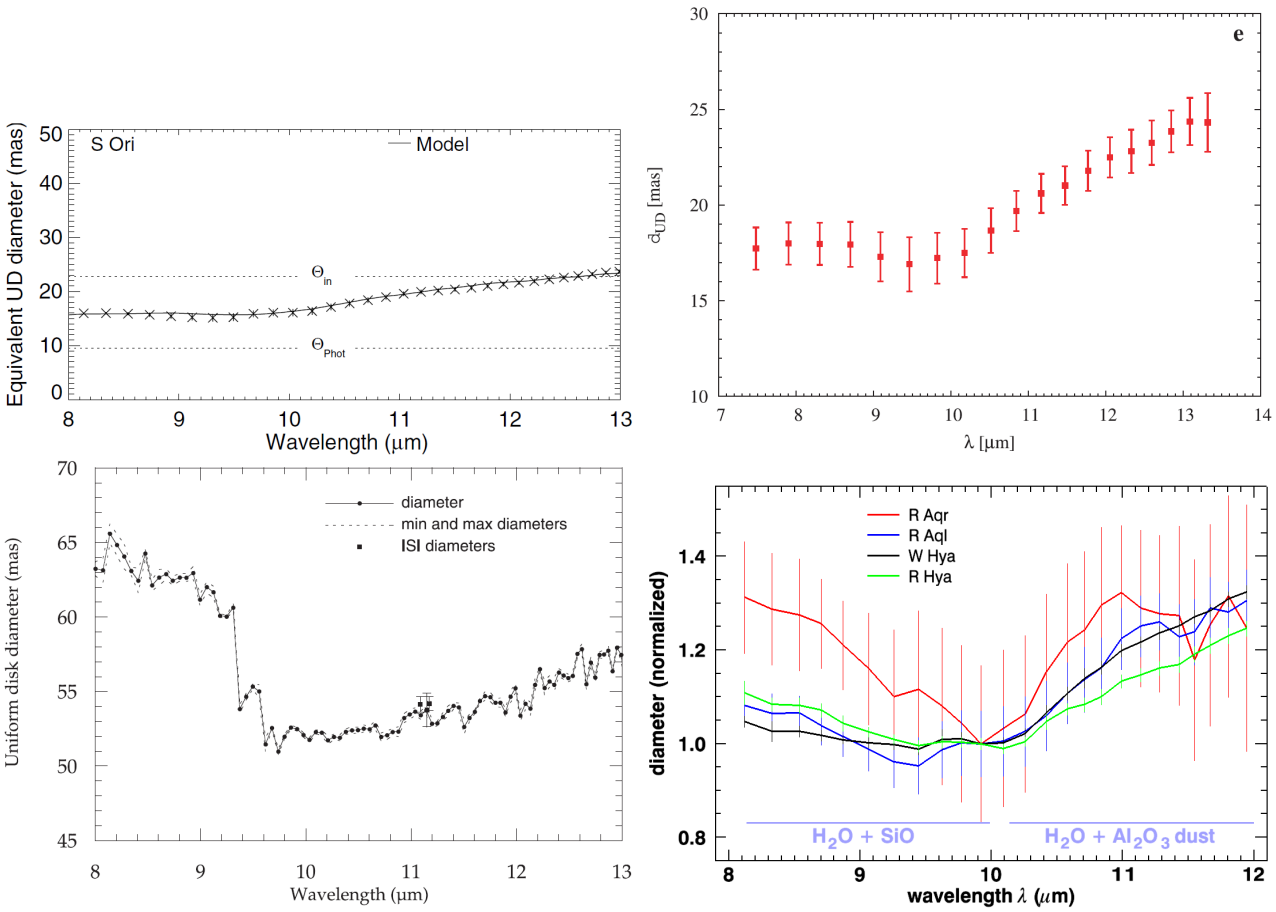

Figure 6.1: Comparison of diameters as function of wavelength in the N-band for O-rich stars. *Top left:* Equivalent UD diameter of S Ori (cf. Figure 5d in Wittkowski et al., 2007). *Top right:* Equivalent UD diameter of RR Sco (cf. Figure 1a in Ohnaka et al., 2005). *Bottom left:* Equivalent UD diameter of α Orionis (cf. Figure 2 in Perrin et al., 2007). *Bottom right:* Normalized equivalent FDD diameters of the O-rich Miras studied in this work. The diameters are normalized to one at around 10 μm (exactly 9.92 μm).

responsible for this appearance. The diameter ratio $\theta_{12\mu m}/\theta_{10\mu m}$ is for RR Sco approximately 1.3 and for S Ori between 1.3 and 1.5. This increase is comparable with the increase detected in the sample studied in this work[2]. From Table 6.1 it can be inferred that for the four O-rich stars the enlargement is on the order of 25% to 30%.

Even the increases between the K-band diameter and the diameter at 10 μm is similar. The ratio, $\theta_{10\mu m}/\theta_{2.2\mu m}$, is for RR Sco approximately 1.8 and for S Ori between 1.6 and 2.2, while the enlargements of the O-rich Miras studied in this work are on the order of 1.6[3] (cf. Table 6.1). R Aqr is in this relation an exception (see below).

Ohnaka et al. (2005) modeled RR Sco by adding a molecule layer of H_2O and SiO, and a dust layer, consisting of corundum and silicates, to a static star with a fixed temperature. This

[2]The relative increase is independent of the model, i.e. it does not matter if a UD or FDD is used.

[3]For this ratio the same models must be used. Therefore, the ratios given in Table 6.1 are converted, i.e. they are multiplied by 0.87 (cf. footnote on page 135).

composition reproduced the N-band diameter behavior very reasonably, but with a large inner radius for the dust shell of 7.5 $R_\star$, while the molecule layer was located at a more expected radius of 2.3 $R_\star$. The large dust shell radius might be due to the mix of 80% corundum (Al_2O_3) and 20% silicates, and the fact that for both dust species the same density profile and inner condensation radius was used.

Wittkowski et al. (2007) modeled S Ori with the dynamic atmospheres of Ireland et al. (2004b,c), where the molecular layers are naturally included and only the dust shell has to be added ad hoc. This assumes that the stellar atmosphere and dust shell are spatially separated. They allowed different density profiles and condensation radii for the corundum and silicate dust, whereas the model without silicates fitted the data better. The inner boundary of the Al_2O_3 dust shell varied, dependent on the pulsation phase, between 1.8 and 2.4 photospheric radii. At visual minimum the dust shell was more compact with a larger optical depth and at smaller radii, while at maximum phase the opposite was the case.

The molecular sphere of the RSG star α Orionis was modeled by Perrin et al. (2007) with a geometrically thin shell whose radius varied from 1.31 to 1.43 $R_\star$ across the N band with a characteristic temperature of 1550 K. Their spherical shell contained H_2O, SiO and Al_2O_3. The larger diameter between 8 and 10 μm was attributed to an observed large optical depth caused by SiO.

The wavelength dependent diameter of the O-rich stars studied in this work can be explained by a combination of the above models. The overall larger diameter in the mid-IR originates from a warm molecular layer[4] of H_2O, and the gradual increase longword of 10 μm arises from the presence of corundum dust close to this layer. A nearby molecular shell consistent of SiO is probably the reason for the diameter enlargement between 8 and 10 μm in R Aqr. These radiative important constituents are labeled in the lower right panel of Figure 6.1. The formation of dust consisting of Al_2O_3 grains at these short distances from the stellar surface is consistent with the empirical results by Lorenz-Martins & Pompeia (2000), as well as with recent theoretical calculations by Ireland & Scholz (2006). It should be mentioned that metallic Fe might have some effects as well (McDonald et al., 2010).

Maser: A possible relevance of SiO at shorter wavelengths is supported by the occurrence of SiO masers in the region of the water vapor layer and inner boundary of the Al_2O_3 dust shell. Nevertheless, H_2O contributes also with significant opacities in the wavelength region between 8 and 10 μm, which means that there might be no need to assume high abundances of SiO in the molecular shell, but only enough to exhibit maser emission in shock regions. For R Aqr this might be different (see below).

The SiO ring to UD diameter[5] ratio is on the order of 0.9 for R Aql and W Hya, while it is 1.3 for R Aqr[6]. However, if the SiO ring diameters are compared with the K-band diameters it becomes clear that for all stars the SiO masers are located at a similar distance to the star,

[4]It should be mentioned again that the high abundance of certain molecules in such a layer is the result of the capability to form certain molecules at a specific distance from the star and their dilution when reaching larger distances. For all atmospheric molecules exists such a shell, only their total abundance and radiative properties determine if the molsphere is detected or not.

[5]Again, the values listed in Table 6.1 are multiplied by 0.87.

[6]There are no SiO maser ring diameters published for R Hya.

even for R Aqr. This is almost identical to what was found for S Ori (Wittkowski et al., 2007). These values are consistent with theoretical estimates and earlier observations of O-rich stars in the literature. The maser spots are therefore co-located with the close dust shell.

H_2O maser emission ring diameters are available for R Aql and W Hya. They are located at about 15 and 4 photospheric radii, respectively. This large difference is surprising, but might be related to the highly elongated emission structure seen in R Aql and its higher mass loss rate (Lane et al., 1987). The detected OH maser emission in W Hya shows that the interstellar radiation field already destroys water molecules at photospheric radii as close as 20 to 30.

Equivalent blackbody temperature: Dust can only exists close to the star if the temperature is below the condensation temperature of the dust species. An estimate of an equivalent blackbody temperature[7] can be derived from the total flux S_ν (in Jy), the flux ratio $\epsilon_{\rm FDD}$ and the diameter $\theta_{\rm FDD}$ (in rad[8]) measured with MIDI via

$$T_b \;=\; \epsilon_{\rm FDD}\,\frac{h\nu}{k}\,\frac{1}{\ln\left(\frac{2h\nu^3}{I_\nu c^2}+1\right)}\,, \tag{6.1}$$

with $I_\nu = S_\nu/(10^{26}\pi\theta^2_{\rm FDD})$ the spectral brightness and ν the frequency of the observation. The obtained temperatures are plotted on Figure 6.2 for all stars in the sample. R Aql, R Hya and W Hya show a very similar trend with temperatures between 600 and 900 K. R Aqr exhibits a comparable trend, but with a small increase longward of 11 μm. The typical error is on the order of 100 K with the largest error coming from the total flux determination, but it should be kept in mind that these temperatures are averages over several pulsation cycles. However, the temperatures are low enough that dust condensation can take place. Interestingly, R Aqr and V Hya have on average the lowest temperature, showing that the high amount of dust in both systems influence the temperature structure and vice versa. Therefore, the formation of seed grains consisting of corundum is possible in the molecular layers. Since Al_2O_3 has only a moderate abundance and a low absorption efficiency at optical and near-IR wavelengths, it cannot be responsible to initiate the mass loss (e.g. Woitke, 2006b). In Section 2.3.1 it was discussed that scattering on large Fe-free silicate grains may solve this problem (e.g. Mg_2SiO_4 can form at about 2 photospheric radii, i.e. at about 1000 K). However, these transparent grains are not detectable with MIDI.

Silicate dust shell: Due to the fact that the flux contribution of the star/layer is below one, it was concluded that a circumstellar dust shell exists around these stars. Except for R Aqr, the flux fraction, $\epsilon_{\rm FDD}$, of the star/layer is on the order of 80% for the O-rich stars in the sample (cf. Table 6.1). The analysis of the ISO spectra in Section 5.1.2 has shown that features of silicate dust emission are present. Therefore, it can be assumed that the surrounding dust shell consists mainly of silicates (e.g. $MgFeSiO_4$ forms at photospheric radii larger than 10). A silicate dust condensation radius could only be reliably constrained for R Aqr. Its inner

[7]The temperature that a blackbody would need to have in order to emit radiation of the observed intensity at a given wavelength.

[8]In order to convert from mas to rad, the diameter must be multiplied by $2\pi/(1000{\cdot}3600{\cdot}360)$.

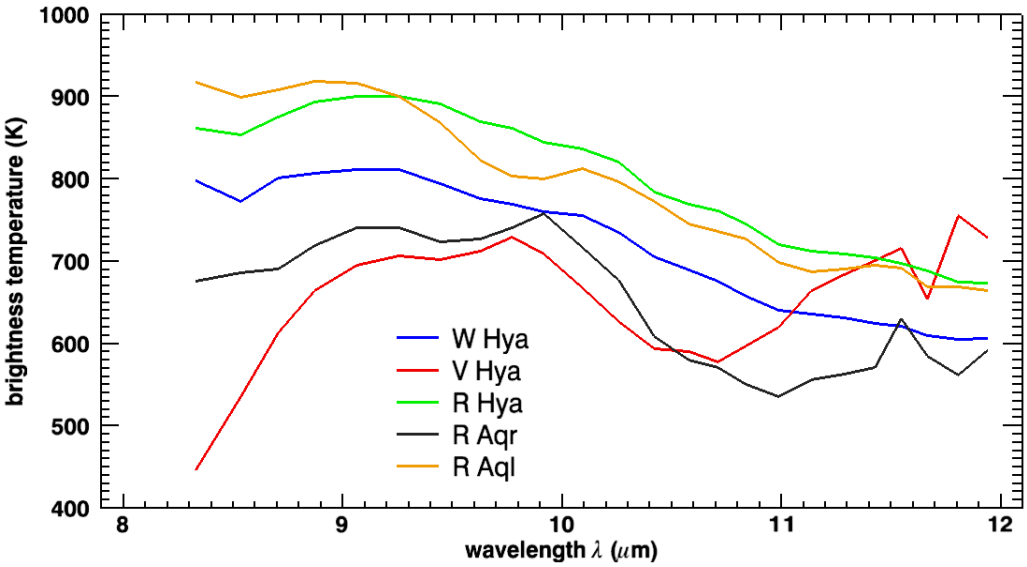

Figure 6.2: Equivalent blackbody temperature of all five star in the sample as function of wavelength. The C-rich Mira V Hya is already included for completeness.

characteristic silicate dust shell radius is located at a distance of about 5 times the layer radius, i.e. about 7 times the photospheric radius.

However, lower limits for the condensation radius were obtained for R Aql, R Hya and W Hya as well. Their dust shells have inner condensation radii of 15 to 20 times the layer radius. This means that the main silicate emission comes from regions more extended than 30 to 40 times the photospheric radius. This is larger than expected for O-rich stars (e.g. Höfner & Andersen, 2007), but could be related for R Aql and R Hya to their recent thermal pulse with a short period of enhanced mass loss. A outer detached shell may contribute largely to the total silicate dust emission. For W Hya, with a lower limit for the silicate dust shell of about 25 times the photospheric radius, it can be still explained with the standard expectation of about 10 to 20 radii. However, W Hya is also know to have a very extended dust shell (Hawkins, 1990).

At these large radii, corundum dust grains are no longer detectable, since they are covered by silicate grains (SiO is absorbed on Al_2O_3). The presence of the circumstellar dust shell is responsible for the decrease of the relative flux contribution of the star/layer with increasing wavelength in all observed stars, since colder dust is generally probed at longer wavelength.

R Aqr: The only O-rich star which fits not very well in the previous interpretation is R Aqr. The FDD diameter to K-band diameter ratio is much smaller, while the SiO maser emission is located at a similar distance from the star. An overabundance of SiO and a strong silicate dust emission could already be inferred from the spectrum (e.g. Angeloni et al., 2007, cf. Section 2.4.2). Therefore, a high dust content in the symbiotic system, locked by the additional gravitational attraction of the WD, can explain the spectral features originating close to the star, the small mid-IR layer diameter, the small silicate dust shell diameter and the low flux contribution of the molecular shell/star.

The high SiO abundance favors a closer dust formation. Even though more Al_2O_3 grains

are probably present as well, they are covered closer to the star by SiO. This is probably the reason, in addition to extinction, why the diameter increase longward of 10 μm is first strong, but reaches a constant value at 11 μm. In addition, the ionizing radiation of the compact companion prevents the formation of large amounts of water vapor, i.e. H_2O cannot sufficiently form from OH and H in the reaction equilibrium. Therefore, the FDD diameter is only marginally larger than the K-band diameter. At shorter wavelengths (< 10 μm), the flux contribution of the SiO molecular shell is so high that the apparent FDD diameter gets larger (cf. α Orionis). In addition, the large scatter in the visibility measurements may have influence on the FDD diameter fit as well (see discussion in the next section for V Hya). Apart from that, the overabundance of OH explains the apparent large diameter at L-band (cf. Section 5.3).

The SiO maser shell diameter is not strongly influenced by that, since specific physical conditions are necessary in order to exhibit maser emission. These conditions are solely present at a certain distance from the star. Only the intensity and number of maser spots are increased compared to other O-rich stars (cf. Lane et al., 1987). The ionizing radiation has no large impact on the dust, and large amounts of silicate dust can form, resulting in a strong silicate emission feature and a high flux contribution of the dust shell.

Visibilities: With the previous results, the shapes of the visibility curves can be understood qualitatively (cf. Section 5.2.1). In the plots for R Hya and W Hya, the visibility increase between 8 and 10 μm corresponds to the optically thick partially resolved stellar disk (including the close molecular layers) at an almost constant FDD diameter, while in the region between 10 and 12 μm the flux contribution of the spatially resolved, optically thin Al_2O_3 dust shell becomes more relevant. This leads longward of 10 μm to the nearly flat gradient and an increased FDD diameter (Ohnaka et al., 2005; Wittkowski et al., 2007). In addition, extinction of the stellar dust shell becomes important. At very low visibilities the opposite effect is notable due to their location in the second lobe. At very high visibilities (> 0.5), a decrease of the visibility in the region between 8 and 10 μm can be seen in particular for R Aql and R Aqr. This originates from the detected surrounding dust shell in both stars.

In almost all visibilities of all stars, there are small features and a higher scatter between 9.5 and 10 μm. This is caused by the telluric ozone feature, which introduces difficulties in the calibration process at these wavelengths.

Dynamic models: It is clear that a quantitative modeling is necessary to support the above findings, in particular, if the derived constituents of the close molecular and dust layer (H_2O, SiO, Al_2O_3) can really provide sufficient opacities to explain the derived diameter dependence on wavelength. In order to quantify results, it will be necessary to apply dynamic atmospheric models of e.g. Ireland et al. (2004b,c). Even if Al_2O_3 dust is not included in this models so far, and has to be added ad hoc[9], this will give more detailed insights in the physical processes at work there. The inner Al_2O_3 and outer silicate dust shell can be modeled with specific radiative transfer codes, e.g. DUSTY[10] or MC3D[11].

[9] Dynamic atmospheric models, including both the molecular layers and close dust formation, are on the way (Scholz and Ireland, private communication).

[10] http://www.pa.uky.edu/∼moshe/dusty/ and Ivezic & Elitzur (1997)

[11] http://www.astrophysik.uni-kiel.de/∼wolf/public/mc3d/

6.1.2 C-rich AGB stars

The study of the oxygen-rich stars in the sample has shown that dense molecular layers, extending to up to 2 photospheric radii, are present in these stars in agreement with findings in other oxygen-rich late-type stars. In contrast, the physical properties of the outer atmosphere of carbon stars and their temporal variations have not yet been well probed. Hydrostatic and dynamic model atmospheres of carbon-rich Miras as well as non-Mira carbon stars fail to explain observed spectra longward of about 5 μm (Jørgensen et al., 2000; Gautschy-Loidl et al., 2004). These models predict very strong absorption due to C_2H_2 and HCN at 7 and 14 μm, but the observed ISO spectra of carbon stars show only weak absorption due to these molecular species. However, Aoki et al. (1998, 1999) and Paladini et al. (2009) proposed that emission from extended warm molecular layers, containing C_2H_2 and HCN, may be responsible for the discrepancy between the ISO spectra and the photospheric models. Both species are among the most abundant in C-rich atmospheres.

Diameter measurements for C-rich stars were e.g. performed by van Belle et al. (1997), Thompson et al. (2002) and the authors listed in Table 5.9 (page 140) for V Hya in the K and H-band. The only other observation with MIDI of a C-rich star was conducted by Ohnaka et al. (2007) for V Oph. While in the K and H-band the spectrum is contaminated with CO bands, the absorption features of C_2H_2 and HCN, as well as emission from SiC and featureless amorphous carbon (AMC) dust, plays an important role in the N-band. In addition, molecules such as silane and ammonia may provide high opacities in carbon-rich stars and supergiants as well (see Monnier et al., 2000, and references therein).

Comparison: Ohnaka et al. (2007) modeled V Oph with a dust shell, consisting of AMC (85%) and SiC (15%), with a multi-dimensional Monte Carlo code (Ohnaka et al., 2006), and added a polyatomic molecular layer, consisting of C_2H_2 and HCN, where the opacities of these molecules were calculated with an appropriate band model assuming LTE. This model is in the following compared with V Hya.

Figure 6.3 shows the equivalent UD and FDD diameters obtained for V Oph and V Hya, respectively. Clearly, the diameter dependence on wavelength is different for both stars. Only in the broad SiC emission band at around 11.3 μm, the apparent diameters of both stars are increased due to the higher flux contribution of this emission in the outer atmosphere. The simultaneous diameter enlargements shortward of 8.5 μm and longward of 11.5 μm due to C_2H_2 can only be seen in V Oph. The contribution of HCN in these wavelength regions is weak and Ohnaka et al. (2007) gave only upper limits of its column density.

There are possibly several reasons for this discrepancy. Compared to V Oph, the flux contribution of the AMC dust shell is much higher in V Hya (almost nothing in V Oph compared to up to 85% in V Hya). This has a significant impact on the model fitting. The apparent strong increase of the diameter shortward of 10 μm might result from difficulties to fit a FDD with a low flux contribution to the low visibilities at high spatial frequencies. At spatial frequencies larger than 20 arcsec^{-1} the data show a high scatter due to influence from the pulsation, the strong asymmetry and the secondary long period as well (cf. Section 2.4.4). The position angles of the observations for example are similar to the position angles of the high velocity wind. This means that an asymmetry, independently pronounced at different wavelengths, might be

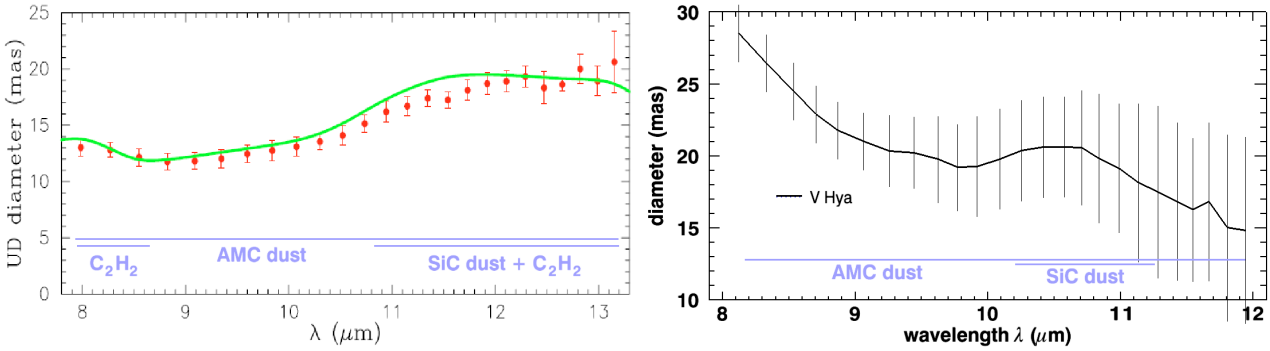

Figure 6.3: Comparison of the diameter as function of wavelength in the N-band for C-rich stars. *Left:* Equivalent UD diameter of V Oph (cf. Figure 6b in Ohnaka et al., 2007). *Right:* Equivalent FDD diameter of the C-rich Mira V Hya obtained in this work.

present and results in higher diameters at short wavelength. In addition, V Hya exhibits a high mass loss rate, and temporal fluctuations of the density and emissivity may have influences as well, even if the FDD diameter fit is done to the full data set. In order to constrain a FDD diameter better, measurements at larger projected baselines would be necessary.

V Hya shows some similarities to R Aqr except for the underlying chemistry. As for R Aqr, the average N-band FDD diameter is only about 1.3 times larger than in the K-band, and the dust condensation radius is at about 5 times the FDD radius. However, in C-rich stars it is not expected that the K-band diameter is a good tracer for the true photospheric radius, and the condensation of AMC dust happens anyway at smaller radii, i.e. higher temperatures (e.g. Gail & Sedlmayr, 1987; Gautschy-Loidl et al., 2004; Woitke, 2006b; Wachter et al., 2008).

Therefore, it can only be concluded that SiC and AMC dust is present at small radii, most of the AMC dust condensates at larger radii and that in general carbonaceous dust condensates closer to the star compared to silicate dust in O-rich stars. This condensation sequence is consistent with the non-LTE grain formation calculation of Kozasa et al. (1996). The Gaussian fit to the data shows also that colder dust is traced with longer wavelengths, as expected. The brightness distribution of such an AMC dust shell could be described with the emission of a shell that has an inner boundary and a quadratic power law density decrease further out, since this could easily reproduce the sinusoidal behavior of the visibilities as function of spatial frequency[12] (cf. Figure 5.23, page 125). This was checked for V Hya with the radiative transfer code DUSTY with some simple assumptions (Ohnaka, private communication), but further detailed calculations are necessary.

The presence of H_2C_2 and HCN cannot be confirmed directly. However, the trend of the visibility as function of wavelength (Figure 5.15, page 110) is very similar to the one of V Oph[13],

[12]Such a dust distribution gives in the mid-IR brightness distribution a ring like structure with a smooth outer edge and explains why two models, a uniform ring and a Gaussian, fitted the data set appropriately. Note also that for the oxygen-rich stars in the sample the sinusoidal behavior was not detected, but since the dust shell was not sampled very well with the MIDI observations and the flux contribution of the dust shell is low, this can be expected (except maybe for R Aqr, but for this star there are not enough visibility data to confirm this).

[13]Even similar to the oxygen rich stars in the sample, i.e. an optically thick partially resolved stellar disk (including the close molecular layers) at an almost constant FDD diameter and the flux contribution of the

suggesting the same atmospheric conditions. Since the equivalent blackbody temperature is low enough in the extended atmosphere, as shown in Figure 6.2, it is plausible that polyatomic molecules may form behind shock fronts and a molecular layer is established. The flux contribution of a possible close optical thick molecular layer is then just too low to be detectable. Since no reliable photospheric angular size was found in the literature, it cannot be derived if the optically thick emission from a C_2H_2 layer, together with the dust emission, is responsible for a N-band angular size significantly larger than the photospheric size, and that C_2H_2 plays a role similar to H_2O in oxygen-rich environments as was postulated for V Oph (Ohnaka et al., 2007). Noteworthy, the equivalent blackbody temperature shortward of 9 μm gets very low, supporting the fact that in this wavelength region the model fit might not work very well.

Dynamic models: As for the oxygen-rich stars, it is necessary to compare with dynamic model atmospheres, computed with parameters corresponding to V Hya, for a better understanding of the physical processes responsible for molecule and dust formation close to the star. Otherwise it is difficult to identify the constituents and their relative contribution across the atmosphere and CSE, since the apparent diameter at different wavelengths is highly dependent on the probed species and temperature regions.

6.2 Intracycle and Cycle-to-Cycle Variations

AGB stars are highly variable at visual wavelengths. Even in the mid-IR, typical flux variations on the order of 20% could be detected in this study with a phase offset of about 0.15 (cf. Table 5.2, page 101). Therefore, it is important to know how this relates to changes of the apparent angular size of the photosphere, molecular layers and dust shells, and how this influence the dust formation and mass loss. This can be compared with the predictions of dynamic model atmospheres of e.g. Ireland et al. (2004c) for O-rich stars and Woitke (2006b) for C-rich stars.

In this work, the average FDD diameter across the N-band is compared for different visual light phases and cycles. The result is shown in Figure 6.4. Since at different wavelengths within the N-band different constituents are traced, taking the average might be not an optimal way in order to search for diameter variations. However, it turned out that the wavelength dependent shape of the apparent size did not vary significantly. This means that the H_2O molecular and alumina dust shell changed in a similar way in the case of the oxygen-rich stars. The results for the carbon rich star V Hya in this sample were not reliable and cannot be compared here (cf. Section 5.2.6).

Intracycle variations: From the left panel of Figure 6.4 it can be inferred that the diameter at minimum visual light is smaller than at maximum visual light for all four oxygen-rich stars, and that their intracycle variations are on the order of 10% to 30%. A sinusoid is fitted to the data to illustrate these effects. The obtained peak-to-peak diameter variations are very similar to those listed in Table 6.1 (page 142), and are therefore not repeated. A few things have to

spatially resolved, optically thin SiC and AMC dust close shell can explain the visibility shapes of V Hya as well.

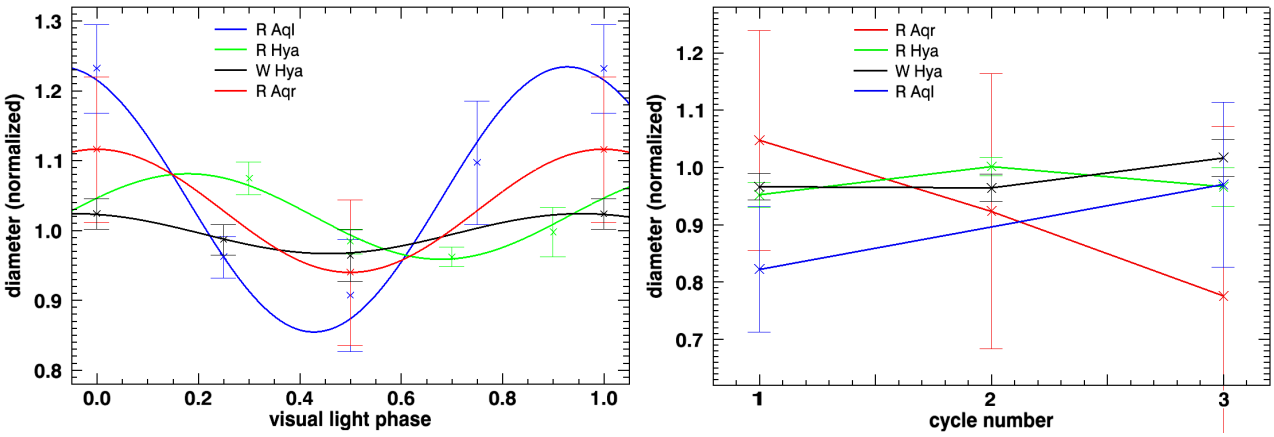

Figure 6.4: Intracycle *(left)* and cycle-to-cycle variations *(right)* for all oxygen-rich stars in the sample. It was not possible to obtain reliable results for the carbon-rich star V Hya, see text. Measurements are repeated in the left panel and a sinusoid is fitted to the data points.

be kept in mind concerning this plot. First, the results for R Aqr are not significant, second, there are no observations available for R Hya at maximum light, and third, a large phase range is used for each phase bin.

However, the trends are similar and can again be compared with the findings of Wittkowski et al. (2007) for S Ori[14]. The continuum photospheric diameter and inner Al_2O_3 dust shell diameter of S Ori changed by about 15% and 40% between visual minimum and post visual maximum, respectively. Their continuum photospheric diameter is the Rosseland diameter obtained from fitting the model of Ireland et al. (2004c) to the observations, and the inner dust shell diameter was derived by employing the Monte Carlo radiative transfer code of Ohnaka et al. (2006) (cf. Section 6.1.1). The molecular layers are naturally included in the model of Ireland et al. (2004c) and no meaningful diameter can be given for these shells.

The equivalent FDD diameter obtained in this work with MIDI probes the region between or near one of the above diameter definitions. The exact location depends on the flux contribution of all constituents (continuum photosphere, atmospheric layers of H_2O and SiO, and nearby corundum dust) as function of wavelength and pulsation phase. However, Wittkowski et al. (2007) fitted an equivalent UD diameter to their model and obtained a quantity measurable with interferometry. An example of this, showing the Rosseland mean diameter, $\Theta_{\rm Phot}$, the inner dust shell diameter, $\Theta_{\rm in}$, and the equivalent UD model diameter (black line), was displayed in the upper left panel of Figure 6.1 for one specific phase of S Ori. The UD diameter of S Ori at 10 μm changed by about 30% between maximum and minimum. This value can be used to compare with the results obtained in this work.

W Hya shows a relatively small maximum to minimum diameter variation of only 6% compared to the Mira star S Ori, but this can be expected since W Hya has a smaller visual amplitude and is classified as SRa/Mira. Only a lower limit of the diameter variation could be determined for R Hya because of the lack of data at visual maximum. Assuming that R Hya exhibits in reality a larger variation (the data in the plot suggest this as well), then the typical diameter variations of all Mira variables in the sample (R Aql, R Aqr and R Hya) are on the order of 20%

[14]Most N-band observations of other AGB stars do not have a good phase coverage.

to 30% (cf. Table 6.1). This is comparable to S Ori and therefore consistent with the model predictions of Ireland et al. (2004c). The averaging over large phase ranges may have resulted in a lower diameter variability. For comparison, variations of the apparent size are much larger in the J, H and K-band. Millan-Gabet et al. (2005) found for a sample of Mira stars that at visual maximum the stars appear twice as large as at visual minimum. From the left panel of Figure 6.4, it can also be inferred that the minimum diameter of R Hya occurs after visual minimum, which is similar to the findings for S Ori (Wittkowski et al., 2007).

The observed smaller angular diameter near visual minimum and the larger angular diameter near visual maximum can be explained by the phase-dependent water vapor (Matsuura et al., 2002) and corundum dust presence (Wittkowski et al., 2007). The star is hotter at visual maximum, and H_2O molecules and Al_2O_3 dust can only exist further out. At visual minimum, dust forms closer to the stellar surface and in larger amounts (otherwise it would be not detectable with MIDI), and suggests that the mass loss rate is higher in this phase. The scenario can be as follows: A new (inner) dust layer forms[15] behind shock fronts at visual minimum, but still with a low degree of condensation. At post minimum, this new dust layer is fully grown and is lifted up, and at visual maximum, the condensation front moves outwards and only small amounts of dust can form due to higher temperatures. In the next minimum, new dust forms again closer to the photosphere, while the previously accelerated material may no longer contribute to the N-band flux (Ireland et al., 2004a; Ohnaka et al., 2007; Wittkowski et al., 2007). However, a different scenario could be possible as well. Suh (2004) concluded for the optically bright oxygen-rich Miras o Cet and Z Cyg that the mass loss is higher near visual maximum because of a higher stellar luminosity, but needs more condensations at visual maximum.

The observations made in this work show only that Al_2O_3 dust exists closer to the star at visual minimum and further away at visual maximum. How this relates to the acceleration of the wind and the mass loss rate cannot be determined conclusively. Al_2O_3 can exist in the upper atmosphere without mass loss and possibly relevant micrometer-sized Fe-free silicates are not traced with MIDI. Therefore, it can still be possible that the wind formation and mass loss is to a certain amount decoupled from the pulsation (cf. e.g. models by Höfner & Dorfi, 1997), even if it can speculated that Fe-free silicates form together with Al_2O_3. Simultaneous observations tracing the relevant constituents and providing kinematic information are necessary (e.g. very long baseline radio line observations of molecules/masers), and a comparison with dynamic model atmospheres can only be of limited success as long as the dust formation is not included. Even the role of large amounts of water vapor in molecular shells and the radiation pressure on water molecules may need more detailed calculations.

The outer silicate dust shell could only be studied for R Aqr and did not show any temporal variations. Except that R Aqr has some specific properties (cf. Section 5.2.4), a temporal stability can be expected, since the heating and cooling time scales of such a large silicate dust shell is longer as the pulsation time scale.

Cycle-to-cycle variations: The right panel of Figure 6.4 shows the cycle-to-cycle variations of all oxygen-rich stars in the sample. Note that for R Aql the intermediate cycle is missing and that for R Aqr a long term influence of the compact companion cannot be ruled out

[15] Al_2O_3 dust which is detectable with MIDI and possibly Fe-free silicates which are needed to accelerate the wind, but are not traced with MIDI.

(cf. Section 5.2.4). In addition, the uncertainties for both stars are very high and the shown behavior is not very significant.

The cycle-to-cycle fluctuations of the atmospheric region probed with MIDI are more reliable for R Hya and W Hya. Both stars show a maximal variation on the order of 5%, and this is therefore much lower than intracycle variations. These cycle-to-cycle variations refer to a comparison of apparent diameters at narrow phase intervals near visual minima.

This gives an order of magnitude estimation on how large pulsation instabilities in AGB stars are, but also reflects the chaotic atmospheric behavior. These variations are smaller than might be expected. If different cycles are compared in Figure 2.13 (page 22, Höfner & Dorfi, 1997), Ireland et al. (2004c) (Figure 5 and 6), Ireland & Scholz (2006) (Figure 1) and Ireland et al. (2008) (Figure 1), it can be derived that the location of mass shells and dust condensation radii can vary by up to 20% with an estimated mean of 10%. However, it should be kept in mind that the movement of theoretical mass shells and dust condensation radii cannot be directly compared to the changes in the atmospheric radius-density structure that is traced by interferometric observations.

On the other hand, these marginal size changes are not surprising if compared with the findings of cycle-to-cycle variations in the near-IR. Theoretical models predict cycle-to-cycle nonrepeatability of the photospheric diameters in the K-band of tens of percent (Hofmann et al., 1998; Jacob & Scholz, 2002; Ireland et al., 2004b). If this scales as the near to mid-IR ratio in intracycle variations then the low cycle-to-cycle variations are easily explainable. Observations in the K-band show even smaller cycle-to-cycle variations as predicted, and are on the order of 10% (Thompson et al., 2002; Thompson & Creech-Eakman, 2004). However, this verifies that the folding of consecutive pulsation cycles in the previous diameter and intracycle analysis is an acceptable assumption.

6.3 Asymmetry

Asymmetries can only be interpreted for R Hya and W Hya, since R Aql and R Aqr have an insufficient uv-coverage, and the results for V Hya are inconsistent. R Hya does not show any signs of a departure from circular symmetry within the measurement uncertainties, while W Hya exhibits a small elliptical asymmetry. Figure 6.5 illustrates the asymmetric appearance of W Hya. The left panel shows the fit of an elliptical FDD for a representative wavelength, and the right panel displays the corresponding appearance on the sky for this model and mid-IR wavelength.

However, Lattanzi et al. (1997) and Tuthill et al. (1999) found in the visual for W Hya a PA[16] of 143° and (94 ± 33)°, respectively. From the photospheric radio continuum, Reid & Menten (2007) determined a PA of (83 ± 18)°, whereas Szymczak et al. (1998) found for the projected angle of the magnetic field on the plane of the sky, obtained from OH maser observations, a value of about −20° and a velocity discontinuity along the N-S axis. Muller et al. (2008) detected in the HCN position velocity a SE-NW gradient.

Table 6.2 shows determinations of asymmetries from various authors reported for R Hya and

[16]Position angles of the major axis of elongated brightness distributions on the sky are compared.

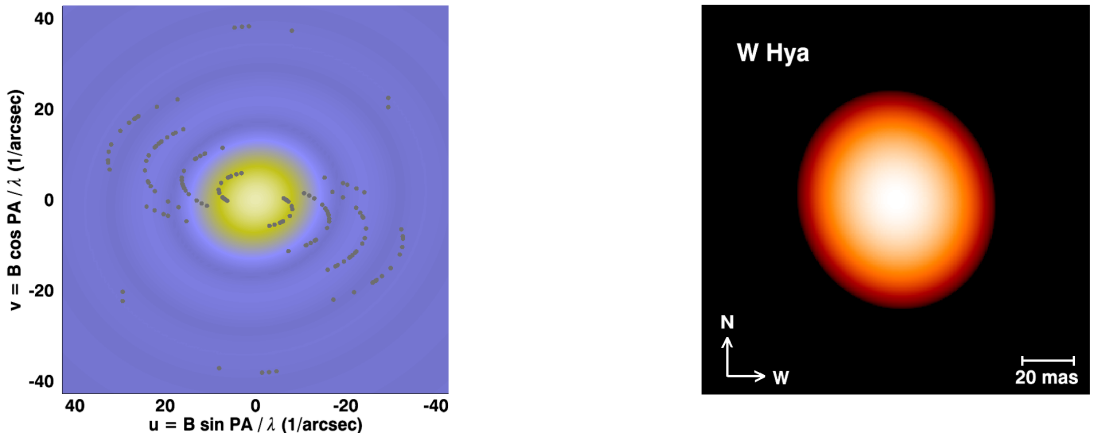

Figure 6.5: Asymmetry model of W Hya. Shown is the elliptical FDD fit for wavelength bin 6 (9.07 μm). *Left:* The model visibility (yellow = high visibility, blue = low visibility) plotted together with the data points in the uv-plane. The major axis in Fourier space has a position angle of 105°. *Right:* The corresponding image with a position angle of the major axis of 15° on the sky. North is up and East is left. The size is 150 × 150 mas.

W Hya. No asymmetries were reported for R Hya, while contradictory position angles (PA) were found for W Hya. The non-detection of an asymmetry for R Hya in this study is therefore consistent with the results of Ireland et al. (2004a) and Monnier et al. (2004). Interestingly, both authors did not find any departure from symmetry for W Hya as well.

The detected velocity gradients, the magnetic field alignment and the first noted visual PA determinations are similar to the PA obtained in this work, with a maximum deviation of 45°, while the radio and the second noted visual PA determinations are perpendicular to this value. A velocity gradient suggests a rotation of the star, a rotating tilted disk or a bipolar outflow. On the other hand, the wide range of measured PA at close photospheric radii could be related to a non-radial pulsation and/or a non-uniform molecule and dust formation probed at different wavelengths. A similar varying non-symmetric brightness distributions is also possible due to stellar spots or large convection zones. A deformation as a result of a close companion can be most probably excluded, since no evidence for such a scenario has been reported so far. Rotation of the star should also be too slow to be detectable. Scattering by dust in the CSE and instrumental polarization effects could be a possibility as well, but should not be significant in the mid-IR (Ireland & Scholz, 2006).

A large scale temporal dependence of the asymmetry could be the reason for different asymmetries detected at different epochs, even if this is very vague (in particular since this study did not show a time dependence, at least not over two years). The similar position angles of the velocity gradients at larger radii and the PA obtained in this work suggests as best explanation a more or less bipolar outflow due to asymmetric ejections of incomplete close molecular and dust shells. A connection to the highly elongated structures seen in planetary nebulae cannot be drawn, since W Hya is in an earlier AGB phase.

From this investigation and the previously published results summarized in Section 2.4 (in particular Table 2.4, page 30) follows, that except for R Hya all stars in the sample show asymmetries, and it can be concluded that asymmetries with different peculiarity are common.

Table 6.2: Position Angle (PA) determinations attempts for R Hya and W Hya by various authors. The approximate probed regions are given in the last column (inner = 50 – 100 mas, outer ≈ 1000 mas).

R Hya: Author	Obs Date	PA (°)	Wavelength	Region
Ireland et al. (2004a)	2001 Feb 8/9	–[a]	680 – 940 nm	inner
Monnier et al. (2004)	2000 Jan/Feb	–[a]	2.26 μm (K-band)	inner
this work	2007-2009	–[a]	8 – 12 μm (N-band)	inner
W Hya: Author	Obs Date	PA (°)	Wavelength	Region
Lattanzi et al. (1997)	1995 Dec 17	143[b]	583 nm	inner
Tuthill et al. (1999)	1993 Jun	94 ± 33	700/710 nm	inner
Ireland et al. (2004a)	2001 Feb 8/9	–[a]	680 – 940 nm	inner
Monnier et al. (2004)	2000 Jan/Feb	–[a]	2.25 μm (K-band)	inner
Reid & Menten (2007)	2000 Oct/Nov	83 ± 18	43 GHz (radio continuum)	inner
this work	2007-2009	11 ± 20	8 – 12 μm (N-band)	inner
Szymczak et al. (1998)	1996 Jan 15	−20	1667 MHz (OH maser), magnetic	outer
	1996 Jan 15	N-S	1667 MHz (OH maser), velocity	outer
Muller et al. (2008)	2008 Apr 13/15	SE-NW	266 GHz (thermal HCN(3-2) line)	outer

[a] No departures from symmetry could be detected within the measurement uncertainties.; [b] Since observations are at two perpendicular baselines, the true major axis cannot be recovered.

Chapter 7

Summary and Outlook

In this chapter, the conclusions are summarized and the findings are compared with the proposed goals and strategies (Chapter 1 and Section 4.1.1). At the end, possible future work is outlined.

Summary: Five AGB stars, namely R Aql, R Aqr, R Hya, V Hya and W Hya, were observed over a period of nearly 3 years covering several pulsation cycles. All stars were for the first time monitored in the thermal mid-IR with the interferometric instrument MIDI. These high-resolution observations were sensitive to the structure of the stellar atmosphere, consisting of the continuum photosphere and overlying molecular layers, as well as to the properties of the dust shell. The large amount of data resulted in a good uv-coverage for R Hya and W Hya.

The following conclusions can be drawn from modeling and analyzing these observations:

- Except for R Aql, a clear periodic flux variation is found in the N-band ($8 - 13$ μm). The typical semi-amplitude is on the order of 20% to 30% for the Miras and 10% for the semiregular/Mira variable W Hya. The amplitude is probably also related with the dust content in the system and the mass loss rate. The mid-IR maximum occurs always after the visual maximum at on average phase 0.15 ± 0.05.

- In the MIDI spectrum of R Aqr, the silicate dust emission feature could be clearly identified, while it is not present in the spectra of the other oxygen-rich stars R Aql, R Hya and W Hya. This has been attributed to field-of-view effects. The expected SiC dust emission feature is detected in the MIDI spectrum of the carbon star V Hya.

- The obtained visibility data can be best fitted with a fully limb-darkened disk (FDD), which accounts to some extend for surrounding atmospheric layers. A uniform disk (UD) is not a good representation for the brightness distribution of the stars. Therefore, a FDD should be preferred in order to obtain simple diameter estimations in the mid-IR.

- The trend of the FDD diameter as function of wavelength is similar for all O-rich stars in the sample. The apparent size is almost constant between 8 and 10 μm[1] and gradually increases at wavelengths longer than 10 μm. The enlargement is for all stars between 25% and 30%. In contrast, the relative flux contribution of the FDD decreases, reflecting the increased flux contribution from a surrounding silicate dust shell.

- The measured apparent mid-IR diameters at 10 μm are about two times larger compared to the photospheric diameters traced by K-band observations found in the literature (except for R Aqr and V Hya). This ratio is consistent with observations of other AGB

[1] The linear diameters of these stars are between 5 and 7 AU in this wavelength regime.

stars and theoretical models. The smaller ratio of 1.3 for R Aqr and V Hya can be explained with the presence of a compact companion and therefore a large dust content bound in the system.

- The obtained diameter trends for the O-rich stars are compared with the findings of Ohnaka et al. (2005) and Wittkowski et al. (2007) for RR Sco and S Ori, respectively. It can be concluded that the overall larger diameter in the mid-IR originates from a warm optically thick molecular layer of H_2O, and the gradual increase longword of 10 μm can be attributed to the contribution of a spatially resolved, optically thin, close corundum (Al_2O_3) dust shell. A significant contribution of SiO shortward of 10 μm cannot be ruled out for R Aqr. These observations of a larger sample of stars than available before confirm previous results, and emphasize the need for dynamic model atmospheres with a consistently included close dust formation.

- A comparison with available SiO maser ring diameters shows that the SiO maser emission is co-located with the layer[2] probed with MIDI at 10 μm for R Aql, R Aqr and W Hya, which is consistent with findings in other AGB stars (no maser emission data are available for R Hya and V Hya).

- The carbon rich star V Hya is compared with observations of V Oph by Ohnaka et al. (2007). The increase of the apparent diameter around the SiC feature (11.3 μm) is detected in both stars, while the overall shape of the diameter as function of wavelength is clearly different. This is attributed to difficulties in fitting a layer/stellar diameter in the presence of a dominating amorphous carbon (AMC) dust shell (similar to R Aqr). Therefore, it can only be concluded that AMC and SiC dust is present close to the star, and only speculated that a molecular shell consisting of C_2H_2 and HCN may exist.

- It is found that the silicate dust shells are located fairly far away from the star, at radii between 25 and 40 times the photospheric radius (this is just a lower limit for R Hya and W Hya), which is larger than expected. Only the dust shell of R Aqr is closer to the star, which is related to its symbiotic character.

- A reliable periodic intracycle variation of the layer diameter could only be obtained for R Aql, R Hya and W Hya. Their observed angular diameters are smaller at visual minimum than at visual maximum. The Miras R Aql and R Hya have peak-to-peak angular size changes of 20% to 30%, while the semiregular/Mira variable W Hya exhibits only a small size variation of 6%. The diameter variation can be explained with the phase-dependent water vapor and corundum dust presence and its temperature sensitivity. Since this variation traces only the location of constituents which are not relevant for the wind formation, no firm conclusions can be drawn concerning the mass loss mechanism. One can only speculate that more dust forms at visual minimum.

- Maximal diameter changes due to cycle-to-cycle variations are on the order of 6%, and are therefore lower as intracycle variations. This could only be determined for R Hya and W Hya.

[2]It should be emphasized again that the equivalent FDD diameter probes a region whose exact location depends on the flux contribution of all constituents (continuum photosphere, atmospheric layers, and nearby dust) as function of wavelength and pulsation phase.

- Asymmetries are investigated for R Hya and W Hya. While R Hya does not show any deviations from symmetry, an asymmetry of the extended atmosphere of W Hya can be confirmed. An elliptical FDD fitted the data with a position angle of $(11 \pm 20)^\circ$ and an axis ratio of (0.87 ± 0.07). The best explanation of this appearance could be a more or less bipolar outflow due to asymmetric ejections of incomplete molecular and dust shells.

The observation of close molecular layers and dust shells confirm the molsphere model. Primarily, the detected close dust shell consisting of Al_2O_3, i.e. well below the distance at which the silicate dust shell is traced, is now revealed for a few times. This supports the dust-driven wind scenario and the need for self-consistent dynamic model atmospheres with consistently included dust formation close to the star. It can also be concluded that a good phase and uv-coverage over the pulsation cycle can be crucial, and that interferometric observations in the N-band are an irreplaceable tool to resolve close stellar structures and searching for atmospheric constituents.

Limitations: Most of the proposed goals of Chapter 1 could be accomplished. However, a few items remain open. First, there could be no clear connection established between the dust condensation and wind formation. Second, the silicate dust shell could not be constrained for a few of the oxygen-rich stars due to a lack of observations at short baselines. Third, the pulsation phase coverage allowed only for some of the stars a reliable analysis of the apparent diameter as function of phase and cycle, and the uv-coverage was only sufficient for two stars.

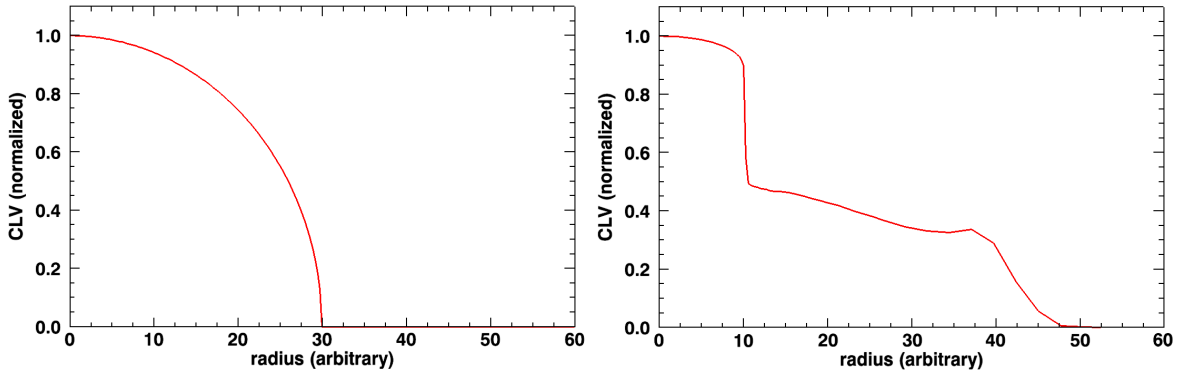

Figure 7.1: Center to limb variation (CLV) of a fully limb-darkened disk *(left)* and of an atmospheric model of Ireland et al. (2004b,c) for mid-IR wavelengths *(right)*.

The majority of the above conclusions rely on fits of a relatively simple FDD to the observational data. Figure 7.1 shows that this can only be an approximation, even if this model represented the data quite well. The emission region of the molecular layers in the atmospheric model of Ireland et al. (2004b,c) (and private communication by Scholz and Ireland) is more extended. In order to obtain a more meaningfully (Rosseland) diameter and the exact composition, it will be necessary to apply more sophisticated models to the data.

Future prospects: The large amount of data and the still ongoing observation program will make it possible to gain more knowledge on what happens in AGB stars by continuing this work. The following things could be achieved:

- A big reward could be gained by comparing the data with dynamical model atmospheres (e.g. Ireland & Scholz, 2006), and, if not included, by the use of certain radiative transfer codes (e.g. MC3D or DUSTY) in order to model the dust shell.
- The current software is limited by a low accuracy of the photometry and difficulties to remove the infrared background. An improved reduction software can lead to calibrated visibilities with lower scatter and errors. This could allow to study the influence of convection and clumps in the dust shell on the visibility and may allow to reconstruct an image of the stars with a sufficient uv-coverage.
- Additional observations on short projected baselines would enable the possibility to constrain the extension of the dust shell.
- Complementary and time coordinated SiO maser observations could give additional kinematic information of the dust formation zone probed with MIDI.

Appendix A

Visibility Models

A.1 Introduction

As shown in Section 3.1, interferometric data can be interpreted by fitting the Fourier transform of an assumed brightness distribution of the object. Figure A.1 shows the convention used for the Fourier/uv plane and sky plane again. The position angle (PA, ϑ) is defined as East (E) of North (N) and corresponds for an elliptical model to the major axis in the sky plane and to the minor axis in the Fourier plane.

The applied two-component models are listed in Table A.1. Given are the sections, where the details of the models are described, the number of free parameters (FP), the model names and the names of the stars where that model fitted reasonably. The parameters used in the next sections, where the detailed visibility (V) and intensity functions (I) are shown, have the following meanings: $J_{1 \text{ or } 3/2}$ is a Bessel function of the first kind of the order 1 or 3/2, respectively, θ refers always to an angular diameter and ϵ to the relative flux of the first

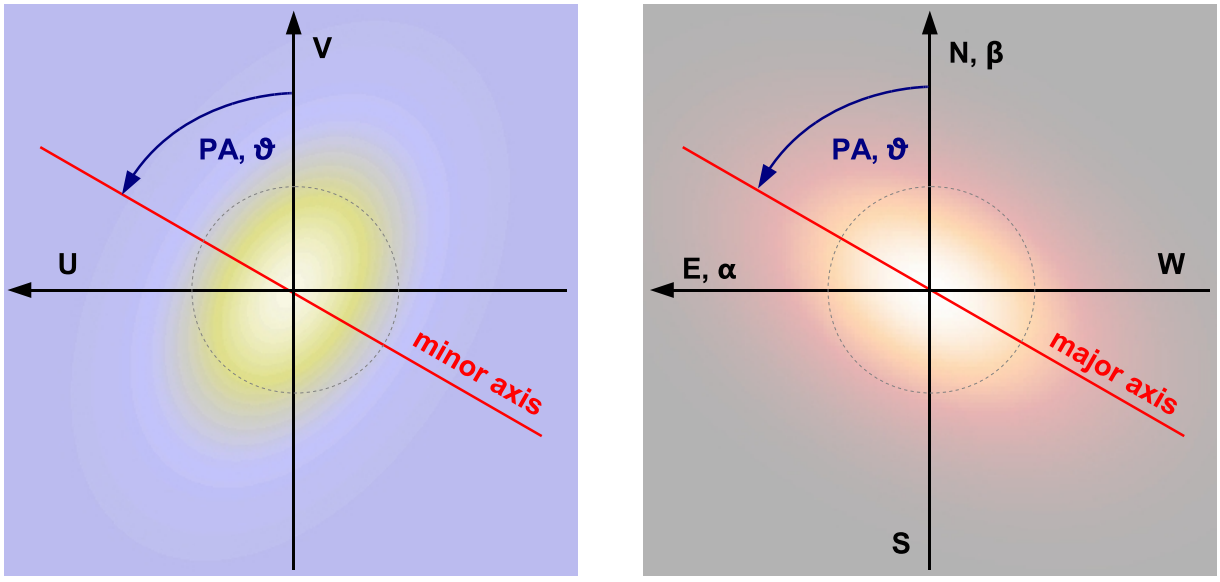

Figure A.1: Coordinate convention for the Fourier/uv plane (*left*) and sky plane (*right*). The position angle (PA, ϑ) is defined as East (E) of North (N) and corresponds to the major axis of an elliptical model in the sky plane. The East (α) and North (β) direction are parallel to the Right Ascension and Declination, and the u and v direction, respectively. The dashed line shows a circular model for comparison.

Table A.1: Visibility models used in this study. The *relative* models have an additional free parameter (FP) in order to account for an over-resolved component. For more details see Section 3.1.6 and in particular equation 3.43.

Section	FP	Model name	Star
A.2	2	(relative) circular uniform disk (UD)	R Aql
A.3	4	(relative) elliptical uniform disk (UD)	
A.4	2	(relative) circular Gaussian (G)	R Aql
A.5	4	(relative) elliptical Gaussian (G)	
A.6	2	(relative) circular fully limb-darkened disk (FDD)	W Hya, R Hya
A.7	4	(relative) elliptical fully limb-darkened disk (FDD)	W Hya, R Hya
A.8	2	circular uniform ring (UR)	
A.9	4	circular uniform disk + circular uniform ring	V Hya
A.10	3	circular uniform disk + circular Gaussian	R Aql, R Aqr, V Hya
A.11	5	circular uniform disk + elliptical Gaussian	
A.12	4	circular FDD + circular uniform ring	V Hya
A.13	3	circular FDD + circular Gaussian	R Aql, R Aqr, V Hya
A.14	5	circular FDD + elliptical Gaussian	
A.15	3	point binary	
A.16	5	uniform disk binary	

component. For a definition of the coordinates used ($r, \rho, r_{\vartheta,\eta}$ and $\rho_{\vartheta,\eta}$) see Section 3.1.6. The wavelength for the given examples is always 8.1 μm.

The *upper three plots* refer always to the Fourier plane. The upper left panel shows the total visibility (solid red line) and the visibility of the components if applicable (other blue dotted-dashed line/s, no norm applied) as function of the spatial frequency u (in 1/arcsec). The upper middle panel shows a 3D representation of the total visibility in the uv-plane (u and v in 1/arcsec), while the upper right panel shows a 2D representation of it (yellow = high visibility, blue = low visibility; u and v in 1/arcsec).

The *lower three plots* present always the normalized brightness distribution. The lower left panel shows the normalized intensity as function of the angular separation α[1]. The lower middle panel shows a 3D representation of the normalized brightness distribution in the sky plane (α and β in mas), while the lower right panel shows a 2D representation of it (N is up, E is left; α and β in mas).

If no over-resolved components exists, i.e. the visibility is one at zero spatial frequency, ϵ can be omitted in the *relative* models summarized in Table A.1. They have then one less free parameter. Note that the orientation of the coordinate system is different in the 2D and 3D representations.

[1]Note that the intensity is not integrated along the perpendicular dimension. A two arm interferometer sees the integrated intensity according to equation 3.40.

A.2 Relative Circular Uniform Disk

This model can be used for a first order approximation of a stellar surface.

$$V(r) = \epsilon \frac{2J_1(\pi\theta r)}{\pi\theta r} \tag{A.1}$$

$$I(\rho) = \begin{cases} \epsilon \frac{4}{\pi\theta^2} & \text{if } \rho \leq \frac{\theta}{2} \\ 0 & \text{otherwise} \end{cases} \tag{A.2}$$

with ϵ ... relative disk flux and θ ... disk diameter.

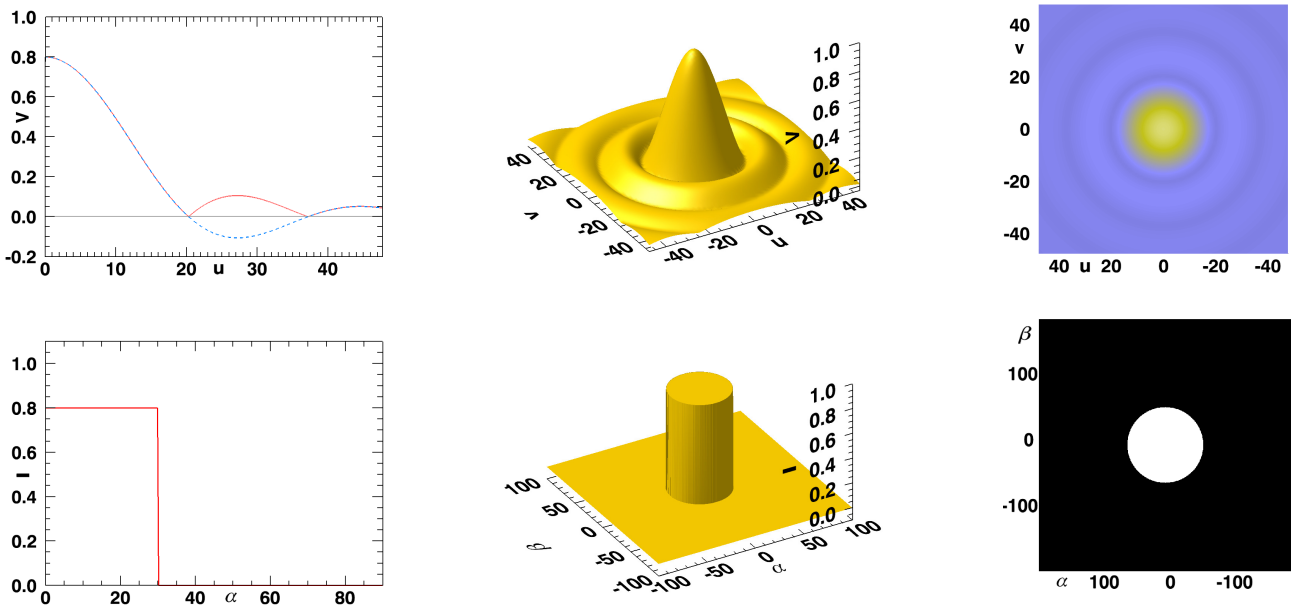

Figure A.2: Model example: $\epsilon = 0.8$, $\theta = 60$ mas, $\lambda = 8.1$ μm. Fourier plane (u,v)-coordinates are in 1/arcsec and sky plane (α,β)-coordinates are in mas. See Section A.1 for a description (page 161 – 162).

A.3 Relative Elliptical Uniform Disk

This represents the same as in A.2, but for an elliptical approximation.

$$V\left(r_{\vartheta,\eta}\right) = \epsilon \left(\frac{2J_1(\pi\theta_{\mathrm{maj}} r_{\vartheta,\eta})}{\pi\theta_{\mathrm{maj}} r_{\vartheta,\eta}}\right) \tag{A.3}$$

$$I\left(\alpha_\vartheta, \beta_\vartheta\right) = \begin{cases} \epsilon \frac{4}{\pi} \frac{1}{\theta_{\mathrm{maj}}\theta_{\mathrm{min}}} & \text{if } \frac{4\,\alpha_\vartheta^2}{\theta_{\mathrm{min}}^2} + \frac{4\,\beta_\vartheta^2}{\theta_{\mathrm{maj}}^2} \leq 1 \\ 0 & \text{otherwise} \end{cases} \tag{A.4}$$

with ϵ ... relative disk flux, θ_{min} ... minor diameter, θ_{maj} ... major diameter and ϑ ... position angle.

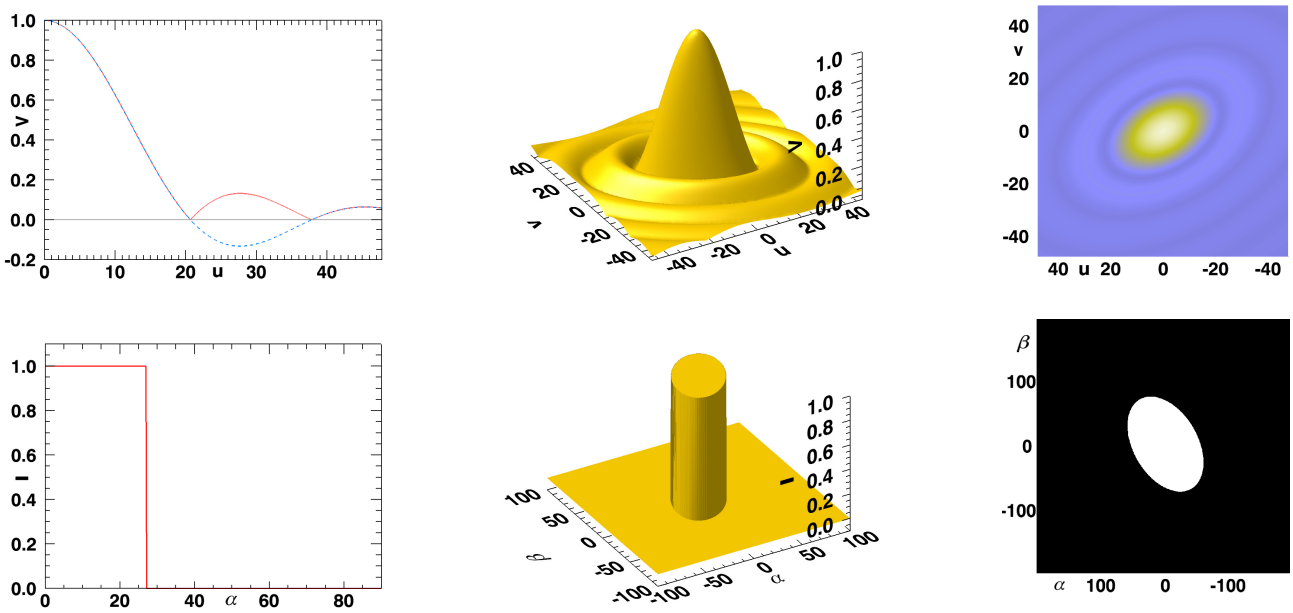

Figure A.3: Model example: $\epsilon = 1.0$, $\theta_{\mathrm{min}} = 50$ mas, $\theta_{\mathrm{maj}} = 80$ mas, $\vartheta = 30$ deg, $\lambda = 8.1$ μm. Fourier plane (u,v)-coordinates are in 1/arcsec and sky plane (α,β)-coordinates are in mas. See Section A.1 for a description (page 161 – 162).

A.4 Relative Circular Gaussian

This is a basic representation of an envelope and useful for a first order approximation.

$$V(r) = \epsilon \exp\left\{-\frac{(\pi\theta r)^2}{4\ln 2}\right\} \tag{A.5}$$

$$I(\rho) = \epsilon \frac{4\ln 2}{\pi\theta^2} \exp\left\{-\frac{4\rho^2 \ln 2}{\theta^2}\right\} \tag{A.6}$$

with ϵ ... relative Gaussian flux and θ ... Gaussian FWHM.

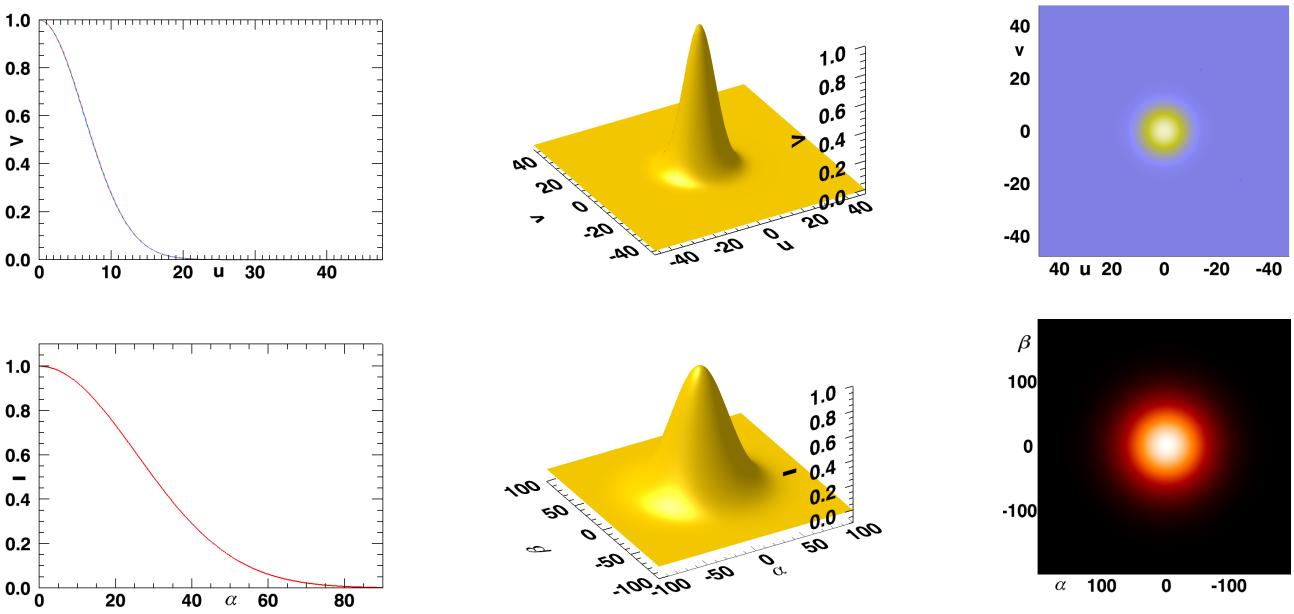

Figure A.4: Model example: $\epsilon = 1.0$, $\theta = 60$ mas, $\lambda = 8.1$ μm. Fourier plane (u,v)-coordinates are in 1/arcsec and sky plane (α,β)-coordinates are in mas. See Section A.1 for a description (page 161 – 162).

A.5 Relative Elliptical Gaussian

This represents the same as in A.4, but for an elliptical approximation.

$$V\left(r_{\vartheta,\eta}\right) \;=\; \epsilon\ \exp - \left\{ \frac{\left(\pi\theta_{\mathrm{maj}} r_{\vartheta,\eta}\right)^2}{4\ln 2} \right\} \tag{A.7}$$

$$I\left(\rho_{\vartheta,\eta}\right) \;=\; \epsilon\ \frac{4\ln 2}{\pi\eta\theta^2_{\mathrm{maj}}} \exp - \left\{ \frac{4\rho^2_{\vartheta,\eta}\ln 2}{\theta^2_{\mathrm{maj}}} \right\} \tag{A.8}$$

with ϵ . . . relative Gaussian flux, θ_{min} . . . minor FWHM, θ_{maj} . . . major FWHM and ϑ . . . position angle.

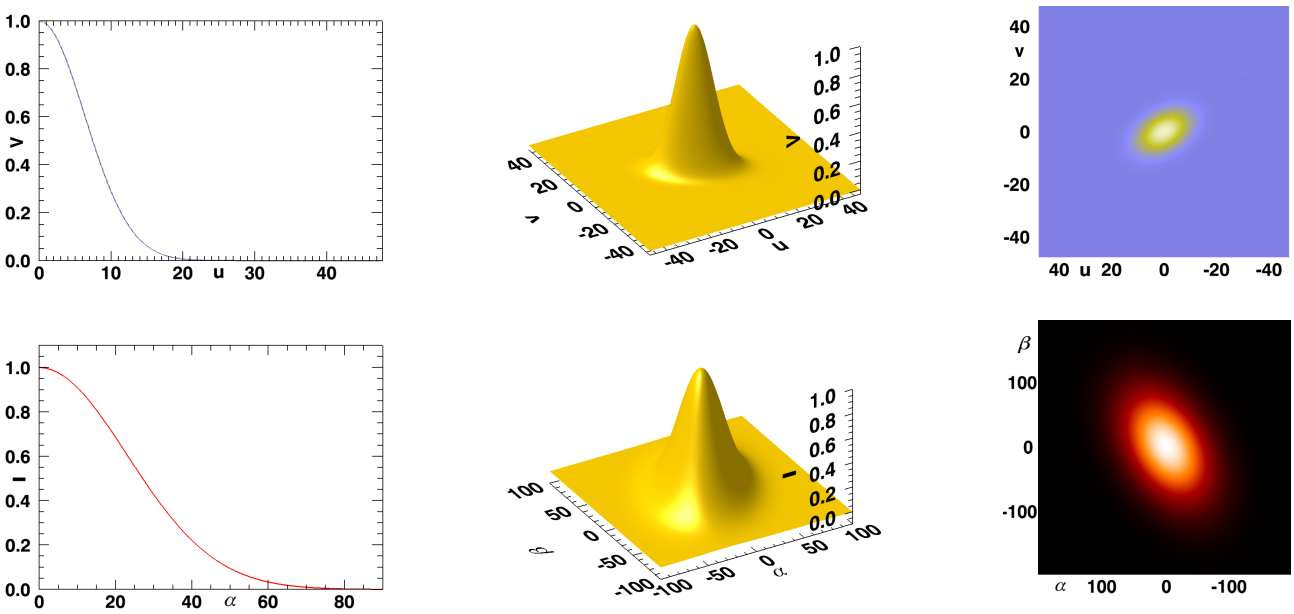

Figure A.5: Model example: $\epsilon = 1.0$, $\theta_{\mathrm{min}} = 50$ mas, $\theta_{\mathrm{maj}} = 80$ mas, $\vartheta = 30$ deg, $\lambda = 8.1$ μm. Fourier plane (u,v)-coordinates are in 1/arcsec and sky plane (α,β)-coordinates are in mas. See Section A.1 for a description (page 161 – 162).

A.6 Relative Circular Fully Limb-Darkened Disk

This model can be used for a stellar surface with pronounced limb darkening or an extended atmosphere.

$$V\left(r\right) = \epsilon \frac{3\sqrt{\pi} J_{\frac{3}{2}}(\pi\theta r)}{\sqrt{2}(\pi\theta r)^{\frac{3}{2}}} \tag{A.9}$$

$$I\left(\rho\right) = \begin{cases} \epsilon \frac{8}{\pi^2\theta^2}\sqrt{1-\left(\frac{2\rho}{\theta}\right)^2} & \text{if } \rho \leq \frac{\theta}{2} \\ 0 & \text{otherwise} \end{cases} \tag{A.10}$$

with ϵ . . . relative fully limb-darkened disk flux and θ . . . fully limb-darkened disk diameter.

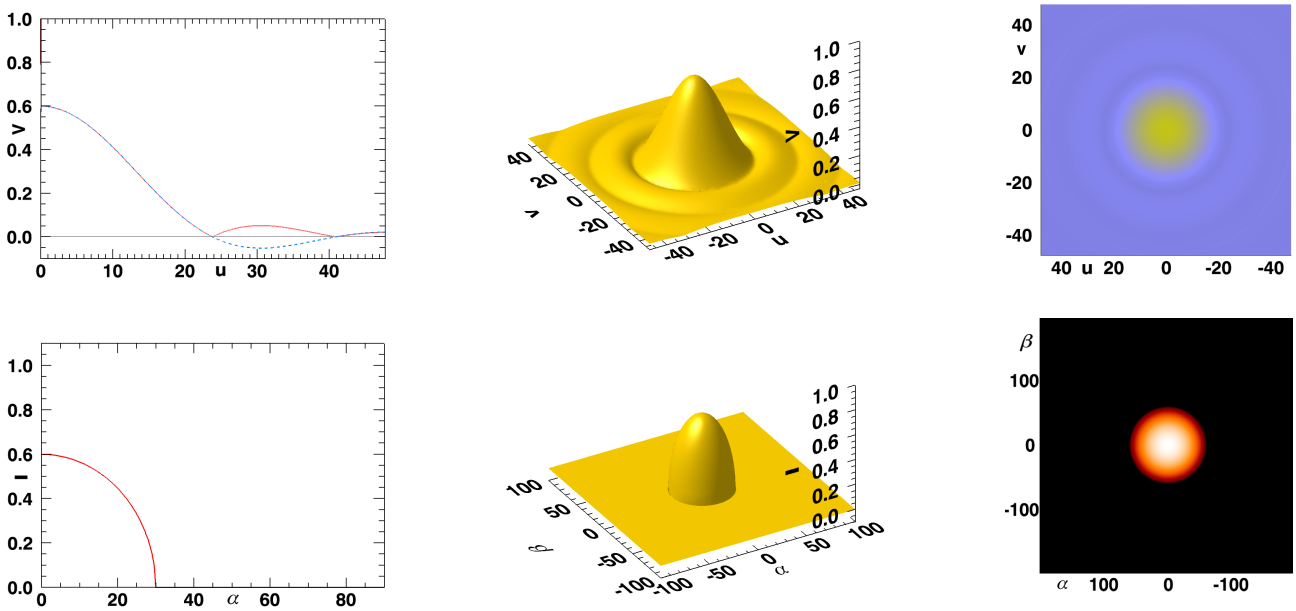

Figure A.6: Model example: $\epsilon = 0.6$, $\theta = 60$ mas, $\lambda = 8.1$ μm. Fourier plane (u,v)-coordinates are in 1/arcsec and sky plane (α,β)-coordinates are in mas. See Section A.1 for a description (page 161 – 162).

A.7 Relative Elliptical Fully Limb-Darkened Disk

This represents the same as in A.6, but for an elliptical approximation.

$$V\left(r_{\vartheta,\eta}\right) = \epsilon \frac{3\sqrt{\pi} J_{\frac{3}{2}}(\pi\theta_{\mathrm{maj}} r_{\vartheta,\eta})}{\sqrt{2}(\pi r_{\vartheta,\eta}\theta_{\mathrm{maj}})^{\frac{3}{2}}} \tag{A.11}$$

$$I\left(\rho_{\vartheta,\eta}\right) = \begin{cases} \epsilon \frac{8}{\pi^2 \eta \theta_{\mathrm{maj}}^2} \sqrt{1 - \left(\frac{2\rho_{\vartheta,\eta}}{\theta_{\mathrm{maj}}}\right)^2} & \text{if } \rho \leq \frac{\theta}{2} \\ 0 & \text{otherwise} \end{cases} \tag{A.12}$$

with ϵ ... relative fully limb-darkened disk flux, θ_{min} ... fully limb-darkened disk minor diameter, θ_{maj} ... fully limb-darkened disk major diameter and ϑ ... position angle.

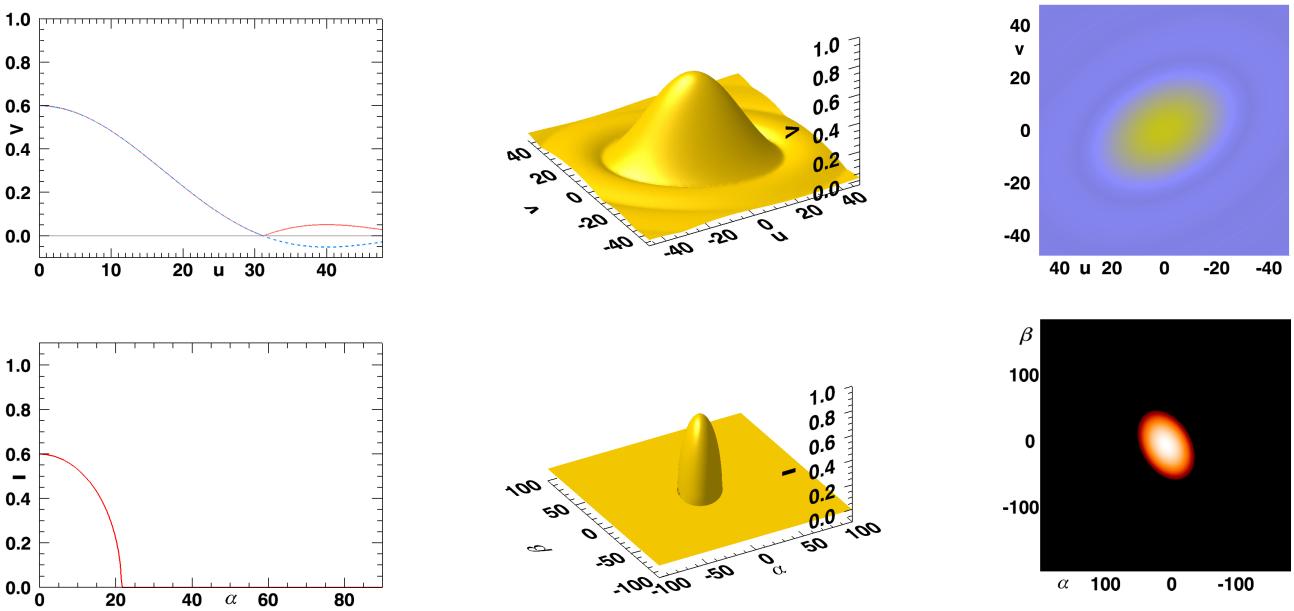

Figure A.7: Model example: $\epsilon = 0.6$, $\theta_{\mathrm{min}} = 40$ mas, $\theta_{\mathrm{maj}} = 60$ mas, $\vartheta = 30$ deg, $\lambda = 8.1$ μm. Fourier plane (u,v)-coordinates are in 1/arcsec and sky plane (α,β)-coordinates are in mas. See Section A.1 for a description (page 161 – 162).

A.8 Circular Uniform Ring

This model is a good first approximation for a distinct shell or a face on accretion disk.

$$V(r) = \frac{2}{\theta_2^2 - \theta_1^2}\left(\theta_2^2 \frac{J_1(\pi\theta_2 r)}{\pi\theta_2 r} - \theta_1^2 \frac{J_1(\pi\theta_1 r)}{\pi\theta_1 r}\right) \tag{A.13}$$

$$I(\rho) = \begin{cases} \frac{4}{\pi}\frac{1}{\theta_2^2-\theta_1^2} & \text{if } \frac{\theta_1}{2} \le \rho \le \frac{\theta_2}{2} \\ 0 & \text{otherwise} \end{cases} \tag{A.14}$$

with θ_1 ... inner diameter and θ_2 ... outer diameter.

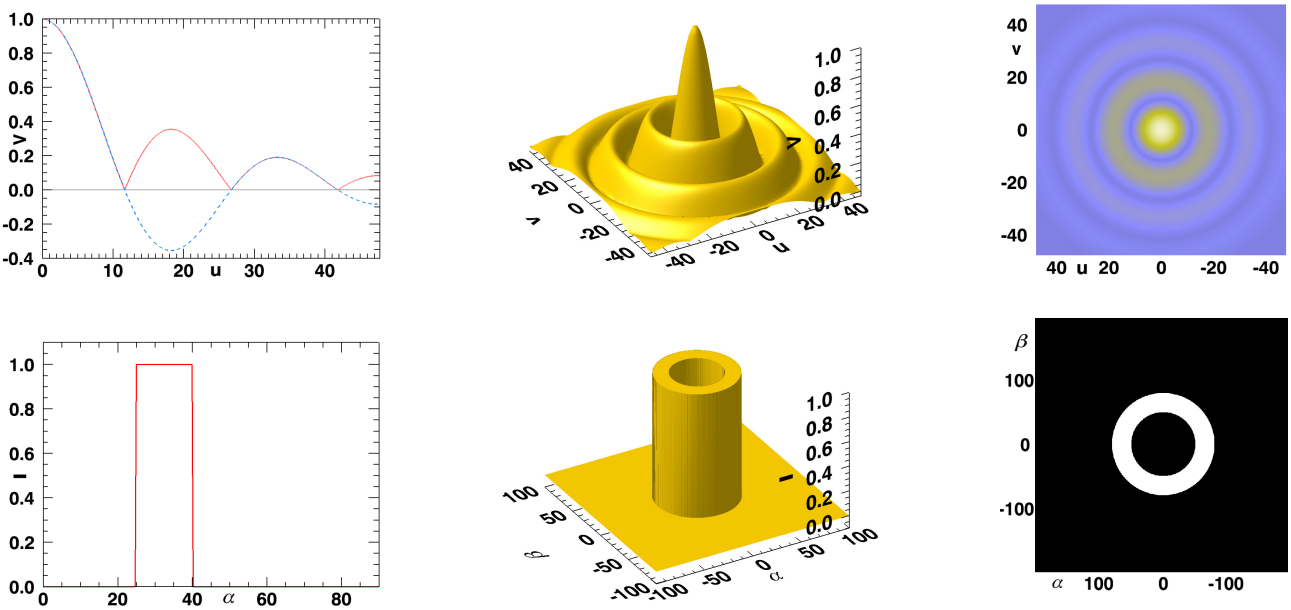

Figure A.8: Model example: $\theta_1 = 50$ mas, $\theta_2 = 80$ mas, $\lambda = 8.1$ μm. Fourier plane (u,v)-coordinates are in 1/arcsec and sky plane (α,β)-coordinates are in mas. See Section A.1 for a description (page 161 – 162).

A.9 Circular Uniform Disk + Circular Uniform Ring

This model approximates a sharp edged stellar surface with an additional distinct shell.

$$V(r) = \epsilon \frac{2J_1(\pi\theta_0 r)}{\pi\theta_0 r} + \frac{2(1-\epsilon)}{\theta_2^2-\theta_1^2}\left(\theta_2^2 \frac{J_1(\pi\theta_2 r)}{\pi\theta_2 r} - \theta_1^2 \frac{J_1(\pi\theta_1 r)}{\pi\theta_1 r}\right) \tag{A.15}$$

$$I(\rho) = \begin{cases} \epsilon \frac{4}{\pi\theta_0^2} & \text{if } \rho \le \frac{\theta_0}{2} \\ 0 & \text{otherwise} \end{cases} + \begin{cases} (1-\epsilon)\frac{4}{\pi(\theta_2^2-\theta_1^2)} & \text{if } \frac{\theta_1}{2} \le \rho \le \frac{\theta_2}{2} \\ 0 & \text{otherwise} \end{cases} \tag{A.16}$$

with θ_0 ... disk diameter, θ_1 ... inner ring diameter, θ_2 ... outer ring diameter and ϵ ... relative flux of disk.

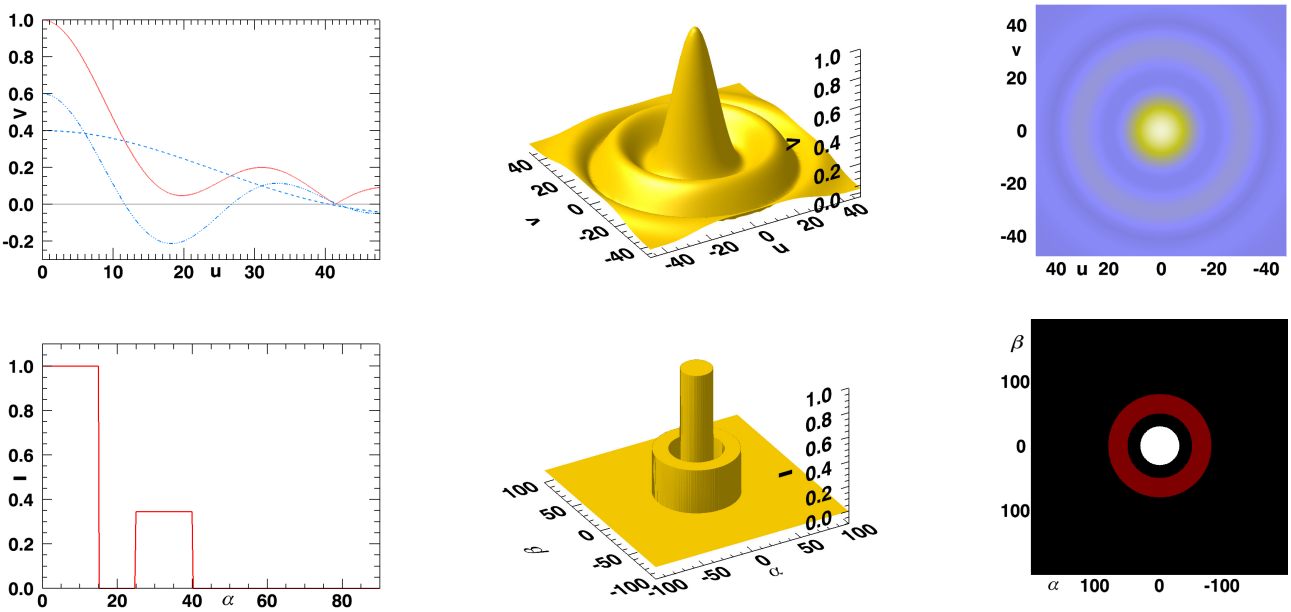

Figure A.9: Model example: $\theta_0 = 30$ mas, $\theta_1 = 50$ mas, $\theta_2 = 80$ mas, $\epsilon = 0.4$, $\lambda = 8.1$ μm. Fourier plane (u,v)-coordinates are in 1/arcsec and sky plane (α,β)-coordinates are in mas. See Section A.1 for a description (page 161 – 162).

A.10 Circular Uniform Disk + Circular Gaussian

This model approximates a sharp edged stellar surface with an additional extended envelope.

$$V\,(r) \;=\; \epsilon\,\frac{2J_1(\pi\theta_0 r)}{\pi\theta_0 r} + (1-\epsilon)\exp\left\{-\frac{(\pi\theta_1 r)^2}{4\ln 2}\right\} \tag{A.17}$$

$$I\,(\rho) \;=\; (1-\epsilon)\frac{4\ln 2}{\pi\theta_1^2}\exp-\left\{\frac{4\rho^2\ln 2}{\theta_1^2}\right\} + \left\{\begin{array}{ll}\epsilon\frac{4}{\pi\theta_0^2} & \text{if } \rho \le \frac{\theta_0}{2}\\ 0 & \text{otherwise}\end{array}\right. \tag{A.18}$$

with θ_0 ... disk diameter, θ_1 ... Gaussian FWHM and ϵ ... relative flux of disk.

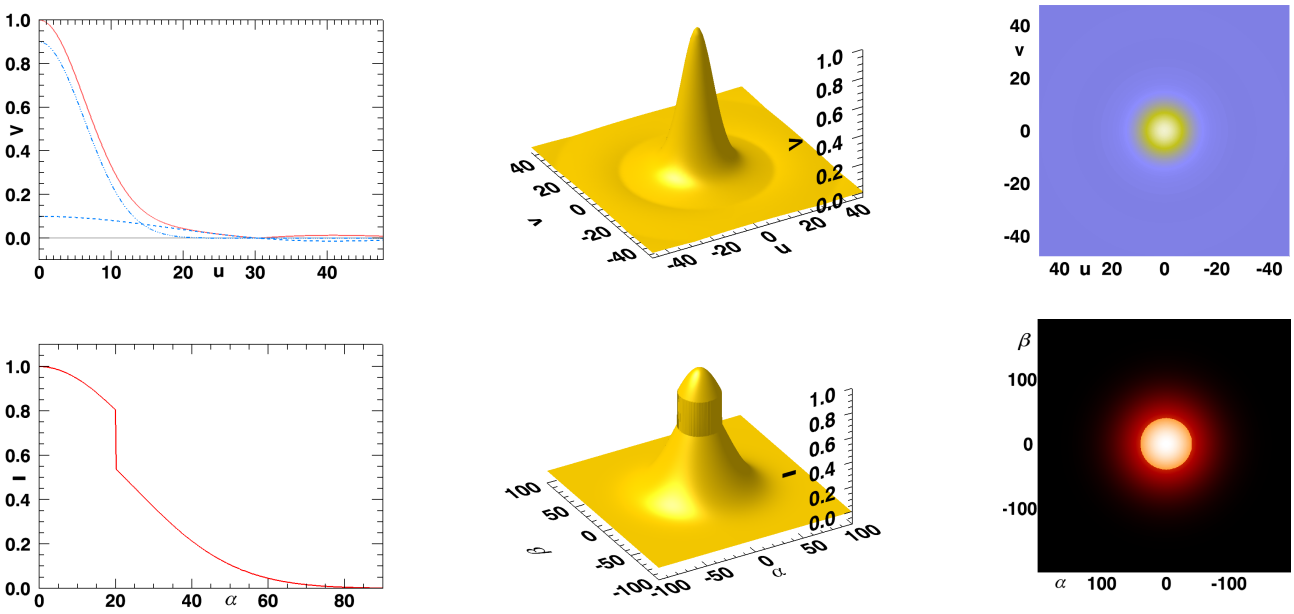

Figure A.10: Model example: $\theta_0 = 40$ mas, $\theta_1 = 60$ mas, $\epsilon = 0.1$, $\lambda = 8.1$ μm. Fourier plane (u,v)-coordinates are in 1/arcsec and sky plane (α,β)-coordinates are in mas. See Section A.1 for a description (page 161 – 162).

A.11 Circular Uniform Disk + Elliptical Gaussian

This model approximates a sharp edged stellar surface with an additional elliptical extended envelope.

$$V\ (r, r_{\vartheta,\eta}) \quad = \quad \epsilon\ \frac{2J_1(\pi\theta_0 r)}{\pi\theta_0 r} + (1-\epsilon)\exp\left\{-\frac{(\pi\theta_{\rm maj} r_{\vartheta,\eta})^2}{4\ln 2}\right\} \tag{A.19}$$

$$I\ (\rho, \rho_{\vartheta,\eta}) \quad = \quad (1-\epsilon)\frac{4\ln 2}{\pi\eta\theta_{\rm maj}^2}\exp-\left\{\frac{4\rho_{\vartheta,\eta}^2\ln 2}{\theta_{\rm maj}^2}\right\} + \begin{cases} \epsilon\ \frac{4}{\pi\theta_0^2} & \text{if } \rho \le \frac{\theta_0}{2} \\ 0 & \text{otherwise} \end{cases} \tag{A.20}$$

with θ_0 ... disk diameter, $\theta_{\rm min}$ ... minor Gaussian FWHM, $\theta_{\rm maj}$ ... major Gaussian FWHM, ϑ ... Gaussian position angle and ϵ ... relative flux of disk.

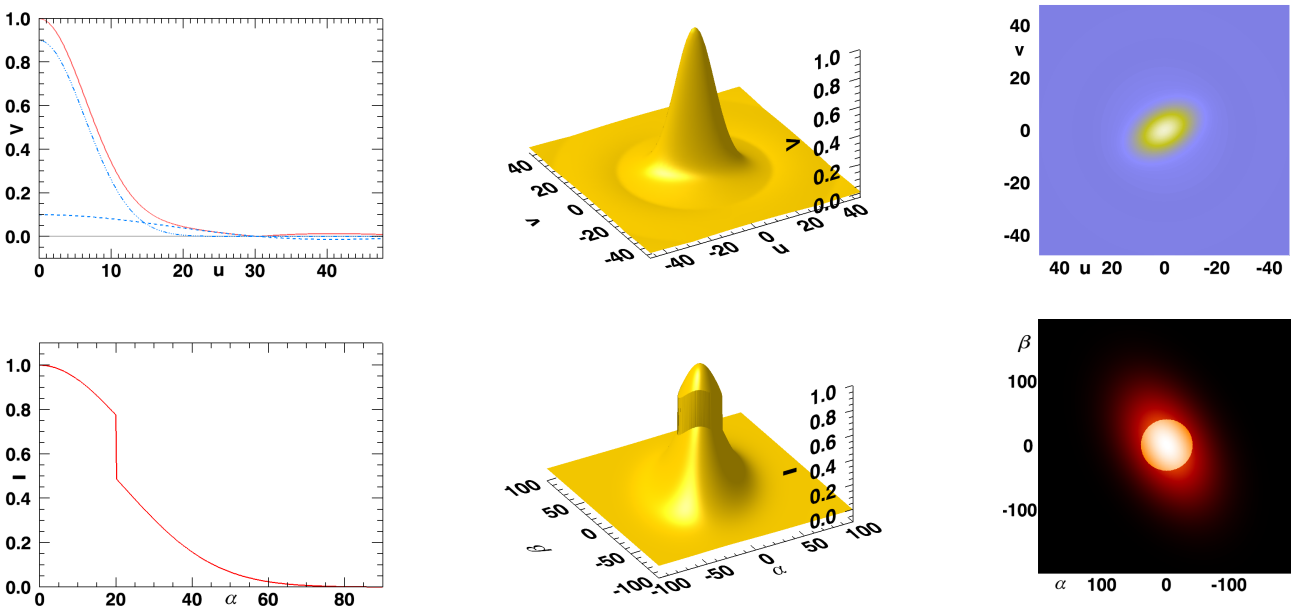

Figure A.11: Model example: $\theta_0 = 40$ mas, $\theta_{\rm min} = 50$ mas, $\theta_{\rm maj} = 80$ mas, $\vartheta = 30$ deg, $\epsilon = 0.1$, $\lambda = 8.1$ μm. Fourier plane (u,v)-coordinates are in 1/arcsec and sky plane (α,β)-coordinates are in mas. See Section A.1 for a description (page 161 – 162).

A.12 Circular Fully Limb-Darkened Disk + Circular Uniform Ring

This model approximates a limb-darkened stellar surface with an additional distinct shell.

$$V\left(r\right) = \epsilon \frac{3\sqrt{\pi}J_{\frac{3}{2}}(\pi\theta_0 r)}{\sqrt{2}(\pi\theta_0 r)^{\frac{3}{2}}} + \frac{2(1-\epsilon)}{\theta_2^2-\theta_1^2}\left(\theta_2^2\frac{J_1(\pi\theta_2 r)}{\pi\theta_2 r} - \theta_1^2\frac{J_1(\pi\theta_1 r)}{\pi\theta_1 r}\right) \tag{A.21}$$

$$I\left(\rho\right) = \begin{cases} \epsilon\frac{8}{\pi^2\theta_0^2}\sqrt{1-\left(\frac{2\rho}{\theta_0}\right)^2} & \text{if } \rho \le \frac{\theta_0}{2} \\ 0 & \text{otherwise} \end{cases} + \begin{cases} (1-\epsilon)\frac{4}{\pi(\theta_2^2-\theta_1^2)} & \text{if } \frac{\theta_1}{2} \le \rho \le \frac{\theta_2}{2} \\ 0 & \text{otherwise} \end{cases} \tag{A.22}$$

with θ_0 ... fully limb-darkened disk diameter, θ_1 ... inner ring diameter, θ_2 ... outer ring diameter and ϵ ... relative flux of fully limb-darkened disk.

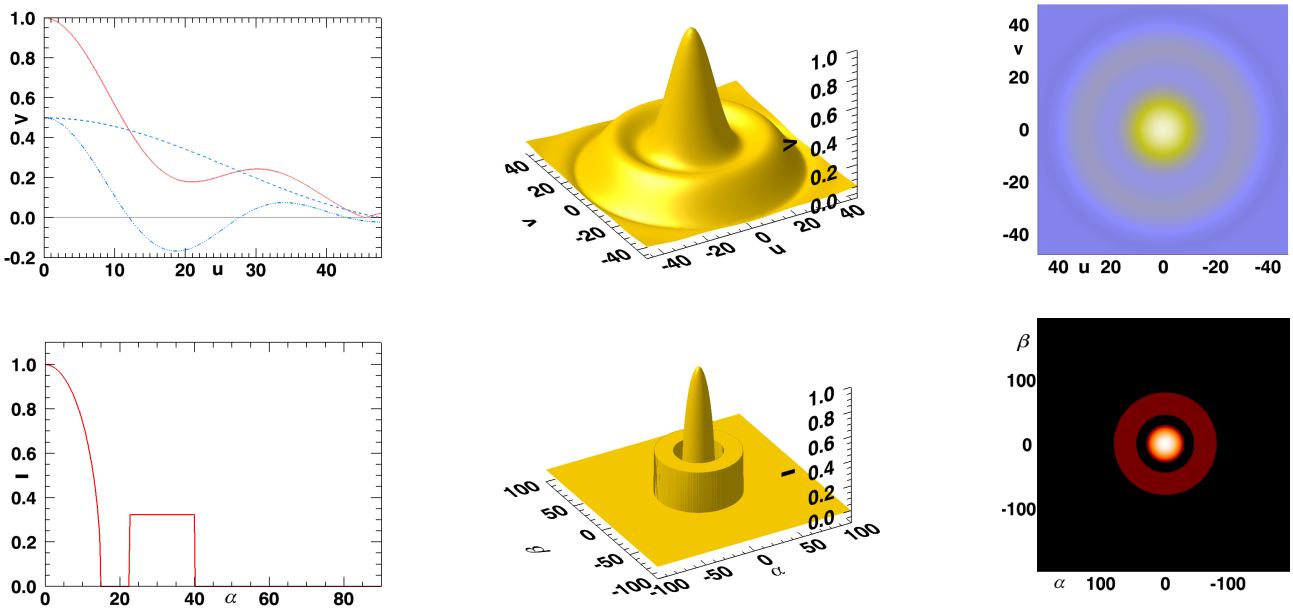

Figure A.12: Model example: $\theta_0 = 30$ mas, $\theta_1 = 45$ mas, $\theta_2 = 80$ mas, $\epsilon = 0.5$, $\lambda = 8.1$ μm. Fourier plane (u,v)-coordinates are in 1/arcsec and sky plane (α,β)-coordinates are in mas. See Section A.1 for a description (page 161 – 162).

A.13 Circular Fully Limb-Darkened Disk + Circular Gaussian

This model approximates a limb-darkened stellar surface with an additional extended envelope.

$$V\left(r\right) \;=\; \epsilon\,\frac{3\sqrt{\pi}J_{\frac{3}{2}}(\pi\theta_0 r)}{\sqrt{2}(\pi\theta_0 r)^{\frac{3}{2}}} + (1-\epsilon)\exp\left\{-\frac{(\pi\theta_1 r)^2}{4\ln 2}\right\} \tag{A.23}$$

$$I\left(\rho\right) \;=\; (1-\epsilon)\frac{4\ln 2}{\pi\theta_1^2}\exp-\left\{\frac{4\rho^2\ln 2}{\theta_1^2}\right\} + \begin{cases} \epsilon\,\frac{8}{\pi^2\theta_0^2}\sqrt{1-\left(\frac{2\rho}{\theta_0}\right)^2} & \text{if } \rho \le \frac{\theta_0}{2} \\ 0 & \text{otherwise} \end{cases} \tag{A.24}$$

with θ_0 ... fully limb-darkened disk diameter, θ_1 ... Gaussian FWHM and ϵ ... relative fully limb-darkened disk flux.

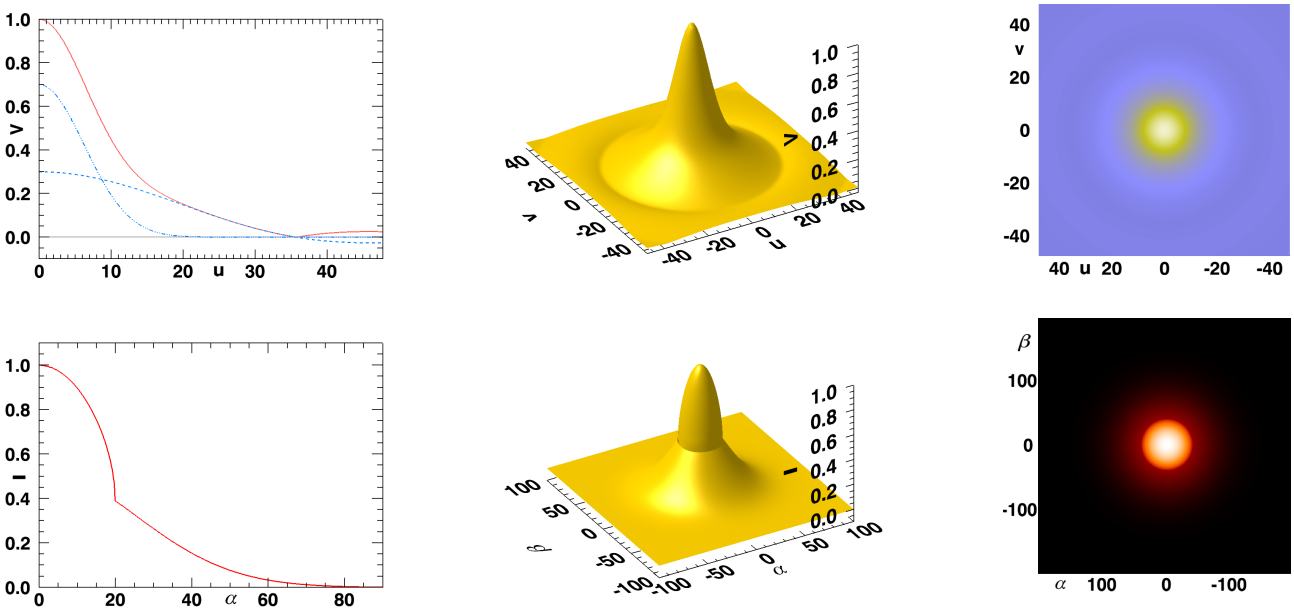

Figure A.13: Model example: $\theta_0 = 40$ mas, $\theta_1 = 60$ mas, $\epsilon = 0.3$, $\lambda = 8.1$ μm. Fourier plane (u,v)-coordinates are in 1/arcsec and sky plane (α,β)-coordinates are in mas. See Section A.1 for a description (page 161 – 162).

A.14 Circular Fully Limb-Darkened Disk + Elliptical Gaussian

This model approximates a limb-darkened stellar surface with an additional extended elliptical envelope.

$$V\,(r, r_{\vartheta,\eta}) \;=\; \epsilon\,\frac{3\sqrt{\pi}J_{\frac{3}{2}}(\pi\theta_0 r)}{\sqrt{2}(\pi\theta_0 r)^{\frac{3}{2}}} + (1-\epsilon)\exp-\left\{\frac{(\pi\theta_{\rm maj} r_{\vartheta,\eta})^2}{4\ln 2}\right\} \tag{A.25}$$

$$I\,(\rho, \rho_{\vartheta,\eta}) \;=\; (1-\epsilon)\frac{4\ln 2}{\pi\eta\theta^2_{\rm maj}}\exp-\left\{\frac{4\rho^2_{\vartheta,\eta}\ln 2}{\theta^2_{\rm maj}}\right\} + \begin{cases} \epsilon\,\frac{8}{\pi^2\theta_0^2}\sqrt{1-\left(\frac{2\rho}{\theta_0}\right)^2} & \text{if } \rho \le \frac{\theta}{2} \\ 0 & \text{otherwise} \end{cases} \tag{A.26}$$

with θ_0 ... fully limb-darkened disk diameter, $\theta_{\rm min}$ ... minor Gaussian FWHM, $\theta_{\rm maj}$ ... major Gaussian FWHM, ϑ ... Gaussian position angle and ϵ ... relative fully limb-darkened disk flux

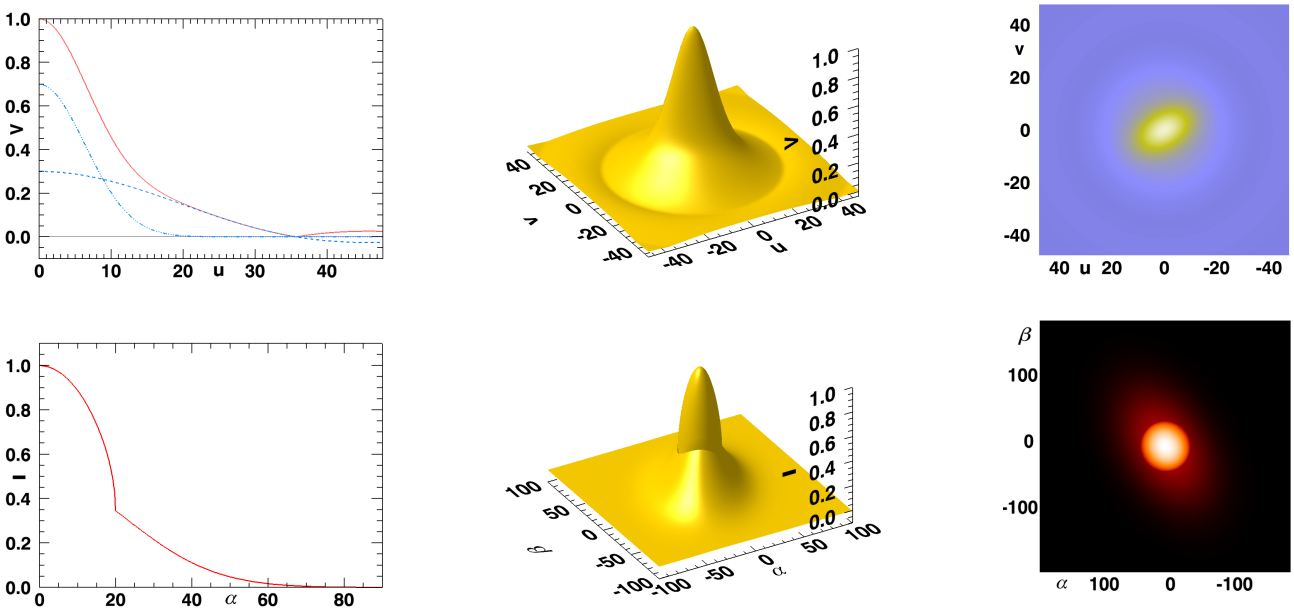

Figure A.14: Model example: $\theta_0 = 40$ mas, $\theta_{\rm min} = 50$ mas, $\theta_{\rm maj} = 80$ mas, $\vartheta = 30$ deg, $\epsilon = 0.3$, $\lambda = 8.1$ μm. Fourier plane (u,v)-coordinates are in 1/arcsec and sky plane (α,β)-coordinates are in mas. See Section A.1 for a description (page 161 – 162).

A.15 Point Binary

A binary system with two unresolved points sources is represented by this model. Note, that δ refers here to the Dirac delta function.

$$V(u,v) = \sqrt{\epsilon^2 + (1-\epsilon)^2 + 2\epsilon(1-\epsilon)\cos(2\pi s[u\sin\vartheta + v\cos\vartheta])} \quad \text{(A.27)}$$

$$I(\alpha,\beta) = \epsilon\,\delta(\alpha - \frac{1}{2}s\cos\vartheta, \beta - \frac{1}{2}s\sin\vartheta) + (1-\epsilon)\,\delta(\alpha + \frac{1}{2}s\cos\vartheta, \beta + \frac{1}{2}s\sin\vartheta) \quad \text{(A.28)}$$

with s . . . binary separation, ϑ . . . position angle and ϵ . . . relative flux of first binary component.

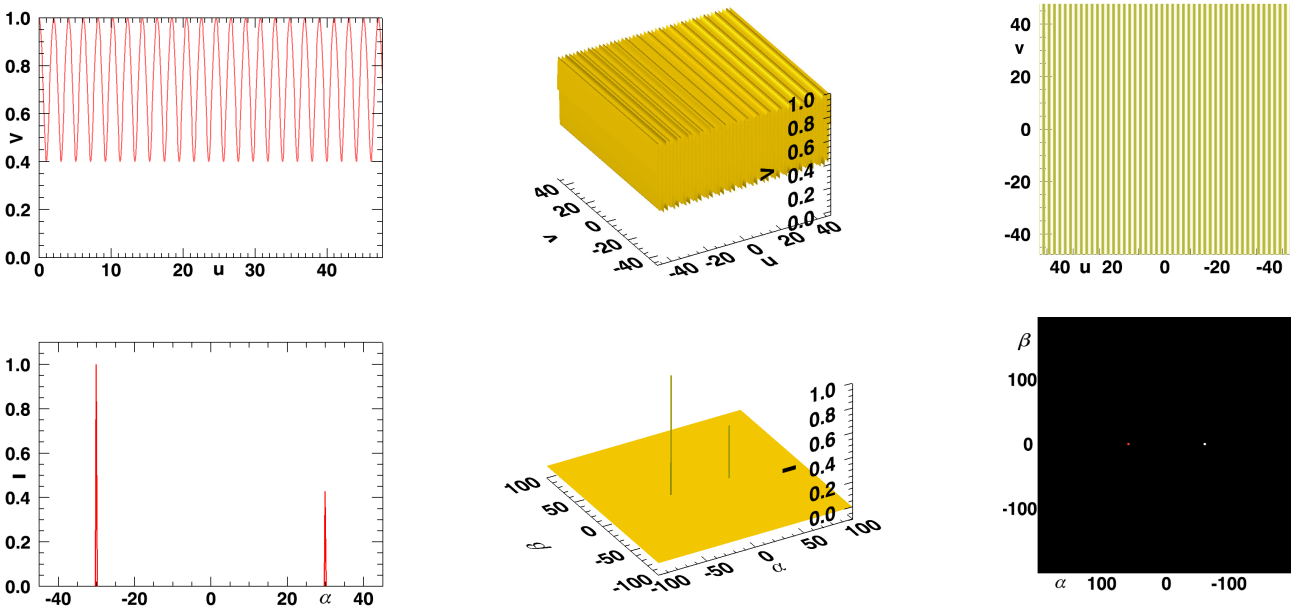

Figure A.15: Model example: $s = 60$ mas, $\vartheta = 90$ deg, $\epsilon = 0.3$, $\lambda = 8.1$ μm. Fourier plane (u,v)-coordinates are in 1/arcsec and sky plane (α,β)-coordinates are in mas. See Section A.1 for a description (page 161 – 162).

A.16 Uniform Disk Binary

A binary system consisting of two resolved uniform disk stellar surfaces is represented by this model.

$$V(u,v) = \frac{4\epsilon^2\theta_1^2 J_1^2(\pi\theta_1 r) + 4(1-\epsilon)^2\theta_2^2 J_1^2(\pi\theta_2 r)}{\pi^2(\epsilon\theta_1^2 r + (1-\epsilon)\theta_2^2 r)^2} \tag{A.29}$$

$$+ \frac{8\epsilon(1-\epsilon)\theta_1\theta_2 J_1(\pi\theta_1 r)J_1(\pi\theta_2 r)\cos(2\pi s[u\sin\vartheta + v\cos\vartheta])}{\pi^2(\epsilon\theta_1^2 r + (1-\epsilon)\theta_2^2 r)^2} \tag{A.30}$$

$$I\,(\alpha,\beta) = \begin{cases} \epsilon\,\frac{4}{\pi\theta_1^2} & \text{if } \sqrt{(\alpha - \frac{1}{2}s\cos\vartheta)^2 + (\beta - \frac{1}{2}s\sin\vartheta)^2} \le \frac{\theta_1}{2} \\ 0 & \text{otherwise} \end{cases} \tag{A.31}$$

$$+ \begin{cases} (1-\epsilon)\frac{4}{\pi\theta_2^2} & \text{if } \sqrt{(\alpha + \frac{1}{2}s\cos\vartheta)^2 + (\beta + \frac{1}{2}s\sin\vartheta)^2} \le \frac{\theta_2}{2} \\ 0 & \text{otherwise} \end{cases} \tag{A.32}$$

with θ_1 ... diameter disk 1, θ_2 ... diameter disk 2, ϑ ... position angle, ϵ ... relative flux of first binary component and s ... binary separation.

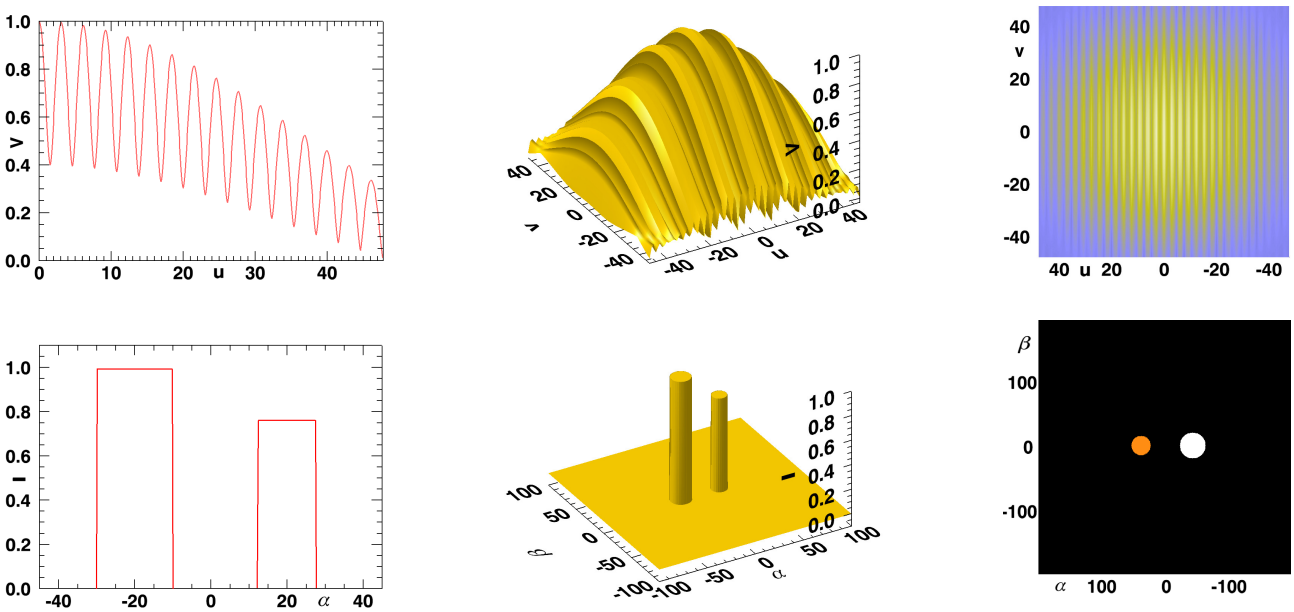

Figure A.16: Model example: $\theta_1 = 20$ mas, $\theta_2 = 15$ mas, $\vartheta = 180$ deg, $\epsilon = 0.3$, $s = 40$ mas, $\lambda = 8.1$ μm. Fourier plane (u,v)-coordinates are in 1/arcsec and sky plane (α,β)-coordinates are in mas. See Section A.1 for a description (page 161 – 162).

Appendix B

Observation Logs

The observation logs of the MIDI observations used for this study are shown in this appendix. Table B.1 gives an overview of the data sorted by semester, and Appendices B.1 to B.5 list the details. Given are the observation epoch (Date and Time), the semester (P: P79 to P83), the used AT stations (AT: A = E0-G0, B = G0-H0, B* = A0-D0, C = E0-H0, D = D0-H0, E = D0-G1 and F = H0-G1, where B* has the same ground baseline length and orientation as B), the dispersive element (Disp: GRISM or PRISM), the number of used calibrators as function of available calibrators (Cal), the projected baseline length (B), the position angle of the baseline vector on the sky (PA), the pulsation phase (Phase), the elevation (H) and a quality flag (QF). The quality flag shows if a observation is used for the model fitting. Rejected observations are flagged as *not used* (see Section 4.2.3 for reasons why a value may not been used).

Table B.1: Overview of the course of observations used for this study. Given are the number of visibility measurements obtained with MIDI in `SCI-PHOT` mode for each of the five stars. Note that for the last two semester the observation program was still ongoing.

Semester[a]	Program ID	Disperser	R Aql	R Aqr	R Hya	V Hya	W Hya
79	079.D-0140	GRISM	11	10	18	8	22
80	080.D-0005	PRISM	6	10	16	26	17
81	081.D-0198	PRISM	15	7	16	8	18
82	082.D-0641	PRISM	0	4	12	20	14
83	083.D-0294	PRISM	8	8	10	1	12

[a] Semester 79 = 1st April, 2007 to 30th September, 2007; Semester 80 = 1st October, 2007 to 31st March, 2008; Semester 81 = 1st April, 2008 to 30th September, 2008; Semester 82 = 1st October, 2008 to 31st March, 2009; and Semester 83 = 1st April, 2009 to 30th September, 2009.

B.1 Observation Log of R Aql

Table B.2: Observation log of R Aql.

Date	Time	P	AT	Disp	Cal	B(m)	PA(°)	Phase	H(°)	QF
2007-04-17	09:06:23.779	P79	B	GRISM	2 of 3	29.05	74.77	0.78	53.87	used
2007-04-25	08:09:12.338	P79	D	GRISM	2 of 2	54.90	74.83	0.81	50.84	used
2007-05-09	09:51:15.000	P79	D	GRISM	0 of 1	63.39	71.22	0.85	52.97	not used
2007-06-19	08:25:08.000	P79	B	GRISM	0 of 2	28.98	66.54	0.02	41.70	not used
2007-06-20	03:28:40.000	P79	C	GRISM	4 of 6	34.14	73.90	0.02	41.23	used
2007-06-20	04:42:25.000	P79	B	GRISM	0 of 1	28.64	74.81	0.02	52.51	not used
2007-06-21	08:30:51.000	P79	A	GRISM	0 of 2	14.04	65.19	0.02	39.22	not used
2007-06-22	08:05:24.000	P79	C	GRISM	1 of 1	44.27	67.37	0.02	43.09	used
2007-10-02	23:37:29.000	P80	A	PRISM	1 of 1	16.01	72.65	0.40	56.10	used
2007-10-05	00:24:43.000	P79	B	GRISM	1 of 2	31.24	70.22	0.41	50.57	used
2007-10-05	23:33:31.000	P80	B	PRISM	1 of 1	32.00	72.56	0.41	55.85	used
2007-10-06	23:43:58.000	P80	C	PRISM	2 of 2	47.87	71.90	0.42	54.73	used
2007-10-07	00:11:23.000	P80	C	PRISM	2 of 2	47.08	70.51	0.42	51.29	used
2008-03-06	09:16:57.330	P80	D	PRISM	1 of 1	31.21	69.28	0.98	28.48	used
2008-03-06	09:26:46.124	P80	D	PRISM	1 of 1	33.42	70.36	0.98	30.49	used
2008-03-25	09:31:47.779	P79	A	GRISM	0 of 1	12.33	74.45	0.05	45.38	not used
2008-04-02	09:00:39.945	P81	A	PRISM	3 of 3	12.34	74.46	0.07	45.44	used
2008-04-02	09:39:51.946	P81	C	PRISM	3 of 4	41.50	74.83	0.07	51.25	used
2008-04-04	09:30:40.946	P81	B	PRISM	1 of 1	27.57	74.82	0.08	51.08	used
2008-04-04	09:39:46.960	P81	B	PRISM	1 of 1	28.17	74.82	0.08	52.22	used
2008-04-27	08:24:58.000	P81	D	PRISM	1 of 1	58.66	74.76	0.17	53.96	used
2008-04-27	08:36:46.960	P81	D	PRISM	1 of 1	59.45	74.69	0.17	55.04	used
2008-05-23	05:54:09.000	P79	D	GRISM	1 of 1	52.03	74.69	0.26	47.67	used
2008-05-26	05:17:58.000	P81	D	PRISM	1 of 1	49.44	74.46	0.27	43.68	used
2008-06-01	06:08:05.138	P81	A	PRISM	4 of 4	70.28	128.84	0.30	54.02	used
2008-06-01	06:16:17.960	P81	A	PRISM	4 of 4	69.88	128.81	0.30	54.79	used
2008-06-01	06:56:41.946	P81	A	PRISM	4 of 4	67.14	129.21	0.30	57.02	used
2008-06-01	07:04:33.959	P81	A	PRISM	0 of 4	66.46	129.40	0.30	57.13	not used
2008-06-06	07:46:19.000	P81	A	PRISM	0 of 2	15.96	71.90	0.32	54.21	not used
2008-06-06	09:40:04.000	P81	C	PRISM	0 of 1	41.28	64.31	0.32	36.72	not used
2008-06-07	06:16:17.945	P81	C	PRISM	1 of 1	45.96	74.42	0.32	56.43	used
2008-06-07	06:39:05.000	P81	B	PRISM	3 of 3	31.67	73.66	0.32	57.11	used
2009-04-20	08:01:43.946	P83	B	PRISM	3 of 3	25.57	74.61	0.49	47.18	used
2009-04-23	06:40:13.946	P83	C	PRISM	2 of 6	28.53	72.10	0.50	34.71	used
2009-04-23	07:53:25.946	P83	C	PRISM	6 of 6	38.78	74.66	0.50	47.72	used
2009-05-02	09:38:45.000	P83	D	PRISM	3 of 3	63.97	72.88	0.53	56.23	used
2009-06-03	05:35:12.000	P83	A	PRISM	1 of 3	13.88	74.85	0.65	51.00	used
2009-06-03	06:52:23.000	P83	A	PRISM	1 of 3	15.69	74.01	0.65	57.07	used
2009-06-26	04:31:29.000	P83	D	PRISM	1 of 2	58.70	74.75	0.73	54.09	used
2009-07-03	05:21:54.000	P83	B	PRISM	1 of 2	31.88	73.27	0.76	56.82	used

B.2 Observation Log of R Aqr

Table B.3: Observation log of R Aqr.

Date	Time	P	AT	Disp	Cal	B(m)	PA(°)	Phase	H(°)	QF
2007-05-16	10:06:28.000	P79	D	GRISM	1 of 1	51.09	53.81	0.50	50.38	used
2007-06-18	09:46:44.000	P79	A	GRISM	2 of 4	15.53	67.42	0.59	74.20	used
2007-06-19	09:34:00.000	P79	B	GRISM	0 of 2	30.79	66.67	0.59	72.48	not used
2007-06-20	08:25:38.000	P79	C	GRISM	4 of 6	42.81	61.15	0.59	58.66	used
2007-06-21	06:59:42.000	P79	A	GRISM	2 of 2	11.32	45.06	0.59	40.09	used
2007-07-02	07:18:59.000	P79	B	GRISM	2 of 3	26.64	56.61	0.62	54.29	used
2007-07-27	10:07:03.000	P79	D	GRISM	1 of 1	57.40	78.05	0.68	60.39	used
2007-10-04	06:26:11.000	P79	A	GRISM	0 of 1	12.59	79.91	0.86	49.04	not used
2007-10-04	02:12:15.000	P80	B	PRISM	2 of 2	30.08	64.81	0.86	68.14	used
2007-10-04	04:10:49.000	P80	B	PRISM	2 of 2	31.80	73.85	0.86	77.57	used
2007-10-04	05:28:51.000	P80	A	PRISM	1 of 1	14.50	77.84	0.86	61.91	used
2007-10-05	05:16:14.000	P79	B	GRISM	0 of 2	29.57	77.35	0.86	63.83	not used
2007-10-06	01:57:28.000	P80	C	PRISM	2 of 2	44.52	63.84	0.87	66.67	used
2007-10-07	05:54:46.000	P79	C	GRISM	1 of 1	40.31	79.13	0.87	53.48	used
2007-10-07	01:16:29.000	P80	C	PRISM	2 of 2	41.29	58.76	0.87	58.52	used
2007-10-07	02:00:53.165	P80	A	PRISM	1 of 1	14.88	64.02	0.87	68.23	used
2007-11-30	00:31:14.000	P80	D	PRISM	0 of 1	47.51	74.32	0.01	76.85	not used
2007-12-02	00:23:50.000	P80	D	PRISM	0 of 3	63.42	74.20	0.01	76.78	not used
2008-05-22	09:16:47.000	P81	D	PRISM	0 of 3	48.10	49.62	0.43	45.12	not used
2008-05-30	07:15:31.945	P80	D	PRISM	0 of 5	36.48	21.26	0.47	24.69	not used
2008-05-30	09:49:08.137	P80	D	PRISM	2 of 5	55.36	59.13	0.47	59.52	used
2008-06-06	08:15:59.945	P81	A	PRISM	0 of 2	11.72	47.73	0.49	44.70	not used
2008-06-06	09:53:36.946	P81	C	PRISM	1 of 1	44.07	63.13	0.49	66.54	used
2008-06-07	09:21:11.000	P81	B	PRISM	3 of 3	28.21	60.38	0.49	60.30	used
2008-06-07	09:54:00.945	P81	B	PRISM	3 of 3	29.58	63.60	0.49	67.47	used
2008-09-25	05:26:02.000	P81	D	PRISM	1 of 1	61.26	76.25	0.78	69.53	used
2008-09-28	05:26:37.330	P81	A	PRISM	1 of 1	15.23	76.49	0.78	66.90	used
2008-12-28	01:14:16.000	P82	A	PRISM	0 of 1	12.25	80.18	0.01	43.58	not used
2008-12-31	00:43:23.000	P82	B	PRISM	1 of 2	26.09	79.50	0.02	47.72	used
2008-12-31	01:14:25.000	P82	B	PRISM	1 of 2	23.39	80.52	0.02	40.95	used
2009-01-01	00:12:38.000	P82	C	PRISM	1 of 1	39.63	79.35	0.03	53.72	used
2009-05-25	09:28:26.000	P83	D	PRISM	0 of 1	50.56	53.10	0.39	50.22	not used
2009-06-03	09:04:03.000	P83	A	PRISM	2 of 3	13.01	55.02	0.42	52.70	used
2009-06-03	09:40:43.000	P83	C	PRISM	1 of 1	42.32	60.38	0.42	60.93	used
2009-07-03	06:48:28.000	P83	B	PRISM	1 of 2	24.83	51.87	0.50	48.71	used
2009-07-30	08:40:36.000	P83	D	PRISM	1 of 1	63.29	74.41	0.57	75.51	used
2009-08-14	08:16:39.000	P83	C	PRISM	0 of 1	45.81	76.36	0.62	68.58	not used
2009-08-14	08:38:16.000	P83	A	PRISM	0 of 1	14.85	77.26	0.62	63.93	not used
2009-08-14	09:30:22.000	P83	B	PRISM	0 of 1	26.11	79.49	0.62	52.30	not used

B.3 Observation Log of R Hya

Table B.4: Observation log of R Hya.

Date	Time	P	AT	Disp	Cal	B(m)	PA(°)	Phase	H(°)	QF
2007-04-12	02:08:09.000	P79	A	GRISM	2 of 3	13.48	48.88	0.60	52.64	used
2007-04-17	07:28:33.338	P79	B	GRISM	2 of 3	24.73	86.35	0.61	49.77	used
2007-04-18	07:10:38.780	P79	A	GRISM	3 of 3	12.92	85.18	0.61	52.93	used
2007-04-22	01:35:49.071	P79	D	GRISM	8 of 8	54.75	50.43	0.62	55.11	used
2007-04-22	07:13:32.070	P79	D	GRISM	8 of 8	48.03	87.13	0.62	47.83	used
2007-04-25	01:23:03.779	P79	E	GRISM	0 of 2	63.50	123.87	0.63	54.00	not used
2007-04-25	04:23:39.780	P79	F	GRISM	2 of 2	71.55	9.98	0.63	84.59	used
2007-05-16	23:52:59.000	P79	B	GRISM	0 of 1	27.96	52.53	0.69	52.30	not used
2007-06-20	01:20:22.000	P79	C	GRISM	6 of 6	46.25	77.60	0.78	76.25	used
2007-06-21	22:54:49.000	P79	C	GRISM	1 of 1	46.13	62.66	0.78	71.24	used
2007-07-02	23:17:47.000	P79	C	GRISM	5 of 5	47.95	69.99	0.81	86.20	used
2007-07-02	01:42:07.000	P79	C	GRISM	0 of 5	41.92	82.60	0.81	60.55	not used
2007-07-03	22:54:48.000	P79	A	GRISM	0 of 2	15.91	68.30	0.82	81.96	not used
2007-07-03	00:28:49.000	P79	A	GRISM	2 of 2	15.57	76.81	0.82	76.34	used
2007-07-04	23:58:37.000	P79	B	GRISM	0 of 4	31.72	74.45	0.82	82.30	not used
2007-07-04	02:19:46.000	P79	B	GRISM	0 of 4	24.68	86.41	0.82	50.24	not used
2007-12-26	08:39:14.000	P79	D	GRISM	1 of 1	51.86	44.87	0.29	45.73	used
2008-02-20	07:53:42.000	P80	D	PRISM	4 of 4	63.89	69.61	0.44	85.31	used
2008-02-20	08:42:11.000	P80	D	PRISM	6 of 4	63.50	74.33	0.44	83.27	used
2008-02-21	09:02:26.000	P79	D	GRISM	0 of 2	62.50	76.42	0.44	77.80	not used
2008-02-22	07:02:15.000	P80	B*	PRISM	0 of 6	31.22	64.71	0.45	75.47	not used
2008-02-22	07:54:30.156	P80	B*	PRISM	0 of 6	32.00	70.49	0.45	87.16	not used
2008-03-02	06:36:33.000	P80	E	PRISM	2 of 2	70.92	129.91	0.47	77.67	used
2008-03-02	07:52:58.000	P80	F	PRISM	1 of 2	71.55	10.27	0.47	84.61	used
2008-03-02	08:28:33.000	P80	D	PRISM	2 of 2	62.29	76.75	0.47	76.56	used
2008-03-13	04:43:47.000	P80	B	PRISM	7 of 8	29.03	56.32	0.50	61.84	used
2008-03-13	07:00:13.945	P80	B	PRISM	7 of 8	31.97	72.36	0.50	86.68	used
2008-03-13	09:09:41.945	P80	B	PRISM	7 of 8	27.22	83.52	0.50	57.36	used
2008-03-14	05:39:07.000	P80	A	PRISM	4 of 6	15.57	64.36	0.50	75.34	used
2008-03-14	07:02:11.000	P80	A	PRISM	4 of 6	15.96	73.21	0.50	85.40	used
2008-03-14	08:51:47.000	P80	A	PRISM	4 of 6	13.98	82.60	0.50	60.53	used
2008-03-25	06:08:58.000	P80	C	PRISM	6 of 6	47.97	72.15	0.53	87.51	used
2008-03-25	07:59:34.945	P80	C	PRISM	6 of 6	42.97	81.63	0.53	62.57	used
2008-03-31	04:48:31.000	P80	C	PRISM	1 of 1	47.29	66.29	0.54	79.04	used
2008-04-01	03:50:22.946	P81	B	PRISM	2 of 2	29.75	58.88	0.55	66.69	used
2008-04-02	06:42:37.945	P81	C	PRISM	4 of 4	46.11	77.84	0.55	72.93	used
2008-04-02	08:01:14.946	P81	A	PRISM	3 of 3	13.26	84.39	0.55	55.05	used
2008-04-03	07:04:02.946	P81	B	PRISM	2 of 2	29.69	79.96	0.55	67.16	used
2008-04-28	01:55:35.946	P81	D	PRISM	6 of 6	58.79	57.60	0.62	64.72	used
2008-04-28	02:57:39.946	P81	E	PRISM	2 of 2	70.99	130.09	0.62	78.85	used
2008-04-28	04:06:01.945	P81	F	PRISM	1 of 2	71.55	9.69	0.62	85.24	used
2008-04-28	07:13:08.945	P81	D	PRISM	6 of 6	44.07	89.17	0.62	42.84	used
2008-05-25	00:16:55.000	P81	D	PRISM	2 of 2	59.74	59.31	0.69	66.43	used
2008-07-03	01:31:24.000	P81	A	PRISM	1 of 2	14.10	82.30	0.79	61.43	used
2008-07-03	02:43:24.000	P81	C	PRISM	2 of 2	33.75	88.69	0.79	45.14	used
2008-07-06	03:20:45.000	P81	D	PRISM	2 of 2	35.68	93.62	0.80	34.14	used
2009-01-16	08:03:46.946	P82	F	PRISM	4 of 5	71.54	-7.84	0.32	57.04	used
2009-01-16	08:34:11.000	P82	D	PRISM	1 of 2	58.75	57.54	0.32	63.95	used

...continues on next page

Date	Time	P	AT	Disp	Cal	B(m)	PA(°)	Phase	H(°)	QF
2009-01-17	07:50:45.946	P82	E	PRISM	2 of 2	63.99	124.02	0.32	54.99	used
2009-01-21	07:17:41.000	P81	B	PRISM	5 of 5	26.59	47.49	0.33	51.06	used
2009-01-21	09:02:59.000	P82	B	PRISM	5 of 5	31.10	64.15	0.33	74.98	used
2009-01-22	07:23:42.945	P81	C	PRISM	4 of 5	40.45	48.91	0.34	53.31	used
2009-01-22	07:36:00.946	P81	C	PRISM	4 of 5	41.40	51.25	0.34	56.10	used
2009-01-25	08:13:46.945	P82	A	PRISM	8 of 8	14.94	59.33	0.34	67.36	used
2009-01-25	08:50:11.945	P82	A	PRISM	8 of 8	15.56	64.18	0.34	75.65	used
2009-01-26	09:11:32.000	P82	B	PRISM	1 of 1	31.71	67.44	0.35	81.40	used
2009-01-27	08:13:44.945	P82	C	PRISM	4 of 4	45.26	60.42	0.35	69.14	used
2009-01-27	08:39:07.946	P82	C	PRISM	4 of 4	46.52	63.77	0.35	74.92	used
2009-01-27	08:46:50.123	P82	C	PRISM	4 of 4	46.83	64.72	0.35	76.68	used
2009-02-16	07:39:19.000	P82	D	PRISM	2 of 2	63.27	66.95	0.40	79.20	used
2009-03-16	08:08:24.000	P82	D	PRISM	2 of 3	59.80	79.60	0.48	68.84	used
2009-03-16	08:36:32.000	P81	D	PRISM	2 of 3	56.78	82.00	0.48	62.43	used
2009-04-20	07:34:42.945	P83	B	PRISM	2 of 3	23.02	88.14	0.57	45.29	used
2009-04-23	05:28:10.000	P83	C	PRISM	6 of 6	45.43	78.85	0.58	71.30	used
2009-04-23	07:05:14.946	P83	C	PRISM	6 of 6	36.81	86.57	0.58	49.27	used
2009-04-24	06:05:35.000	P83	B	PRISM	2 of 2	28.16	82.31	0.58	61.90	used
2009-05-02	01:44:52.000	P83	D	PRISM	3 of 3	59.37	58.63	0.60	65.64	used
2009-05-03	01:50:41.946	P83	E	PRISM	2 of 2	68.81	126.71	0.61	67.85	used
2009-05-03	06:19:20.000	P83	F	PRISM	1 of 3	70.55	22.78	0.61	50.75	used
2009-05-24	23:13:50.000	P83	D	PRISM	1 of 1	53.58	48.26	0.66	51.89	used
2009-06-04	23:30:42.000	P83	C	PRISM	3 of 3	44.27	58.02	0.69	64.64	used
2009-06-04	03:46:00.000	P83	A	PRISM	1 of 2	13.39	84.09	0.69	56.99	used

B.4 Observation Log of V Hya

Table B.5: Observation log of V Hya.

Date	Time	P	AT	Disp	Cal	B(m)	PA(°)	Phase	H(°)	QF
2007-04-12	03:45:42.000	P79	A	GRISM	3 of 3	15.01	78.79	0.68	68.63	used
2007-04-14	04:01:23.388	P79	C	GRISM	1 of 1	43.49	80.29	0.68	63.90	used
2007-04-14	04:56:33.000	P79	B	GRISM	0 of 1	24.46	84.98	0.68	50.71	not used
2007-04-22	23:36:20.000	P79	D	GRISM	1 of 8	58.41	58.54	0.70	63.41	used
2007-04-22	03:48:12.779	P79	D	GRISM	2 of 8	55.34	81.89	0.70	58.22	used
2007-12-02	07:58:13.000	P80	D	PRISM	0 of 3	52.05	48.04	0.12	50.30	not used
2007-12-02	08:58:00.000	P80	D	PRISM	1 of 3	58.65	58.93	0.12	63.90	used
2007-12-12	06:16:34.000	P80	F	PRISM	1 of 1	71.54	-16.21	0.14	36.30	used
2007-12-12	07:28:52.000	P80	D	PRISM	2 of 3	53.33	50.29	0.14	52.60	used
2007-12-12	08:19:04.000	P80	E	PRISM	1 of 1	68.45	126.54	0.14	64.00	used
2007-12-12	09:05:20.166	P80	D	PRISM	2 of 3	61.77	64.26	0.14	74.50	used
2008-01-10	07:13:33.000	P80	B	PRISM	2 of 2	31.14	65.29	0.20	76.50	used
2008-01-10	05:03:32.000	P79	B	GRISM	1 of 1	25.01	44.22	0.20	45.49	used
2008-01-11	04:54:29.000	P80	B	PRISM	1 of 1	24.73	43.11	0.20	45.60	used
2008-01-12	05:27:07.000	P80	A	PRISM	0 of 2	13.39	50.69	0.20	52.60	not used
2008-01-12	06:18:56.000	P80	A	PRISM	0 of 2	14.65	58.83	0.20	64.40	not used
2008-01-12	04:37:00.000	P79	A	GRISM	0 of 1	11.96	39.65	0.20	41.26	not used

...continues on next page

Date	Time	P	AT	Disp	Cal	B(m)	PA(°)	Phase	H(°)	QF
2008-02-20	04:42:41.000	P80	D	PRISM	0 of 4	62.75	66.32	0.28	78.50	not used
2008-02-21	03:27:22.000	P80	D	PRISM	0 of 3	57.55	57.17	0.28	61.20	not used
2008-02-22	03:37:17.000	P80	B*	PRISM	0 of 6	29.39	59.09	0.28	64.30	not used
2008-02-22	04:25:40.000	P80	B*	PRISM	0 of 6	31.15	65.28	0.28	75.30	not used
2008-03-11	02:14:28.945	P80	A	PRISM	3 of 3	14.29	56.53	0.31	61.60	used
2008-03-11	02:48:44.946	P80	A	PRISM	3 of 3	15.05	61.44	0.31	69.40	used
2008-03-13	01:21:28.946	P80	B	PRISM	7 of 8	26.17	48.54	0.32	51.30	used
2008-03-13	01:53:55.946	P80	B	PRISM	7 of 8	27.93	54.46	0.32	58.70	used
2008-03-13	03:34:35.946	P80	B	PRISM	7 of 8	31.64	67.68	0.32	81.40	used
2008-03-25	02:22:58.000	P80	C	PRISM	6 of 6	46.74	65.36	0.34	76.70	used
2008-03-25	02:02:04.000	P79	C	GRISM	1 of 1	45.74	62.80	0.34	71.28	used
2008-03-27	00:03:49.946	P80	A	PRISM	1 of 1	12.56	44.63	0.34	47.10	used
2008-03-27	00:54:34.945	P80	C	PRISM	1 of 2	41.87	54.41	0.34	58.60	used
2008-04-02	05:13:23.946	P81	C	PRISM	2 of 4	40.95	82.29	0.35	56.96	used
2008-04-07	00:24:01.946	P81	A	PRISM	1 of 1	14.18	55.86	0.36	60.61	used
2008-04-07	01:01:29.000	P81	C	PRISM	1 of 1	45.24	61.65	0.36	69.13	used
2008-04-07	01:47:45.945	P81	B	PRISM	2 of 2	31.47	66.78	0.36	79.52	used
2008-04-08	00:39:00.946	P81	A	PRISM	1 of 1	14.64	58.73	0.36	64.91	used
2008-04-08	01:37:05.946	P81	B	PRISM	2 of 2	31.32	66.04	0.36	78.03	used
2008-04-28	01:24:40.000	P81	D	PRISM	6 of 6	63.91	72.77	0.40	84.97	used
2008-11-30	07:49:13.000	P81	D	PRISM	1 of 1	51.02	46.15	0.81	47.18	used
2008-12-27	07:24:08.000	P82	A	PRISM	1 of 1	14.84	60.02	0.86	65.61	used
2008-12-27	08:14:23.000	P80	C	PRISM	0 of 1	47.04	66.21	0.86	76.98	not used
2009-01-16	05:01:58.946	P82	E	PRISM	0 of 1	62.98	124.49	0.90	57.84	not used
2009-01-16	06:54:20.000	P82	F	PRISM	4 of 5	71.35	1.97	0.90	76.67	used
2009-01-19	06:37:49.000	P82	D	PRISM	2 of 2	62.41	65.54	0.91	75.61	used
2009-01-19	06:51:54.959	P82	D	PRISM	2 of 2	62.80	66.42	0.91	78.75	used
2009-01-20	04:05:35.000	P80	C	PRISM	2 of 4	36.00	39.97	0.91	41.95	used
2009-01-20	04:50:06.946	P82	C	PRISM	1 of 4	39.53	49.19	0.91	52.04	used
2009-01-20	06:41:18.946	P82	B	PRISM	1 of 1	31.23	65.66	0.91	77.27	used
2009-01-22	05:59:08.945	P82	B	PRISM	0 of 1	30.12	61.51	0.91	69.54	not used
2009-01-22	06:07:04.959	P82	B	PRISM	0 of 1	30.41	62.53	0.91	71.34	not used
2009-01-22	06:42:31.946	P82	C	PRISM	3 of 5	47.18	66.67	0.91	79.28	used
2009-01-25	03:35:25.945	P82	A	PRISM	2 of 8	11.64	36.53	0.92	39.57	used
2009-01-25	07:17:58.945	P82	A	PRISM	8 of 8	16.01	71.37	0.92	86.60	used
2009-02-19	01:53:34.000	P82	D	PRISM	0 of 1	46.81	37.21	0.97	38.77	not used
2009-02-27	06:54:56.945	P82	B	PRISM	1 of 1	29.27	79.89	0.98	64.50	used
2009-02-28	03:28:46.946	P82	B	PRISM	2 of 2	29.92	60.86	0.98	68.43	used
2009-02-28	04:04:29.946	P82	B	PRISM	2 of 2	31.14	65.27	0.98	76.49	used
2009-03-08	00:42:31.015	P82	C	PRISM	3 of 3	34.29	34.38	1.00	37.82	used
2009-03-08	02:14:47.000	P80	C	PRISM	3 of 3	42.15	55.01	1.00	58.75	used
2009-03-08	02:52:36.000	P80	C	PRISM	3 of 3	44.78	60.63	1.00	67.36	used
2009-03-08	03:50:00.000	P82	A	PRISM	1 of 1	15.81	67.46	1.00	80.24	used
2009-03-17	03:16:00.000	P82	D	PRISM	2 of 2	63.26	67.61	0.01	80.54	used
2009-03-17	03:48:12.000	P82	D	PRISM	2 of 2	63.98	70.78	0.01	86.38	used
2009-05-03	23:43:46.000	P83	D	PRISM	0 of 2	62.16	65.02	0.09	75.35	not used

B.5 Observation Log of W Hya

Table B.6: Observation log of W Hya.

Date	Time	P	AT	Disp	Cal	B(m)	PA(°)	Phase	H(°)	QF
2007-04-12	02:57:09.780	P79	A	GRISM	2 of 3	14.54	51.81	0.30	59.82	used
2007-04-13	02:51:02.000	P79	B	GRISM	1 of 1	29.10	51.92	0.30	59.35	used
2007-04-17	08:15:53.780	P79	B	GRISM	2 of 3	22.34	94.12	0.31	44.34	used
2007-04-22	02:31:40.780	P79	D	GRISM	7 of 8	59.53	54.92	0.33	63.73	used
2007-04-22	02:48:28.584	P79	D	GRISM	7 of 8	59.53	54.92	0.33	67.43	used
2007-04-22	08:06:53.780	P79	D	GRISM	7 of 8	42.06	96.19	0.33	41.16	used
2007-04-22	08:25:20.584	P79	D	GRISM	7 of 8	38.56	99.06	0.33	37.15	used
2007-04-24	02:42:17.779	P79	E	GRISM	0 of 2	67.30	125.04	0.33	66.93	not used
2007-04-25	02:10:55.779	P79	E	GRISM	0 of 2	64.92	123.16	0.34	60.89	not used
2007-04-25	03:29:08.779	P79	F	GRISM	2 of 2	71.47	2.19	0.34	77.99	used
2007-06-18	02:23:18.000	P79	A	GRISM	2 of 4	13.25	87.72	0.47	68.26	used
2007-06-20	23:27:30.000	P79	C	GRISM	4 of 6	46.98	62.82	0.48	73.36	used
2007-06-20	02:24:23.000	P79	C	GRISM	3 of 6	43.73	82.84	0.48	66.29	used
2007-07-02	23:48:46.388	P79	C	GRISM	5 of 5	48.00	70.64	0.51	86.12	used
2007-07-02	02:14:19.000	P79	C	GRISM	0 of 5	40.49	86.86	0.51	58.11	not used
2007-07-04	00:23:51.779	P79	B	GRISM	4 of 4	31.55	75.51	0.52	80.46	used
2007-07-04	02:44:50.779	P79	B	GRISM	2 of 4	24.39	90.99	0.52	49.68	used
2008-01-10	09:20:59.000	P80	B	PRISM	2 of 2	30.08	56.39	0.01	64.48	used
2008-02-20	06:31:50.000	P79	D	GRISM	1 of 1	59.95	55.89	0.11	62.71	used
2008-02-20	07:25:12.157	P80	D	PRISM	4 of 4	62.76	63.21	0.11	74.43	used
2008-02-21	07:58:11.314	P80	D	PRISM	0 of 3	63.89	68.30	0.11	82.19	not used
2008-02-22	08:40:15.000	P80	B*	PRISM	5 of 6	31.85	73.49	0.12	84.87	used
2008-02-22	09:21:23.000	P80	B*	PRISM	5 of 6	31.00	78.00	0.12	76.76	used
2008-03-02	05:59:59.000	P80	E	PRISM	2 of 2	66.93	124.69	0.14	65.23	used
2008-03-02	07:17:04.000	P80	F	PRISM	2 of 2	71.45	4.51	0.14	81.83	used
2008-03-03	07:48:42.000	P80	D	PRISM	2 of 2	63.91	72.10	0.14	86.15	used
2008-03-06	08:39:48.948	P79	D	GRISM	1 of 1	61.71	78.46	0.15	74.71	used
2008-03-11	03:09:01.000	P79	A	GRISM	1 of 1	12.33	28.02	0.16	35.53	used
2008-03-11	04:33:26.945	P80	A	PRISM	2 of 3	13.98	46.70	0.16	53.96	used
2008-03-12	08:27:50.780	P79	A	GRISM	1 of 1	15.23	79.71	0.17	72.19	used
2008-03-13	08:21:25.779	P79	B	GRISM	1 of 1	30.54	79.42	0.17	72.73	used
2008-03-13	06:43:20.946	P80	B	PRISM	7 of 8	31.94	68.34	0.17	83.64	used
2008-03-13	08:36:22.015	P80	B	PRISM	7 of 8	29.95	81.01	0.17	69.46	used
2008-03-14	06:15:12.000	P80	A	PRISM	0 of 6	15.86	65.67	0.17	78.81	not used
2008-03-14	07:37:10.000	P80	A	PRISM	4 of 6	15.80	75.37	0.17	81.30	used
2008-03-14	08:15:55.000	P80	A	PRISM	4 of 6	15.26	79.55	0.17	73.06	used
2008-03-25	05:50:47.945	P80	C	PRISM	6 of 6	47.86	67.68	0.20	82.63	used
2008-03-25	06:49:57.000	P80	C	PRISM	6 of 6	47.38	75.34	0.20	82.10	used
2008-03-25	08:29:03.946	P80	C	PRISM	6 of 6	41.85	85.29	0.20	60.68	used
2008-04-01	03:19:19.946	P81	B	PRISM	2 of 2	28.32	48.37	0.22	55.82	used
2008-04-02	07:15:08.000	P81	C	PRISM	4 of 4	44.91	81.06	0.22	70.02	used
2008-04-02	08:27:30.946	P81	A	PRISM	2 of 3	12.96	88.65	0.22	54.09	used
2008-04-03	07:30:06.946	P81	B	PRISM	2 of 2	29.19	82.75	0.22	65.86	used
2008-04-28	02:07:43.945	P81	D	PRISM	6 of 6	59.43	54.70	0.29	63.43	used
2008-04-28	03:22:49.945	P81	E	PRISM	0 of 2	70.58	130.03	0.29	79.76	not used
2008-04-28	04:32:03.946	P81	F	PRISM	0 of 2	71.32	10.41	0.29	82.91	not used
2008-04-28	07:26:33.946	P81	D	PRISM	6 of 6	45.23	93.72	0.29	45.03	used
2008-05-25	00:47:31.946	P81	D	PRISM	2 of 2	61.21	58.90	0.36	69.14	used

...continues on next page

Date	Time	P	AT	Disp	Cal	B(m)	PA(°)	Phase	H(°)	QF
2008-05-30	06:27:43.000	P81	D	PRISM	4 of 5	30.02	107.46	0.37	30.52	used
2008-07-03	02:02:08.000	P81	A	PRISM	1 of 2	13.67	86.31	0.46	59.29	used
2008-07-03	03:16:32.000	P81	C	PRISM	2 of 2	32.03	95.67	0.46	42.96	used
2008-07-06	03:37:07.000	P81	D	PRISM	2 of 2	36.87	100.52	0.46	35.93	used
2009-01-16	07:37:13.000	P82	F	PRISM	4 of 5	71.23	-12.23	0.96	47.49	used
2009-01-16	09:00:36.946	P82	D	PRISM	1 of 2	60.22	56.51	0.96	65.83	used
2009-01-17	08:29:59.000	P82	E	PRISM	0 of 2	65.19	123.34	0.97	59.95	not used
2009-01-20	09:20:51.946	P82	C	PRISM	1 of 4	46.78	61.99	0.97	73.72	used
2009-01-21	06:43:47.000	P81	B	PRISM	5 of 5	25.33	32.67	0.98	40.11	used
2009-01-21	07:49:39.000	P82	B	PRISM	5 of 5	28.19	47.79	0.98	54.53	used
2009-01-21	08:34:37.946	P82	B	PRISM	5 of 5	29.88	55.45	0.98	64.44	used
2009-01-22	08:01:20.945	P81	C	PRISM	2 of 5	43.10	50.26	0.98	57.97	used
2009-01-22	08:28:05.945	P82	C	PRISM	2 of 5	44.68	55.03	0.98	63.87	used
2009-01-22	08:52:48.945	P82	A	PRISM	1 of 1	45.94	59.00	0.98	69.30	used
2009-01-25	06:14:06.946	P81	A	PRISM	5 of 8	12.34	28.13	0.99	37.08	used
2009-01-25	06:49:17.945	P81	A	PRISM	5 of 8	13.05	37.34	0.99	44.74	used
2009-01-25	07:48:24.945	P82	A	PRISM	6 of 8	14.35	50.06	0.99	57.72	used
2009-01-25	09:18:30.946	P82	A	PRISM	6 of 8	15.78	64.41	0.99	77.45	used
2009-01-27	07:19:44.945	P81	C	PRISM	4 of 4	41.69	45.93	0.99	53.14	used
2009-01-27	07:48:31.946	P82	C	PRISM	4 of 4	43.52	51.53	0.99	59.47	used
2009-02-16	08:23:26.000	P82	D	PRISM	2 of 2	63.97	69.21	0.04	83.79	used
2009-02-16	09:14:12.157	P82	D	PRISM	2 of 2	63.24	75.18	0.04	82.52	used
2009-03-16	07:35:32.000	P82	D	PRISM	2 of 3	62.93	76.01	0.12	80.23	used
2009-04-20	08:24:34.110	P83	B	PRISM	3 of 3	20.28	97.36	0.21	39.46	used
2009-04-23	05:46:08.000	P83	C	PRISM	6 of 6	45.26	80.46	0.21	71.65	used
2009-04-23	07:28:38.339	P83	C	PRISM	6 of 6	36.25	91.34	0.21	49.10	used
2009-04-24	06:34:19.945	P83	B	PRISM	2 of 2	27.75	85.53	0.22	60.19	used
2009-05-02	01:08:03.000	P83	D	PRISM	3 of 3	55.99	46.91	0.24	53.53	used
2009-05-03	02:27:23.000	P83	E	PRISM	2 of 2	69.19	127.28	0.24	71.86	used
2009-05-03	03:37:32.000	P83	F	PRISM	1 of 3	71.42	7.00	0.24	85.70	used
2009-05-03	00:20:11.000	P83	D	PRISM	1 of 2	52.46	38.03	0.24	44.76	used
2009-06-04	00:02:52.000	P83	C	PRISM	3 of 3	45.75	58.37	0.32	67.76	used
2009-06-04	00:14:52.000	P83	C	PRISM	3 of 3	46.29	60.19	0.32	70.39	used
2009-06-04	04:32:35.000	P83	A	PRISM	1 of 2	12.40	90.40	0.32	51.50	used
2009-08-15	23:59:26.000	P83	A	PRISM	1 of 2	11.73	92.45	0.51	48.45	used

Bibliography

Aoki, W., Tsuji, T., & Ohnaka, K. 1998, A&A, 340, 222

Aoki, W., Tsuji, T., & Ohnaka, K. 1999, A&A, 350, 945

Angeloni, R., Contini, M., Ciroi, S., & Rafanelli, P. 2007, AJ, 134, 205

Arndt, T. U., Fleischer, A. J., & Sedlmayr, E. 1997, A&A, 327, 614

Balick, B., & Frank, A. 1997, Planetary Nebulae, 180, 190

Barnbaum, C., Morris, M., & Kahane, C. 1995, ApJ, 450, 862

Baschek, B., Scholz, M., & Wehrse, R. 1991, A&A, 246, 374

Bedding, T. R., Conn, B. C., & Zijlstra, A. A. 2000, IAU Colloq. 176: The Impact of Large-Scale Surveys on Pulsating Star Research, 203, 96

Begemann, B., Dorschner, J., Henning, T., Mutschke, H., Guertler, J., Koempe, C., & Nass, R. 1997, ApJ, 476, 199

Benson, P. J., Little-Marenin, I. R., Woods, T. C., Attridge, J. M., Blais, K. A., Rudolph, D. B., Rubiera, M. E., & Keefe, H. L. 1990, ApJS, 74, 911

Bergeat, J., Knapik, A., & Rutily, B. 1998, A&A, 332, L53

Blommaert, J. A. D. L., et al. 2006, A&A, 460, 555

Boboltz, D. A., Diamond, P. J., & Kemball, A. J. 1997, ApJ, 487, L147

Bowers, P. F., Johnston, K. J., & de Vegt, C. 1989, ApJ, 340, 479

Brand, J., et al. 1994, A&AS, 103, 541

Bujarrabal, V., Gomez-Gonzalez, J., & Planesas, P. 1989, A&A, 219, 256

Burgarella, D., Vogel, M., & Paresce, F. 1992, A&A, 262, 83

Chapman, J. M., Sivagnanam, P., Cohen, R. J., & Le Squeren, A. M. 1994, MNRAS, 268, 475

Cohen, M., Walker, R. G., Carter, B., Hammersley, P., Kidger, M., & Noguchi, K. 1999, AJ, 117, 1864

Colavita, M. M. 1999, PASP, 111, 111

Contini, M., & Formiggini, L. 2003, MNRAS, 339, 148

Corradi, R. L. M., Brandi, E., Ferrer, O. E., & Schwarz, H. E. 1999, A&A, 343, 841

Cotton, W. D., et al. 2004, A&A, 414, 275

Cotton, W. D., et al. 2006, A&A, 456, 339

Cotton, W. D., Perrin, G., & Lopez, B. 2008, A&A, 477, 853

Cotton, W. D., Ragland, S., Pluzhnik, E. A., Danchi, W. C., Traub, W. A., Willson, L. A., & Lacasse, M. G. 2010, ApJS, 188, 506

Danchi, W. C., Bester, M., Degiacomi, C. G., Greenhill, L. J., & Townes, C. H. 1994, AJ, 107, 1469

Decin, L. 2000, Ph.D. Thesis, Katholieke Universiteit Leuven

Decin, L., Blomme, L., Reyniers, M., Ryde, N., Hinkle, K. H., & de Koter, A. 2008, A&A, 484, 401

Dominik, C., & Tielens, A. G. G. M. 1997, ApJ, 480, 647

Dorfi, E. A., & Höfner, S. 1996, A&A, 313, 605

Dougherty, S. M., Bode, M. F., Lloyd, H. M., Davis, R. J., & Eyres, S. P. 1995, MNRAS, 272, 843

Draine, B. T., & Lee, H. M. 1984, ApJ, 285, 89

Draine, B. T. 2003, ARA&A, 41, 241

ESO. 2003, VLT Whitebook, Education & Public Relations Department, Karl-Schwarzschild-Strasse 2, D-85748 Garching, Germany

Etoka, S., & Le Squeren, A. M. 2000, A&AS, 146, 179

Fedele, D., Wittkowski, M., Paresce, F., Scholz, M., Wood, P. R., & Ciroi, S. 2005, A&A, 431, 1019

Fleischer, A. J., Gauger, A., & Sedlmayr, E. 1992, A&A, 266, 321

Fox, M. W., & Wood, P. R. 1982, ApJ, 259, 198

Fried, D. L. 1965, Journal of the Optical Society of America (1917 – 1983), 55, 1427

Gail, H. P., & Sedlmayr, E. 1987, A&A, 171, 197

Gautschy-Loidl, R., Höfner, S., Jørgensen, U. G., & Hron, J. 2004, A&A, 422, 289

Gehrz, R. D., & Woolf, N. J. 1971, ApJ, 165, 285

Gehrz, R. 1989, Interstellar Dust, 135, 445

Girardi, L., & Bertelli, G. 1998, MNRAS, 300, 533

Glindemann, A., et al. 2000, Proc. SPIE, 4006, 2

Gomez Balboa, A. M., & Lepine, J. R. D. 1986, A&A, 159, 166

Greaves, J., & Howarth, J. J. 2000, Journal of the British Astronomical Association, 110, 131

Greaves, J. 1998, Journal of the British Astronomical Association, 108, 320

Groenewegen, M. A. T., & de Jong, T. 1994, A&A, 283, 463

Groenewegen, M. A. T., Baas, F., Blommaert, J. A. D. L., Stehle, R., Josselin, E., & Tilanus, R. P. J. 1999, A&AS, 140, 197

Groenewegen, M. A. T., Sloan, G. C., Soszyński, I., & Petersen, E. A. 2009, A&A, 506, 1277

Gromadzki, M., & Mikołajewska, J. 2009, A&A, 495, 931

Gustafsson, B., Edvardsson, B., Eriksson, K., Mizuno-Wiedner, M., Jørgensen, U. G., & Plez, B. 2003, Stellar Atmosphere Modeling, 288, 331

Habing, H. J., & Olofsson, H. 2004, Springer, *Asymptotic Giant Branch Stars*

Habing, H. J., Tignon, J., & Tielens, A. G. G. M. 1994, A&A, 286, 523

Hagen, W. 1982, PASP, 94, 835

Haniff, C. A., Scholz, M., & Tuthill, P. G. 1995, MNRAS, 276, 640

Hashimoto, O., Izumiura, H., Kester, D. J. M., & Bontekoe, T. R. 1998, A&A, 329, 213

Hawkins, G. W. 1990, A&A, 229, L5

He, J. H., Szczerba, R., Chen, P. S., & Sobolev, A. M. 2005, A&A, 434, 201

Henney, W. J., & Dyson, J. E. 1992, A&A, 261, 301

Herbig, G. H. 1980, IAU Circ., 3535, 2

Herwig, F. 2005, ARA&A, 43, 435

Hinkle, K. H., Scharlach, W. W. G., & Hall, D. N. B. 1984, ApJS, 56, 1

Hinkle, K. H., & Barnes, T. G. 1979, ApJ, 227, 923

Hinkle, K. H., Wilson, T. D., Scharlach, W. W. G., & Fekel, F. C. 1989, AJ, 98, 1820

Hirano, N., et al. 2004, ApJ, 616, L43

Hofmann, K.-H., Scholz, M., & Wood, P. R. 1998, A&A, 339, 846

Hofmann, K.-H., et al. 2000, Proc. SPIE, 4006, 688

Höfner, S., & Dorfi, E. A. 1997, A&A, 319, 648

Höfner, S., & Andersen, A. C. 2007, A&A, 465, L39

Höfner, S. 2008, A&A, 491, L1

Hollis, J. M., Michalitsianos, A. G., Kafatos, M., & McAlister, H. A. 1985, ApJ, 289, 765

Hollis, J. M., Oliversen, R. J., Michalitsianos, A. G., Kafatos, M., & Wagner, R. M. 1991, ApJ, 377, 227

Hollis, J. M., Pedelty, J. A., & Lyon, R. G. 1997, ApJ, 482, L85

Hollis, J. M., Pedelty, J. A., Forster, J. R., White, S. M., Boboltz, D. A., & Alcolea, J. 2000, ApJ, 543, L81

Hollis, J. M., Boboltz, D. A., Pedelty, J. A., White, S. M., & Forster, J. R. 2001, ApJ, 559, L37

Hron, J., Loidl, R., Hoefner, S., Jorgensen, U. G., Aringer, B., & Kerschbaum, F. 1998, A&A, 335, L69

Hughes, S. M. G., & Wood, P. R. 1990, AJ, 99, 784

Humphreys, E. M. L., Gray, M. D., Yates, J. A., & Field, D. 1997, MNRAS, 287, 663

Ireland, M. J., Tuthill, P. G., Bedding, T. R., Robertson, J. G., & Jacob, A. P. 2004a, MNRAS, 350, 365

Ireland, M. J., Scholz, M., & Wood, P. R. 2004b, MNRAS, 352, 318

Ireland, M. J., Scholz, M., Tuthill, P. G., & Wood, P. R. 2004c, MNRAS, 355, 444

Ireland, M., Tithill, P., Robertson, G., Bedding, T., Jacob, A., Monnier, J., & Danchi, W. 2004d, IAU Colloq. 193: Variable Stars in the Local Group, 310, 327

Ireland, M. J., & Scholz, M. 2006, MNRAS, 367, 1585

Ireland, M. J., Scholz, M., & Wood, P. R. 2008, MNRAS, 391, 1994

Ivezic, Z., & Elitzur, M. 1995, ApJ, 445, 415

Ivezic, Z., & Elitzur, M. 1997, MNRAS, 287, 799

Ivison, R. J., Seaquist, E. R., & Hall, P. J. 1994, MNRAS, 269, 218

Ivison, R. J., Yates, J. A., & Hall, P. J. 1998, MNRAS, 295, 813

Jacob, A. P., & Scholz, M. 2002, MNRAS, 336, 1377

Jaffe, W. J. 2004, Proc. SPIE, 5491, 715

Johnson, J. J., te Lintel Hekkert, P., & Harrison, T. 1991, BAAS, 23, 1410

Johnson, J. J. 1993, BAAS, 25, 1423

Jørgensen, U. G., Hron, J., & Loidl, R. 2000, A&A, 356, 253

Jura, M. 1996, ApJ, 472, 806

Jura, M. In T.J.Bernatowicz, E. Zinner, editor, 1997, AIP: Woodbury, N.Y., *Astrophysical Implications of the Laboratory Study of Presolar Materials*, page 379

Jura, M., & Kleinmann, S. G. 1992, ApJS, 79, 105

Justtanont, K., Feuchtgruber, H., de Jong, T., Cami, J., Waters, L. B. F. M., Yamamura, I., & Onaka, T. 1998, A&A, 330, L17

Justtanont, K., de Jong, T., Tielens, A. G. G. M., Feuchtgruber, H., & Waters, L. B. F. M. 2004, A&A, 417, 625

Justtanont, K., et al. 2005, A&A, 439, 627

Kafatos, M., Michalitsianos, A. G., & Hollis, J. M. 1986, ApJS, 62, 853

Kahane, C., Maizels, C., & Jura, M. 1988, ApJ, 328, L25

Kahane, C., Audinos, P., Barnbaum, C., & Morris, M. 1996, A&A, 314, 871

Kellogg, E., Pedelty, J. A., & Lyon, R. G. 2001, ApJ, 563, L151

Kellogg, E., Anderson, C., Korreck, K., DePasquale, J., Nichols, J., Sokoloski, J. L., Krauss, M., & Pedelty, J. 2007, ApJ, 664, 1079

Kessler, M. F., et al. 1996, A&A, 315, L27

Knapp, G. R., & Morris, M. 1985, ApJ, 292, 640

Knapp, G. R., Jorissen, A., & Young, K. 1997, A&A, 326, 318

Knapp, G. R., Young, K., Lee, E., & Jorissen, A. 1998, ApJS, 117, 209

Knapp, G. R., Dobrovolsky, S. I., Ivezić , Z., Young, K., Crosas, M., Mattei, J. A., & Rupen, M. P. 1999, A&A, 351, 97

Knapp, G. R., Crosas, M., Young, K., & Ivezić, Ž. 2000, ApJ, 534, 324

Knapp, G. R., Pourbaix, D., Platais, I., & Jorissen, A. 2003, VizieR Online Data Catalog, 340, 30993

Köhler, R. 2005, Astronomische Nachrichten, 326, 563

Kotnik-Karuza, D., Jurkic, T., & Friedjung, M. 2007, Baltic Astronomy, 16, 98

Kozasa, T., Dorschner, J., Henning, T., & Stognienko, R. 1996, A&A, 307, 551

Lagadec, E., Mékarnia, D., de Freitas Pacheco, J. A., & Dougados, C. 2005, A&A, 433, 553

Lagadec, E., Chesneau, O., Zijlstra, A. A., Matsuura, M., & Mékarnia, D. 2007, Asymmetrical Planetary Nebulae IV,

Lambert, D. L., Gustafsson, B., Eriksson, K., & Hinkle, K. H. 1986, ApJS, 62, 373

Lane, A. P., Johnston, K. J., Spencer, J. H., Bowers, P. F., & Diamond, P. J. 1987, ApJ, 323, 756

Lattanzi, M. G., Munari, U., Whitelock, P. A., & Feast, M. W. 1997, ApJ, 485, 328

Lawson, P. R. 2000a, Principles of Long Baseline Stellar Interferometry

Lawson, P. R., Colavita, M. M., Dumont, P. J., & Lane, B. F. 2000b, Proc. SPIE, 4006, 397

Lebzelter, T., Posch, T., Hinkle, K., Wood, P. R., & Bouwman, J. 2006, ApJ, 653, L145

Leinert, C., et al. 2003, Ap&SS, 286, 73

Lewis, B. M., David, P., & Le Squeren, A. M. 1995, A&AS, 111, 237

Little, S. J., Little-Marenin, I. R., & Bauer, W. H. 1987, AJ, 94, 981

Lloyd Evans, T. 1991, MNRAS, 248, 479

Lord, S. D. 1992, NASA Tech. Mem., 103957

Lorenz-Martins, S., & Pompeia, L. 2000, MNRAS, 315, 856

Loup, C., Forveille, T., Omont, A., & Paul, J. F. 1993, A&AS, 99, 291

Luttermoser, D. G. 2000, ApJ, 536, 923

Luttermoser, D. G., & Brown, A. 1992, ApJ, 384, 634

Luttermoser, D. G., & Mahar, S. 1998, Cool Stars, Stellar Systems, and the Sun, 154, 1613

Maercker, M., et al. 2009, A&A, 494, 243

Markwick, A. J., 2000, PhD thesis, UMIST, *Chemistry in Dynamically Evolving Astrophysical Regions*

Mason, B. D., Wycoff, G. L., Hartkopf, W. I., Douglass, G. G., & Worley, C. E. 2001, AJ, 122, 3466

Matsuura, M., Yamamura, I., Cami, J., Onaka, T., & Murakami, H. 2002, A&A, 383, 972

Matthews, L. D., & Reid, M. J. 2007, Why Galaxies Care About AGB Stars: Their Importance as Actors and Probes, 378, 319

Mayall, M. W. 1965, JRASC, 59, 245

McDonald, I., Sloan, G. C., Zijlstra, A. A., Matsunaga, N., Matsuura, M., Kraemer, K. E., Bernard-Salas, J., & Markwick, A. J. 2010, ApJ, 717, L92

McIntosh, G. C., & Rustan, G. 2007, AJ, 134, 2113

Meier, S. R., & Kafatos, M. 1995, ApJ, 451, 359

Mennesson, B., et al. 2002, ApJ, 579, 446

Michelson, A. A., & Morley, E. W. 1887, Philos. Mag., 24, 449

MIDI Science Group 2003, *MIDI Guaranteed Time Observations Full Observing Proposals*, ESO Doc. No. VLT-SCI-MID-15820-304, Issue 1.0

Millan-Gabet, R., et al. 2003, Proc. SPIE, 4838, 202

Millan-Gabet, R., Pedretti, E., Monnier, J. D., Schloerb, F. P., Traub, W. A., Carleton, N. P., Lacasse, M. G., & Segransan, D. 2005, ApJ, 620, 961

Miyoshi, M., Matsumoto, K., Kameno, S., Takaba, H., & Lwata, T. 1994, Nature, 371, 395

Monnier, J. D., Danchi, W. C., Hale, D. S., Tuthill, P. G., & Townes, C. H. 2000, ApJ, 543, 868

Monnier, J. D. 2003, Reports on Progress in Physics, 66, 789

Monnier, J. D., et al. 2004, ApJ, 605, 436

Morris, M. 1987, PASP, 99, 1115

Muller, S., Dinh-V-Trung, He, J.-H., & Lim, J. 2008, ApJ, 684, L33

Neugebauer, G., et al. 1984, ApJ, 278, L1

Nichols, J., & Slavin, J. D. 2009, ApJ, 699, 902

Noll, R. J. 1976, Journal of the Optical Society of America (1917 – 1983), 66, 207

Ohnaka, K. 2004, A&A, 424, 1011

Ohnaka, K., et al. 2005, A&A, 429, 1057

Ohnaka, K., et al. 2006, A&A, 445, 1015

Ohnaka, K., Driebe, T., Weigelt, G., & Wittkowski, M. 2007, A&A, 466, 1099

Olivier, E. A., & Wood, P. R. 2003, ApJ, 584, 1035

Olivier, E. A., Whitelock, P., & Marang, F. 2001, MNRAS, 326, 490

Olofsson, H., González Delgado, D., Kerschbaum, F., & Schöier, F. L. 2002, A&A, 391, 1053

Onaka, T., de Jong, T., & Willem, F. J. 1989, A&A, 218, 169

Paladini, C., Aringer, B., Hron, J., Nowotny, W., Sacuto, S., Höfner, S. 2009, A&A, 501, 1073

Pardo, J. R., Alcolea, J., Bujarrabal, V., Colomer, F., del Romero, A., & de Vicente, P. 2004, A&A, 424, 145

Paresce, F., et al. 1991, ApJ, 369, L67

Paresce, F., & Hack, W. 1994, A&A, 287, 154

Parker, E. N. 1958, ApJ, 128, 664

Pauls, T. A., Young, J. S., Cotton, W. D., & Monnier, J. D. 2005, PASP, 117, 1255

Percheron, I. 2008, New Astronomy Review, 52, 186

Perrin, G., et al. 2004, A&A, 426, 279

Perrin, G., et al. 2007, A&A, 474, 599

Perryman, M. A. C., et al. 1997, A&A, 323, L49

Perryman, M. A. C., & ESA 1997, ESA Special Publication, 1200

Pojmanski, G., Pilecki, B., & Szczygiel, D. 2005, Acta Astronomica, 55, 275

Posch, T., Kerschbaum, F., Mutschke, H., Fabian, D., Dorschner, J., & Hron, J. 1999, A&A, 352, 609

Quirrenbach, A. 1999, in Principles of Long-Baseline Interferometry, ed. P. R. Lawson, Michelson Fellowship Program, 71 – 86

Quirrenbach, A. 2001, ARA&A, 39, 353

Ragland, S., et al. 2006, ApJ, 652, 650

Ragland, S., et al. 2008, ApJ, 679, 746

Ramstedt, S., Schöier, F. L., Olofsson, H., & Lundgren, A. A. 2008, A&A, 487, 645

Ratzka, T. 2005, Ph.D. Thesis, University Heidelberg

Reid, M. J., & Menten, K. M. 1990, ApJ, 360, L51

Reid, M. J., & Menten, K. M. 2007, ApJ, 671, 2068

Reimers, D., 1975, *Sociètè Royale des Sciences de Liège, Memoires*, 8, 369

Sahai, R., Morris, M., Knapp, G. R., Young, K., & Barnbaum, C. 2003, Nature, 426, 261

Sahai, R., Sugerman, B. E. K., & Hinkle, K. 2009, ApJ, 699, 1015

Sahai, R., & Wannier, P. G. 1988, A&A, 201, L9

Samus, N. N., Durlevich, O. V., & et al. 2009, VizieR Online Data Catalog, 1, 2025

Schöier, F. L., & Olofsson, H. 2001, A&A, 368, 969

Scholz, M. 2001, MNRAS, 321, 347

Schwarzschild, M. 1975, ApJ, 195, 137

Sedlmayr, E. 1994, IAU Colloq. 146: Molecules in the Stellar Environment, 428, 163

Skrutskie, M. F., et al. 2006, AJ, 131, 1163

Sloan, G. C., Little-Marenin, I. R., & Price, S. D. 1998a, AJ, 115, 809

Sloan, G. C., & Price, S. D. 1998b, ApJS, 119, 141

Smith, B. J., Price, S. D., & Moffett, A. J. 2006, AJ, 131, 612

Soker, N. 1992, ApJ, 389, 628

Steffen, M., & Schönberner, D. 2000, A&A, 357, 180

Stute, M., & Sahai, R. 2007, ApJ, 665, 698

Suh, K.-W. 2004, ApJ, 615, 485

Szymczak, M., Cohen, R. J., & Richards, A. M. S. 1998, MNRAS, 297, 1151

Takaba, H., Iwate, T., Miyaji, T., & Deguchi, S. 2001, PASJ, 53, 517

Tatebe, K., Chandler, A. A., Hale, D. D. S., & Townes, C. H. 2006, ApJ, 652, 666

Tej, A., Lançon, A., & Scholz, M. 2003, A&A, 401, 347

Teyssier, D., Hernandez, R., Bujarrabal, V., Yoshida, H., & Phillips, T. G. 2006, A&A, 450, 167

Tielens A.G.G.M. 1990, in From Miras to Planetary Nebulae: Which Path for Stellar Evolution? Proceedings of the International Colloquium, Montpellier, France. Gif-sur-Yvette, France: Editions Frontieres, p. 186

Thompson, R. R., Creech-Eakman, M. J., & van Belle, G. T. 2002, ApJ, 577, 447

Thompson, R. R., & Creech-Eakman, M. J. 2004, Bulletin of the American Astronomical Society, 36, 1357

Trammell, S. R., Dinerstein, H. L., & Goodrich, R. W. 1994, AJ, 108, 984

Traub, W. A. 1999, in Principles of Long-Baseline Interferometry, ed. P. R. Lawson, Michelson Fellowship Program, 3158

Tristram, K. R. W. 2007, Ph.D. Thesis, University Heidelberg

Tsuji, T., Unno, W., Kaifu, N., Izumiura, H., Ukita, N., Cho, S., & Koyama, K. 1988, ApJ, 327, L23

Tsuji, T., Ohnaka, K., Aoki, W., & Yamamura, I. 1997, A&A, 320, L1

Tuthill, P. G., Haniff, C. A., & Baldwin, J. E. 1999, MNRAS, 306, 353

Tuthill, P. G., Danchi, W. C., Hale, D. S., Monnier, J. D., & Townes, C. H. 2000, ApJ, 534, 907

Ueta, T., et al. 2006, ApJ, 648, L39

van Belle, G. T., Dyck, H. M., Benson, J. A., & Lacasse, M. G. 1996, AJ, 112, 2147

van Belle, G. T., Dyck, H. M., Thompson, R. R., Benson, J. A., & Kannappan, S. J. 1997, AJ, 114, 2150

van Belle, G. T., et al. 1999, AJ, 117, 521

van Belle, G. T., Thompson, R. R., & Creech-Eakman, M. J. 2002, AJ, 124, 1706

van Leeuwen, F., Feast, M. W., Whitelock, P. A., & Yudin, B. 1997, MNRAS, 287, 955

Vassiliadis, E., & Wood, P. R. 1993, ApJ, 413, 641

Verhoelst, T., van der Zypen, N., Hony, S., Decin, L., Cami, J., & Eriksson, K. 2009, A&A, 498, 127

Vlemmings, W., Diamond, P. J., & van Langevelde, H. J. 2001, A&A, 375, L1

Vlemmings, W. H. T., van Langevelde, H. J., Diamond, P. J., Habing, H. J., & Schilizzi, R. T. 2003, A&A, 407, 213

Wachter, A., Winters, J. M., Schröder, K.-P., & Sedlmayr, E. 2008, A&A, 486, 497

Wallerstein, G., & Greenstein, J. L. 1980, PASP, 92, 275

Wareing, C. J., et al. 2006, MNRAS, 372, L63

Weiner, J., Hale, D. D. S., & Townes, C. H. 2003, ApJ, 588, 1064

Werner, M. W., et al. 2004, ApJS, 154, 1

Whitelock, P., & Feast, M. 2000, MNRAS, 319, 759

Whitelock, P. A., Feast, M. W., van Loon, J. T., & Zijlstra, A. A. 2003, MNRAS, 342, 86

Whitelock, P. A., Feast, M. W., & van Leeuwen, F. 2008, MNRAS, 386, 313

Wilson, R. E. 1953, Carnegie Institute Washington D.C. Publication, 0

Willson, L. A., Garnavich, P., & Mattei, J. A. 1981, Information Bulletin on Variable Stars, 1961, 1

Wittkowski, M., Boboltz, D. A., Ohnaka, K., Driebe, T., & Scholz, M. 2007, A&A, 470, 191

Woitke, P., & Niccolini, G. 2005, A&A, 433, 1101

Woitke, P. 2006, A&A, 460, L9

Woitke, P. 2006, A&A, 452, 537

Wood, P. R., & Zarro, D. M. 1981, ApJ, 247, 247

Wood, P. R. 2000, Publications of the Astronomical Society of Australia, 17, 18

Woodruff, H. C., Tuthill, P. G., Monnier, J. D., Ireland, M. J., Bedding, T. R., Lacour, S., Danchi, W. C., & Scholz, M. 2008, ApJ, 673, 418

Woodruff, H. C., et al. 2004, A&A, 421, 703

Woodruff, H. C., et al. 2009, ApJ, 691, 1328

Wyatt, S. P., & Cahn, J. H. 1983, ApJ, 275, 225

Yamamura, I., de Jong, T., & Cami, J. 1999, A&A, 348, L55

Young, T. 1804, Philos. Trans. R. Soc. London, 94, 1

Young, K., Phillips, T. G., & Knapp, G. R. 1993, ApJ, 409, 725

Zijlstra, A. A., Bedding, T. R., & Mattei, J. A. 2002, MNRAS, 334, 498

Ziurys, L. M., Tenenbaum, E. D., Pulliam, R. L., Woolf, N. J., & Milam, S. N. 2009, ApJ, 695, 1604

Zubko, V., & Elitzur, M. 2000, ApJ, 544, L137

Zuckerman, B., Palmer, P., Morris, M., Turner, B. E., Gilra, D. P., Bowers, P. F., & Gilmore, W. 1977, ApJ, 211, L97

Zuckerman, B., & Dyck, H. M. 1986, ApJ, 311, 345

Acknowledgment

I would like to thank the *International Max-Planck Research School* (IMPRS) for its financial support with a fellowship, and the PIs, Andreas Quirrenbach and Bruno Lopez, of the MIDI GTO program on late-type stars for providing me with the data analyzed in this thesis.

I thank also Walter Jaffe, Rainer Köhler and others involved for making publicly available the MIDI data reduction software packages and in particular the `SCI-PHOT` reduction routines.

I acknowledge with thanks the variable star observations from the AAVSO International Database contributed by observers worldwide and used in this research. This research has made use of the SIMBAD database, operated at the CDS, France, the ISO/IRAS database and NASA's Astrophysical Data System.

I thank Markus Wittkowski and Keiichi Ohnaka for fruitful discussion, and Henry Woodroff and Mike Ireland for making diameter data sets available.

I would also like to thank all those people who helped me on my way to finally hand in this thesis. First of all, I would like to thank my supervisor Andreas Quirrenbach for his guidance over the more than last three years.

Cornelis Dullemond agreeing to referee the thesis, and Joachim Krautter and Matthias Bartelmann for being jury members at the defense.

My friends at the Landessternwarte and MPIA, and the people who proofreaded this thesis, including Ingo Stilz, Rainer Köhler, Sabine Reffert, Nicholas Elias, Ralf Launhardt, André Germeroth, André Müller and many more.

Yun Zhao for giving me so much support during the last years. Thank you for loving and marrying me.

A big thank you to my family, who is always supporting me, including my mom, my dad, my sister and my grandparents. In particular my grandpa, who cannot celebrate this day with me.

Finally a heartily thank you to all the people I have not mentioned specifically here, but who helped me on my long way.